LABORATORY AND MODELLING STUDIES OF THE SORPTION OF ARSENIC ON GOETHITE.

~~AN EXPERIMENTAL AND MODELLING STUDY OF THE SORPTION OF ARSENIC ON GOETHITE~~

Alison Lynne Carruthers

Department of Chemistry,
University College London,
Gower Street,
London, UK

This thesis is submitted for fulfilment of the award of Ph.D.

November 2004

ProQuest LLC
789 East Eisenhower Parkway
P.O. Box 1346
Ann Arbor, MI 48106-1346

ABSTRACT

An understanding of arsenic interactions with mineral surfaces in aqueous environments is important if arsenic transport in groundwater is to be predicted. This study contributes to the understanding of arsenic (As(V)) adsorption onto goethite (α-FeOOH) by linking equilibrium batch experiments and dynamic column experiments to the use of atomistic modelling. In this way the mechanisms of arsenic adsorption onto goethite surfaces are explored.

The equilibrium batch experiments illustrate the declining affinity of As(V) as a negatively charged oxy-anion to sorption on goethite, with increasing solution pH. These experiments also demonstrate that non-linear, Freundlich or Langmuir adsorption is favoured. Partition coefficients obtained are consistent with previously published values.

Column experiments using goethite distributed in quartz grains under a range of conditions of flow velocity, influent arsenic concentration and goethite mass concentration, being more representative of natural conditions of groundwater flow, have provided new observations on As(V) adsorption. The one-dimensional solute transport code BIO1D has been used to simulate the advection and sorption processes and to fit partition coefficients to the experimental breakthrough curves. Linear and Freundlich isotherms both provide a close representation of the experimental data. The results demonstrate that the partition coefficients under dynamic flow conditions are up to three orders of magnitude less than those derived from the equilibrium batch experiments. Also, the partition coefficients show an inverse relationship with flow velocity, indicating a kinetic effect.

Experimental variation of the column redox conditions has enabled the determination of a pseudo-partition coefficient for sorption under anaerobic conditions, which is up to a quarter of that derived under aerobic conditions.

Atomistic modelling shows that the (011) and (111) surfaces of goethite are preferential for binding As(V) as $AsO(OH)_3$. The model simulations also indicate

that monodentate–mononuclear complexes are favoured over bidentate–binuclear formations. The results show a preferential orientation for the adsorbed As(V) molecule, with the hydroxyl groups lying parallel and the oxygen anion perpendicular to the goethite surface. The preferred complexation mechanisms and the relative energetics calculated using the atomistic models are good indicators of the non-linear adsorption observed in the experimental work.

TABLE OF CONTENTS

FIGURES

TABLES

THESIS STRUCTURE

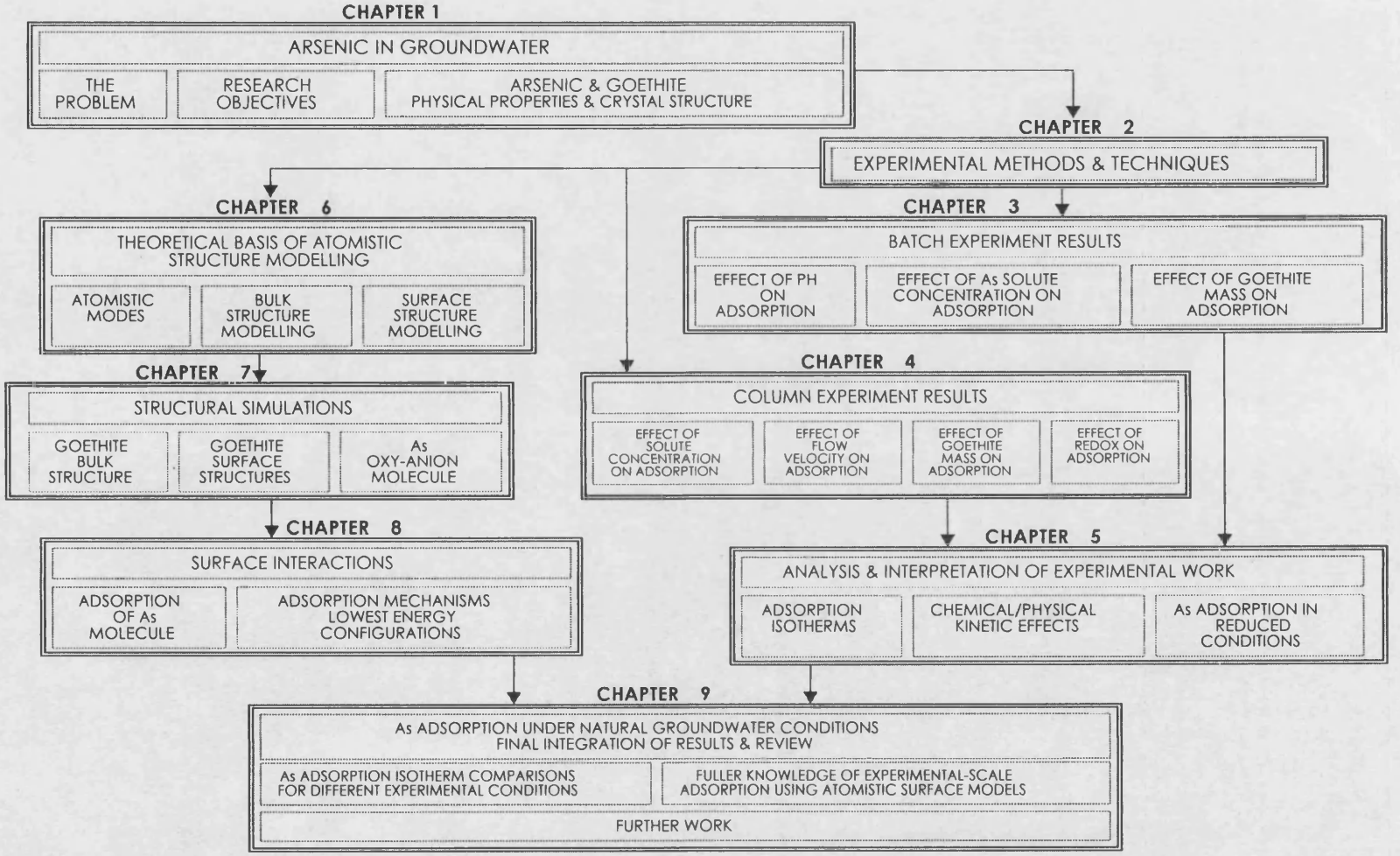

1. INTRODUCTION

1.1. ARSENIC IN GROUNDWATER – THE PROBLEM

Arsenic is an element that is found in natural environments and usually occurs within the concentration range of 1.0 – 10.0 μg/l in aqueous systems. Igneous rocks and limestones tend to contain the lower concentrations, whereas higher amounts are usually found within sandstone and shales (Smedley and Kinniburgh, 2002). It is in areas of exceptionally high concentrations where there is most concern, owing to the toxic properties of this element.

Arsenic is toxic and causes health problems when absorbed by the human body in sufficient quantities. For example, the early stages of chronic arsenic poisoning manifests itself by the formation of skin lesions and the appearance of black spots leading, in some cases, to a variety of cancers (Chakraborti *et al.*, 1999). Owing to the toxicity of arsenic, the World Health Organisation (WHO) has set a drinking water guideline value of 10 μg/l. In most natural water used for drinking purposes the arsenic concentration is well below this limit, nonetheless there are a number of examples where the concentrations are far exceeded (Smedley and Kinniburgh, 2002). The most severe, in terms of both arsenic concentration and the size of population effected, is the case of the Bengal Basin of Bangladesh and neighbouring West Bengal in India (Smedley and Kinniburgh, 2002).

Within the natural environment arsenic transport is influenced by a number of geochemical and physical conditions. A couple of contrasting examples of the diverse environmental conditions for elevated concentrations of arsenic include the Bengal Basin and La Pampa, Argentina. Groundwater in the Bengal Basin is naturally reducing with circum-neutral pH. In this case naturally occurring arsenic is believed to be released by reduction of iron-oxides and hydroxides present within the sediment, and by reduction of arsenic from As(V) to As(III). By contrast the ground waters in La Pampa, Argentina are universally

geochemically oxidising and arsenic is released due to the high alkalinity of the groundwater (Smedley *et al.*, 2002).

The iron-oxhydroxide mineral, goethite, is the most common iron oxide mineral found in solids (O'Reilly *et al.*, 2001) and arsenic has been found to have a high affinity for goethite in natural aquifer sediments (Smedley & Kinniburgh, 2002 and Stollenwerk, 2003). For example sediments surrounding the Ashanti mining region in Ghana (Bowell, 1994) and Bangladesh Holocene sediments (Ravenscroft *et al.*, 2001). Other iron oxide minerals such as ferrihydrite or magnetite also strongly adsorb arsenic but have not been considered within the scope of this study. Goethite has been chosen as a precursor to understand the processes of arsenic adsorption using experiments and modelling that can be further applied to more complex minerals.

The exposure of humans to arsenic from drinking water and the movement of arsenic towards boreholes used for the water supply is of concern and in need of understanding. To predict the movement of arsenic towards tubewells the arsenic interactions with mineral surfaces within the aqueous system has been the subject of extensive hydrogeochemical studies to understand the processes both qualitatively and quantitatively.

1.2. AIMS AND OBJECTIVES

1.2.1. Research Strategy

The contamination, and therefore elevated concentrations of arsenic in groundwater is widespread and may have severe effects upon much of the population exposed. Fully understanding its source, transmission and deposition is very important in helping alleviate its effects. Although there are various suggestions as to the mechanisms of arsenic release, it is the transport of arsenic through the aquifers that is of interest in this study. In particular, it is the parameters describing arsenic sorption in groundwater systems that are poorly defined. The study aims to provide an insight into the adsorption mechanisms involved in the adsorption of arsenic onto goethite, an important aquifer mineral.

Although there have been several published batch experiments studying the adsorption onto iron oxides and hydroxides, the new experiments in the current study will expand on these by using column experiments to determine dynamic adsorption whilst maintaining consistency between the batch and columns.

There are few published column experiment studies that attempt to address arsenic adsorption onto the important mineral goethite. The new batch experiments describe equilibrium adsorption, and also derive a set of partition coefficients that are consistent and comparable with those found from the columns. The column experiments aim to explore dynamic adsorption, under a variety of initial arsenic concentrations, goethite mass present within the columns, and also kinetic effects by altering the flow rate through the column.

Finally, the experiments attempt to explore the effect of chemical reduction upon arsenic transport within the column. This experiment is secondary to the study due to the potential difficulties that may be encountered when assessing As(III) adsorption without inducing a completely anaerobic experimental and sampling environment. However this experiment may be used as a guide to

future redox column experiments. The column experiments and batch experiments are concerned only with monitoring arsenic interactions with goethite (α-FeOOH). Goethite was chosen as a suitable adsorbent as it one of the most common aquifer minerals and from previous investigations of arsenic contaminated groundwaters, is known to have a high affinity with arsenic. In all experiments it is the pentavalent form of arsenic that is used for the initial solutions as it is the more stable form under normal laboratory conditions and could be used to assess comparative studies herein, without added complexities of possible oxidation of As(III).

Concurrent with the experimental work, atomistic modelling was used to simulate the interactions between arsenic and iron oxy-hydroxide (goethite) surfaces. The modelling results are indicative of those areas on common surfaces that are likely binding sites and also the likely type of binding involved. With knowledge of the adsorption sites, and knowing the distribution of those surfaces over the crystal morphology, an indication of the amounts of arsenic adsorbed is possible and this allows comparison with the experimental results.

1.2.2. Summary of Objectives

Two scales of observation were used to identify As-goethite surface interactions for describing the adsorption and desorption processes of arsenic under natural groundwater conditions.

1. **Macroscopic scale experiments to identify:**

   the amount of As adsorption in terms of partition coefficients for:

   - equilibrium adsorption using batch experiments;
   - dynamic adsorption using column experiments to simulate natural flow conditions; and
   - adsorption under different groundwater redox conditions;

   the effect of groundwater pH on adsorption;

   the effect of chemical or physical kinetics on adsorption under natural flow conditions; and

   the extent of arsenic desorption under reducing groundwater conditions.

2. **Atomic scale structured models to identify:**

   As-goethite surface interactions describing the structural mechanisms of adsorption that require:

   - a successful model of the goethite bulk and surface structure;
   - a successful model of a representative As oxy-anion in solution; and
   - simulations of force-field interactions between the As oxy-anion and goethite surface; and

   a fuller knowledge of the experimental-scale adsorption using atomic-level calculations.

Cross correlation and linkage between the two approaches provides a fuller understanding of the process of adsorption and As–goethite interface interactions in aqueous conditions.

1.3. STUDIES OF ARSENIC OCCURRENCE IN GROUNDWATER

1.3.1. Geochemical Conditions of As Occurrence in Groundwater

In general there are three groups defining the sources of elevated arsenic within groundwaters (Smedley and Kinniburgh, 2002). These include:

(1) naturally occurring arsenic in low temperature groundwaters, usually in young sediments (Quaternary, Holocene and Recent);

(2) arsenic in geothermal waters; and

(3) elevated arsenic concentrations resulting from mining activity.

Examples of each of these groups are found worldwide including Argentina, Bangladesh, West Bengal (India), Mexico and SW USA, where natural contamination, and elevated levels above background, occurs (Smedley *et al.* (2002) and BGS and MML (1999)); in Japan, New Zealand, Iceland and California in the USA, where geothermal waters contribute towards elevated aqueous arsenic concentrations (Welch *et al.* (1988) and Yokoyama *et al.* (1993)); and in parts of Ghana, South Africa, Thailand and throughout the USA, including Alaska, Idaho, Nevada and California, where arsenic, released from oxidised sulphide minerals related to mining activity, has caused severe and localised elevated concentrations (Smedley & Kinniburgh (2002), Carrillo-Chavez *et al.* (2000)).

The mode of arsenic release into the environment differs between each group and the diversity of arsenic occurrence is illustrated in the following examples. In Bangladesh and West Bengal (India) a combined population of 36 million is exposed to elevated levels of arsenic in groundwater (Smedley & Kinniburgh, 2002). During the late 1970s and early 1980s tubewells were drilled into the shallow aquifers (usually less than 100 m depth) in an attempt to overcome the problem of drinking bacterially contaminated surface water. The aquifer in which the arsenic-rich water resides is the Holocene mica-rich sand and silts deposited by the Ganges, Brahmaputra and Meghna river systems (Smedley & Kinniburgh, 2002). A chemically reducing environment, imposed by the presence of organic matter within the sedimentary sequence in the shallow

aquifer, is thought to be the cause of such high arsenic concentrations. The exact mechanism of arsenic release is still debated, although there are several theories (Ravenscroft *et al.*, 2001). One way in which arsenic may be released is by reduction (from As(V) to As(III)) in the solid phase leading to desorption from iron oxides. Alternatively, reductive dissolution of the iron mineral phase or reductive changes to the mineral surface structure and properties may result in the release of arsenic (Stollenwerk, 2003). Arsenic in these regions occurs naturally and is adsorbed onto iron oxides and oxyhydroxides within the young aquifer sediments (Ravenscroft *et al.*, 2001). However, due to the reductive nature of the groundwater any iron phases present dissolve, as Fe(III) phases reduce to Fe(II) (Nickson *et al.*, 2000). The redox reaction involving iron oxy-hydroxides is shown to be (Ravenscroft *et al.*, 2001):

$$8FeOOH + CH_3COOH + 14H_2CO_3 \rightarrow 8Fe^{2+} + 16HCO_3^- + 12H_2O \qquad \textit{Eqn. 1.3.1.}$$

Where the carbon molecules (acetate) represent the presence of organic matter. The arsenic is released into groundwater under these conditions and tests for arsenic in hand-tubewell drinking water in the past decade have highlighted the extent and severity of contamination above background levels. A study of 27 districts in West Bengal, by Chakraborti *et al.* (1999) found that 60 % of sampled water contained arsenic levels exceeding the WHO guideline of 10 μg/l and 24 % contained arsenic concentrations greater than 50 μg/l, which is currently the drinking water limit for arsenic in Bangladesh and West Bengal, India.

Microbially reduced conditions have also been identified for several groundwater environments with elevated As concentrations. For example Islam *et al.* (2004) and McArthur *et al.* (2004) have found that As mobilisation within the Bengal Basin occurs as a result of metal-reducing bacteria. Similarly Harrington *et al.* (1998) identified As(III) generation and mobilisation in Coeur d'Alene Lake sediments, Idaho occurring through microbial electron transfer to As. Microbial reduction of iron through electron transfer can also occur aiding As mobilisation (Jones *et al.* (2000), Raab & Feldmann (2003) and Cummings *et al.* (1999)).

Although it is an unlikely method of arsenic release in Bangladesh owing to the geochemical conditions, the oxidation of sulphide minerals such as pyrite (FeS_2) or arsenopyrite (FeAsS) could also lead to arsenic in groundwater (McArthur *et al.*, 2001). Consequently in highly reducing environments the formation of pyrite may incorporate soluble arsenic within the structure. Other important minerals associated with arsenic are highlighted in Table 1.3.1 and include jarosite and magnetite (Smedley and Kinniburgh, 2002). Arsenic can substitute for a number of elements, such as Si^{4+}, Al^{3+}, Fe^{3+} and Ti^{4+} and can therefore occur within a variety of rock forming minerals, although in comparably small concentrations (Smedley and Kinniburgh, 2002).

Rock Forming Mineral	As Concentration Range (mg/kg)
Iron oxyhydroxide (FeOOH)	76 000
Magnetite (Fe_3O_4)	2.7 – 41
Biotite ($2K[Mg_2Fe][AlSi_3]O_{10}(OH)_2$)	1.4
Jarosite ($KFe_3(SO_4)_3 \cdot 9H_2O$)	34 – 1000
Siderite ($FeCO_3$)	<3

Table 1.3.1. Summary of a selection of important As-bearing iron rock forming minerals, after Smedley and Kinniburgh, 2002.

In Vietnam the contamination caused by arsenic also occurs within deltaic sediments, along the Mekong and Red rivers. Like the process for arsenic release in Bangladesh, the strongly reducing conditions of the shallow aquifer lead to elevated levels of Fe, Mn and As (Polya *et al.*, 2004 and Berg *et al.*, 2001). In this case, research in the area is as recent as 2000 (Berg *et al.*, 2001) and a correlation has been identified between high rains during the monsoon season, and lower arsenic concentrations (Smedley & Kinniburgh, 2002).

In contrast to the two examples above, arsenic contamination in the Lagunera Region (North-central Mexico) occurs under arid, oxidising conditions. Arsenic concentrations have been measured between 8 and 624 μg/l, and out of those tubewells sampled by Del Razo *et al.* (1990), more than 90 % contained arsenic in the pentavalent form [As(V)], with <10 % as the trivalent species [As(III)].

In central Argentina 95 % of groundwater sampled from the Quaternary aquifers of the La Pampa Province contain arsenic in excess of 10 μg/l with 73 % exceeding 50 μg/l (Smedley *et al.*, 2002). The high concentrations of arsenic (4 – 5300 μg/l) in the groundwater is associated with aerobic and alkaline geochemical conditions and arsenic mobilisation is considered to result from desorption from Fe and Mn oxides under the high pH conditions (Smedley *et al.*, 2002).

In the South Carson Desert (Nevada, USA) the granitic and volcanic uplands are the source of arsenic, where concentrations are around 100 μg/l, but can locally be as high as 1000 μg/l (Welch & Lico, 1998). Evaporative concentration and reductive dissolution of the iron oxide phases, enhanced by sedimentary organic matter, are the causes for such high concentrations (Welch & Lico, 1998). Similarly, the reducing condition of groundwater within the Lower Madison River Valley (Montana, USA) promotes the re-release of previously sorbed arsenic (Nimick, 1998).

Mining of ores containing arsenic is particularly prevalent in Mexico. Examples include that of the San Antonio – El Truifno mining district in Baja California, Mexico. For 200 years mining in this area has been rife and surrounding the mineralised areas the arsenic concentrations are especially high (410 μg/l) when compared with the arsenic concentrations away from the mineralised zones (10 μg/l) (Carrillo–Chavez *et al.*, 2000). In this case, the high arsenic concentrations also correspond with high levels of sulphate and bicarbonate (Carrillo–Chavez *et al.*, 2000). In the Zimpan Valley, Mexico, it is the leaching of mine tailings and arsenic bearing rocks that are the cause of contamination (Armienta *et al.*, 2001). The highest concentrations of arsenic (around 750 μg/l) found in the wells in this area may have been released during arsenopyrite oxidation (Armienta *et al.*, 2001). Mining and smelting of the Khetri copper and Zawar lead and zinc deposits in India have contributed to the oxidation of metallic sulphides, and subsequent release of arsenic (Madhavan & Subramanian, 2000). Another example of arsenic contamination, where concentrations are greater than background levels, involves the mining of gold in the Ashanti region in Ghana. In this case the gold is associated with sulphide mineralization, including arsenopyrite, which becomes oxidised during the

mining procedure, and hence releases arsenic into solution. However, it is the relatively more reducing localised groundwaters (redox potential between 220 and 250 mV) that contain the highest arsenic concentrations (Smedley and Kinniburgh, 2002).

1.3.2. Arsenic Transport in Groundwater

To understand and predict the transport and movement of arsenic in groundwater environments, macroscopic transport flow models are useful. However, to accurately simulate the movement of arsenic under different environmental conditions, it is important to understand the physio-chemical mechanisms by which arsenic travels in aqueous environments. This knowledge is essential to extend the modelling for predicting the movement of arsenic-rich groundwater in contaminant plumes surrounding mining spoils or the transport of arsenic to drinking tube-wells in Bangladesh.

The transport of solutes is modelled using the advection and dispersion equation (ADE), also known as the solute transport equation, which describes the spread of the solute with time by advection and dispersion only. The addition of a sorption term to the equation describes the retardation of arsenic in solution in terms of the mass of arsenic adsorbed per mass of goethite, as defined by suitable adsorption isotherms.

Solute Transport Equation (Srinivasan & Mercer, 1987):

$$D(\partial^2C/\partial x^2) - V_x(\partial C/\partial x) - [1+S(C)]\,(\partial C/\partial t) = 0 \qquad \textit{Eqn. 1.3.2.}$$

C = Solute concentration in pore water (M/L^3)
D = Longitudinal hydrodynamic dispersion coefficient (L^2/T)
x = Distance (L)
V_x = Interstitial field velocity (L/T); assumed uniform
S(C) = Amount of adsorption, described by an adsorption isotherm as a function of C ($M_{arsenic}/M_{goethite}$)
t = Time (T)

A study by Cuthbert (1999) attempted to model the transport of arsenic within the groundwater in Bangladesh. The modelling focused on the adsorption of arsenic onto natural aquifer minerals (mostly iron oxides and hydroxides) in terms of partition coefficients. The parameters used for the models were from pre-simulated adsorption isotherms of arsenic adsorption onto iron oxide minerals. However, the coefficient values and parameters did not account for the redox environment within the groundwater, and were determined in terms of equilibrium adsorption and not for dynamic flow.

1.4. ARSENIC CHARACTERISTICS

Arsenic (As) is an unusual element, in that it is a group V metalloid that displays non-metallic properties (Norman, 1998). It has a ground state electron configuration of $[Ar]3d^{10}4s^24p^3$, and its ionic radius and valency allow it to substitute for other elements, for example in sulphides (Madhavan & Subramanian, 2000). Arsenic tends to form complexes with metallic elements, or covalently bond to elements such as carbon, hydrogen or oxygen (Gorby, 1994).

There are two types of arsenic compound in nature (Naqvi *et al.*, 1994):

(a) aqueous compounds of O, Cl or S which are usually more toxic and mobile in groundwater than organic compounds formed when As is bound to C and H, such as $CH_3AsO(OH)_2$ and other methylated arsenic species; and

(b) solid-phase As sulphides such as arsenopyrite (FeAsS), realgar (As_4S_4) and orpiment (As_2S_3) (Norman, 1988), although it can also be found in association with scorodite and tennantite ores in the Mexican mining valley of Zimpan (Armienta *et al.*, 2001).

Other important inorganic As hosts include pyrite (FeS_2), the iron arsenate loellingite ($FeAs_2$) and substitution of As for sulphate in jarosite ($KFe_3(SO_4)_3{\cdot}9H_2O$) (Fitts *et al.*, 1997). Secondary arsenic phases include claudetite (As_2O_3), scorodite ($FeAsO_4{\cdot}H_2O$), Annabergite $(Ni,Co)_3(AsO_4)_2{\cdot}8H_2O$), Hoernesite ($Mg_3(AsO_4)_2{\cdot}8H_2O$) and Conichalcite ($CaCu(AsO_4)(OH)$) (Smedley and Kinniburgh, 2002).

As(III) and As(V) have a high affinity for iron, aluminium and manganese oxides, which are often amorphous and are thus not classified as minerals, in aquifer sediments (Jackson and Miller, 2000). In Bangladesh sediments As is associated with iron oxides that are common in the aquifer material (Nickson *et al.*, 1998). It is the combination of abundance and the surface chemistries in aquifer sediments that makes them important As sources and sinks (Stollenwerk, 2003).

Dissolved arsenic occurs in two valency states, as arsenate [As(V)] or as arsenite [As(III)], depending on the environmental parameters controlling the species type (Fetter, 1998). The stability diagram (Figure 1.4.1) illustrates the various species of arsenic likely to exist under a range of pH and redox conditions within the aqueous environment. In oxygen-rich conditions, As(V) is most likely to be found in the form of the arsenic acid series (H_3AsO_4, $H_2AsO_4^-$, $HAsO_4^{2-}$ and AsO_4^{3-}). However, under reducing conditions As(III) is more dominant, forming arsenious acids H_3AsO_3, $H_2AsO_3^-$ and $HAsO_3^{2-}$ (Ferguson & Gavis, 1972).

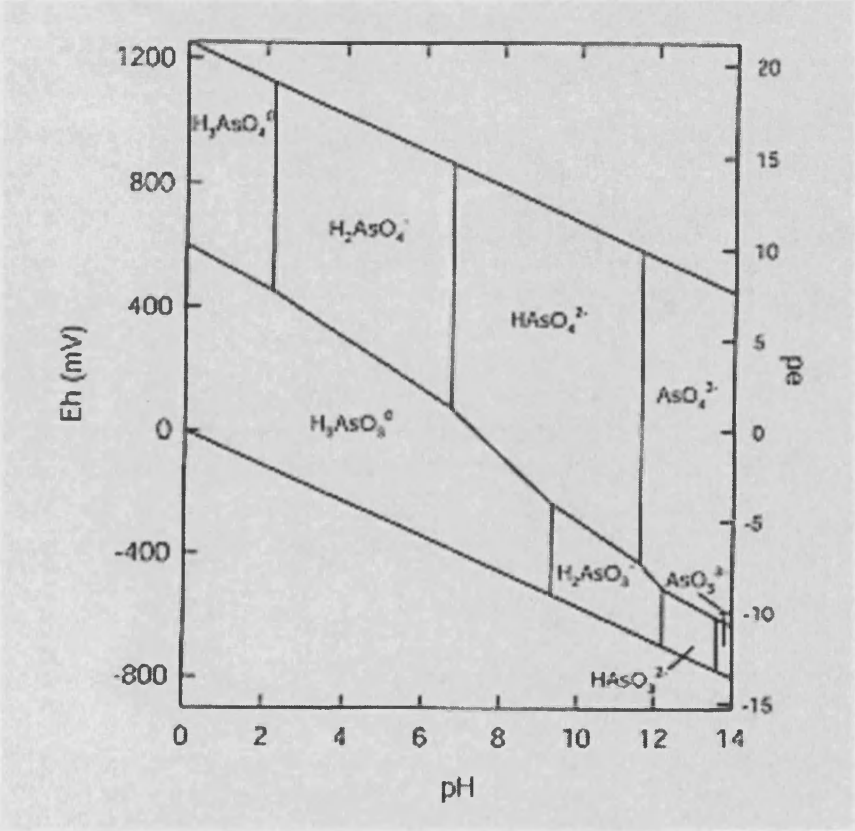

Figure 1.4.1. Arsenic stability diagram (Smedley and Kinniburgh, 2002). [As] = 10^{-6} M and [CO_3] = 10^{-3} M.

1.5. GOETHITE CHARACTERISTICS

Goethite (α-FeO.OH) is one of the most ubiquitous rock forming minerals, usually formed in oxygen-rich environments from the weathering of iron-rich minerals. Goethite is also commonly found in bogs and springs as inorganic and biogenic precipitates formed in aqueous conditions (Klein & Hurlbut, 1993). Although goethite can comprise between 1 and 5 % of a soil composition, its surface area as a whole can extend to between 50 and 70 % of the total soil surface area (Rakovan *et al.*, 1999). This is due to the fine acicular morphology of goethite, with individual crystals up to 4 μm in length and with surface areas ranging from 27 to 33 m^2/g (Randall *et al.*, 1999). Goethite also displays a high affinity for adsorbing cations and anions, including metallic and metalloid elements. It is this feature that has prompted much of the research into the characteristics of goethite and the surface interactions between goethite and various aqueous contaminants [(Collins *et al.*, 1999), (Su & Suarez, 2000), (Suzuki *et al.*, 2001), (Rakovan *et al.*, 1999), (Randall *et al.*, 1999), (Ostergren *et al.*, 2000 [i & ii]) and (Farquhar *et al.*, 2002)].

Goethite falls into the orthorhombic crystal class, with a symmetry of *pnma*, although the *pbnm* space group has been applied to more recent experimental studies to retain the original crystallographic axes assigned to goethite (Manceau *et al.*, 2000). It forms acicular crystals (Figure 1.5.1), which are often flattened parallel to the perfect cleavage plane (010).

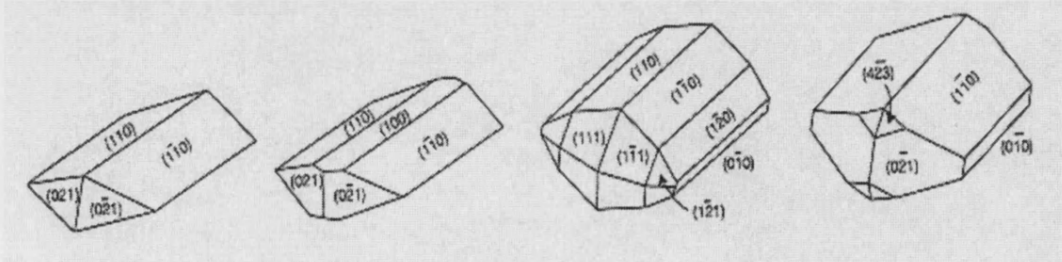

Figure 1.5.1. Examples of both natural and synthetic goethite morphology (from Manceau *et al.*, 2000).

The goethite unit cell has a typical 'a' length of 4.608 Å, 'b' of 9.956 Å, and 'c' of 2.021 Å (Cornell & Schwertmann, 1996). Cornell and Schwertmann (1996) also suggest that the 'a' cell length is proportional to crystal disorder, and so greater disorder will increase the 'a' cell length. The crystal structure of goethite is isostructural with diaspore (AlO.OH) and one unit cell, of repeating unit, will contain four (FeO.OH) units. The goethite structure is constructed with O^{2-} and OH^- ions stacked along the [100] plane, with the Fe^{3+} ions falling into double rows, and separated by empty double rows (Figure 1.5.2) (Cornell & Schwertmann, 1996). The double rows of iron share their edges in an octahedral configuration, and these rows are connected by sharing oxygen at the edges (Rakovan *et al*, 1999). Surrounding every iron atom are three O^{2-} ions and three OH^- groups, which make up the octahedral structure (Figure 1.5.3 and 7.2.1 in Chapter 7.2). It is these octahedra that are then grouped in double chains and linked together by edge-sharing, which lie parallel to the (001) plane. Although the (010) surface is the perfect cleavage, a moderate cleavage exists in the (100) direction, and other important growth surfaces include (110), (120), (111) and (101).

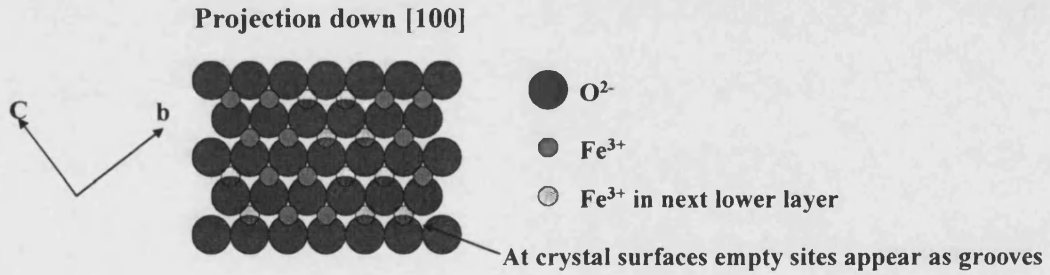

Figure 1.5.2. Schematic representation of the crystal structure of goethite (reproduced from Cornell and Schwertmann, 1996).

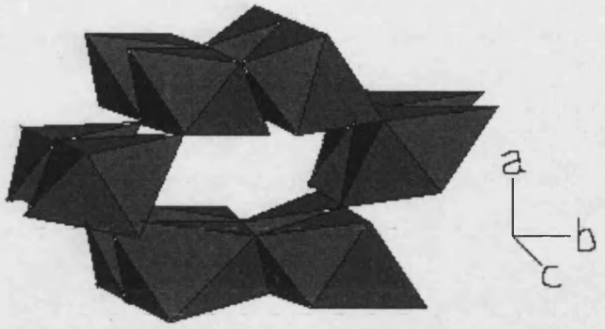

Figure 1.5.3. Schematic illustration of the goethite structure, where the polyhedra represent Fe in octahedral coordination (after Rakovan *et al.* 1999).

Goethite crystals are stable under aerobic conditions because the iron becomes soluble in more reducing environments. This results from the reduction of iron within the goethite from Fe^{3+} to Fe^{2+}, under normal groundwater pH (8 – 5), as illustrated in the redox diagram, Figure 1.5.4.

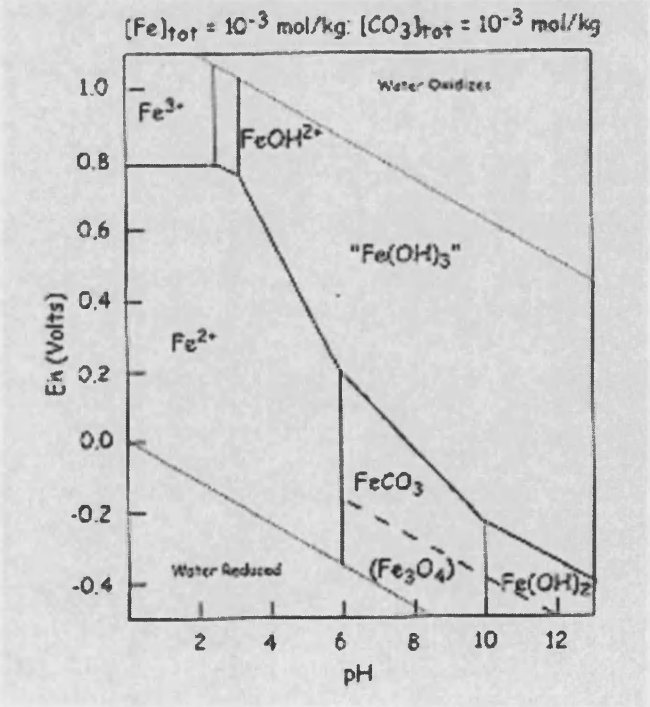

Figure 1.5.4. Redox diagram for iron (from Sherman (2002)).

The surface charge on the goethite surfaces is a significant factor in the adsorption of ions onto its surface (Stollenwerk, 2003). The surface charge largely depends on the pH of the solution in contact with goethite (Bowell, 1994). Experimental studies of the effect of solution pH upon ion adsorption onto various oxide mineral surfaces have illustrated this importance of pH. The same is true for the adsorption of As(V) onto iron oxides and hydroxides (Pierce & Moore, 1982, Haron *et al.*, 1999, Khaodhiar *et al.*, 2000, Loeppert *et al.*, 1997, Bowell, 1994, and Chakravarty *et al.*, 2002). This adsorption dependence on solution pH is because of the control exerted by the Point of Zero Charge (PZC) of the adsobent surface. The PZC of a mineral is the pH of the solution at which the surface charge is zero. For goethite the PZC is 7.3. When the pH of the surrounding solution is less than the PZC, the mineral surface is positively charged and anion exchange reactions are most likely; when the pH is greater than the PZC, the mineral surface is negatively charged and cation exchange predominates (Appelo & Postma, 1994). The surface charge of the mineral is relates to the following protonation reaction (Appelo & Postma, 1994):

$$\equiv SO^- + 2H^+ \longleftrightarrow \equiv SOH + H^+ \longleftrightarrow \equiv SOH_2^+ \qquad \textit{Eqn. 1.5.1.}$$

Where SO represents surface oxygen, either from the adsorbent surface, or from adsorbed water molecules. The adsorption of ions onto the surface can lead to a change in the surface charge, for example (Appelo & Postma, 1994);

$$\equiv SOH + Pb^{2+} \longleftrightarrow \equiv SOPb^+ + H^+ \qquad \textit{Eqn. 1.5.2.}$$

Bowell (1994) observes As(V) adsorption maxima onto goethite and lepidocrocite (γ-FeO.OH) at solution pH 6, whereas for hydrous ferric oxides (HFOs) the maximum is at pH 8 (Chakravarty *et al.*, 2002). Clay minerals, such as montmorillonite and kaolinite, have greater adsorption for As(V) at pH 5 (Goldberg & Glaubig, 1988), whereas, for carbonate minerals the As(V) adsorption is greatest at higher pH, 10 – 12 (Bhumbla & Keefer, 1994). The PZCs of these minerals vary significantly, for example the PZC for goethite is 7.3, whereas for montmorillonite it is less than 2.5, and for calcite ($CaCO_3$) it is 9.5 (Appelo & Postma, 1994).

1.6. PUBLISHED EXPERIMENTS

1.6.1. Batch Experiments

The batch experimental procedures used in this study are similar to those of published studies (such as Carrillo & Drever, 1998, Halter & Pfeifer, 2001, Manning & Goldberg, 1997, and Bowell, 1994) and particularly to Pierce & Moore (1982). Table 1.6.1 establishes the context of the results in the literature, with regards to As adsorption onto iron-oxide minerals. The Pierce and Moore (1982) work was chosen as a guideline due to their close resemblance to the experiments and objectives required herein. In the Pierce and Moore (1982) research an amorphous iron oxy-hydroxide was used as the sorbent and the adsorption of arsenic (arsenite and arsenate) was quantified in terms of solution pH and partition coefficients. The concentrations of arsenic in solution, and the ionic strength of the solution for the batches were varied (Table 1.6.1). Pierce and Moore (1982) interpreted their results in terms of adsorption envelopes, i.e. the amount of arsenic adsorbed in relation to the solution pH, and in terms of the initial/equilibrium arsenic solution concentration. These results were ultimately used for the derivation of adsorption isotherms. Figures 1.6.1a and 1.6.1b show the adsorption envelopes from the Pierce and Moore (1982) data and indicate the different adsorptive properties of amorphous-iron oxide for both arsenate and arsenite under various solution pH and with different initial As concentrations.

Bowell (1994) found a similar trend for As(III) adsorption onto goethite, with maximum adsorption at pH 6. The decreasing trend in As(V) adsorption with increasing solution pH also occurred on lepidicrocite, γ-FeOOH (maximum adsorption at pH 4) and hematite, Fe_2O_3 (maximum adsorption at pH 7) (Bowell, 1994).

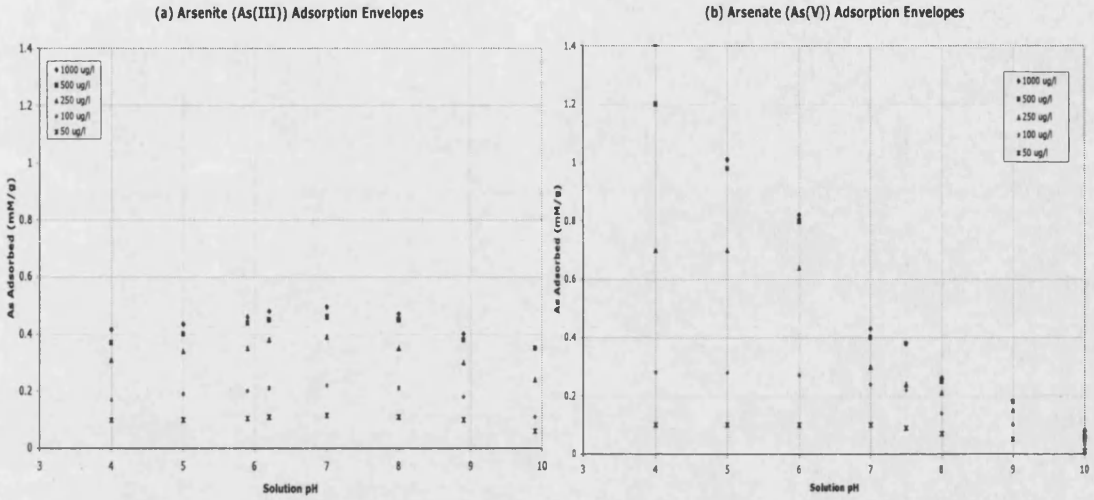

Figure 1.6.1. Adsorption Envelopes for (a) As (III) & (b) As (V) in solution, 0.00445g/l amorphous-iron hydroxide, 0.01M $NaNO_3$. Plots taken from Pierce & Moore (1982).

Other oxide minerals also have a strong affinity for arsenic in solution, and have been researched. Aluminium hydroxides (Halter & Pfeifer, 2001, Lin & Wu, 2001, and Anderson *et al.*, 1976) also demonstrate a strong pH dependence with As(V) adsorption decreasing with increasing solution pH. Undoubtedly iron oxides exhibit the greatest abundance in soils, and have high affinity with arsenic, and so the results of experiments on various iron minerals are widely available (Nickolaidis & Lackovic, 2001, Chakravarty *et al.*, 2002, Khaodiar *et al.*, 2000, Loeppert *et al.*, 1997 and Darland & Inskeep, 1997).

The As(III) adsorption in most batch experiments usually exhibit less adsorption than As(V) (Pierce & Moore, 1982 and Bowell, 1992). Lin and Wu (2001) have suggested that this may be as a result of the ionic species formed in natural waters; with As(V) forming anionic species and As(III) frequently forming non-ionic species and the interaction with charged mineral surfaces.

The temporal kinetics of adsorption between As(V) and As(III) also vary. As(V) adsorption onto oxide mineral surfaces, such as goethite, usually occurs at a faster rate than As(III), especially at low solution pH (Stollenwerk, 2003). The adsorption of arsenic is initially rapid, occurring over a few hours, which then slows as equilibrium is approached, and may take days to reach equilibrium

(Stollenwerk, 2003). Bowell (1994) identifies equilibrium for As(III) as occurring after 12 hours, whereas 48 hours are required for As(V) adsorption onto various iron oxides and hydroxides. This appears to contradict Stollenwerk (2003), although As(V) adsorption may be initially faster than that of As(III), but may slow appreciably more than As(III) in the final approach to equilibrium.

Reference	Aim of Experiment	As Concentration (µg/l)	Amount Fe Oxide	Ionic Concentration	Solution pH
Pierce & Moore (1982)	As(V)/(III) adsorption with respect to pH and partition coefficients. 24 hrs equilibration	7.5 – 75 000	0.0045 g/l HFO	0.01 M $NaNO_3$	4 – 10
Bowell (1994)	Derivation of partition coefficients for difference iron oxides. 24 hr equilibration	1.5 – 40	0.5 g goethite	Not specified	4 – 8
Lumsdon *et al.* (2001)	Assessing behaviour of As in contaminated soils	15 000 – 150 000	2.1 – 5.1 wt% Fe	0.01 M $LiClO_4$	3 – 10
Thirunavukkarasu *et al.* (2003)	Use of Granular Ferric Oxide (GFO) to remove As(V)/(III). Using batch experiments & 6h equilibration	100	0.2 g GFO	Not specified	5 – 8.5
O'Reilly *et al.* (2001)	Kinetics of As adsorption & desorption. Recation time was 45 min – 7 months	0 – 22 500	10 g/l goethite	0.1 M $NaNO_3$	6
Kuhlmeier (1997)	Partitioning of As in contaminated soils from Houston, USA	2700 000	1.54 % Fe	Not specified	7.2
Chakravarty *et al.* (2002)	Removal of As from groundwater using ferruginous MnO_2	120 – 190	0 – 0.8 g	Not specified	2 – 8
Goldberg (2002)	Adsorption of As(V)/(III) onto oxides and clay minerals. With respect to pH range	1500	0.5 g/l Fe oxide	0.01 M NaCl	2.5 – 11
Khaodiar *et al.* (2000)	Adsorption of As onto Fe-oxide coated sand after 24 hr equilibration	75 000 – 300 000	0.74 wt% Fe	0 – 0.1 M $NaNO_3$	3 – 9
Matis *et al.* (1999)	As(V) sorption on goethite & study of flocculation after 24 hr equilibration	68 2000	1 g/l goethite	0 – 0.05 M KNO_3	3 – 11
Hingston *et al.* (1972)	As(V) sorption on goethite. Determination of envelopes after 24 hr equilibration	4900	0.1 g goethite	0.01 – 1 M NaCl	3 - 12

Table 1.6.1. Summary of some previously published arsenic batch experimental studies and their experimental parameters.

1.6.2. Column Experiments

The role of kinetics is also important for understanding the transport of aqueous arsenic, although the effects of this are better described through column experiments.

Published experimental work on arsenic adsorption by column solution migration is scarce. Most experiments concentrate on the derivation of partition coefficients describing the ratio of arsenic adsorbed to the arsenic remaining in solution in equilibrium conditions. The partition description is then applied to macroscopic flow models deployed in simulating contaminant transport. Batch experiments, specifically, lead to a better understanding of adsorption mechanisms.

Column experiments, however, will quantify adsorption under more natural conditions, simulating groundwater flow. This is important when determining partition coefficients for transport modelling, as variations between equilibrium batch coefficients and those from flow-through experiments could be significant. Darland and Inskeep (1997) have ascertained that the batch adsorption rate constants are more than four times less than those derived through column experiments for As(V) and iron-oxide coated sand. Rate constants also increase as porewater velocity is increased. At lower velocities, the arsenic has more time to diffuse into the adsorption sites, and so is retarded to a greater extent, usually with smaller rate constants (Puls & Powell, 1992). This is also a trend observed by Pang *et al.* (2002), using column experiment breakthrough curves (BTCs) to establish kinetic effects on Cd, Zn, Pb adsorption onto alluvial gravels.

The column experiments of Pang *et al.* (2002) applied the flow interruption, or flow cessation, method in order to further appreciate the effect of kinetics. The flow interruption lasted for 2 hours, demonstrating a decrease in the metal concentrations sampled from the column effluent. The change in effluent concentrations during flow interruption suggest that chemical disequilibrium exists as observed in the tailing (long and drawn out) of desorption BTCs (Pang *et al.*, 2002).

1.6.3. Redox Experiments

There are relatively few studies into the transport of arsenic in aqueous environments under different redox conditions. This is perhaps surprising as the mobility of arsenic is highly dependent on the reducing state of the surrounding environment, and there are a number of important examples of such situations where elevated arsenic concentrations in groundwater are a major problem to life systems. Various experiments, such as those described above, have concentrated on the adsorption, desorption and precipitation reactions that occur between pentavalent and trivalent arsenic and other adsorbents. These have been carried out mostly in aerobic conditions. There have been field-scale studies into the redox control of arsenic occurrence in groundwater. For example an investigation by the United States Geological Survey (1999) of arsenic in groundwater from the Willamette Basin in Oregon, USA, has shown that a low dissolved oxygen content (<1 mg/l) in the water is indicative of reducing conditions that result in high dissolved iron (160–1900 μg/l) and an associated release of adsorbed or co-precipitated arsenic. A similar study of the Coeur d'Alene lake sediments in Idaho, USA, also demonstrated the increased concentrations of dissolved iron and arsenic especially at the redox boundary (Harrington *et al.*, 1998).

Rochette *et al.* (2000) have been concerned with the reduction reactions in solutions containing both arsenic and sulphides. Aqueous sulphides such as H_2S or HS^-, usually found in high concentrations in reducing groundwaters, can be strong reductants of arsenate. A study of the kinetics of the As(V) – sulphide reactions found that in more acidic solutions (pH 4), the reactions occurred 300 times faster than those in circumneutral pH solutions. Cummings *et al.* (1999) and Rochette *et al.* (2000) were interested in the application of a known concentration of the iron-reducing bacteria *Shewanella alga* strain BrY to promote arsenic mobility as iron is respiratorily reduced (Fe(III) to Fe(II)).

One of the few studies into mobility and adsorption – desorption of arsenic under experimentally enforced reducing conditions is that by Haury (2001). This study used a number of batch and column experiments to determine the

kinetics and relative quantities of arsenic and iron release, using catechol (1,2 dihydroxybenzene) as a reductant. Catechol is used as a model compound for organic substances that consume oxygen in aqueous environments and result in anaerobic conditions. Catechol was also used in goethite dissolution experiments (Yoshida and Nakashima, 2000) as it forms one of the siderophore ligands, siderophore being a ferric organic ligand excreted by micro-organisms living in iron deficient aqueous environments. This particular study (Yoshida and Nakashima, 2000) noted the dependence of solution pH upon the rates of dissolution, which increased (from 1.2×10^{-8} to 2.2×10^{-8} mol/hr/m^2) as the pH increased from 5 to 9.

The results derived by Haury (2001) suggest that arsenic release is due mainly to the reduction of As (V) to As (III) at the iron hydroxide surfaces with subsequent desorption, and not to the dissolution of goethite. Despite this, a study by Pracht *et al.* (2001) has shown that 10 μmol of catechol can reduce 50 – 60 μmol Fe (III) in the absence of arsenic. Other findings by Pracht *et al.* (2001) suggest that, as Fe (III) is reduced, it has a parallel oxidising effect upon catechol, which eventually oxidises to CO_2 in the following degradation reactions:

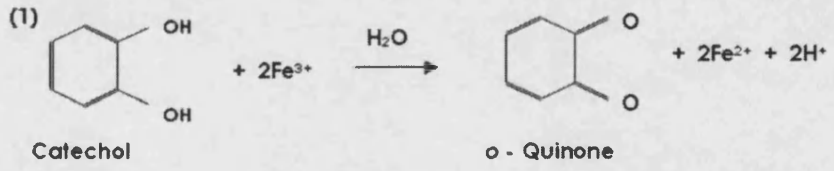

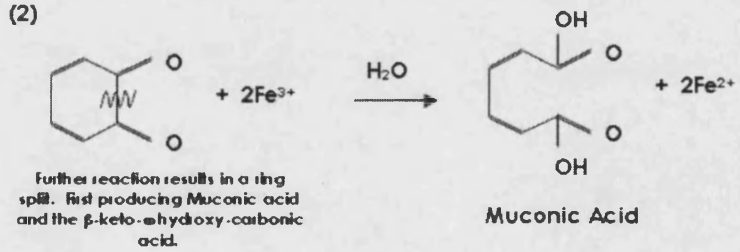

(3) Liberation of CO_2 and other oxidation products:

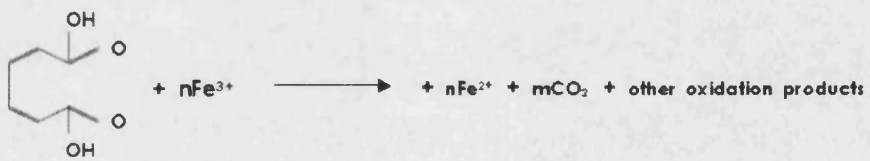

1.6.4. Adsorption Mechanisms

The mechanism of adsorption involves the interaction between an adsorbate (arsenic) and adsorbent (goethite). These mechanisms include the formation of surface complexes and surface precipitation (Scheidegger and Sparks, 1996). Surface precipitation (Figure 1.6.2) is not widely associated with arsenic–metal oxide surface interactions, as sufficient surface coverage is not attained and other factors, such as chemical kinetics, solution chemistry and pH, are not favourable (Stollenwerk, 2003). There are two modes of formation of surface complex: (1) outer-sphere (non-specific adsorption) and (2) inner-sphere (specific adsorption) (Figure 1.6.3). Outer-sphere complexes usually form due to electrostatic attraction forces between the charged metal oxide surface and an oppositely charged ion in solution (Stollenwerk, 2003). The electrostatic bonding is weak and the adsorbing ion remains a significant distance from the oxide surface, separated from the surface by one or more water molecules (Krauskopf and Bird, 1997).

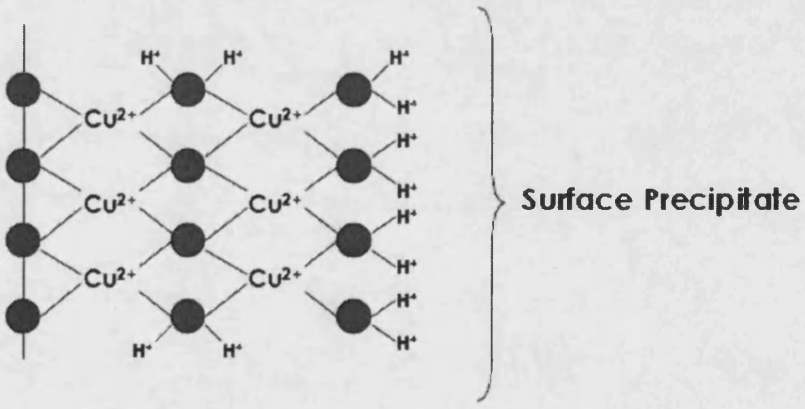

Figure 1.6.2. Surface precipitation example, reproduced from Scheidegger and Sparks (1996). Atoms in red are oxygen.

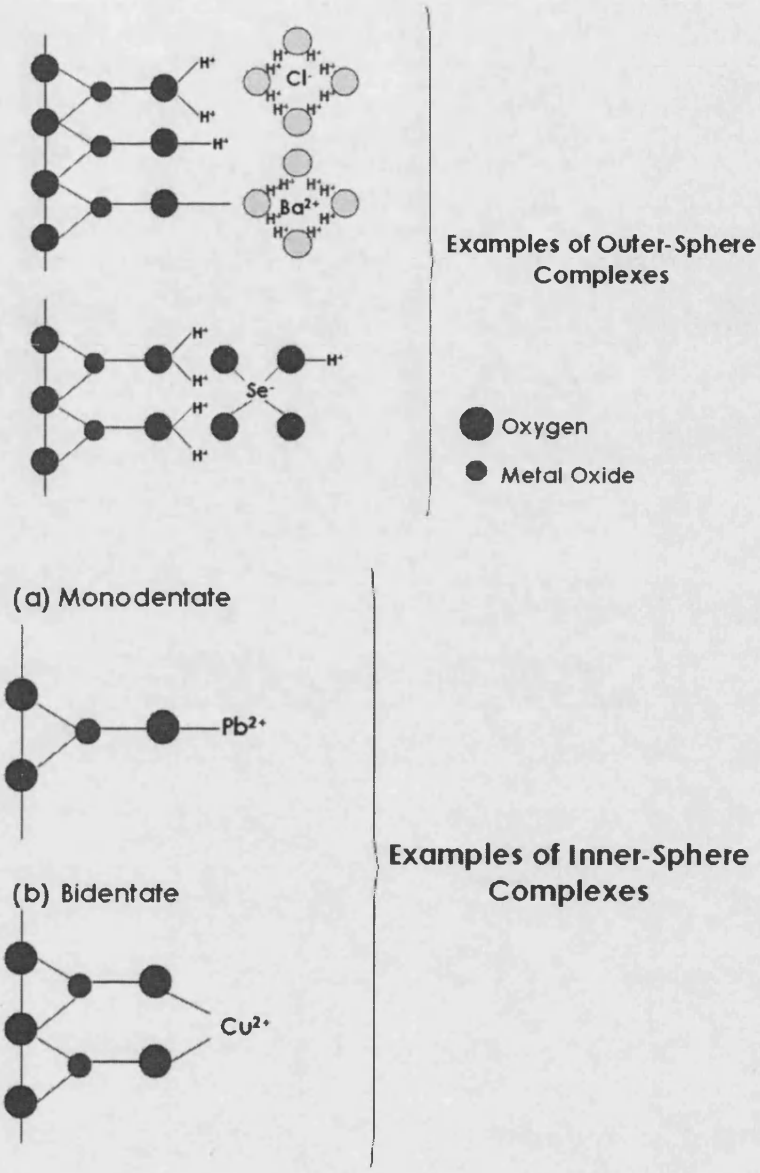

Figure 1.6.3. Example illustrations of surface complexation between a metal oxide surface and various adsorbing ions. Reproduced from Scheidegger & Sparks (1996).

Inner-sphere complexes form using stronger ionic or covalent bonds, although localised electrostatic forces are still important. They bond directly with the oxide surface without interference from water molecules. The inner-sphere complexes are described in terms of the number of bonds with the surface and the number of surface metal ions to which the complex forms.

For example a monodentate-mononuclear (MM) complex has one bond with one surface metal ion:

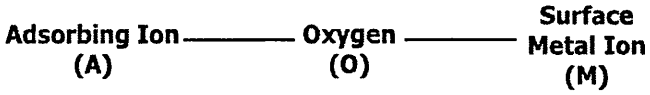

However, a bidentate-binuclear (BB) complex forms two bonds with two surface metal ions:

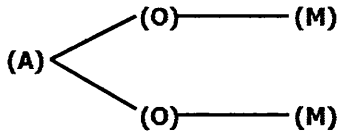

Other complexes include monodentate-binuclear (MB):

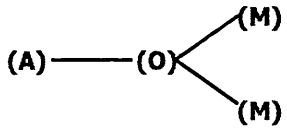

and bidentate-mononuclear (BM):

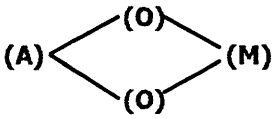

The number of metal ions to which the adsorbing ion binds may be large, although the distribution of surface metal ions and chemistry of solution will restrict this. If the surface coverage of adsorbing ions increases, the number of surface metal ions that the complex binds with also increases (Krauskopf and Bird, 1997).

Previous studies have observed the formation of inner-sphere complexes between arsenic and iron oxide/hydroxide surfaces (Stollenwerk (2003), Farquhar *et al.* (2002), Sun and Doner (1996) and Waychunas *et al.* (1993)). Their evidence was obtained through the application of spectroscopy (EXAFS (Extended X-ray Absorption Fine Structure), XANES (X-ray Absorption Near Edge Structure) or FTIR (Fourier-Transform Infra Red)). Other studies, however, have used experimental indicators such as solution pH and ionic strength to determine the type of surface complexation. For example, outer-sphere complexes are dependent on the ionic strength of the solution and the derived

adsorption envelopes show a decline in adsorption as the ionic strength of the solution increases. This has been observed for the adsorption of As(III) onto amorphous–aluminium oxides and amorphous–iron oxides (Goldberg and Johnston (2001) & Arai *et al.* (2001)). By contrast, inner-sphere complexes are independent of the ionic strength due to closer binding with the oxide surface, and hence interference with the ionic solution is less significant (Stollenwerk, 2003). The majority of As(V) and As(III) – iron oxide adsorption experiments are found to be independent of the solution ionic strength and indicative of inner-sphere adsorption (Khaodhiar *et al.* (2000) & Goldberg and Johnston (2001)). The experiments described in the current study were not designed to investigate the effect of changing ionic strength, as previous research has established the independence of arsenic adsorption on iron oxides with respect to ionic concentration.

The dependence of adsorption on solution pH is observed only when inner-sphere complexes are formed (Stollenwerk, 2003). This is due to changes in the PZC, sometimes referred to as the Iso-Electric Point (IEP) resulting from the adsorption of ions from solution (Stollenwerk, 2003). For example, the adsorption of anions increases the negative charge on the surface and therefore decreases the PZC of the adsorbent (Stollenwerk, 2003). Previous experiments of the adsorption of both As(V) and As(III) onto iron oxides have observed pH dependency, and a correspondence between the magnitude of change in the PZC and the amount of arsenic in solution (Bowell (1994), Stollenwerk (2003), Pierce and Moore (1982), Lumsdon *et al.* (2001), Loeppert *et al.* (1997) & Khaodhiar *et al.* (2000)). Chapter 3 investigates the effect that solution pH has upon adsorption by new batch experiments.

1.7. THESIS STRUCTURE

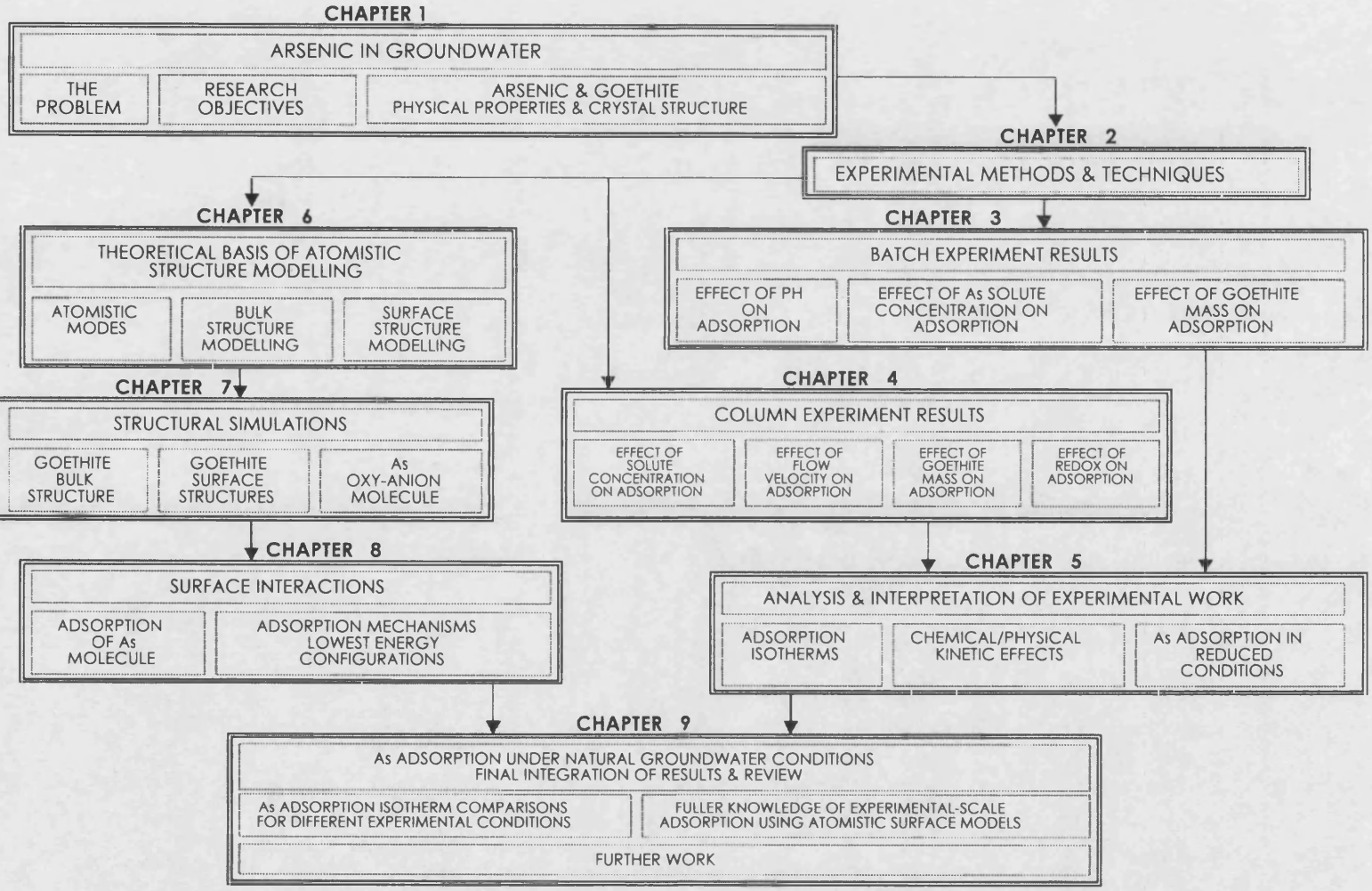

2. MATERIALS AND METHODS

2.1. SYNTHESIS AND CHARACTERISATION OF GOETHITE

Batch and column experiments were performed using synthetic material for the study of surface interactions in aquatic environments, thereby minimising unnecessary variables and complexities. Goethite was selected as the appropriate mineral for the adsorbent due to its ubiquity in aquifer materials, its relevance to the natural processes, and the high affinity arsenic has with it. By using a synthetic material in this way, the risks of impurities within the crystal lattice are greatly reduced, which would otherwise complicate the search for the fundamental mechanisms.

2.1.1. Synthesis of Goethite

The goethite synthesis was carried out according to the Bohm method described in Schwertmann and Cornell (2000) and was produced from a Fe^{III} alkaline system. A potassium hydroxide solution was prepared from 5M potassium hydroxide (KOH) by dissolving in 180ml deionised distilled water until the solution clarified. An iron nitrate solution was also created with 1M $Fe(NO_3)_3$ [of $Fe(NO_3)_3{\cdot}9H_2O$ crystals] dissolved in 100ml deionised water, until the solution turned translucent orange in colour. The two solutions (potassium hydroxide solution and the iron nitrate solution) were combined and the total mixture made up to 2 litres using deionised water. Immediately a red-brown coloured precipitate of 2-line ferrihydrite should appear (Schwertmann and Cornell, 2000) was obtained. The solution was shaken for five minutes and transferred

into 2 litre Nalgene polypropylene containers, which are non-reactive to the highly alkaline solution, and heated in an oven at 70°C for 60 hours.

After the heating period, suspended fine orange-yellow particles were allowed to settle to the bottom of the container. The remaining liquid was decanted off and the outstanding particulates washed once with deionised-distilled water before the excess liquid was again decanted and the residual 'slurry' placed into clipped dialysis tubing (2cm diameter). The slurry within the tubing was left in buckets filled with deionised-distilled water, which were changed every three days, for three weeks. The excess water was decanted from the tubing containing the goethite and at the end of this 'ageing' process the slurry was oven dried for 18 hours at 40°C. The resulting powder provided the required synthetic goethite.

2.1.2. Characterisation of Goethite

2.1.2.1. *X-Ray Crystallographic Character*

The dried synthetic goethite was characterised using the Nonins PDS 120 X-Ray Diffraction (XRD) with an INEL curved 120 position sensitive detector facilities at the Natural History Museum, London. The operating conditions used CuKα radiation and a germanium (111) monochromator with 45 kV and 32 mA. The incidence ray was 0.3 mm high and 5 mm wide, contacting the sample surface with an incidence angle of 5 . The goethite sample was mounted on an XRD stub before introduction into the machine.

The XRD machine collects diffraction patterns characteristic of the crystal structure, which are used as a 'fingerprint' to identify the mineral in question. In this case the synthesised material was identified with goethite from the museum reference collection.

This method is used to determine crystal structures by interpretation of the interference caused when x-rays, fired towards a crystal, are diffracted (scattered and reflected) by atomic layers within the structure. Application of Bragg's equation describes the diffraction (Atkins *et al.*, 1988):

$$\lambda = 2\,d \sin\theta \qquad \textit{Eqn. 2.1.1}$$

Where λ represents the x-ray wavelength (usually 100 pm), characteristic of the distance between atomic layers within the crystal, **d** is the layer spacing and θ is the angle of diffraction. The x-rays that are diffracted can interfere constructively, if the two waves fired and subsequently diffracted are in phase, or destructively when out of phase, where the two waves cancel and destroy one another. Constructive interference for given crystal structures occurs only at characteristic angles (Fullick and Fullick, 1994).

The goethite sample was mounted on an XRD stub before introduction into the machine. Figure 2.1.1 shows the resulting XRD plots for the synthesised goethite at various stages of ageing (up to four weeks). Plots 1a and 1b are derived from the most mature material (four weeks), whereas plots 2 and 3 correspond with the materials aged for two and three weeks respectively. When compared with the natural pure goethite standard (bottom plot), the specific peaks for the synthesised material closely match those of the natural standard, suggesting absence of impurities. Subtle differences however, were observed between the less mature goethite with shorter, wider and sometimes absent peaks compared to those of the more mature and crystalline standard material. The adsorption of arsenic onto the synthetic goethite may be marginally enhanced by the slightly lower crystallinity with regards to the more loosely packed structure characterised by the XRD peaks, although not significantly.

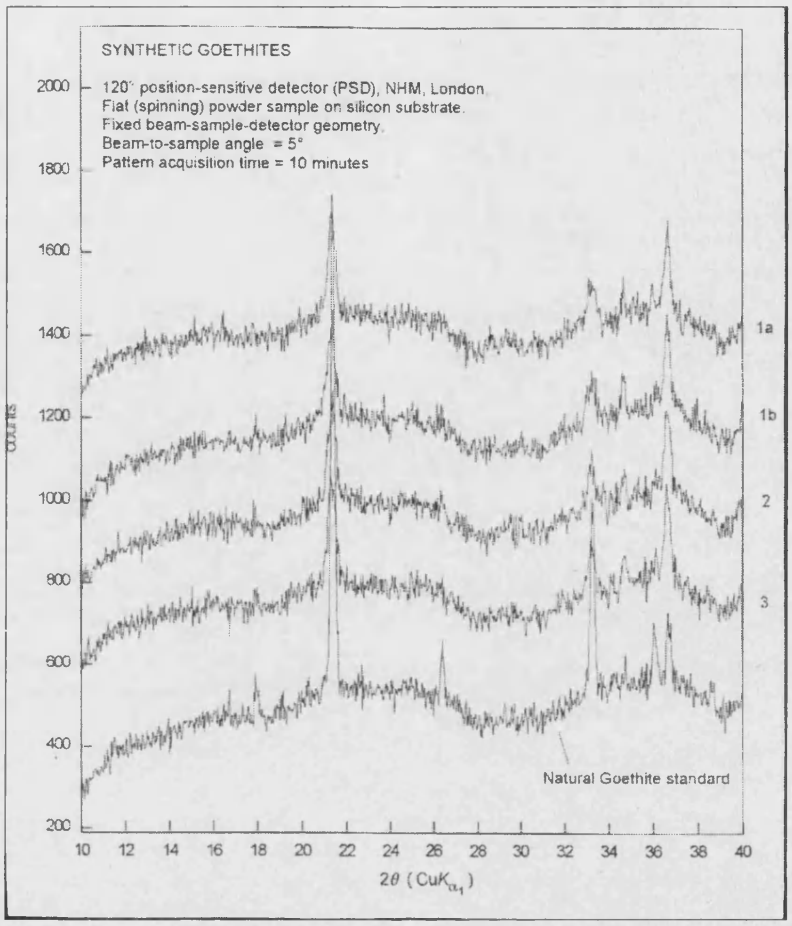

Figure 2.1.1. XRD plots of the synthesised goethite, where θ is the angle of diffraction, and the 2θ range is between 10 and 40 . Samples 1a and 1b were aged for 28 days, sample 2 for 14 days, and sample 3 for 21 days.

2.1.2.2. *Crystal Morphology By SEM*

The crystal morphology was observed accurately using the Scanning Electron Microscopy (SEM) at the Natural History Museum. Like the XRD sample preparation, the dried goethite material was mounted on a stub before analysis. A typical example of the resulting SEM images can be seen in Figure 2.1.2, showing crystals that are acicular, with lengths typically between 0.8 and 1.7 μm, and fall well within the maximum length of 4 μm observed by Randall *et al.* (1999).

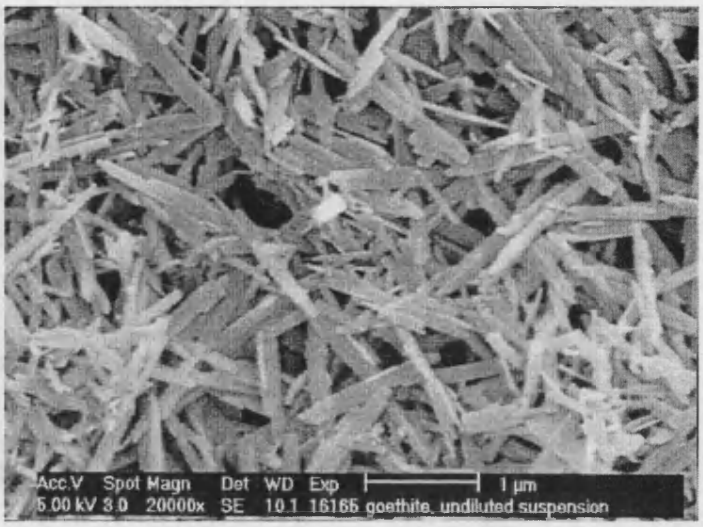

Figure 2.1.2. SEM Image of typical goethite crystal morphology.

2.1.2.3. Surface Area

The surface area of the goethite was established using the Brunauer Emmett Teller (BET) method using equipment available at the Natural History Museum. This technique uses the Langmuir model to determine the amount of nitrogen adsorption onto the mineral surface and therefore the surface area (Sing, 1997). Prior to applying this technique, the sample needed to be oven dried, crushed and sieved (between 106 µm and 20 µm sieve apertures) to remove polycrystalline aggregates or clumps of goethite crystals. The resulting surface area of the synthetic goethite was measured as 17.75 +/- 0.06 m^2/g, which is less than the 50 m^2/g derived by Waychunas *et al.* (1993) and that of Bargar *et al.* (1999), which was 45 m^2/g. Randall *et al.* (1999) also measured slightly larger crystal surface areas of synthetic goethite (27 - 33 +/- 3 m^2/g). The relatively small surface areas measured from the current synthetic material may be as a result of crystal immaturity as the XRD spectrum (Figure 2.1.1) shows, and if the crystals were allowed to remain within the potassium hydroxide and iron nitrate mixture for longer prior to heating, then greater crystal growth could occur.

2.2. EXPERIMENTAL METHODS AND PROCEDURES

The experiments and their results are described in Chapters 3 to 5. This section outlines the preparatory work in terms of:

Preparation of the arsenic solution
Preparation of the goethite slurry
Requirements for consistent measurements
Precautions against unwanted complexities and parameters
Ultimate experimental parameters used.

2.2.1. Batch Experiments

2.2.1.1. Purpose

The general requirement of batch experiments is the exploration under equilibrium conditions of the functional relationship between As adsorption and pH, PZC, mass of the adsorbent goethite and the solution concentration of arsenic.

The batch experiment arrangement was based on work conducted by Bowell (1994), Halter and Pfeifer (2001), and Manning and Goldberg (1997), and a study by Pierce and Moore (1982) provided the framework for the design of the batch experiments. Pierce and Moore were observing the adsorptive properties of both arsenate and arsenite onto an amorphous iron-oxyhydroxide surface, under a range of solution pH conditions.

2.2.1.2. *Solutions and Materials*

The batch experiments used 50ml Nalgene High Density Polyurethane screw-lid bottles. The bottles were new and were pre-washed using only DDW (Deionised Distilled Water), which eliminates the threat of possible container surface reactivity as a result of acid bath washing (using 10 % Aristar HNO_3). The batch experiments were duplicated to check consistency of results (Batches I and II) and also comprise a control batch (Batch III) identical to the other batches and run in sequence but without the adsorbing mineral (goethite). A standard arsenic stock of 1000 µg/l was prepared by dissolving Na_2HAsO_4 ('Sigma-Aldrich' Analar sodium arsenate salts) into DDW and was used to generate more dilute solutions for the individual experimental sets. Individual As concentrations in 50 ml batches were sourced from the same 2 l diluted arsenic stock solution to ensure consistency: the concentrations of which were representative of As concentrations in groundwater (0 – 5000 µg/l; Smedley and Kinniburgh, 2002). To the diluted solution 0.01 M background electrolyte was added from 1M $NaNO_3$ and the solution made up to 2 l with DDW. After the diluted stock solution was dispensed into the individual 50 ml batch containers the initial pH of each batch was measured using a calibrated pH probe.

To determine the effect of pH on adsorption the pH of the individual batch solutions was changed by adding Aristar 0.01-1M NaOH or 0.01-1% HNO_3 with an Eppindorf pipette, and the altered pH was measured. After the solution pH was judged to have settled to a constant value, a measured volume of the goethite slurry was pippetted into the individual batch solutions (I & II Batches) for study of the amount of As adsorption onto goethite. Goethite was not added to the control batches (III Batches). The batch containers were agitated with a rotary shaker (Figure 2.2.1) for a 24 hour equilibrium period, as described by published experiments, including the Pierce and Moore (1982) study.

After the 24 hour period, all batches were taken off the rotary shaker and the pH of each of the batches was again measured (Appendix 3A). Samples were taken from each batch, filtered using Millipore 2.5 mm diameter (0.2 µm) membrane filters, then acidified with 10 % nitric acid (HNO_3) to prevent any

subsequent iron precipitation, and hence further arsenic-goethite reactions from occurring. The acidified samples were also refrigerated (5 C) for 1 week prior to analysis for arsenic adsorption by AAS (Atomic Absorption Spectrometry).

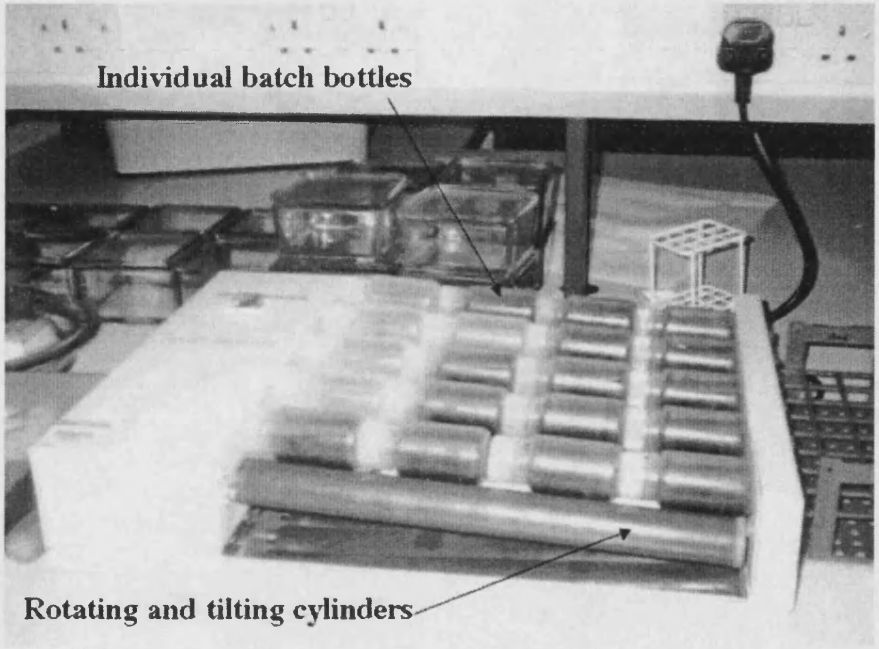

Fig 2.2.1. Illustration of the batch experiment arrangement with the batches continuously agitated on a rotary shaker.

2.2.1.3. Experimental Parameters

In addition to the adsorption vs. pH experiments the work was extended to include the effects of As concentration and goethite mass. Measurement from the experiments allowed deduction of equilibrium sorption partition coefficients, such as K_d (for linear adsorption), from isotherms relating the amount of arsenic adsorbed per mass of adsorbent with respect to arsenic concentration in solution (Section 3.2).

Table 2.2.1 summarises the parameters for each of the experimental batch sets. Batches A and B were not used in the description of the adsorption envelopes (pH effect) nor the adsorption isotherms, discussed later, as they formed the "training" batches to ensure that good skills were developed and acquired for the preparation of subsequent batches.

EXPERIMENT IDENTITY (See Appendix 3A)	GOETHITE MASS IN SOLUTION, m (g/l)	INITIAL ARSENIC SOLUTION CONCENTRATION, C_0 (µg/l)	RANGE OF SOLUTION EQUILIBRIUM pH
A4 – A11	0.00515	150	3.6 – 11.2
B4 – B11	0.00206	150	4.3 – 11.1
C4 – C11	0.0103	150	3.8 – 11.2
D4 – D11	0.0206	150	3.9 – 11.3
E4 – E11	0.0103	300	4.0 – 11.0
F4 – F11	0.0206	300	4.0 – 11.0
G4 – G11	0.0412	300	3.9 – 11.1
H4 – H11	0.0309	300	3.9 – 11.0
I4 – I11	0.0103	750	4.0 – 11.1
J4 – J11	0.0206	750	3.9 – 11.2
K4 – K11	0.0412	750	3.9 – 11.3
L4 – L11	0.0309	750	3.9 – 11.3
M4 – M11	0.0103	1500	3.6 – 11.2
N4 – N11	0.0206	1500	3.7 – 11.2
O4 – O11	0.0412	1500	3.7 – 11.3
P4 – P11	0.0309	1500	3.9 – 11.3

Table 2.2.1. Summary of experimental parameters and conditions.

2.2.2. Column Experiments

2.2.2.1. *Purpose*

The column experiments were designed to explore and understand the dynamic effects of arsenic adsorption. The process involves flushing a column of packed quartz sand and goethite with an arsenic solution, and monitoring the arsenic 'breakthrough' in the column effluent. The mean breakthrough is defined as the time for the effluent to attain 50 % of the total arsenic influent

concentration (i.e. the time for which $C/C_0 = 0.5$, where C_0 is the initial concentration of the influent solution and C is the concentration of the effluent) (Fetter, 1994).

In review, there are five experimental parameters that were varied and these are summarised in Table 2.2.2.

EXPERIMENTAL PARAMETER	TEST PROCEDURE	PURPOSE
Goethite Mass	Near identical columns containing different goethite mass	Effects of As adsorption with increasing adsorbent mass and relationship with partition coefficients
As Concentration	Change influent As concentration in columns	Effect on adsorption and description of dynamic partition coefficients to compare with batch results
Flow Velocity	Change flow rate using variable diameter influent tubes	Kinetic effects and physical or chemical non-equilibrium
Desorption	Flush columns with As-free solution	Describe adsorption reversibility and possible physical or chemical non-equilibrium
Redox	Reducing agent introduced to pre-adsorbed As column sediment	Redox effect on partition coefficient

Table 2.2.2. Summary of experimental parameters and purpose.

2.2.2.2. *Solutions and Materials*

Merck pyrex chromatography columns were packed with a homogeneous mix of synthetic goethite and pure clean quartz sand (Aldrich, SiO_2 60.08 g molecular weight), the latter acting as a non-reactive column fill. A sintered disc with a porosity of 1 μm was placed at the base of the columns to ensure that solids did not exit through the base. The synthetic goethite, produced by the method described in Section 2.1, was crushed gently (using a pestle and

mortar) and passed through 20 and 106 μm sieves (500 mm diameter). Prior to being packed into the columns, the goethite was mixed with the quartz sand by vigorous shaking for at least 2 minutes to create a homogeneous mix. The mix was poured slowly into a column of water, in small quantities to encourage continuous packing. The main aim was to ensure that no air became trapped within the mix. When the column was full a surface layer of smooth clean plastic beads (2 mm diameter) was laid above the sediment mix to encourage non-localised flow of solution on entering the column. The influent tubing was held securely in place at the column mouth using a rubber bung with a seal to prevent the incursion of air.

The arsenic influent solution was made from a stock solution prepared in the same way as for the batch experiments. The 2 l stock was prepared by dissolving Na_2HAsO_4 ('Sigma-Aldrich' Analar sodium arsenate salts) into DDW and adding 0.01 M background electrolyte from 1M $NaNO_3$).

2.2.2.3. *Experimental Parameters*

Each set of experiments used a column array of four columns, packed and treated identically. Each column was of diameter 2.7 cm and an average packed length of 8 cm (Table 2.2.3). The columns differed in the goethite mass within the sediment mix, ranging from 0.01 to 0.2 weight % (Table 2.2.3). Over a series of experiments the concentration of arsenic within the influent was changed. As with the batch experiments, the arsenic solution concentrations were chosen to reflect natural conditions (Table 2.2.3). Finally, the experiments allowed for a variety of flow rates to identify possible kinetic effects upon adsorption (Table 2.2.4). By changing the internal diameter (d) of the tubing it was possible to monitor the effect of varying flow velocity (v) on adsorption:

$$v = (\pi d^2 L) / (4 \cdot t \cdot A) \qquad \textit{Eqn. 2.2.1.}$$

Where:

v	**=**	**Discharge velocity (cm/s)**
d	**=**	**Tubing internal diameter (cm)**
L	**=**	**Tubing length (cm)**
t	**=**	**Time taken for known volume to pass (s)**
A	**=**	**Area of column (cm^2)**

Initial column experiments (See Appendix 4A for results) used a one–channel peristaltic pump (Marlow-Watson) to pump the aqueous solutions from an aspirator bottle into single filled columns. On progression to the series of four column experiments a four-channel single speed peristaltic pump (Figure 2.2.2) was used to flush the four columns simultaneously, using the same solution residing in clean Nalgene polyurethane 10 l aspirator bottles. This ensured the same flow rate into each of the columns.

The discharge velocity (v, cms^{-1}) was determined from the measured pumped flow rate (Q, cm^3s^{-1}) at the column outlet, using the formula; $v = Q/A$, where the cross-sectional area (A) of the column is 5.73 cm^2. The total porosity (n_t) of the sediment in each column was measured experimentally by deriving the void volume. Using accurate volumetric measuring cylinders, a known volume of sediment (V, cm^3) was oven-dried (60 °C for 24 hours) then saturated in a known volume of water and sealed for 24 hours. The void volume (V_v, cm^3) is the difference between the original water volume and the volume after the saturated sample is removed and the total porosity determined (Table 2.4.3) as:

$$n_t = 100 \times (V_v / V) \qquad \textit{Eqn. 2.2.2.}$$

The bulk density of the column sediment is the dry mass divided by the volume of sample, V (Table 2.2.3). In the case of column 2 some of the material was lost during the packing stage but after the porosity measurements were made. The bulk density represents the material after packing, but the porosity represents that of the material and is assumed to remain the same with the reduced proportion of material.

The column experiments were also used to derive the hydraulic conductivity of the column material. For these experiments a water tank was used above the columns to force water through the column by gravity. With measurement of the elevation head in the water tank (hz_{tank}) using the distance from a datum level to the water level in the tank, to the head in the column (hz_{column}), in this case the effluent level above datum. The total hydraulic head, however, comprises the elevation head and the hydraulic head induced by pressure within the column. The pressure head at a specific elevation above the datum

(h_p) relates to fluid pressure (P), fluid density (ρ) and the mass due to gravity (g) (Fetter, 1994):

$$h_p = P / (\rho g) \qquad \textit{Eqn. 2.2.3.}$$

In this case the fluid of concern is water, and the pressure of the fluid in the tank is equal to atmospheric, as no head of water exists above it and so the total hydraulic head at the water level in the tank is equal to the elevation head. The pressure and therefore $h_{p\text{-column}}$ at the effluent level of the column can be estimated by knowing the fluid density by the height of the column of water (Fetter, 1994). For this column test $h_{p\text{-column}}$ is minimal (<0.0001 cm) and contributes only a small proportion towards the total head (h_{column}).

The hydraulic gradient and conductivity are derived using the following equation:

$$i = (h_{tank} - h_{column}) / L \qquad \textit{Eqn. 2.2.4.}$$

Where L is the distance over which flow occurs, in this case the packed length of column. The hydraulic conductivity (K) is determined from Equation 2.2.5, where Q is the measured flow rate through the column and A is the surface area over which flow occurs. Chapter 5.4 gives the hydraulic conductivity range for the column experiments.

$$Q = K \cdot A \cdot i \qquad \textit{Eqn. 2.2.5.}$$

$$\text{or} \quad K = Q / (A \cdot i)$$

	Column 1	Column 2	Column 3	Column 4
Mass of quartz sand within column (g)	**71.51**	**59.89**	**71.52**	**71.01**
Mass of goethite within column (g)	**0.073**	**0.038**	**0.0072**	**0.128**
Goethite (weight %)	**0.1**	**0.05**	**0.01**	**0.2**
Bulk density (g/cm^3)	**1.56**	**1.34**	**1.58**	**1.53**
Total Porosity, n_t (%)	**20**	**21**	**21**	**22**
Packed Length (cm)	**8.0**	**7.8**	**7.9**	**8.1**

Table 2.2.3. Column fill details for the four individual columns.

Experiment Identity	Q (cm^3/s)	v (cm/s)	Influent As Concentration (µg/l)
A	0.0409	0.0071	870
B	0.0145	0.0025	600
C	0.0172	0.0030	280
D	0.0144	0.0025	57
E	0.0094	0.0016	780
G	0.0094	0.0016	540
H	0.0171	0.0030	630
I	0.0171	0.0030	750
J	0.0152	0.0027	630

Table 2.2.4. Summary of experimental variables. Q is the flow rate and v is the discharge velocity = Q/A.

2.2.2.4. Procedure

At the conclusion of individual adsorption experiments, the columns were flushed with an arsenic-free solution to permit desorption measurements. Such data give the extent of irreversible adsorption caused by physical or chemical non-equilibrium. Finally, in order to attain near-complete desorption, the arsenic-free solution contained concentrated Analar NaCl (340 mg/l Cl) to act as a competitive adsorbate and encourage arsenic desorption (A. Osborn, Pers. Comm., 2001). Prior to resuming adsorption experiments the columns were flushed with DDW only.

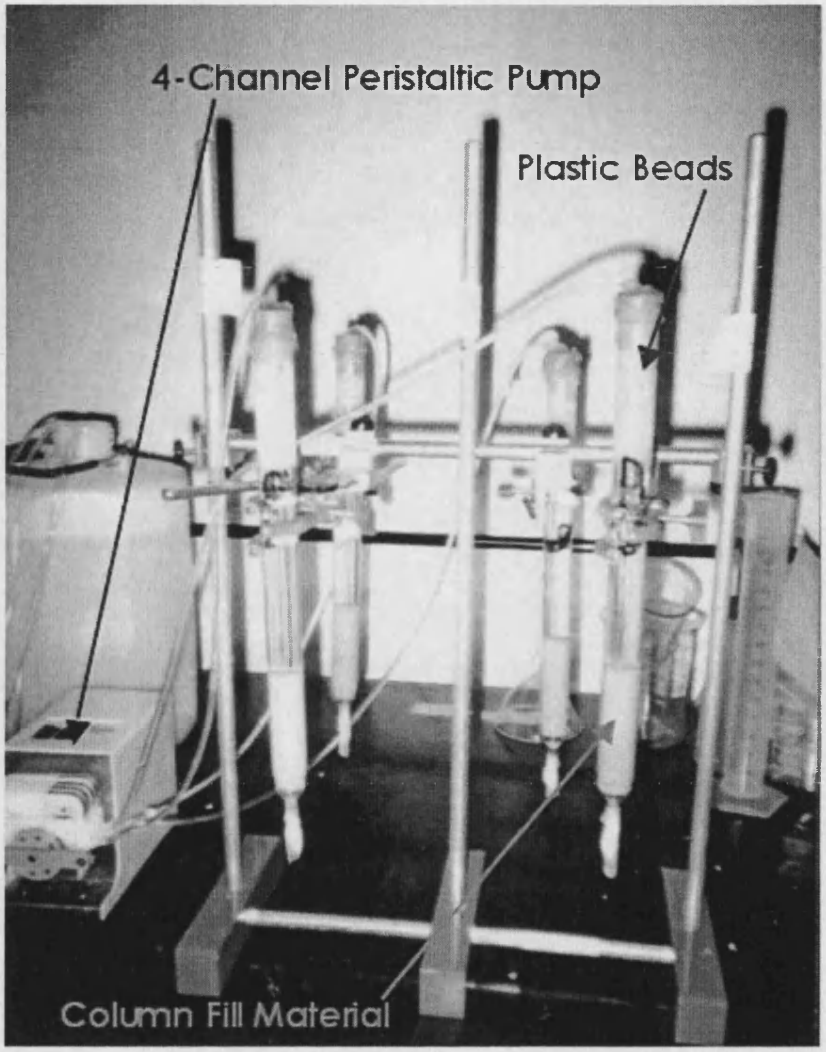

Figure 2.2.2. The four column experimental setup, showing the columns filled with different amounts of goethite, and flow activation by the peristaltic pump.

2.2.3. Redox Experiment

2.2.3.1. *Purpose*

A set of experiments was designed to observe the effects of arsenic adsorption and desorption under a different redox environment, by imposing reducing conditions upon the column experiments. The reducing conditions were introduced to represent the arsenic–mineral interactions that occur in reducing aquifers, such as those in Bangladesh. The partitioning between the arsenic adsorbed and that remaining in solution was determined for comparison with similar calculations under aerobic conditions.

The redox experiments used identical apparatus as the aerobic column experiments, except a multi-port column provided for sequential sampling was added. Figure 2.2.3 illustrates the column arrangement with four sampling ports at equal distances throughout the column permitting arsenic release in progression through the sediment to be monitored.

2.2.3.2. *Solutions and Materials*

The sediment was a homogeneous mixture of quartz sand and goethite inserted into the column using the techniques described in section 2.2.2. Quartz wool at the effluent port acted as a filter to prevent loss of sediment fines and quartz wool at the column inlet allowed for a more uniform distribution of the influent.

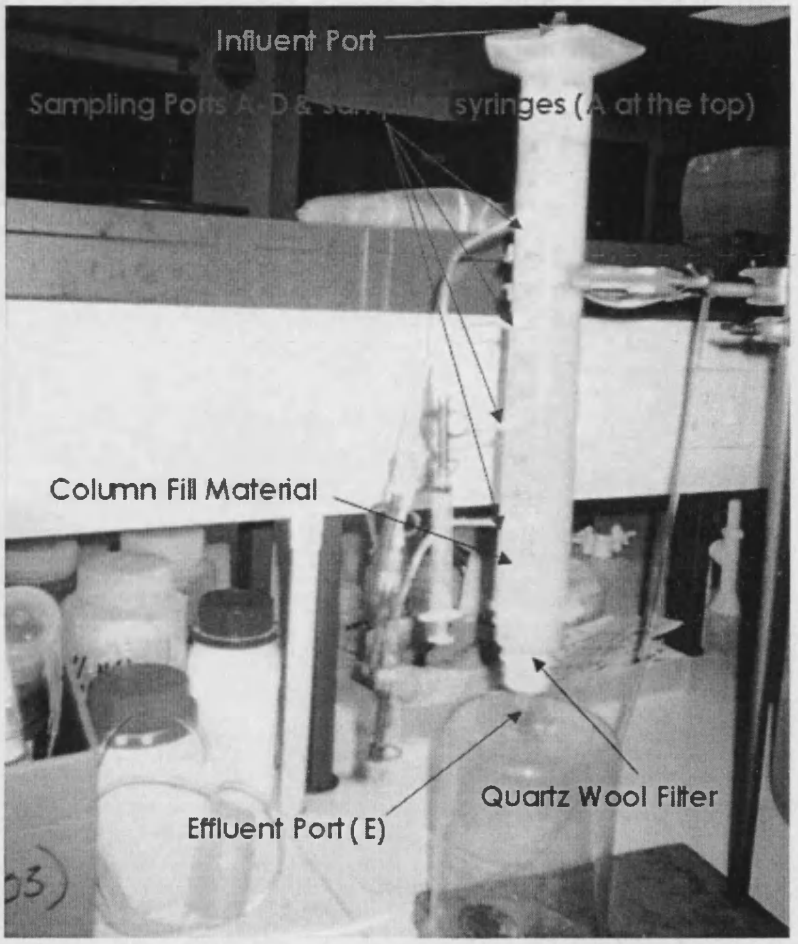

Figure 2.2.3. Redox column arrangement.

2.2.3.3. *Parameters and Methods*

Although two redox experiments were carried out the results are similar. For example, the same goethite wt % was used within the column, the As influent concentration was within the range of those studied for the aerobic column experiments, and the flow rate (Q) was within the same order of magnitude as the faster flow column experiments. The total porosity for the column fill is 10 % lower than those for the aerobic columns, and potentially could lead to reduced goethite – arsenic surface interaction and relatively lower partition coefficients, for both the aerobic and anaerobic sections of the redox experiment.

Only Experiment B will be described from hereon and Table 2.2.5 summarises the Experiment B parameters. Experiment A results are given in Appendix 4B.

EXPERIMENTAL PARAMETER	VALUE
Flow Rate (Q)	0.067 cm^3/s
Goethite Mass	0.92 g (0.2 wt%)
Bulk Density of Sediment (ρ_b)	1.47 g/cm^3
As Influent Concentration	415 µg/l
Catechol Solution Concentration	0.089 g/l
Total Porosity (n_t)	11 %
One Pore Volume	33.12 cm^3

Table 2.2.5. Summary of redox experiment B parameters.

2.2.3.4. Procedure

The procedure for the full redox column experiment was as follows. Arsenic was flushed into the column during the adsorption phase. This was followed with a one pore volume flush with deionised-distilled water to remove dissolved arsenic and ensure the arsenic that remained was purely sorbed to goethite. The subsequent reducing phase of the experiment required an analar grade catechol (1,2 di-hydroxybenzene) solution to be pumped through the column material. Catechol is a known reductant of goethite (see Chapter 1.5.3) (Pracht *et al.*, 2001 & Yoshida and Nakoshima, 2000) and arsenic (Haury, 2001). During the reducing phase both arsenic and iron were monitored in the effluent samples, as well as the pH and Eh (reducing potential). The redox potentials were measured using a platinum electrode coupled with a Ag:Ag-Cl reference electrode, and the meter was calibrated using saturated KCl solution with a reference potential (E_{ref}) of 238 mV (above the SHE, Standard Hydrogen Electrode). Measurements of redox were therefore corrected to the SHE by subtracting the E_{ref} value from the observed values.

2.3. ANALYTICAL TECHNIQUES

2.3.1. Scanning Electron Microscopy

Scanning Electron Microscopy (SEM) techniques were employed for visual inspection of the morphology of the synthetic goethite crystals before and after experiments. The SEM machine in this case was a Phillips XL-30 FEG located in the Natural History Museum, London. The machine used a 5 kV accelerating voltage at a spot size of 3 and a SE detector, as specified on the images, for example Figure 2.3.1. This type of analysis requires a small amount of the sample to be mounted onto an aluminium stub that is coated with a very thin layer of glue (araldite). When the mounted samples have dried they are coated in silver before placement under the microscope. The silver coating ensures that the reflection and absorption of electron rays are enhanced and so acquire the best image quality. This type of microscopy allows for measurement of crystal lengths in the micro-meter scales. Figure 2.3.1 shows an example of a high resolution SEM image of the synthesised goethite crystals prior to use in experiments. Figure 2.3.2 shows an image of the goethite amongst the quartz sand column fill on completion of the experiments. The large particle, with relatively smooth surfaces, is the cleaned quartz grain, and the smaller (1 – 2 μm length) acicular crystals are goethite, which do not appear to have undergone significant morphological alteration during the course of the column experiments.

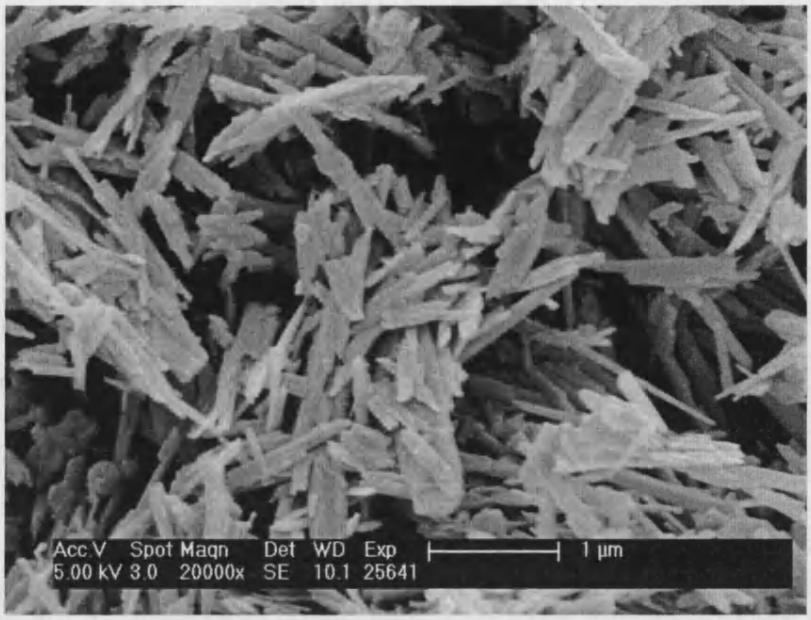

Figure 2.3.1. SEM image of synthetic goethite crystals, before experimentation.

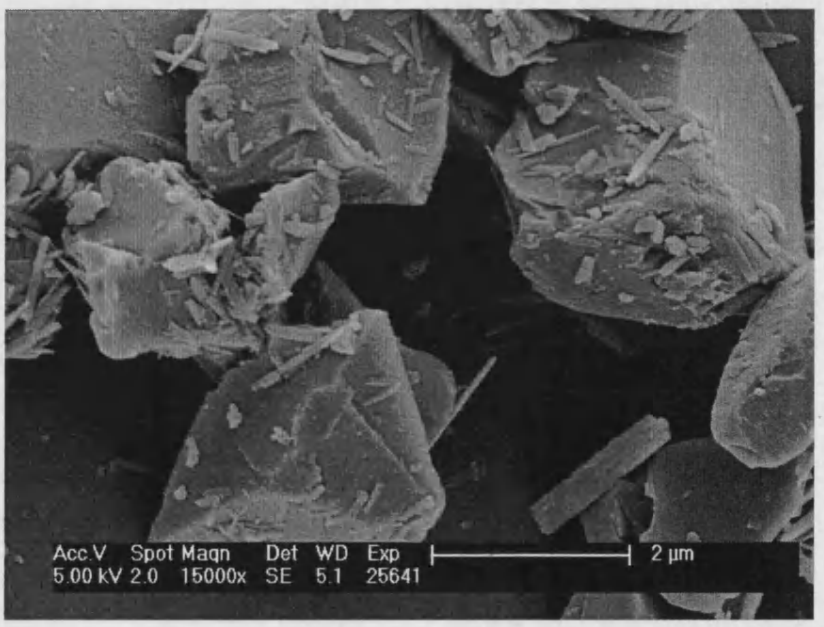

Figure 2.3.2. Column fill material; quartz grains and goethite crystals, after adsorption – desorption column experiment.

For spectral analysis of the material another type of SEM was employed. The JEOL JSM-5900LV analytical microscope with an Oxford Instruments INCA

system Energy Dispersive X-ray spectrometer (EDX) backscatter detector and an accelerating voltage of 20 kV, also at the Natural History Museum, produced visualisation of the material under the microscope, although the definition at the scale required (1 – 2 μm) is limited. However, its main use was for elemental analyses of surfaces. Sample stubs are prepared as before, except that they are coated with carbon. The microscope allows pin-pointing on a surface and subsequent detection and spectral display of elements found.

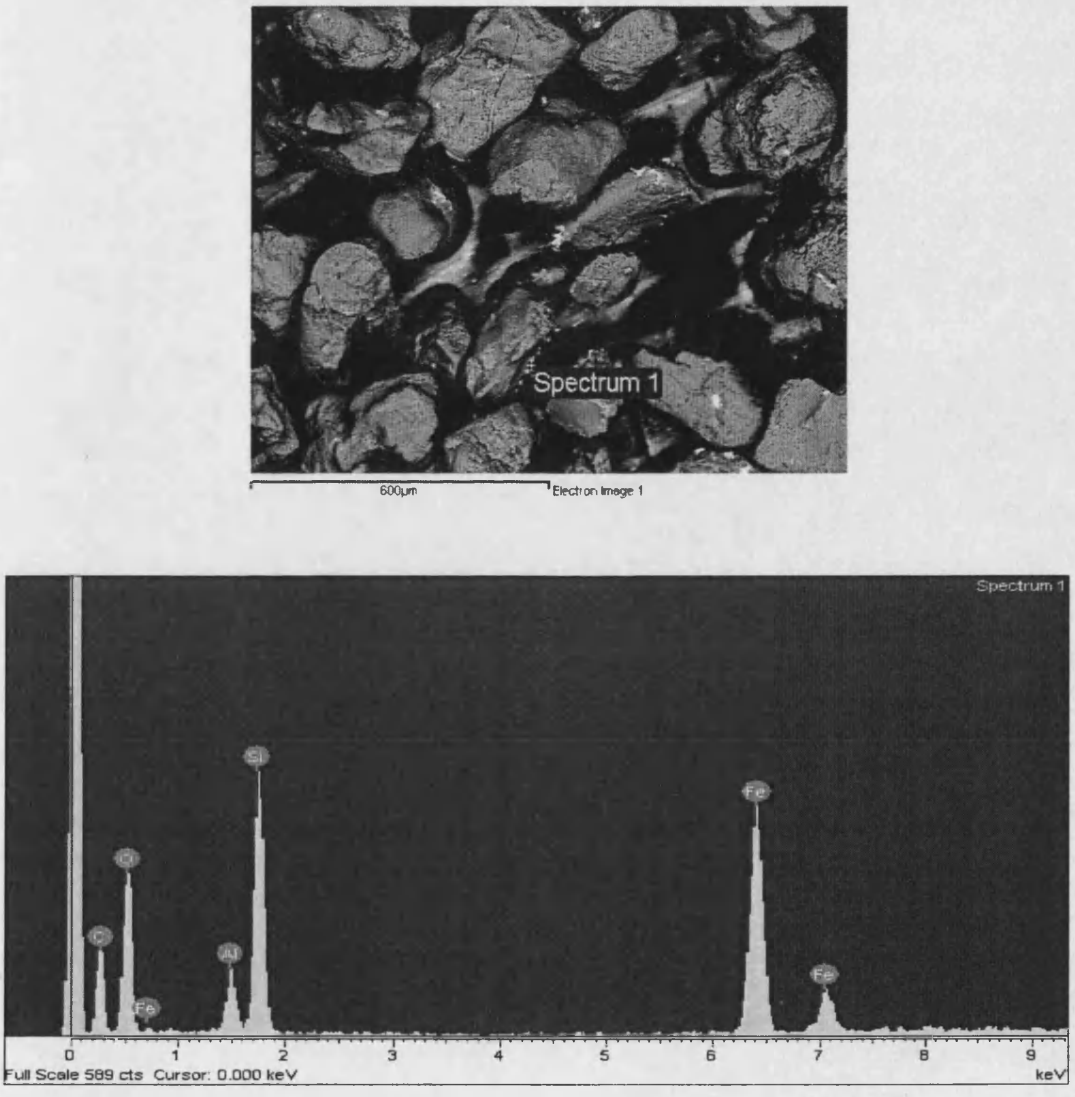

Figure 2.3.3. Quartz grains and goethite from column fill, and associated elemental spectrum, before experiments. The brighter spots relate to areas of high reflectance (goethite). Using analytical SEM.

Figure 2.3.3 shows one of the column filled material samples prior to the experiments. The derived spectrum shows the abundance of silica and oxygen (quartz), and also some iron present in the goethite. The JEOL SEM was also used to observe and compare the column material before and after the column redox experiments. For example, the material was analysed before flushing with arsenic, after flushing with arsenic and then again after flushing with a reducing agent. The set of spectra were ideal for determining the presence of iron and arsenic at any stage during the experiments and therefore whether reductive dissolution of the iron phases had occurred upon reduction. Although this method is only qualitative, it provides information to describe and consolidate results derived by other analytical techniques. The full study is presented in Chapter 5.5.2.

2.3.2. Atomic Absorption Spectrometry

Hydride generation atomic absorption spectrometry was used for the analysis of arsenic concentration within solution samples. As described in Section 2.2.1, when sampling the solutions from the experiments each sample was filtered, using 0.2 μm Nalgene filters and acidified using 10% HNO_3^- (Aristar grade nitric acid). A Varian Atomic Absorption Spectrometer (AAS) machine was used. The machine was fitted with an auto sampler, allowing the prepared samples to be loaded onto the auto sampler in 1.5 ml vials.

Atomic absorption spectrometry utilises interference caused by prescribed atoms, with light of near equal wavelength. When arsenic is atomised (heated to 2500 C) within the sample tube, the atoms produced interfere with light emitted from a hollow cathode arsenic lamp, of wavelength 193.7 nm, and a current of 7 mA. The lamp has a tungsten anode and a cylindrical hollow cathode prepared from arsenic, all sealed within a glass tube filled with an inert argon gas (Levinson, 2004). Since the atoms have a similar wavelength to that of the lamp chosen, interference occurs when those atoms are atomised. The detector is able to measure the amount of interference directly proportional to

the amount of arsenic in solution. With the aid of a digital processor, the spectrometer can be programmed with the SOLAR software package to calculate the solution concentrations.

In order to analyse a solution, a matrix modifier must also be added to the mixture, usually automatically during analysis. The modifier in this case was analar nickel nitrate ($Ni(NO)_3$) and was added to the samples at a constant mass (20μg Ni to 20 μg As) throughout a complete set of batch experiment samples and the volume was determined from the highest expected sample concentration. The purpose of the matrix modifier is to decrease the volatility of the arsenic by producing nickel arsenide. The lower volatility allows for the removal of the other matrix components without losing any of the arsenic present before the atomisation stage (Voth-Beach & Shrader, 1985). The machine requires calibration prior to sample analysis. In this case four standards were used for the calibration and individually pre-prepared. Each contained the components of the experimental solutions, such as 0.01 M $NaNO_3$ and also 10 % HNO_3^-. This ensures that any effect upon the interference by any of the solution components is accounted for post analysis. The four standards used ranged from 0, 10, 20 and 60 μg/l As using analytical grade As, and the calibration implemented a straight line least squares fitting procedure. If the analysed standard concentration falls outside 2 % error, the calibration becomes void and analysis suspended until this criteria is satisfied. As many of the sample concentrations are above the standard cut-off level, dilution procedure is configured within the software so that all samples can be diluted automatically using a known amount of distilled – deionised water.

Once the sample is diluted and mixed with appropriate quantities of matrix modifier (4 μl matrix modifier to 16 μl sample), the sample is inserted into the sampling cuvette (small graphite tube, un-ridged and coated, with a hole within the top wall for the sample to be released). The cuvette is heated, using the spectrometer furnace. Samples are heated in accordance with a particular sequence, which can be programmed into the software. The sequence usually has four phases:

An initial phase, where heating is relatively low (600 C), which expels any organic material.

A second phase when the temperature is increased to expel any other components.

A third phase at the temperature of atomisation (in this case 2400 C). It is during this phase that the detection occurs, as the atom becomes atomised and interference of the light source transpires.

The final phase is used to burn off any residue material remaining within the cuvette before the next sample is inserted, and this usually only lasts a few seconds at the same atomisation temperature, or slightly higher.

Each sample is analysed three times by the machine as part of the pre-programmed sequence to statistically enhance the efficiency and usability of the concentration measurements.

2.3.3. Inductively Coupled Plasma – Atomic Emission Spectrometry

For the analysis of the inherent Iron of the samples in the redox column experiment, Inductively Coupled Plasma – Atomic Emmsion Spectrometry (ICP – AES) was used to establish the solution concentrations. The machine used was the Varian VISTA PRO at the Natural History Museum, London. The solution samples were filtered (0.2 μm filters) and acidified using 10 % HNO_3^-, before analysis. Essential calibration is required before the analysis, and in this instance eight standards were used; 0, 10, 20, 40, 100, 1000, 5000 and 10 000 μg/l, which contained Merck analytical grade iron, and all other components within the samples (catechol, nitric acid and background electrolyte; 0.01M $NaNO_3$).

Samples are placed into an auto-sampler, and once the sequence begins each sample is immersed in argon gas before being carried through a nebuliser and on to the ICP. The iron atoms within the sample are excited by the ICP and lose electrons, which when regained release light photons. The light emitted has a wavelength characteristic of iron. Detection of these wavelengths and

the associated wave amplitude by the spectrometer is recorded and the abundance of that atom present within the sample measured. Each sample is analysed automatically three times to obtain statistically useable concentration values.

3. AN INVESTIGATION OF ARSENIC ADSORPTION BY BATCH EXPERIMENTS

3.1. BATCH EXPERIMENTS INTRODUCTION

A series of batch experiments were performed to derive equilibrium adsorption isotherms and partition coefficients. These are later compared with similar parameters obtained under more dynamic conditions using column experiments. The batch experiments provide evidence and quantification of the dependence of arsenic adsorption on solution pH.

For completeness the results of the batch experiments undertaken in the current study are given in Appendix 3A. Table 2.2.1 in Chapter 2.2.1 defines the experimental conditions and parameters.

Appendix 3B contains the duplicate batch experiment adsorption envelopes which were conducted to ascertain reproducibility of results. The duplicate experiments show a limited spreading of adsorption trend data with respect to solution pH. Although some duplicate batches are not within the acceptable experimental and analytical error (6 %), for example Figure 3.1.1. These discrepancies may highlight the difficulties associated with reproducibility using such low concentrations of arsenic and goethite in small volume batches. With a larger data set to reproduce individual batch reactions, a probabilistic determination of the trends could be identified. The relative adsorption values for the control experiment with zero goethite are below the detection limit for the method of spectroscopic analysis and usually within experimental error. Although some control batches also show discrepancies away from zero adsorption. These may have been caused during the analytical stage with contamination from previously analysed samples, despite actions that were employed to try to remove these effects.

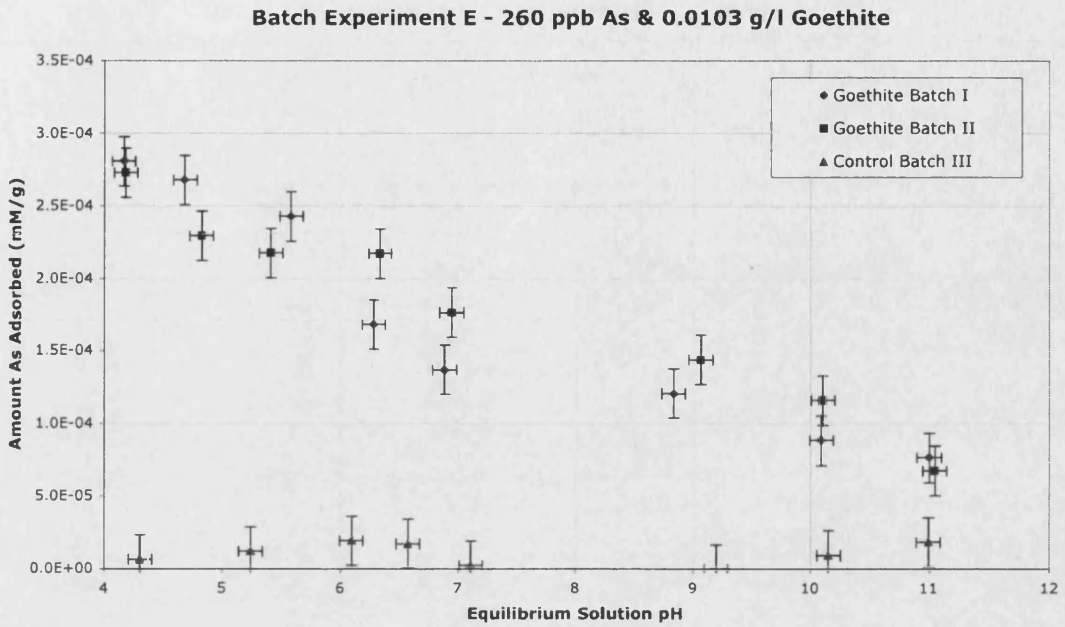

Figure 3.1.1. An example of the duplicate and control batch experiments.

3.2. THE EFFECT OF pH ON ADSORPTION

The dependence of adsorption on pH is observed by using the Point of Zero Charge (PZC) of the adsorbent (goethite) surface (Chapter 1.3). For goethite the PZC is 7.3 at which the goethite surface is neutrally charged. For solution pH less than the PZC the surface is positively charged and hence attracts anions and repels cations. The adsorption of arsenic in anionic form is functionally related to the goethite PZC and changes as the solution pH is varied (Stollenwerk, 2003).

Investigations of the effect of solution pH on arsenic sorption have been reported in the literature (Bowell, (1994), Manning and Goldberg (1997), Pierce and Moore (1982), Lumsdon *et al.* (2001), Chakravarty *et al.* (2002), Anderson *et al.* (1976), and Halter and Pfeifer (2001)).

Figures 3.2.1a – 3.2.1d shows the adsorption pH envelopes for batches containing different quantities of goethite mass. The plots indicate that the adsorption of arsenic (in the As (V) form) by the goethite generally decreases as the solution pH is increased. This was also observed by others (Pierce & Moore (1982) – Chapter 1.3, Figure 1.3.1).

The decreasing trend is associated with and explained by variations of the goethite surface charge and the PZC. At lower solution pH greater As(V) adsorption is observed, corresponding to a positive surface charge on the goethite. On dissolving the sodium arsenate salts the sodium dissociates leaving behind the negatively charged arsenate compound ($HAsO_4^{2-}$), as observed in groundwater (Chakravarty *et al.*, 2002). The negatively charged compound will be strongly attracted to the goethite surface at solution pH between 4 and 7.

The adsorption envelopes also demonstrate some small-scale perturbations. For example, Figures 3.2.1b,c,d show a slight decrease in As adsorption at pH 4, for some of the initial As concentration batches. Also in figures 3.2.1a and

3.2.1d As adsorption increases at pH 10/11 for the As concentration batches 0.3 mg/l and 1.50 mg/l. These unusual dips may result from sampling errors, although some consistency is observed between three of the experiments. For example, in order to achieve the extreme solution pH a comparably larger quantity of alkaline solution may have been added and therefore increasing the overall solution volume and diluting the As solution concentration respectively. Although this error was considered minimal, it may have added to other cumulative errors to produce this anomaly. A larger data set from experiments would be able to confirm whether this anomaly resulted from error or not. Alternatively, a change in the adsorbing complex at extreme low and high pH may result in slightly lower or higher adsorption, respectively. A spectroscopic study by Manning *et al.* (1998) found that at low pH bidentate-binuclear complexes of As were likely to form with goethite and at high pH monodentate-mononuclear were favoured. Further to this, if certain complexes form on specific surfaces or sites at different pH and the goethite present within the batch reactors show a preference for particular surfaces this may also explain these perturbations. Spectroscopic analyses of the different pH batches would help to confirm this.

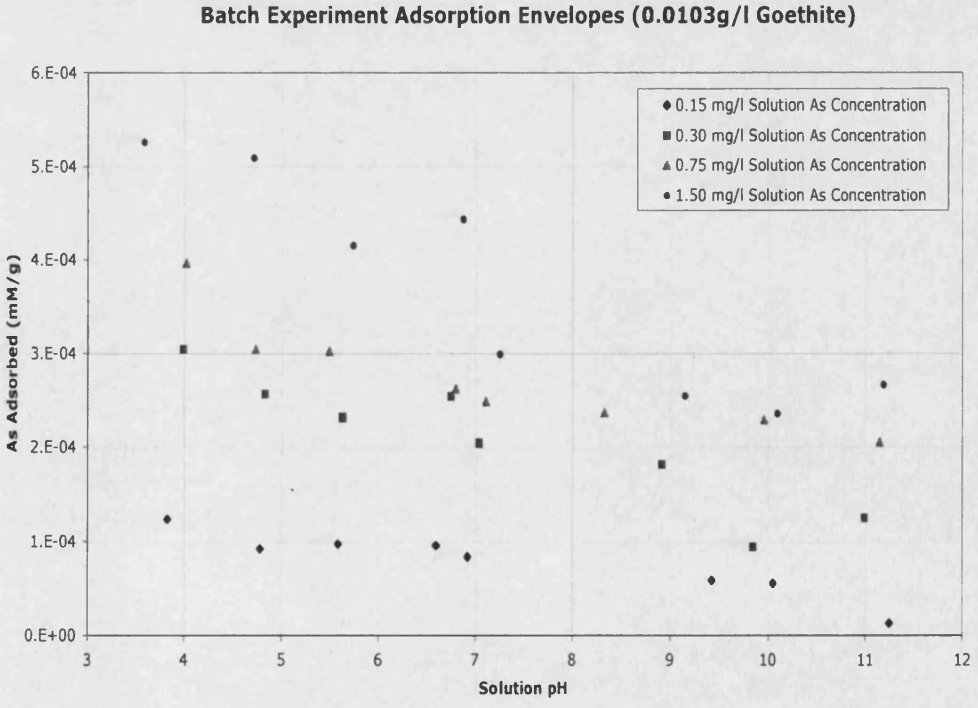

Figure 3.2.1a. Goethite Mass 0.0103 g/l

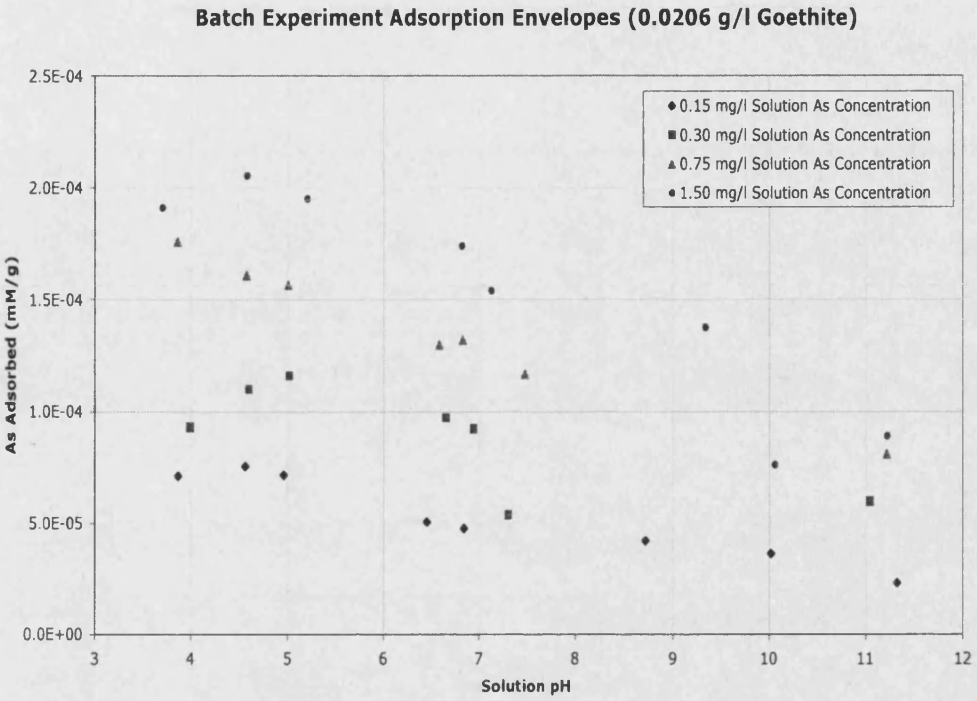

Figure 3.2.1b. Goethite Mass 0.0206 g/l

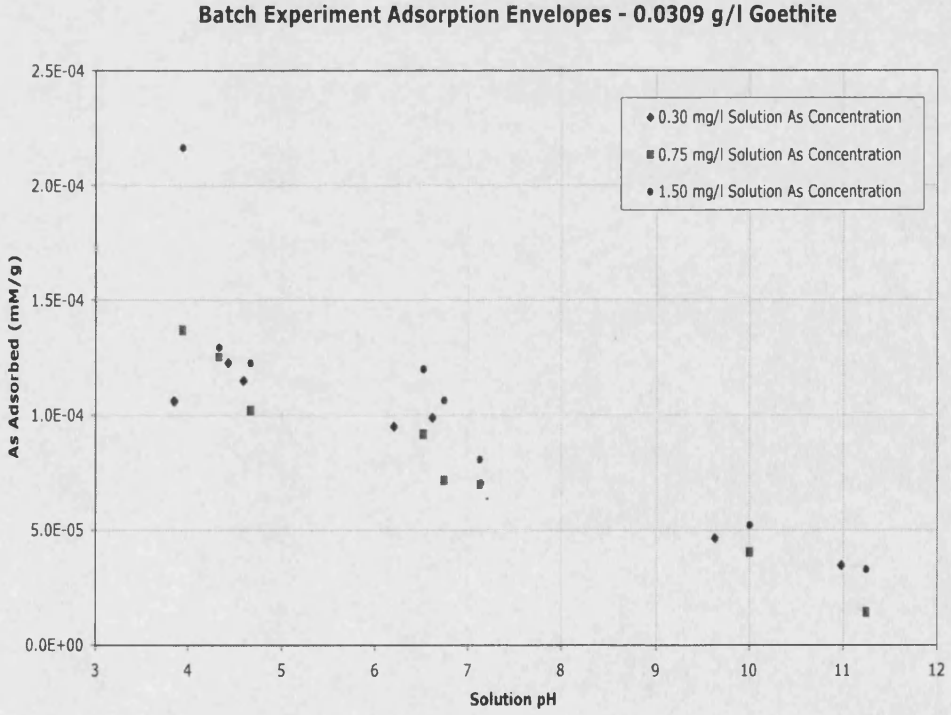

Figure 3.2.1c. Goethite Mass 0.0309 g/l

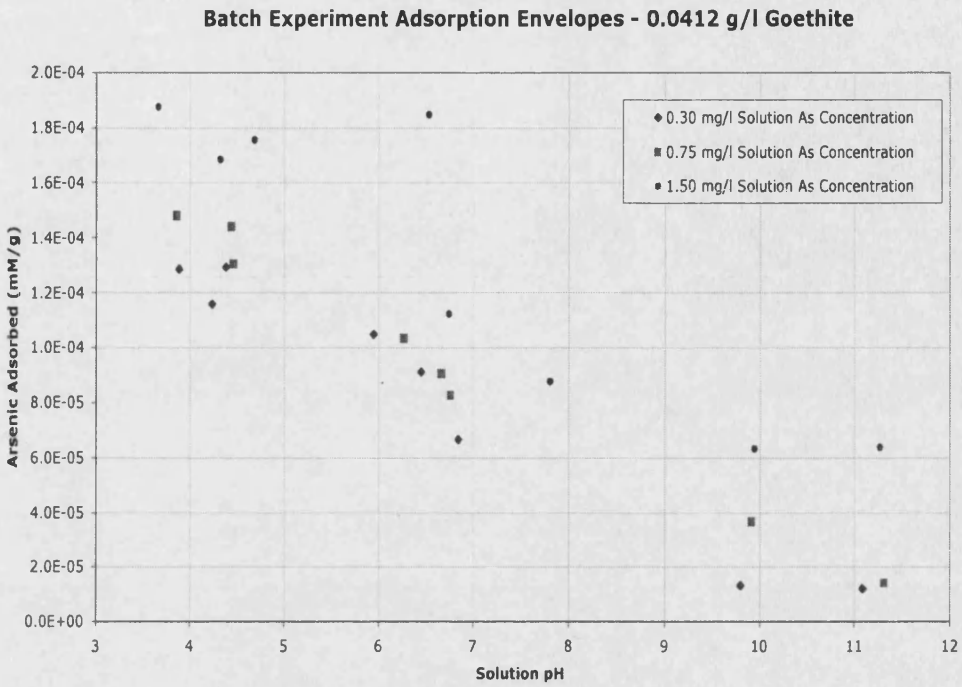

Figure 3.2.1d. Goethite Mass 0.0412 g/l
Figures 3.2.1a-d. Batch experiment adsorption envelopes.

The adsorption envelopes suggest that arsenic adsorption (S) is a function of pH, C_0 (initial As concentration) and m (goethite mass) for the range of values considered, i.e.:

$$S = f(pH, C_0, m) \qquad \textit{Eqn. 3.2.1.}$$

Where f is the functional relationship to the variables (pH, C_0 and m). Figures 3.2.1a – 3.2.1d show that As adsorption decreases as a function of pH and m, and increases as a function of initial As concentration (C_0).

The figures also show that the amount of adsorption increases as the initial arsenic concentration is increased for given goethite mass, suggesting that the adsorption sites on the goethite surface are never completely saturated in this concentration range. By increasing the arsenic solution concentration, more arsenic is available to fill the remaining potential surface adsorbing sites. This implies that the sorption will be described by either a linear or Freundlich isotherm (Chapter 5).

In general, there is a reduction in the adsorbed arsenic as the goethite mass increases, for a given initial As concentration. For example, for the 0.0103 g/l goethite mass concentration (Fig. 3.2.1a) the amount of arsenic adsorbed varied between 1.2 and 5.2×10^{-4} mM/g (over all initial arsenic concentrations 150-1500 μg/l), whereas, for 0.0206 g/l goethite mass concentration (Figure 3.2.1b), the range of arsenic adsorbed varied between 0.25×10^{-4} and 2.0×10^{-4} mM/g for the same initial arsenic concentrations. Ranges of adsorbed arsenic were observed also in the 0.0309 g/l and 0.0412 g/l goethite mass batches. Table 3.2.1 highlights the range of changes of arsenic adsorbed, i.e. the difference between the smallest and largest amounts of arsenic adsorbed for the specific initial arsenic concentrations and goethite mass. The average adsorption range is greatest for the smallest goethite mass over all initial As concentrations. This range drops as the mass of goethite increases. This trend suggests that the proportion of available binding sites is greater in the batches containing more goethite, compared with the 0.0103 g/l batch that the change in range of arsenic adsorbed is not as significant. In other words the proportion of binding sites increase non-linearly with arsenic concentration or goethite mass. This observation will be discussed further in Chapter 5 (Section 5.4), in relation to adsorption isotherms.

The amount of adsorption observed by Pierce and Moore (1982) at typically 0.1–1.4 mM/g is significantly greater than that occurring in these batch experiments. There are many factors that could cause this difference, not least the fact that Pierce and Moore used a different iron oxide mineral HFO (hydrous ferric oxide). It has been suggested that these amorphous minerals can adsorb far greater quantities than their crystalline counterparts with a deterministic set of adsorption sites (Fisher (1999) and Smedley & Kinniburgh (2002)). The amorphous structure allows for greater number of sites for binding, increased by the potential for adsorption within its crystal lattice. The surface area of goethite is about 50 m^2/g (Waychunas *et al.*, 1993), whereas the surface area of HFO is about 380 m^2/g (Hofmann *et al.*, 2004).

INITIAL As CONCENTRATION (μg/l)	GOETHITE MASS (g/l)	RANGE OF CHANGE OF As ADSORPTION (mM/g), $\Delta S \Big\vert_{C_0}^{pH(4,11)\ m}$
150	0.0103	2.80E-04
"	0.0206	1.50E-04
300	0.0103	2.00E-04
"	0.0206	0.90E-04
"	0.0309	1.85E-04
"	0.0412	1.26E-04
750	0.0103	2.10E-04
"	0.0206	0.60E-04
"	0.0309	1.25E-04
"	0.0412	1.00E-04
1500	0.0103	1.20E-04
"	0.0206	0.50E-04
"	0.0309	1.10E-04
"	0.0412	1.18E-04

Table 3.2.1. Summary of the range of change of arsenic adsorption for the different batch experiments.

An alternative way to look at the adsorption range for different batch experiments is in terms of a 'Spread Factor' (SF). The spread factor accounts for the coverage of experimental data in terms of the amount of adsorption (mM/g) encompassing the minimum and maximum amounts of adsorption at a specific solution pH and for a defined range of initial As solute concentrations, i.e. $\Delta S \Big\vert_{C_0}^{pH(4,11)\ m}$:

$$SF = S_{C\text{-}max} - S_{C\text{-}min} \qquad \textit{Eqn. 3.2.2.}$$

Where: $S_{C\text{-}max}$ = Amount As adsorbed (mMg^{-1}) for the max C_0 (initial As concentration experiment)

$S_{C\text{-}min}$ = Amount As adsorbed (mMg^{-1}) for the minimum C_0 experiments

Table 3.2.2 summarises the SF for each goethite mass batch and for different solution pH. Only the experiments with As solute concentrations between 300 and 1500 μg/l were considered in these calculations to maintain consistency throughout the four goethite mass experiments.

The results show that the overall range of the spread factor for the pH extent tested is greatest for those experiments containing the least goethite mass, and the SF generally diminishes as the goethite mass concentration increases. The spread factor also decreases as the solution pH increases and this trend is better illustrated where the goethite mass is smallest and the range of the spread factor is greatest. The reduction in the spread factor with increasing pH corresponds with the effect of the goethite PZC and therefore greater attraction for arsenic at low pH. At high pH (>7.3) the goethite surface has negative charge and the arsenic anions in the solution are less attracted to the goethite. The observed reduction in spread factor over the entire pH range also suggests that there is a limit for potential adsorption at high pH. At these pH conditions, and for constant goethite mass, the amount of arsenic adsorbed is not significantly affected by increased arsenic concentrations. Where the spread factor is converging towards small values at high pH the limiting effect is pronounced. At this point the surface charge on the goethite will be highly negative. This is likely to result in lesser adsorption because of both reduction in potential sites and the low opportunity for attraction of anions.

0.0103 g/l Goethite Batch Experiment	
Solution pH	**SF ($x10^{-4}$)**
4	2.2
5	2.2
6	2.0
7	1.9
8	1.2
9	1.2
10	1.3
11	1.4
Total Range of SF over the entire pH series	**1.0**

0.0206 g/l Goethite Batch Experiment	
Solution pH	**SF ($x10^{-4}$)**
4	1.05
5	0.80
6	0.80
7	0.80
8	0.70
9	0.65
10	0.30
11	0.20
Total Range of SF over the entire pH series	**0.85**

0.0309 g/l Goethite Batch Experiment	
Solution pH	**SF ($x10^{-4}$)**
4	0.45
5	0.30
6	0.30
7	0.25
8	0.20
9	0.15
10	0.10
11	0.15
Total Range of SF over the entire pH series	**0.35**

0.0412 g/l Goethite Batch Experiment	
Solution pH	**SF ($x10^{-4}$)**
4	0.55
5	0.70
6	0.65
7	0.40
8	0.35
9	0.40
10	0.50
11	0.55
Total Range of SF over the entire pH series	**0.35**

Table 3.2.2. The range of Spread Factor (SF) for the different goethite mass experiments and the solution pH extent tested. Total range SF = SF_{max} – SF_{min} specific to each goethite batch experiment.

3.3. THE EFFECT OF ARSENIC CONCENTRATION ON ADSORPTION

Adsorption isotherms relate the amount of arsenic adsorbed (in mg) by a known mass of adsorbent such as goethite (in g) to the amount of arsenic that remains in solution (mg/l) at equilibrium. The subsequent plot of the amount of arsenic adsorbed per mass of goethite, against the amount of arsenic remaining in solution, is the adsorption isotherm.

Studies have indicated that the functionality between the amount of arsenic adsorbed and concentration is usefully modelled by one of three isotherms:

Linear
Freundlich, non-linear
Langmuir, non-linear

If the relationship is linear, then the isotherm has the linear form:

$$S = K_d C \qquad \textit{Eqn. 3.3.1.}$$

Where; **S = Amount arsenic sorbed per mass adsorbent (mg/g)**
K_d = Linear Partition coefficient
C = Equilibrium arsenic concentration in solution (mg/l)

In many situations adsorption is not linear (Domenico & Schwartz, 1998). The Freundlich Isotherm has the following form:

$$S = K_f C^n \qquad \textit{Eqn. 3.3.2.}$$

Where: **K_f = Freundlich partition coefficient**

The Langmuir isotherm also describes non-linear adsorption, but includes the situation when the sorption sites become saturated and an increase in sorbate concentration does not lead to any increase in sorbed mass.

The Langmuir equation has the form:

$$S = (Q^0 K_l C / 1 + K_l C) \qquad \textit{Eqn. 3.3.3.}$$

Where; Q^0 **= Maximum surface sorption capacity**

K_l **= Langmuir partition coefficient**

The experimental isotherms are interpreted and discussed in Chapter 5.2.

4. AN INVESTIGATION OF ADSORPTION BY COLUMN EXPERIMENTS

4.1. COLUMN EXPERMENT INTRODUCTION

In contrast with the equilibrium environment of batch experiments, column experiments provide information about the adsorption of arsenic under realistic fluid flow conditions. Much of the literature is focussed on arsenic adsorption onto iron oxy-hydroxides using batch experiments (Sun & Doner (1999), Bowell (1994), Pierce & Moore (1982), Manning & Goldberg (1997)) and relatively few published results are available on column experiments. Intuition suggests adsorption may not occur to the same extent and may not reach equilibrium under fluid flowing conditions.

Fluid flow experiments were conducted in columns containing different amounts of goethite as a homogeneous mixture with non-reactive quartz sand. Non-reactive conservative tracer experiments determined the consistency of the column packing and later used to define the dispersivity, and physical non-equilibrium in terms of effective porosity for individual experiments. The concentration of the arsenic influent solution was varied across a realistic range of practical environmental arsenic concentrations. The column experiments were used also to investigate kinetic effects under different flow rates through the column. Post experiment 'flushing' (desorption) quantified and identified the presence of irreversible adsorption. Duplicate column experiments are presented in Appendix 4C and show good agreement within the experimental and analytical error of 6 %.

The principle of redox variation is introduced as a factor in the adsorption process.

4.2. PRE-ANALYSIS OF RESULTS

4.2.1. Chloride Tracer Breakthrough

The first order average discharge velocity (v) was determined directly from the effluent flow rate. The average advective velocity (V_x) given in Table 4.2.2 was extracted from the chloride BreakThrough Curves (BTCs) by using the $C/C_0 = 0.5$ time as the average advective time for the solute to travel the length of the column sediment. The effective porosity (n_e) was calculated (Table 5.3.2 in Chapter 5.3) from the chloride BTCs using the following equation (Fetter, 1994):

$$n_e = (100\ Q) / (V_x A) \qquad \textit{Eqn. 4.2.1.}$$

Where: Q = Flow rate (cm^3s^{-1})

A = Cross-sectional area of column (cm^2)

V_x = Fluid flow or advective velocity (cms^{-1})

Chapter 5.3 considers the effect of effective porosity and physical non-equilibrium on the description of arsenic partitioning.

Prior to flushing with an arsenic solution, the hydraulic parameters of the columns, such as the average fluid velocity and the dispersivity, were measured. For this, a number of tracer tests were carried out using NaCl (340 mg/l Cl) and the chloride content of the effluent monitored indirectly using a hand-held calibrated conductivity meter.

Table 2.2.3 in section 2.2 has already summarised the experimental parameters and variables for all column experiments and Table 4.2.1 summarises the tracer experiment sets and their purpose.

EXPERIMENTAL SET	PROCEDURE	PURPOSE
(1) Sand or Goethite	Identical columns – one containing quartz sand only, and one with addition of 0.0683 g goethite	Identify possible effect of goethite on conservative flow
(2) Flow Rate	Using quartz only column and increasing flow rate: $Q_1 = 0.131$ cm^3/s $Q_2 = 0.125$ cm^3/s	To establish flow rate is the dominant control on the transport of conservative solute through column
(3) Progressive Flushing	Using four-column experiment set, column four as an example	To illustrate settlement of columns prior to achieving an equilibrium state (Fig 4.2.2)
(4) Goethite Mass	Using the four-column set	Identify significant differences in conservative solute transport between columns
(5) Flow Rate	Using four column set	Effect of flow rate between the four column set

Table 4.2.1. Summary of the various tracer experiments used during the current study.

General observations and measurements from the experimental sets are as follows:

(1) The results of material tests (Figure 4.2.1 and Appendix 4A) indicate that the incorporation of goethite within the column matrix does not significantly affect the chloride tracer breakthrough. For example, the breakthrough times ($t_{0.5}$) at $C/C_o = 0.5$ for experiment set 1, test 1 and 5 (goethite-quartz and quartz only column fill, respectively) show no significant difference and the BTCs have the same shape. Therefore chloride does not significantly adsorb onto the goethite surfaces under flowing conditions and acts as a conservative non-reactive tracer.

(2) The measured difference between the breakthrough for the quartz column 1 ($Q = 0.131$ cm^3/s) and that for quartz column 2 ($Q = 0.125$ cm^3/s) is significant (Figure 4.2.1). Quartz column 1 has a flow rate which is 1.08 times larger than quartz column 2, and breakthrough for column 1 occurs 1.4 times sooner (370 seconds earlier) than column 2. This implies that the flow rate, as one would expect, plays a crucial role in the transport of all substances flowing within the column.

For analysis of the BTCs in this study, the 'rise time' of the BTC is defined as the corresponding time between C/C_o = 0.1 to 0.9 and is taken as a measure of the combined effect of dispersion and sorption. For experiment set 2 the rise time reduced as the flow rate increased (Figure 4.2.8) corresponding to reduced effects from dispersion and sorption.

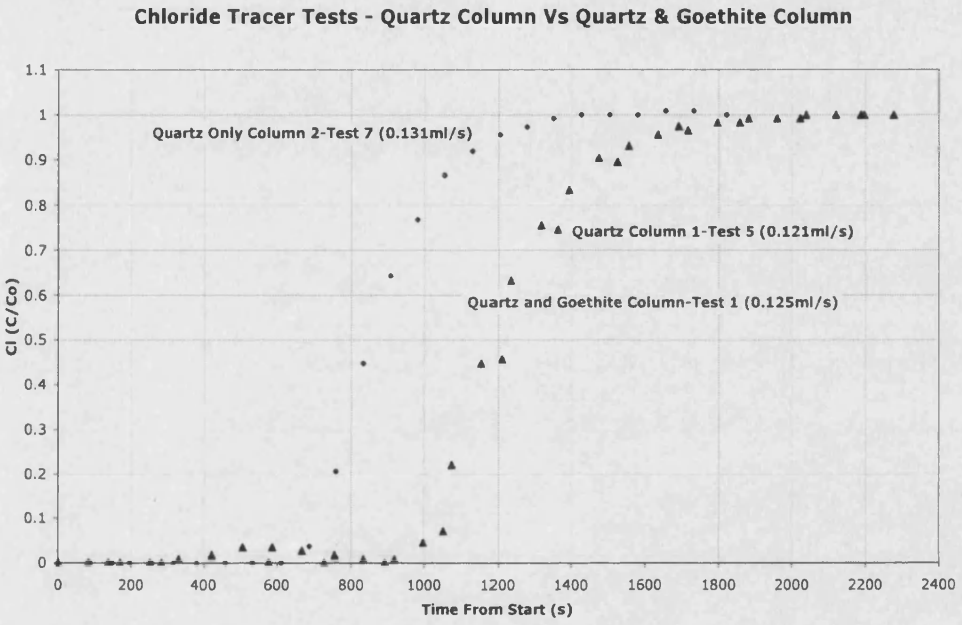

Figure 4.2.1. Chloride tracer breakthrough curves demonstrating the effect of adding goethite to the quartz sand matrix, and also the effect of flow rate.

(3) Chloride tracer experiments on the four-column set (experimental set 3) also demonstrate that the column subtly becomes more physically stable and hence less permeable as the sediment settles. The chloride BTCs (Figure 4.2.2) show the earlier tests to have smoother curves and longer rise times (Table 4.2.2) and therefore more dispersion. The plots become sharper (with shorter rise time) for later tests where settlement of the sediment has occurred.

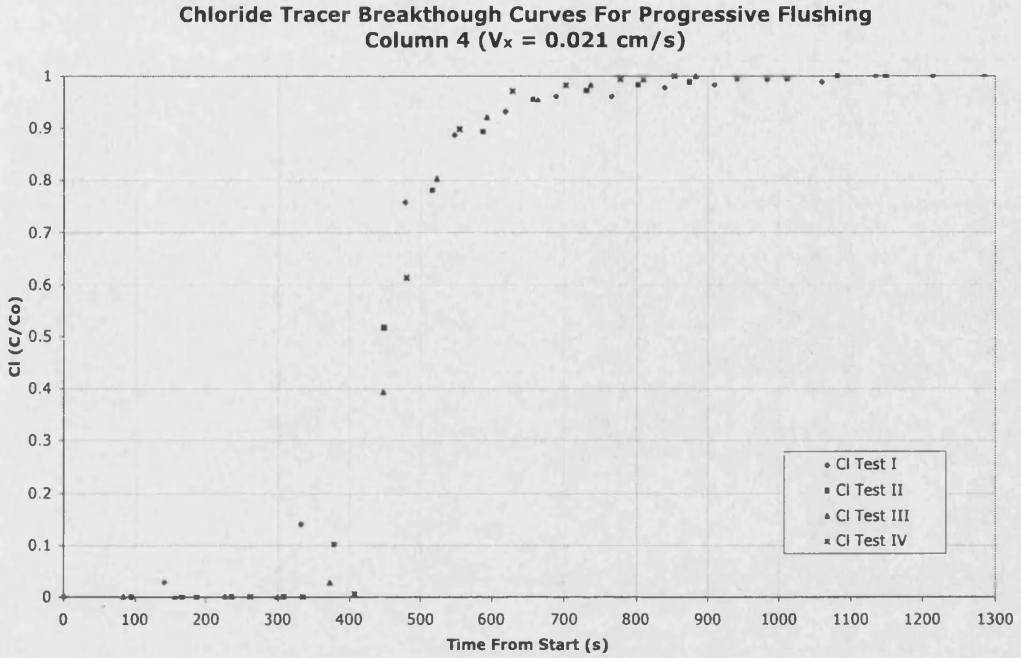

Figure 4.2.2. Experiment set 3; progressive chloride tracer tests (tests I – IV respectively) upon column 4, showing the succession towards physical equilibrium.

(4) Figure 4.2.3 illustrates uniform column flow for the four different goethite mass columns used in the final adsorption experiments and experiment set 4. The short rise times of the curves demonstrate the lack of chloride adsorption and relative dispersion during flow. They also show a slight increase in the breakthrough time with increasing goethite mass (Figure 4.2.4.) but overall a fairly constant rise time (Figure 4.2.5).

The slight increase in the breakthrough time for greater goethite mass (Table 4.2.2) may result from small chloride adsorption onto the goethite or may reflect a decrease in the effective porosity of the column material.

Therefore, due to the insignificant overall difference between Cl BTCs for the four columns, and for ease of differentiation between the non-retarding flow and the As BTCs, a 'common' tracer curve was used to represent all four columns. The chosen tracer plot is that for column 4, as it was the most physically stable curve.

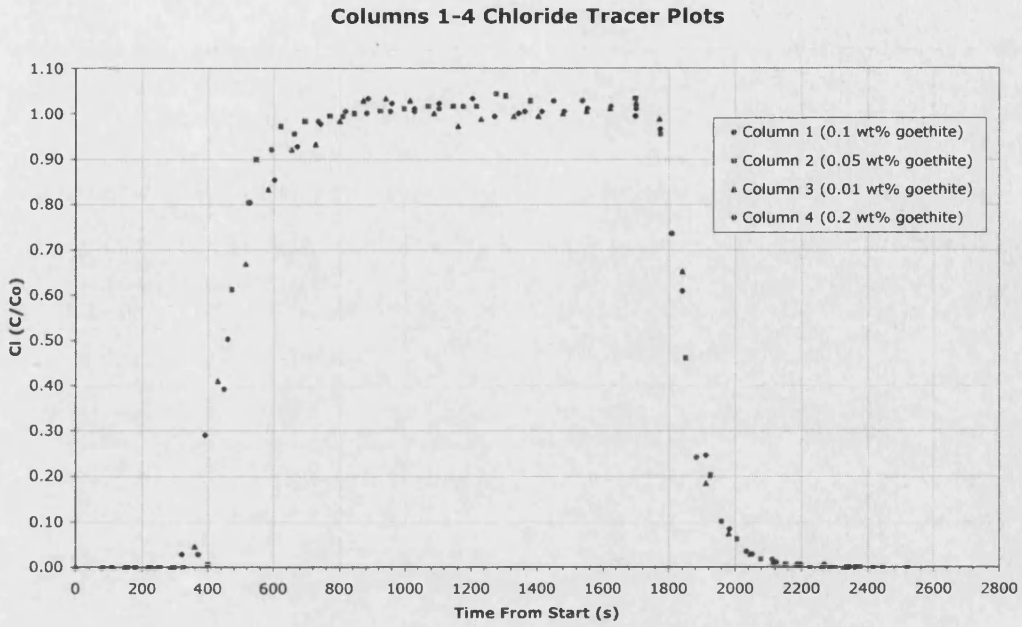

Figure 4.2.3. Chloride breakthrough for columns 1 to 4 (V_x = 0.02 cm/s) and Cl concentration of 340 mg/l.

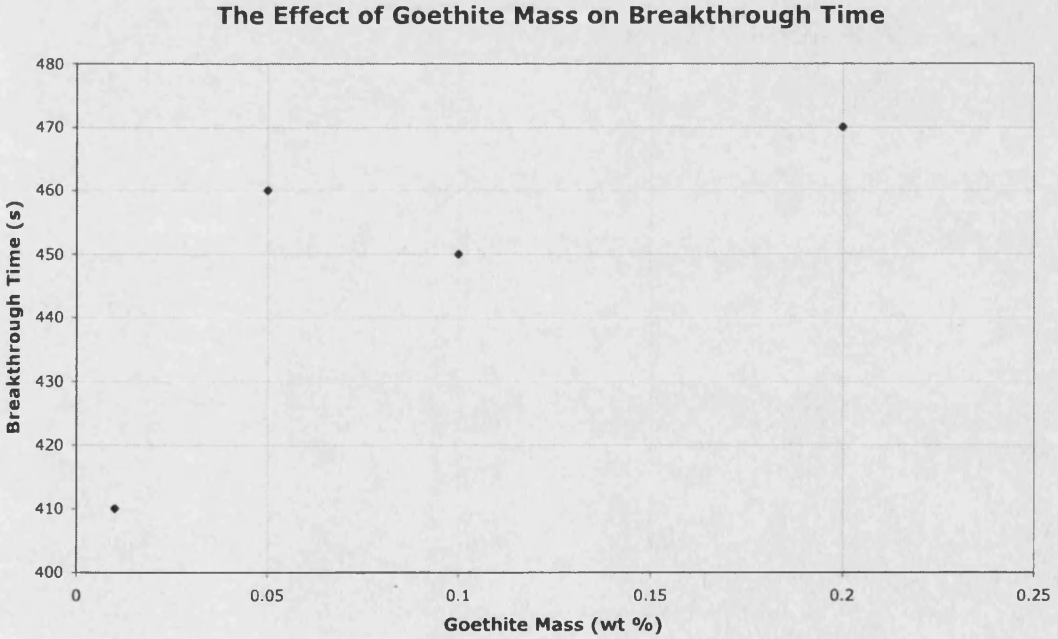

Figure 4.2.4. The effect that goethite mass within the column material has on the breakthrough time.

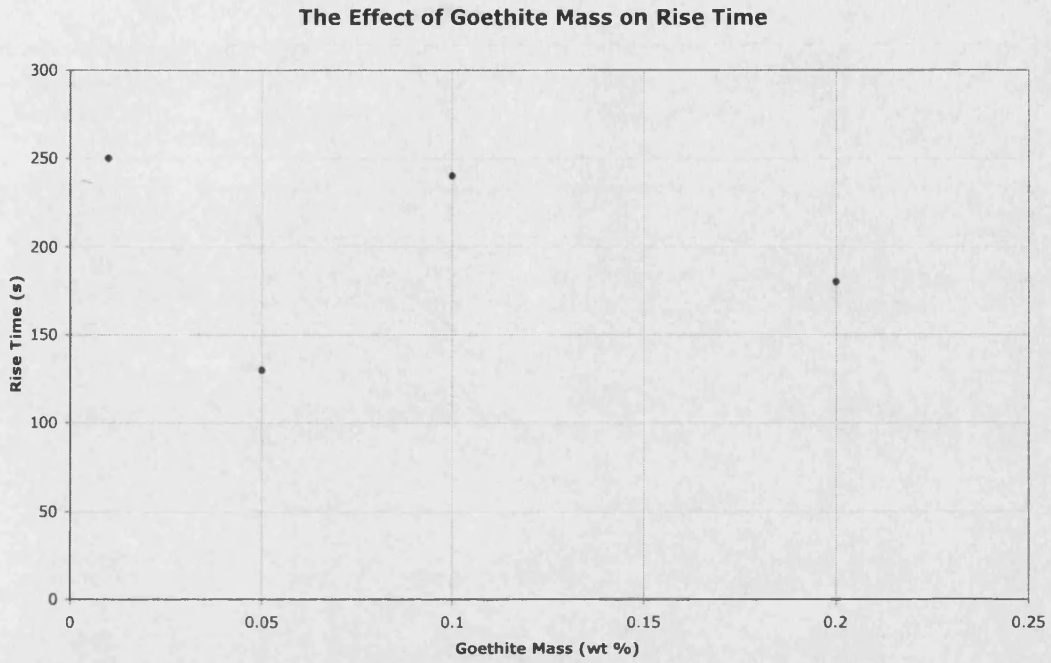

Figure 4.2.5. The relatively constant rise time value for different goethite mass within the column fill.

(5) Tracer tests for the different flow rates used in the final adsorption experiments (experiment set 5) also highlight the effect that increased velocity has on the BTC (Figure 4.2.6). As the flow velocity through the column increased, the breakthrough time occurred sooner (Figure 4.2.7). Similarly, the rise time reduced as the velocity increased, with a reduced opportunity for dispersion (Figure 4.2.8).

These general trends were also observed in the preliminary chloride tests (parts 1 and 2), and the small discontinuity observed between the two sets of results describing the trends (Figures 4.2.6 to 4.2.8) may have arisen from physical differences in the column fill, such as porosity.

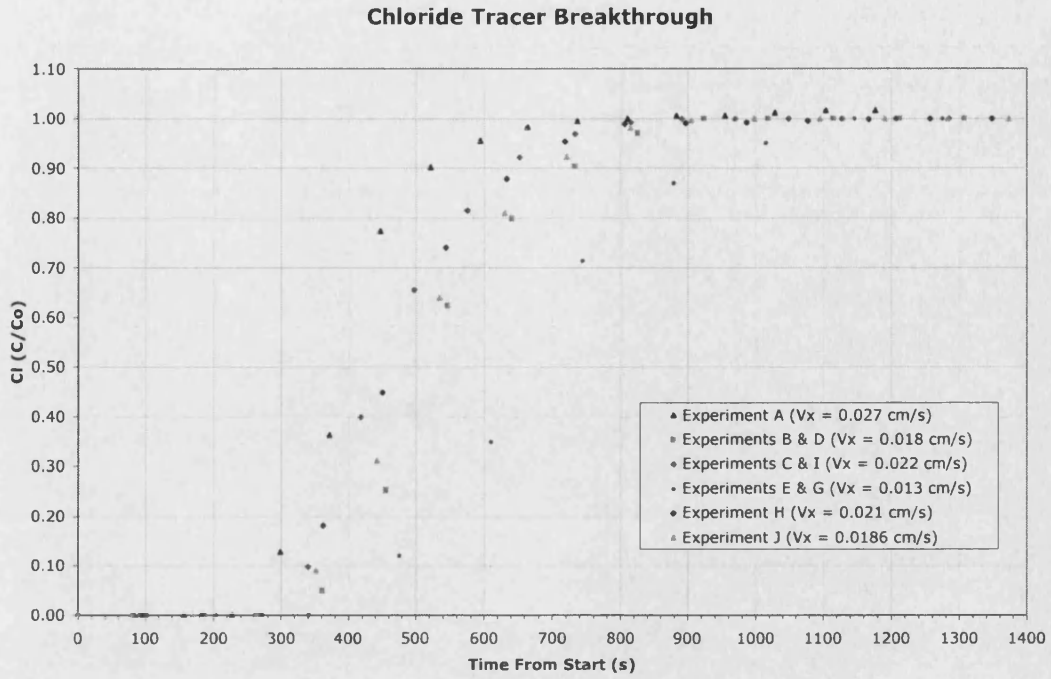

Figure 4.2.6. Chloride tracer plots for all experimental flow rates. Where C is the effluent concentration and C_0 is the initial concentration of the influent solution.

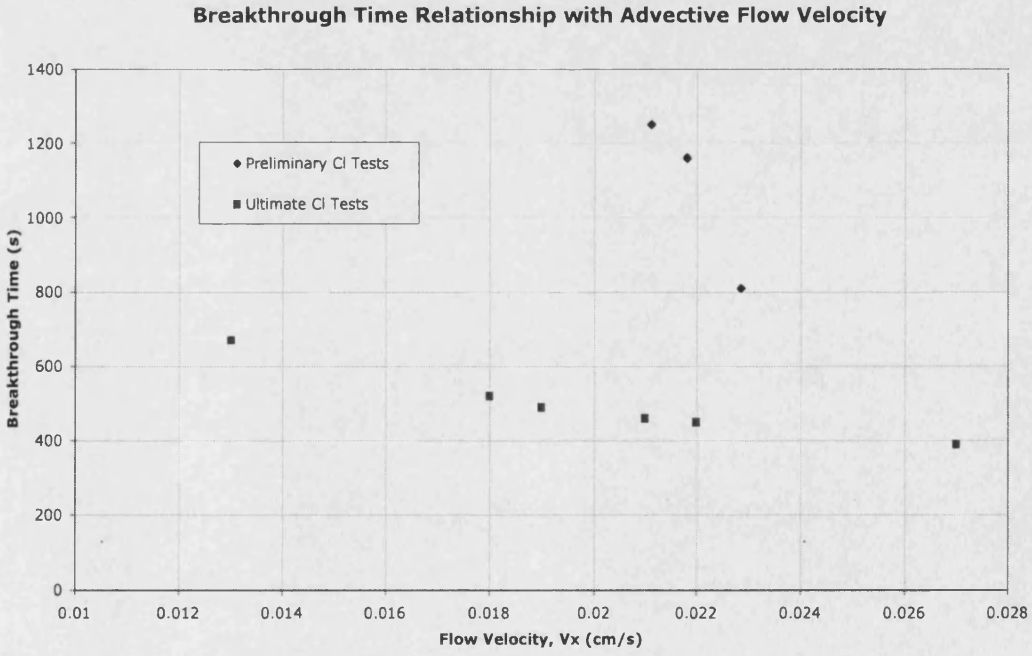

Figure 4.2.7. Relationship between breakthrough time and the flow velocity (V_x) for the preliminary tests (set 2) and the ultimate tests (set 5).

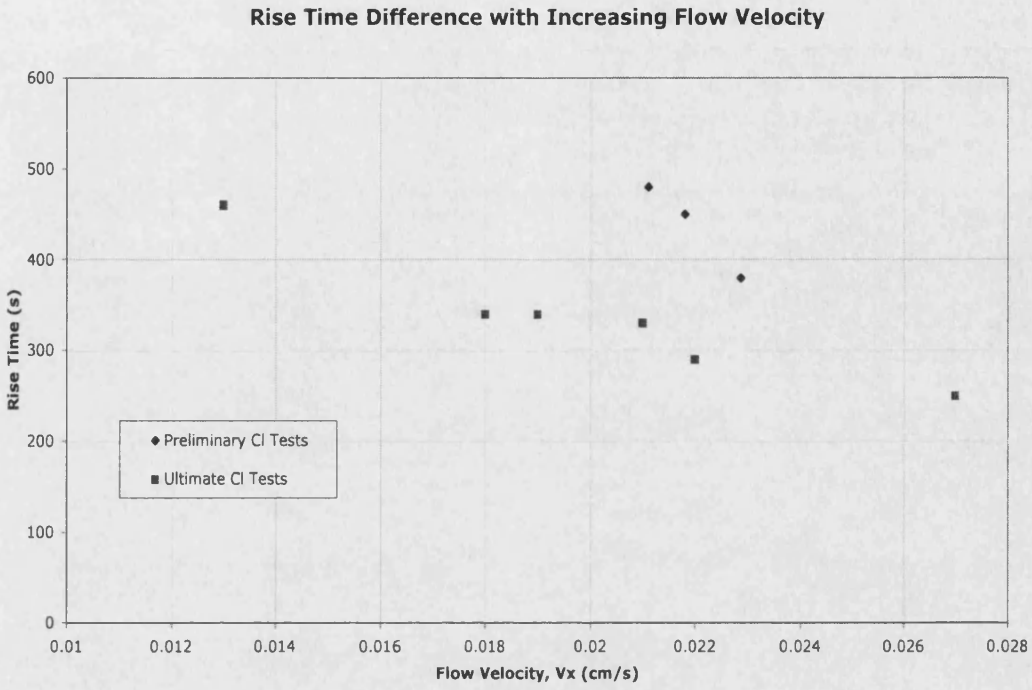

Figure 4.2.8. Relationship between rise time and the advective flow velocity (V_x) for the preliminary tests (set 2) and the ultimate tests (set 5).

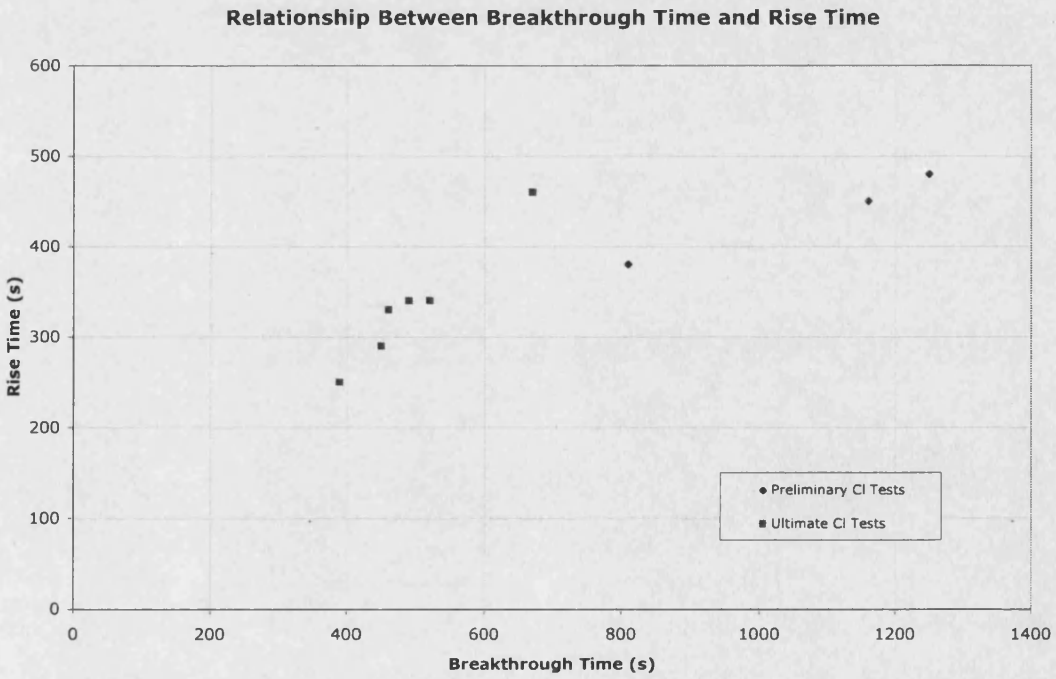

Figure 4.2.9. Relationship between breakthrough time and the rise time for the preliminary tests (set 2) and the ultimate tests (set 5).

Table 4.2.2 summarises the breakthrough times for all chloride experiments described in this section. Figure 4.2.9 illustrates the positive almost linear relationship between the breakthrough time and the rise time that can be described by advective and dispersive effects.

EXPERIMENT	Flow Rate, V_x (cm/s)	BREAKTHROUGH TIME (BT), s ($C/C_0 = 0.5$)	RISE TIME (RT), s (C/C_o = 0.1 to 0.9)
(2) Quartz column, test 7	0.022	1250	480
(2) Quartz & goethite column, test 1	0.024	1160	450
(2) Quartz column, test 5	0.035	810	380
(3) Progressive Test I	0.021	420	240
(3) Progressive Test II	0.021	450	210
(3) Progressive Test III	0.021	470	180
(3) Progressive Test IV	0.021	470	140
(4) Column 3 (0.01 wt% goethite)	0.020	450	240
(4) Column 2 (0.05 wt% goethite)	0.020	460	130
(4) Column 1 (0.1 wt% goethite)	0.020	410	250
(4) Column 4 (0.2 wt% goethite)	0.020	470	180
(5) Experiment A	0.027	390	250
(5) Experiments B & D	0.022	520	340
(5) Experiments C & I	0.020	450	290
(5) Experiments E & G	0.013	670	460
(5) Experiment H	0.024	460	330
(5) Experiment J	0.019	490	340

Table 4.2.2. Chloride tracer breakthrough and rise times for different chloride experiments. The number in brackets identifies the experiment set as described in Table 4.2.1.

4.2.2. The Effect of The Mass of Goethite on Arsenic Adsorption

Columns with different mass of goethite exhibit different breakthrough properties. From the experimental BTCs (for example Figure 4.2.10 and all experiments in Figure 4.2.17) it is observed that the breakthrough time tends to increase as a function of goethite mass, although there is no obvious trend observed between the goethite mass and rise time (Figures 4.2.11 and 4.2.12, respectively). Table 4.2.3 shows the breakthrough times and rise times for all experiments. Table 4.2.4 summarises the general trends observed for the breakthrough times with different goethite mass and flow velocity. There were no strong relationships observed for the rise time and so they do not appear in the summarised Table.

The delayed breakthrough times observed for columns containing greater goethite mass may reflect differences in the physical flow through the columns. Unlike the chloride experiments, there is only a weak positive relationship observed between the breakthrough time and the rise time, and this is due to the addition of the adsorption process (Figure 4.2.13). The later breakthrough times may therefore demonstrate the greater retardation of arsenic through columns containing more goethite.

	COLUMN 3 (0.01 wt%) (s)		COLUMN 2 (0.05 wt%) (s)		COLUMN 1 (0.1 wt%) (s)		COLUMN 4 (0.2 wt%) (s)	
	BT (s)	RT (s)	BT (s)	RT (s)	BT (s)	RT (s)	BT (s)	RT (s)
EXPERIMENT A (870 μg/l & V_x = 0.027 cm/s)	420	450	450	500	500	450	710	700
EXPERIMENT C (280 μg/l & V_x= 0.020 cm/s)	480	390	580	590	620	650	880	860
EXPERIMENT I (750 μg/l & V_x = 0.022 cm/s)	540	480	600	440	650	470	860	660
EXPERIMENT H (630 μg/l & V_x = 0.021 cm/s)	600	600	710	630	790	590	850	410
EXPERIMENT J (630 μg/l & V_x = 0.019 cm/s)	690	680	790	650	870	680	1000	660
EXPERIMENT B (600 μg/l & V_x = 0.018 cm/s)	800	810	940	990	1040	830	1100	560
EXPERIMENT D (57 μg/l & V_x = 0.018 cm/s)	920	510	1000	690	1060	1200	1130	1080
EXPERIMENT E (780 μg/l & V_x = 0.013 cm/s)	1050	540	1070	490	1200	480	1400	860
EXPERIMENT G (540 μg/l & V_x = 0.013 cm/s)	1090	660	1100	560	1150	730	1480	890

Table 4.2.3. The resulting breakthrough times (BT) and rise time (RT) for experiments A – J, and columns 1 – 4, in order of decreasing column flow velocities (V_x).

		GOETHITE MASS	
		LOW	HIGH
VELOCITY	HIGH	OCCURS FAST	OCCURS RELATIVELY FAST
	LOW	OCCURS RELATIVELY SLOW	OCCURS SLOW

Table 4.2.4. Summary of Table 4.2.3. Highlighting the effect of goethite mass and flow velocity on the breakthrough times.

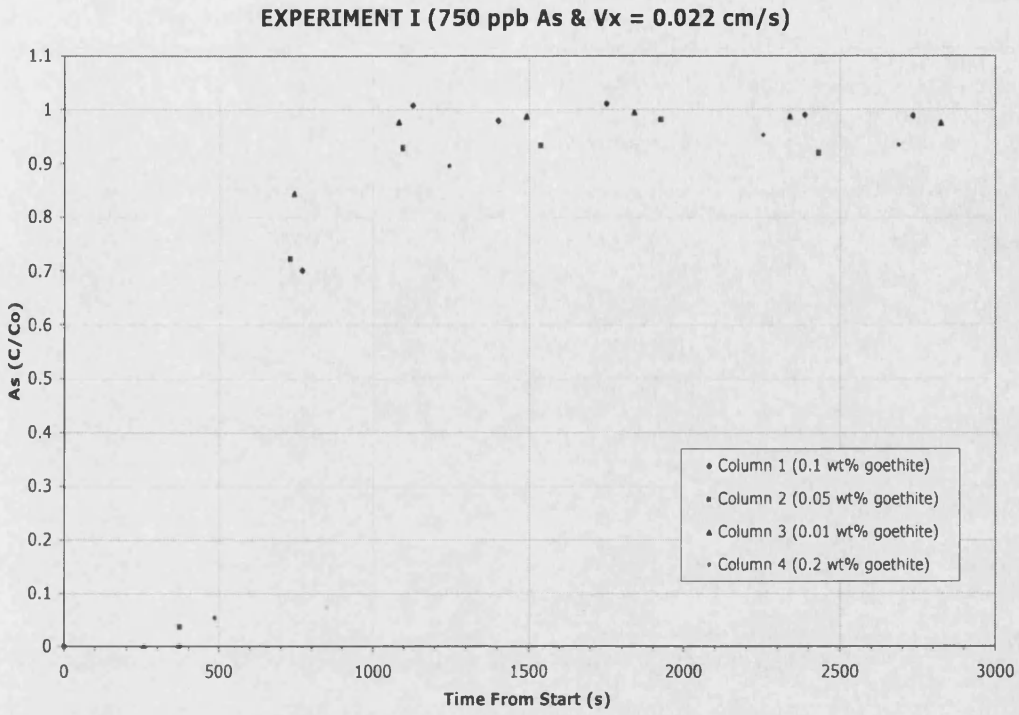

Figure 4.2.10. Experiment I breakthrough plots for the four columns (goethite mass between 0.01 and 0.2 weight%).

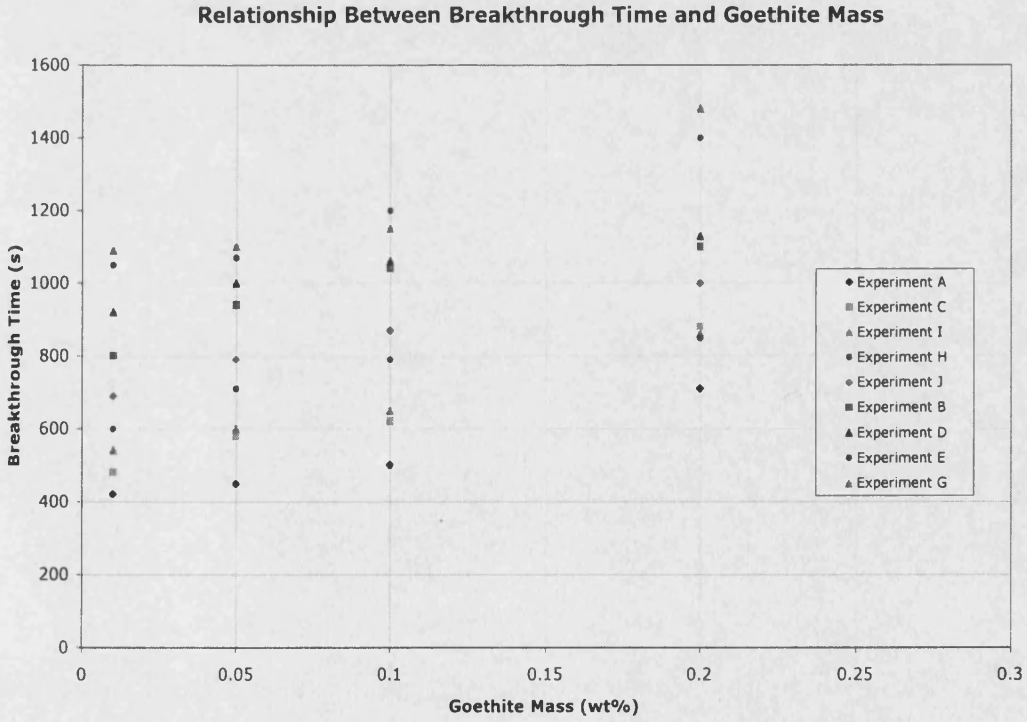

Figure 4.2.11. Plot showing the slight positive trend between breakthrough time and the goethite mass within the column fill.

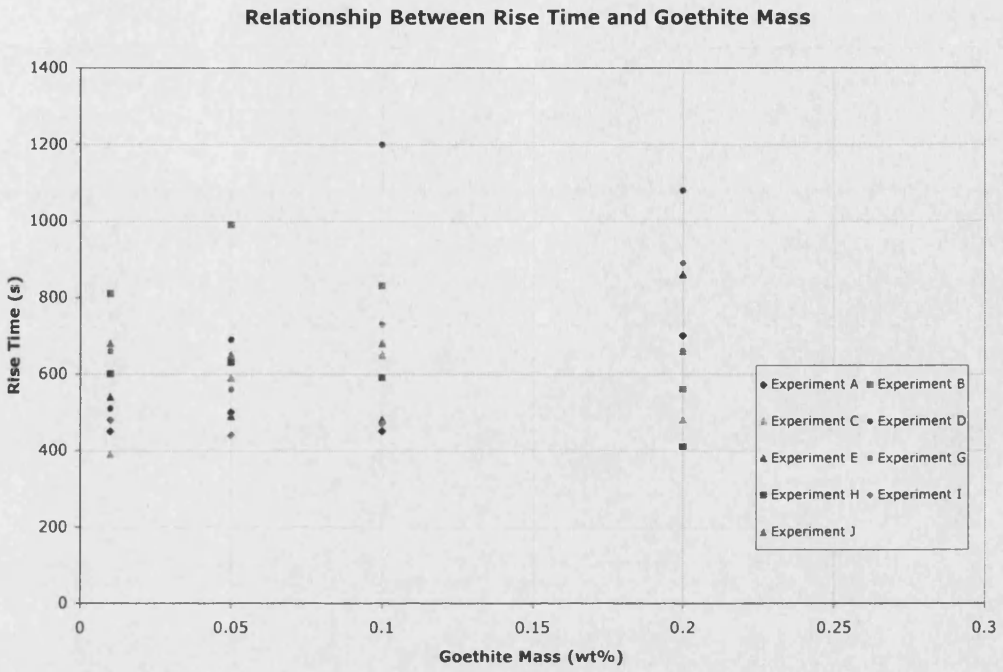

Figure 4.2.12. Plot showing no distinct trend between rise time and the goethite mass within the column fill.

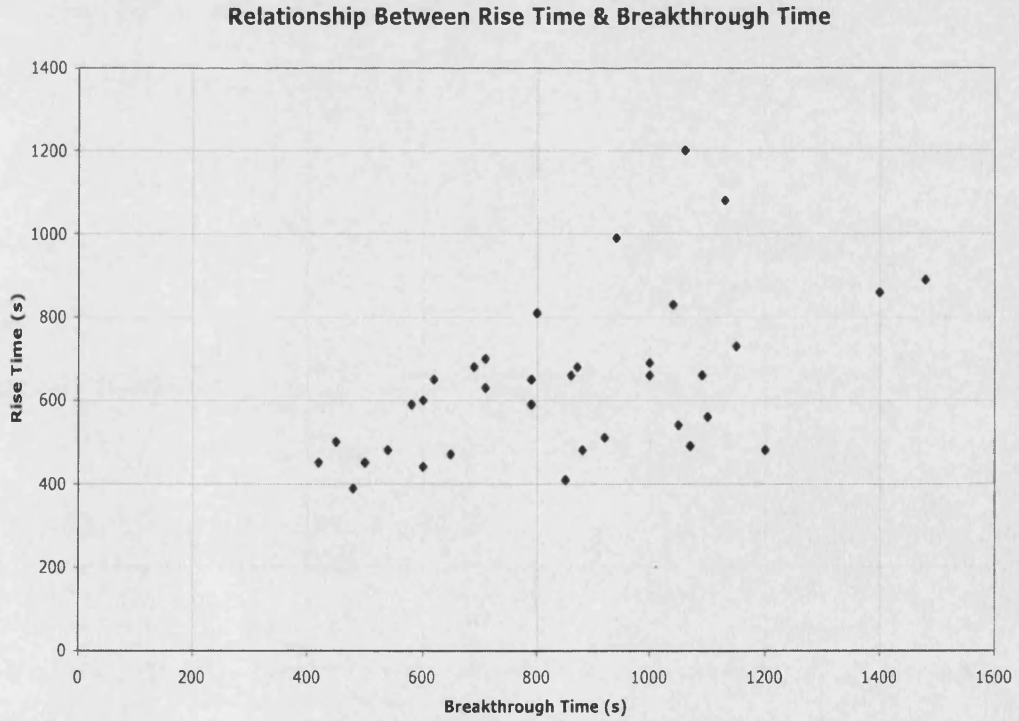

Figure 4.2.13. Plot showing the weak positive trend observed between breakthrough time and rise time for the As adsorption columns.

Table 4.2.5 highlights the breakthrough time differences, i.e. the difference between the breakthrough times observed for different columns. The number in green and brackets depicts the order in which breakthrough difference comes with respect to the partner column experiments. The number in red and in bold is the order that the breakthrough difference occurs within each experiment.

Column Experiment (in order of decreasing flow rates)	Breakthrough Difference (ΔBT): Column 1 – 2 (s)	Breakthrough Difference (ΔBT): Column 2 – 3 (s)	Breakthrough Difference (ΔBT): Column 3 – 4 (s)
A	**30** (3) **1**	**50** (2) **2**	**210** (6) **3**
C	**100** (6) **2**	**40** (1) **1**	**260** (9) **3**
I	**60** (4) **2**	**50** (2) **1**	**210** (6) **3**
H	**110** (8) **3**	**80** (6) **2**	**60** (1) **1**
J	**100** (6) **2**	**80** (6) **1**	**130** (4) **3**
B	**140** (9) **3**	**100** (8) **2**	**60** (1) **1**
D	**80** (5) **3**	**60** (5) **1**	**70** (3) **2**
E	**20** (2) **1**	**130** (9) **2**	**200** (5) **3**
G	**10** (1) **1**	**50** (2) **2**	**230** (8) **3**
Average Breakthrough Difference (ΔBT)	**72 s**	**71 s**	**159 s**

Table 4.2.5. Highlighting the differences between breakthrough times between the four columns.

This table and Figure 4.2.14 show that a linear relationship exists between the difference in the amount of goethite present within the column fill and the difference between breakthrough times. Therefore, ΔBT is functional with Δm,

and this relationship will be further discussed in Chapter 5.3 in terms of partition coefficients.

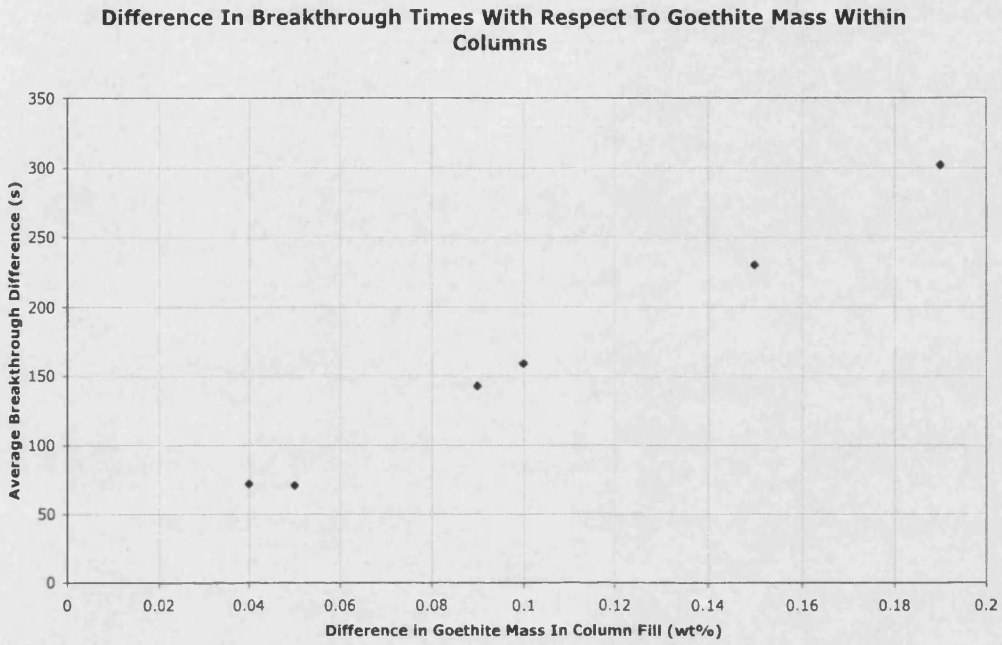

Figure 4.2.14. Plot demonstrating the linear relationship between breakthrough time differences (ΔBT) with respect to the difference in goethite mass (Δm).

4.2.3. The Effect of Influent Arsenic Concentration on Adsorption

A range of influent arsenic concentrations was applied to the four columns and the effect on adsorption quantified under fluid flow.

Table 4.2.6 summarises the breakthrough times for selected experiments with fixed flow velocities and Figures 4.2.15 and 4.2.16 summarise the effect of influent As concentration on the breakthrough time (BT) and rise time (RT), respectively. These plots do not illustrate a distinctive trend between the BT and RT with respect to the influent solute concentration. Although the breakthrough times vary, the difference is not as large as the effects of variation in goethite mass and flow rate (see Table 4.2.4, section 4.2.2.).

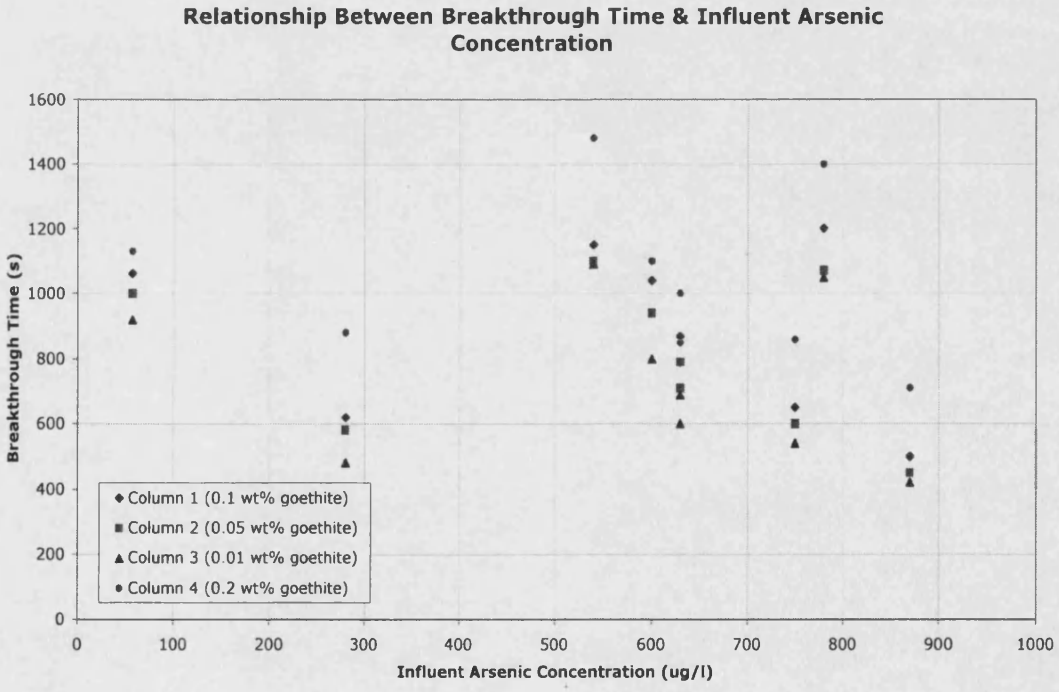

Figure 4.2.15. The effect of As concentration on the breakthrough time for all column experiments.

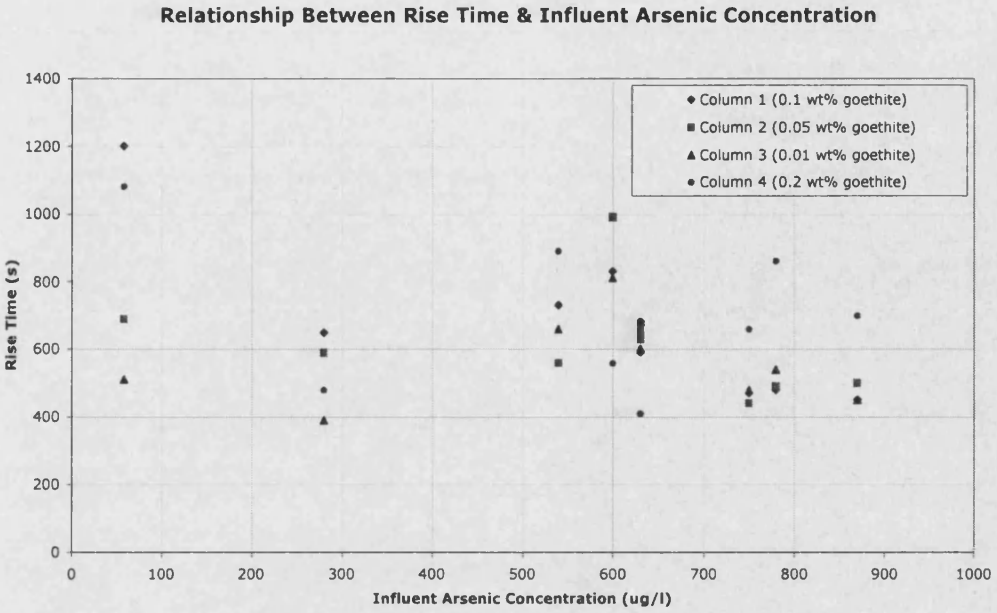

Figure 4.2.16. The effect of As concentration on the rise time for all column experiments.

The change in the BT for the selected experimental pairs (for example {E and G}, {C and I}, and {B and D} Table 4.2.6), with different As concentrations are typically insignificant and only 6 % of the absolute mean average. Therefore, the influent arsenic concentration does not play a dominant role in the adsorption process. This will be further discussed in Chapter 5 when considering derived partition coefficients.

EXPERIMENT	COLUMN 3 (0.01 wt%)	COLUMN 2 (0.05 wt%)	COLUMN 1 (0.1 wt%)	COLUMN 4 (0.2 wt%)	Mean Change in BT (s)
E (As = 780 μg/l) V_x=0.0131 cm/s	1050 s	1070 s	1200 s	1400 s	
G (As = 540 μg/l) V_x=0.0131 cm/s	1090 s	1100 s	1150 s	1480 s	50
C (As = 280 μg/l) V_x=0.0220 cm/s	460 s	580 s	620 s	880 s	
I (As = 750 μg/l) V_x=0.0220 cm/s	540 s	600 s	650 s	860 s	38
B (As = 600 μg/l) V_x=0.0180 cm/s	800 s	940 s	1040 s	1100 s	
D (As = 57 μg/l) V_x=0.0180 cm/s	920 s	1000 s	1060 s	1130 s	58

Table 4.2.6. Summary of the breakthrough times (BT) and the absolute mean change for experiments with the same flow velocities, but different influent arsenic concentrations.

4.2.4. The Effect of Flow Velocity on Adsorption

Understanding kinetic effects upon adsorption through a flowing column is imperative if experimental adsorption is to be compared with real world situations. The adsorption in batch experiments is usually allowed to reach equilibrium, when all available adsorption sites are saturated, before sampling the solution. In column experiments adsorption is constrained by time as well as by restricted contact between the preferential flow paths of the flowing solute and the mineral surfaces. Stollenwerk (2003) reports on the adsorption rate effect on arsenic sorption in batch experiments where more than 90 % is adsorbed within several hours, and the remainder over days as a result of reduced adsorption rates. Reports on kinetic studies applied to column experiments include Darland and Inskeep (1997) and Puls and Powell (1992), who observe lower adsorption rate constants and greater retardation in the batch experiments and columns with slower flow velocities.

Adsorption, or mass transfer, rates (Q_a) are defined as follows (Appelo and Postma, 1994):

$$\mathbf{Q_a = k_a \cdot C \cdot (1 - S/S_m)} \qquad \textit{Eqn. 4.2.2.}$$

Where: k_a = Proportionality rate constant

C = Solute concentration

$(1-S/S_m)$ = Fraction of empty sites (S_m is the maximum number of adsorption sites).

Hence, as the sites become filled the rate of adsorption decreases and the greatest rate of adsorption occurs when the least number of sites are filled.

As the arsenic solution is continually flushed through the column, a maximum adsorption will be attained in time, when a dynamic maximum number of possible sorption sites are filled. The time it takes to achieve this may be dependent on the average linear flow through the columns, as Barnett *et al.* (2000) suggest. They propose that the slower flow velocities through the

columns lead to longer residence times and therefore, greater adsorption. Puls and Powell (1992), during their column experiments of arsenic adsorption onto iron oxide minerals, attributed slower flow rates to the increased time available for diffusion of the arsenic to the adsorption sites.

The flow velocity plays an important part on the breakthrough times of the arsenic (Figures 4.2.17a – 4.2.17d), and Figure 4.2.18 shows the inverse relationship that exists between flow velocity and breakthrough time. In all four columns (1-4) the order in which the experiment breakthrough appears to be consistent. Those experiments that have similar flow velocities, such as B and D (V_x = 0.018 cm/s), but initial arsenic solution concentrations of 600 μg/l and 57 μg/l, respectively, show similar points of breakthrough in each of the four columns. The same can be said for experiments E and G (V_x = 0.013 cm/s), with arsenic solutions of 780 μg/l and 540 μg/l, and experiments C and I (V_x = 0.022 cm/s) using 600 μg/l and 750 μg/l As, respectively. This suggests that the kinetics of adsorption processes to have an effect under dynamic flow rates.

The spread of the breakthrough times over all experimental BTCs for each of the columns (1-4) in Figures 4.2.17a – 4.2.17d show a positive relationship with the goethite mass present within the column fill (Figure 4.2.19). This suggests that there is greater retardation within those columns containing greater goethite mass. The rise time (between C/C_o = 0.1 and 0.9) of the BTC does not show a definitive trend with increasing flow velocity (Figure 4.2.20).

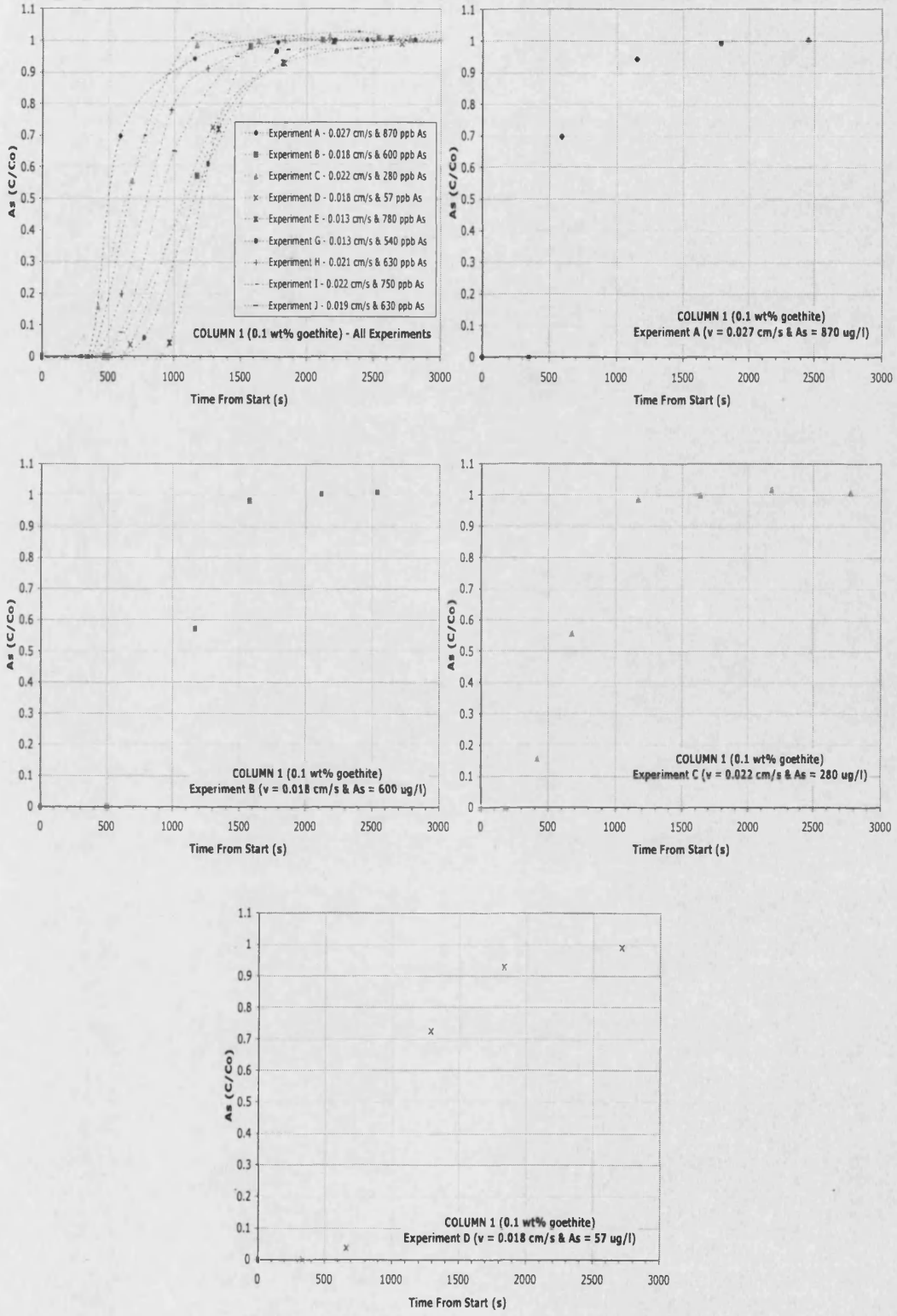

Figure 4.2.17a. Column 1 breakthrough curves for experiments A – D.

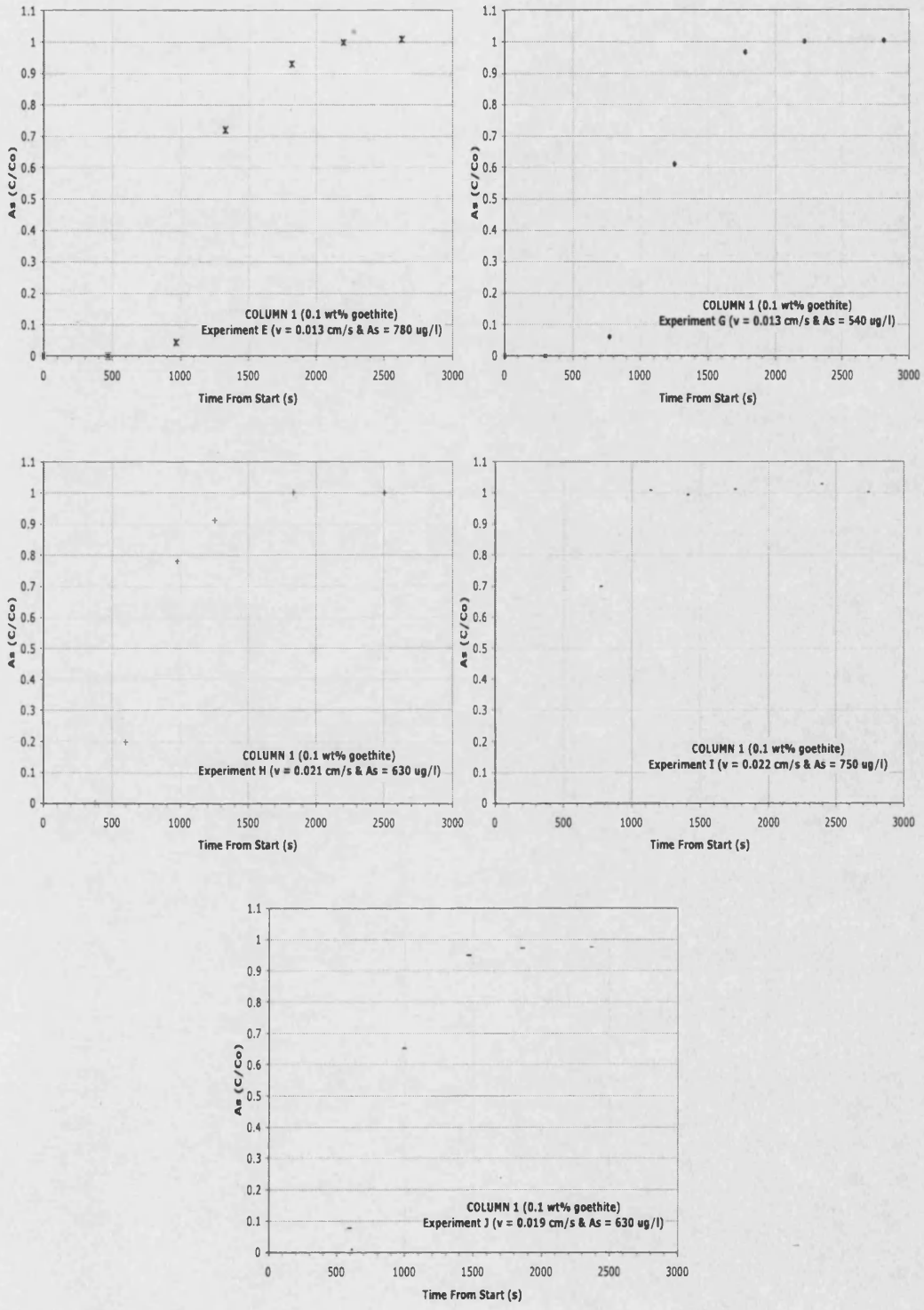

Figure 4.2.17a. Column 1 breakthrough curves for experiments E – J.

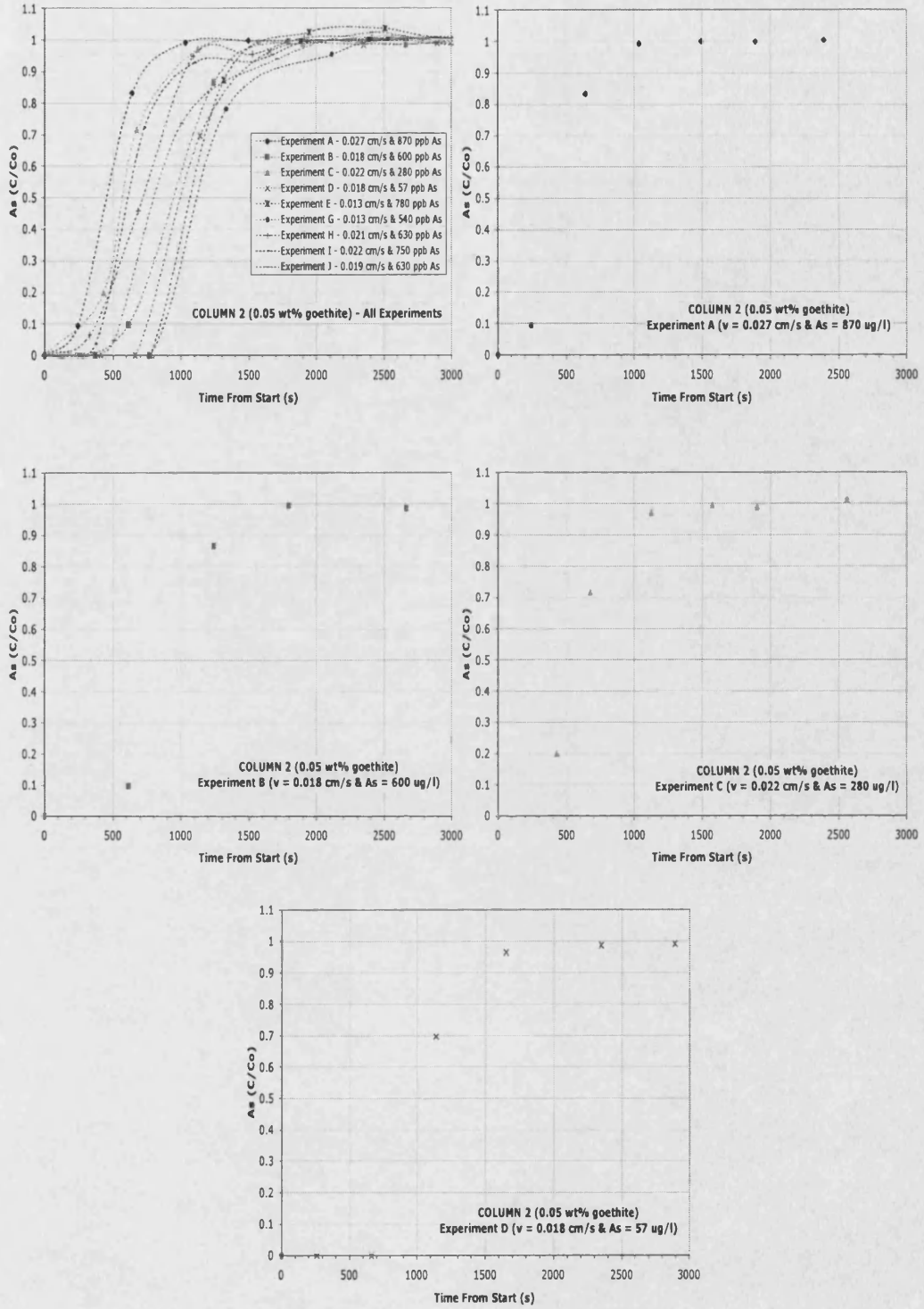

Figure 4.2.17b. Column 2 breakthrough curves for experiments A – D.

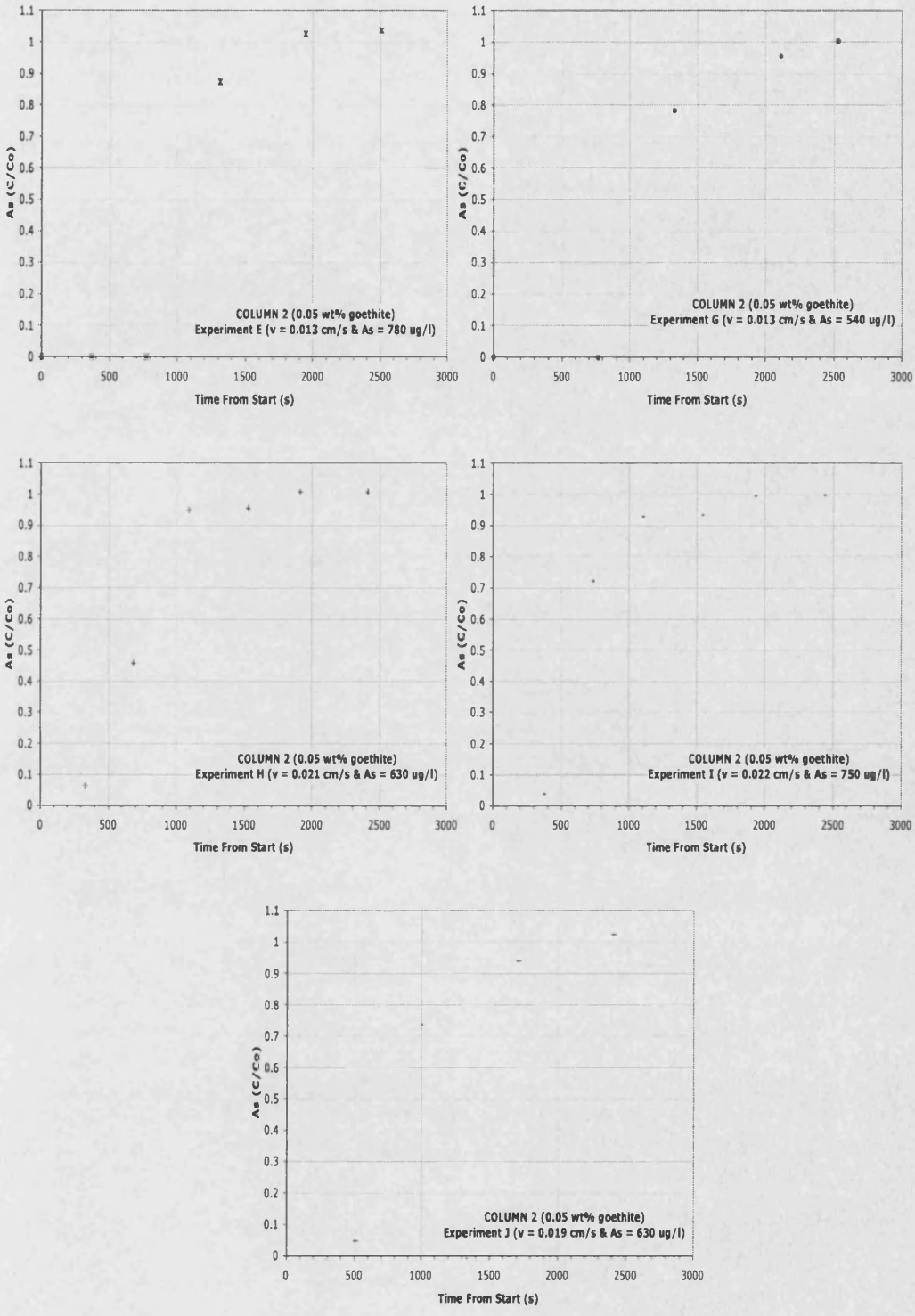

Figure 4.2.17b. Column 2 breakthrough curves for experiments E – J.

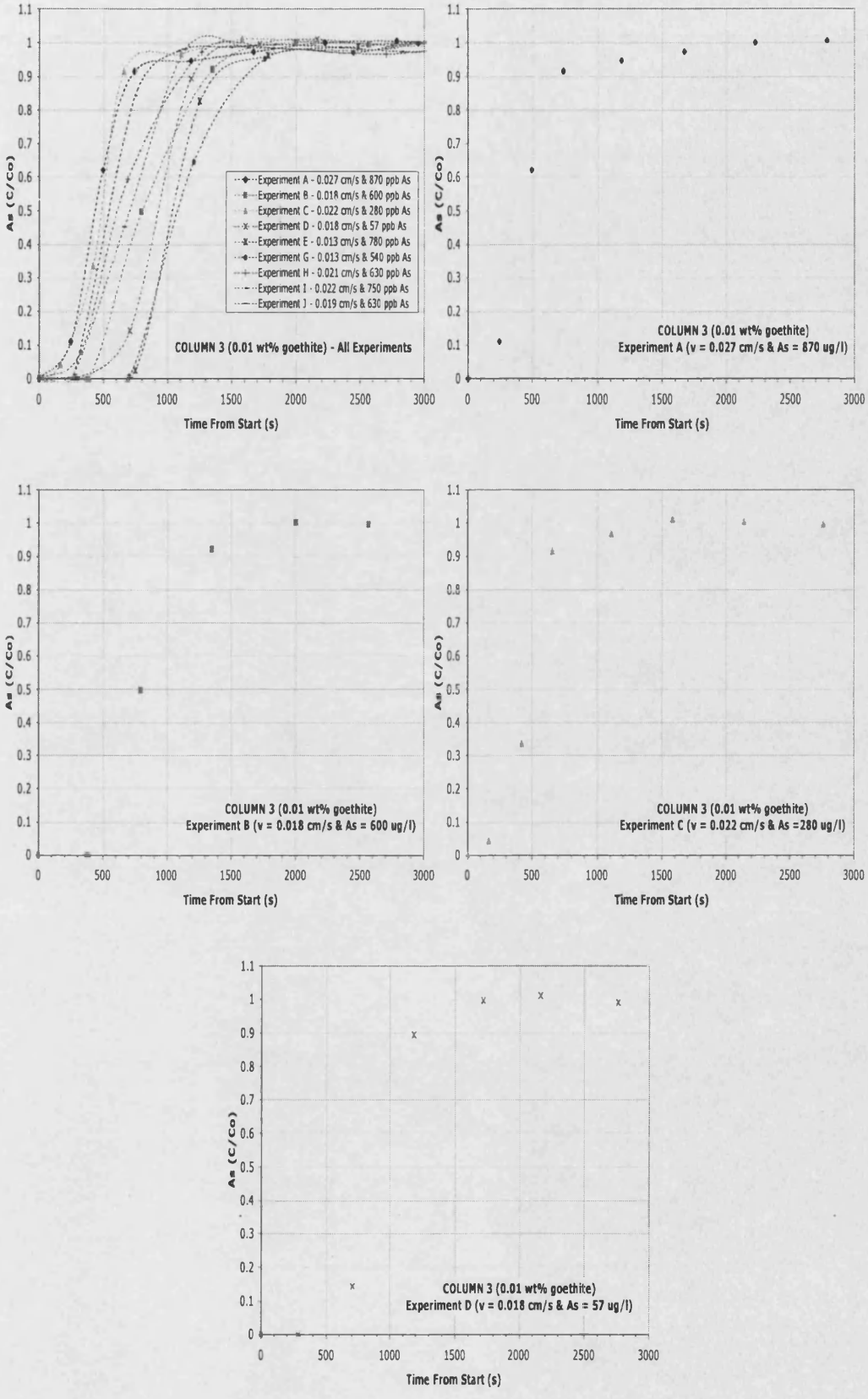

Figure 4.2.17c. Column 3 breakthrough curves, for experiments A – D.

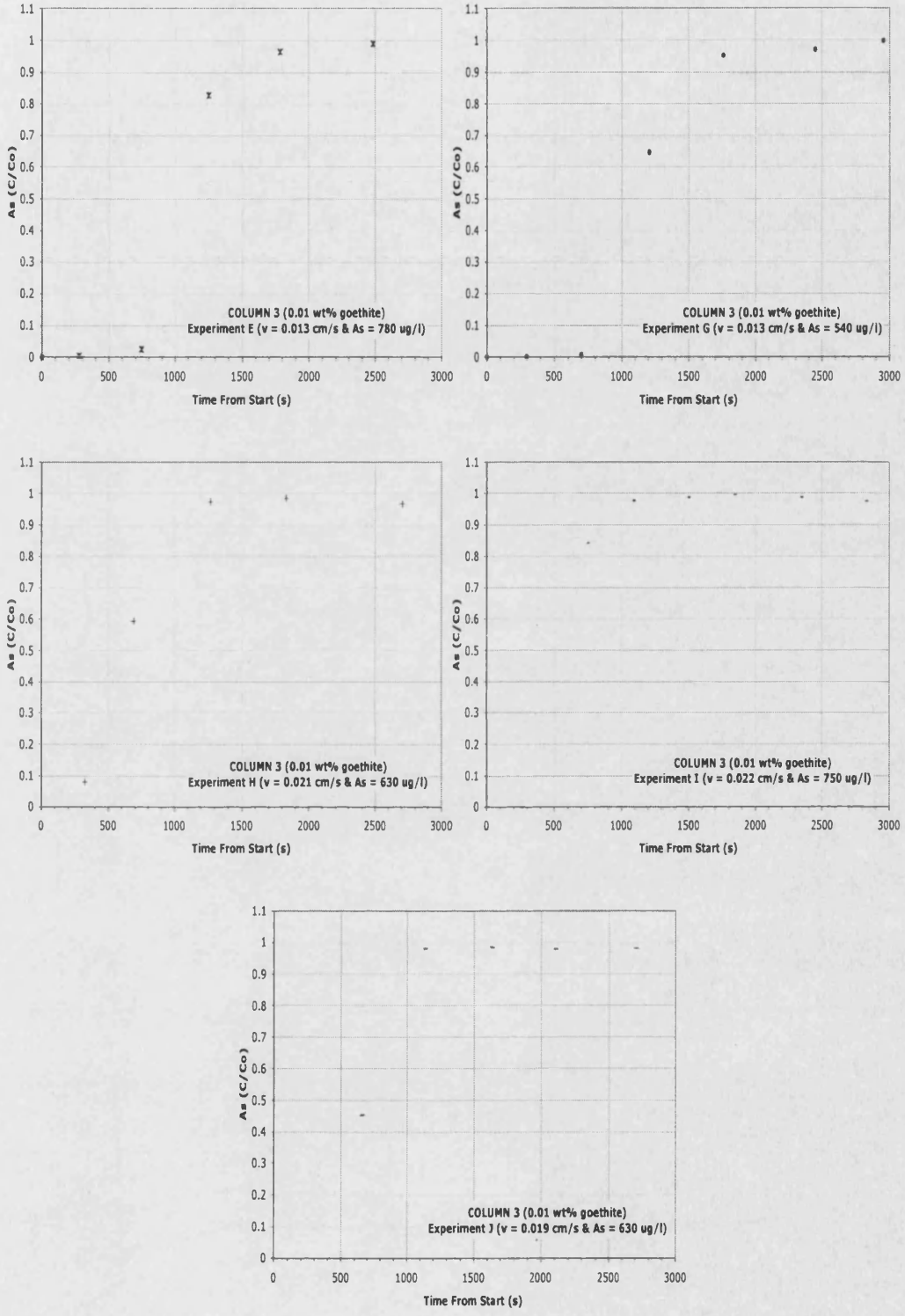

Figure 4.2.17c. Column 3 breakthrough curves, for experiments E – J.

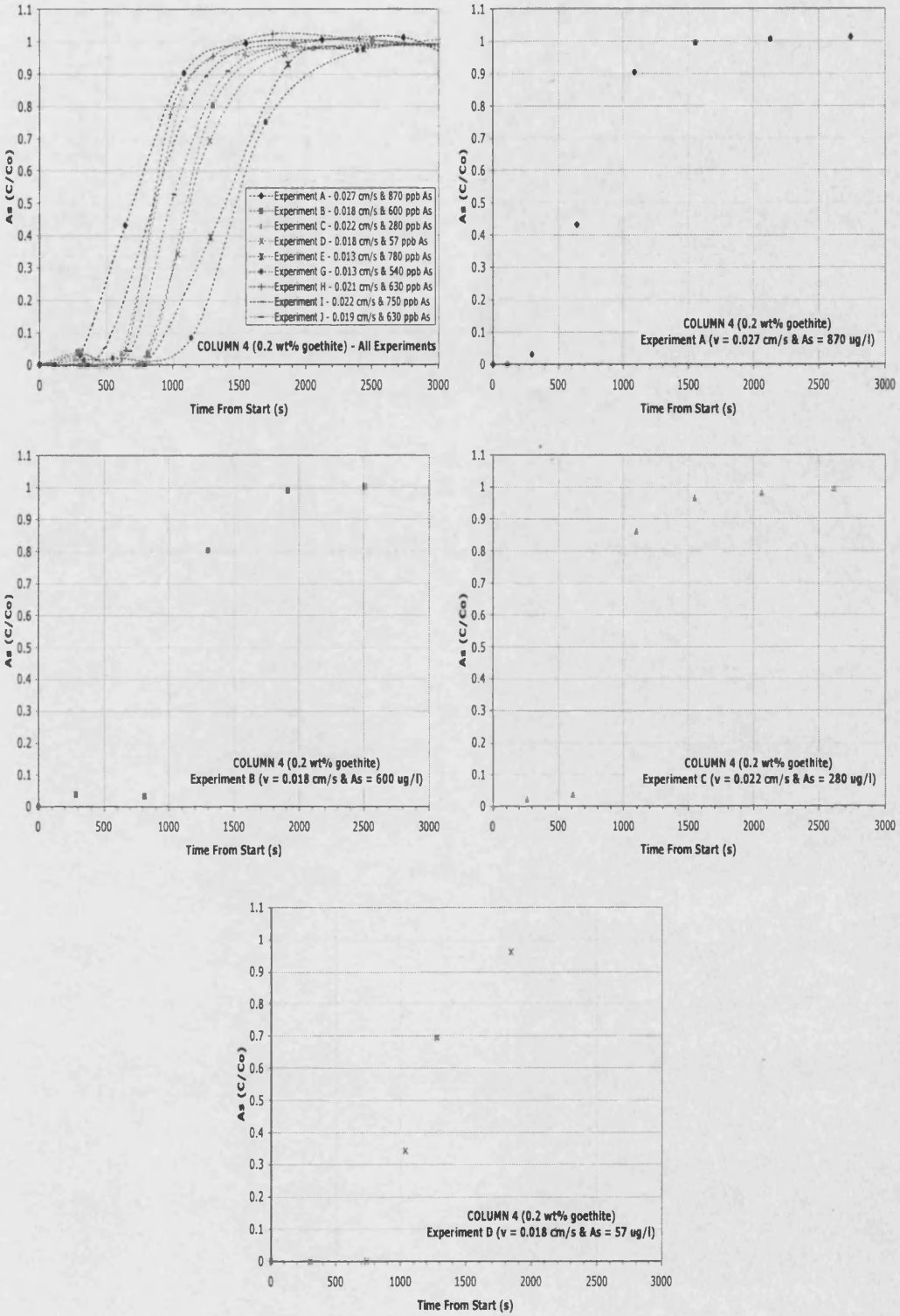

Figures 4.2.17d. Column 4 breakthrough curves for experiments A – D.

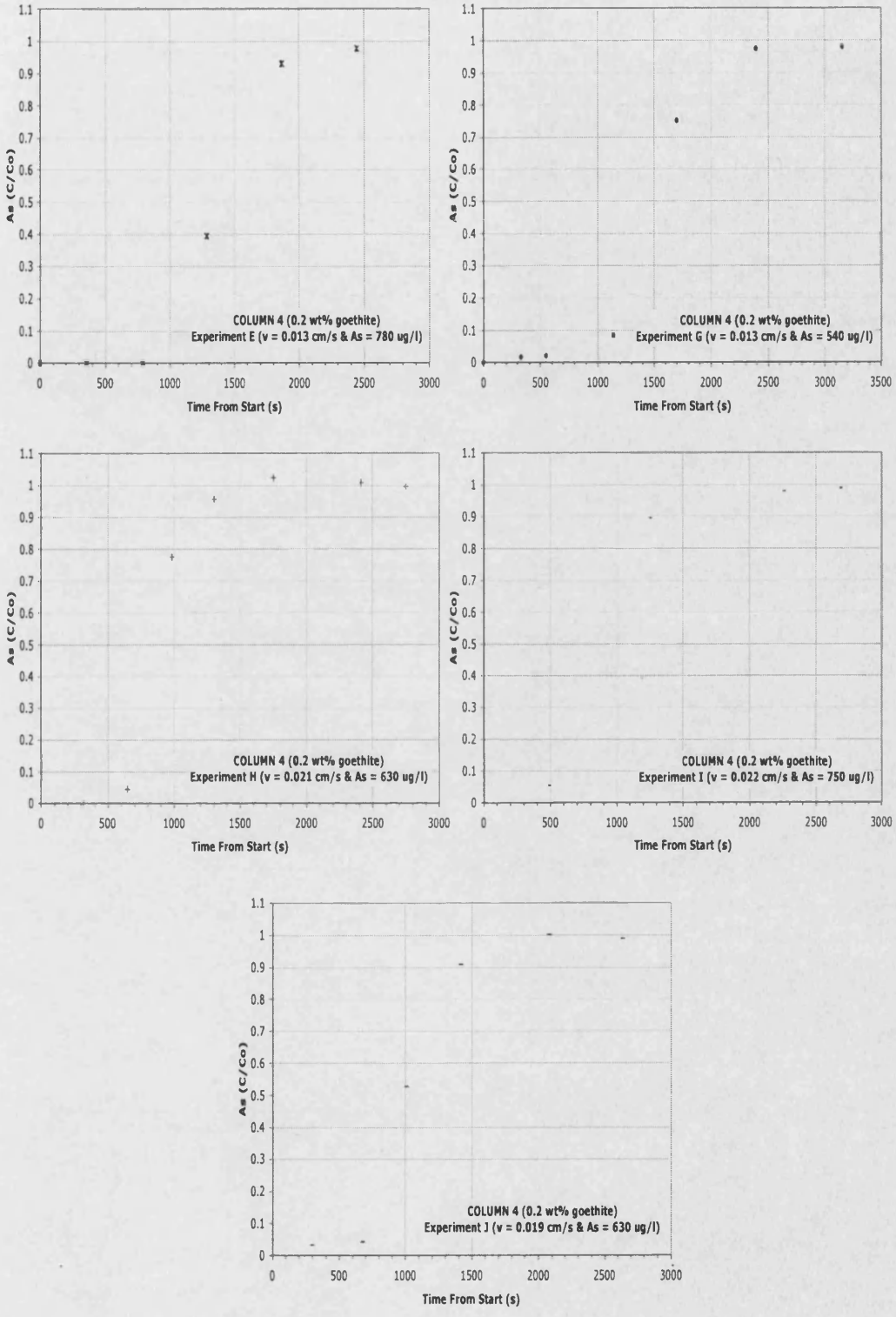

Figures 4.2.17d. Column 4 breakthrough curves for experiments E – J.

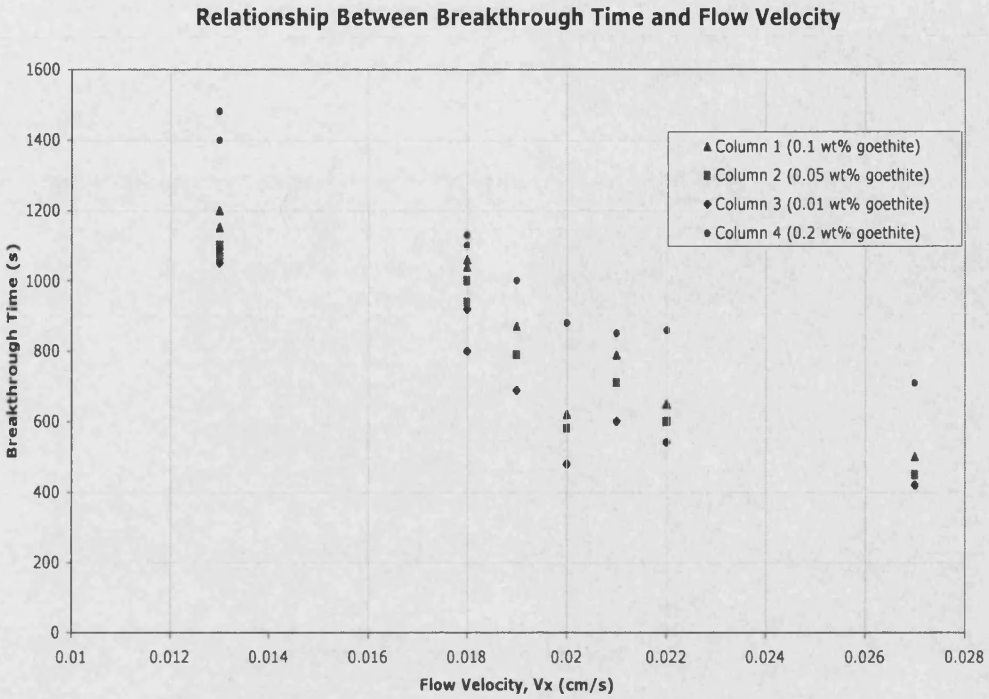

Figure 4.2.18. Inverse relationship between the breakthrough time and increasing flow velocity, V_x, over the entire experimental set.

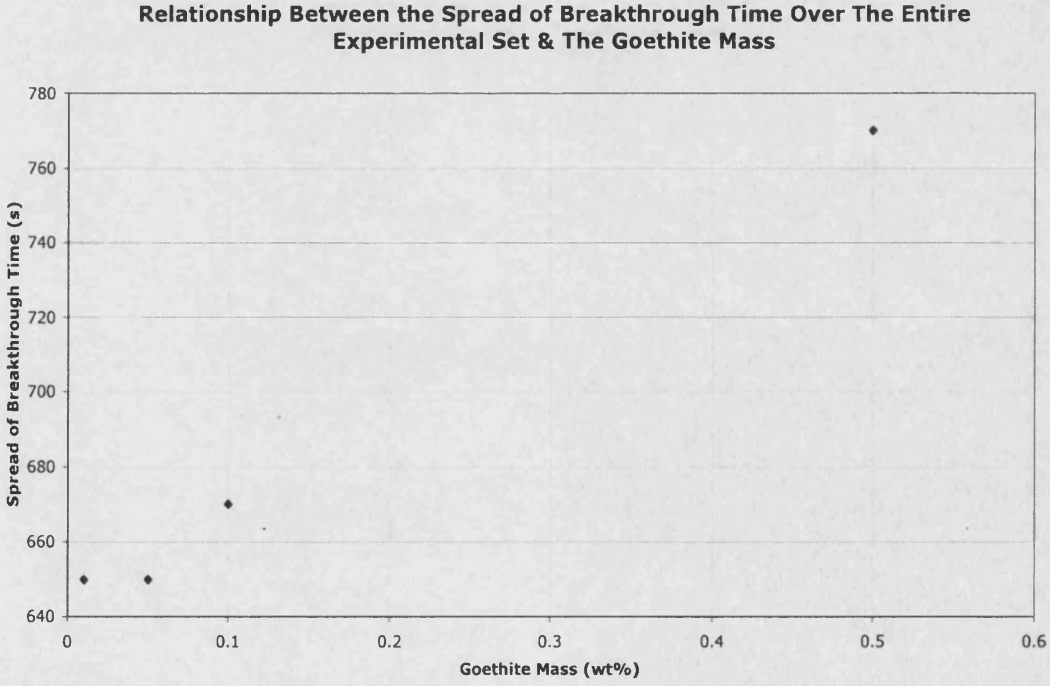

Figure 4.2.19. Positive relationship between the spread of breakthrough times for the entire experimental set and the goethite mass present within the column fill.

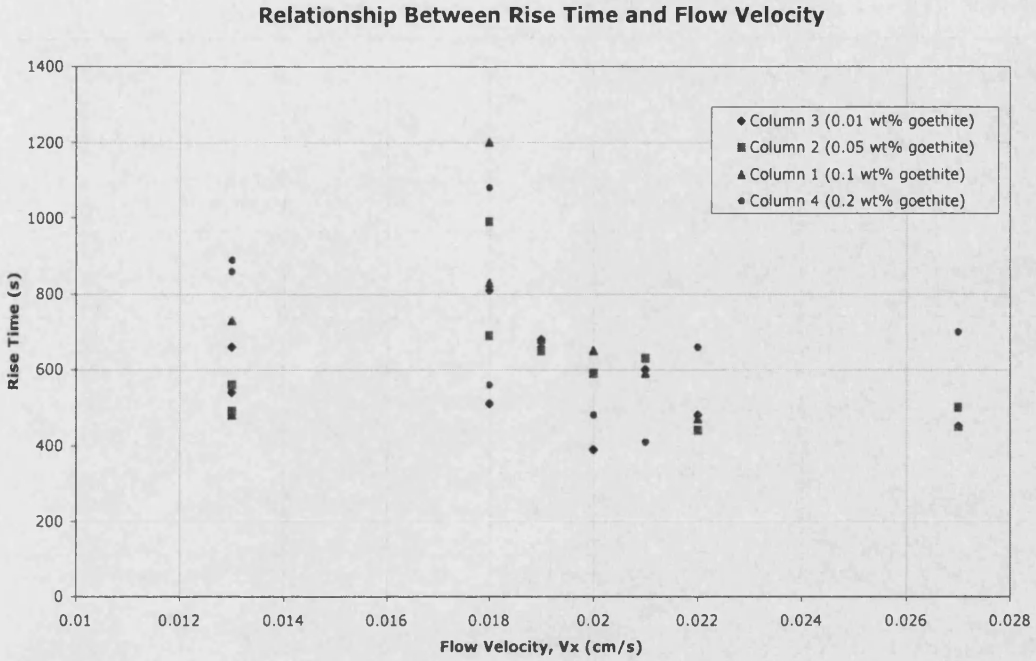

Figure 4.2.20. Plot showing the lack of obvious trend between the rise time and the flow velocity.

By comparing experiments E and I, which use approximately similar influent arsenic concentrations (750 μg/l) but different flow velocities of 0.013 cm/s and 0.022 cm/s, respectively, the effect of flow rate upon adsorption is further demonstrated. Table 4.2.7 shows the difference due to flow rates for these two experiments, and also for experiment pair H and B, which use a lower influent arsenic concentration (600 μg/l) and different flow rates.

By reducing the flow velocity by 1.7 times (Experiment I to E) the breakthrough time increases by an average of 1.8 times, whereas a reduction in velocity of 1.1 times (Experiments H to B) corresponds to a breakthrough occurring 1.3 times later. A definitive trend may become apparent with more experimental data. Hence, ΔBT is approximately proportional to the reciprocal of ΔV_x.

Other published studies have shown that the 'flow interruption' method can be successfully applied in assessing the applicability of chemical disequilibrium. Pang *et al.* (2002) used this method during column experiments to establish whether kinetic non-equilibria were relevant to the adsorption of Cd, Zn and Pb

on alluvial gravels. The flow interruption method involves stopping flow during the increase in concentration as the column is flushed with the reactive substance(s). If chemical non-equilibrium exists then a sharp decline in the effluent concentrations will be observed followed by an increase when the flow is re-started (Appelo & Postma, 1994). Although this method has not been applied during this study, it is still possible to establish any kinetic effects and relationships by comparing associated partitioning coefficients, which will be discussed further in chapter 5.

COLUMN	EXPERIMENT I (V_x = 0.022 cm/s As ~ 750 µg/l)	EXPERIMENT E (V_x = 0.013 cm/s As ~ 750 µg/l)	BT DIFFERENCE (s)	% INCREASE
1 (0.01 wt%)	540	1050	510	94
2 (0.05 wt%)	600	1070	470	78
3 (0.1 wt%)	650	1200	550	85
4 (0.2 wt%)	860	1400	540	63
		Average	***518***	***80***
COLUMN	**EXPERIMENT H (V_x = 0.021 cm/s As ~ 600 µg/l)**	**EXPERMENT B (V_x = 0.018 cm/s As ~ 600 µg/l)**	**BT DIFFERENCE (s)**	**% INCREASE**
1 (0.01 wt%)	600	800	200	33
2 (0.05 wt%)	710	940	230	32
3 (0.1 wt%)	790	1040	250	32
4 (0.2 wt%)	850	1100	250	29
		Average	***233***	***32***

Table 4.2.7. Breakthrough times (BT) for flow velocity (V_x) comparisons, using selected experimental sets that use the same As influent concentration but different flow velocities.

4.2.5. The Column Flushing Process and Arsenic Desorption

The columns were flushed with arsenic-free solution after every experiment to study arsenic desorption. For the desorption process, arsenic was flushed out of the columns using a concentrated NaCl solution (340 mg/l Cl). The aim was to remove arsenic from both the porewater and any sorbed by minerals (A. Osborn, Pers. Comm., 2001).

A set of chloride tracer BTCs were obtained to provide an understanding of the non-reactive solution movement through the columns. Figure 4.2.21 shows the resulting BTCs for chloride flushed into the column and subsequently expelled with DDW under different experimental flow velocities. There is a degree of symmetry with almost equal rise and fall times in the chloride BTCs. Physical equilibrium is attained during the experiments and therefore very little stagnant water remains within the column (Appelo and Postma, 1994). The chloride BTCs also show that the order of breakthrough on flushing the tracer out of the columns is the same as that for flushing chloride into the columns

Similar relationships for the chloride expelled were identified between the 'breakthrough' (BT) and 'fall' times (FT) and flow velocity as were observed for the chloride influent (Section 4.2.1). Figures 4.2.22 and 4.2.23 show the inverse relationship between BT and FT with increasing flow velocity. The BT and FT demonstrate a strong positive linear relationship with each other (Figure 4.2.24) as was also observed for the chloride influent BTCs.

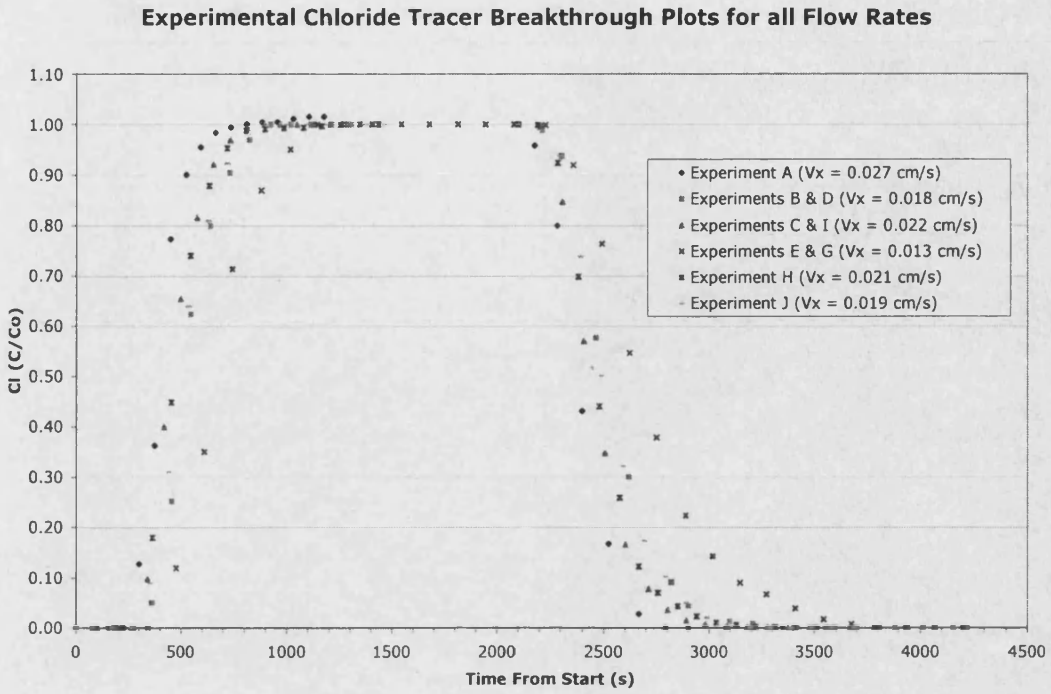

Figure 4.2.21. Chloride tracer breakthrough curves for all experiments.

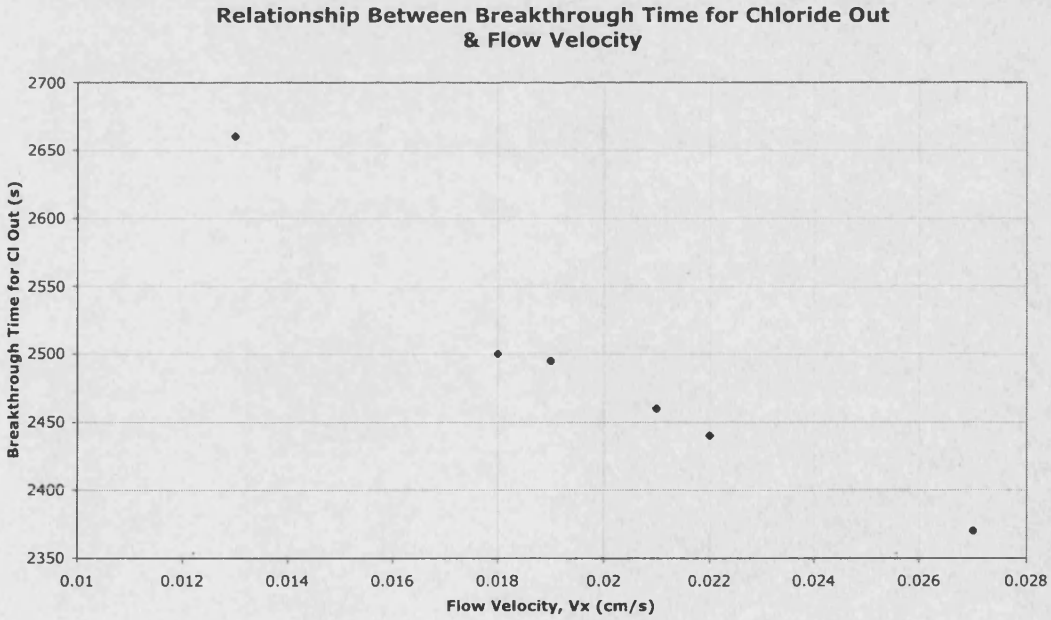

Figure 4.2.22. The inverse relationship between the chloride effluent breakthrough time ($C/C_o = 0.5$) with increasing flow velocity.

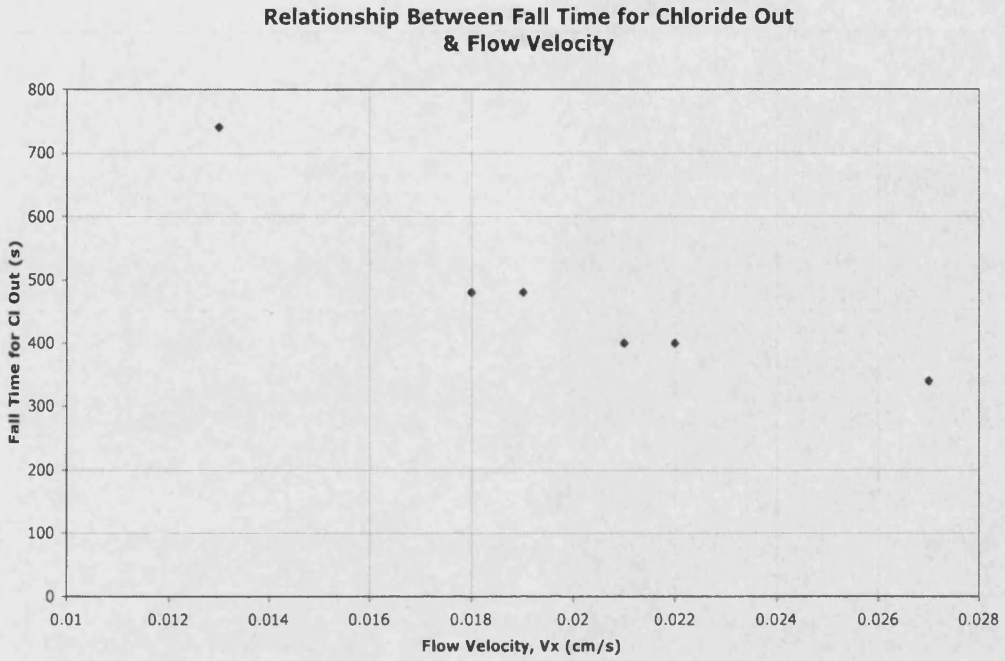

Figure 4.2.23. The inverse relationship between the chloride effluent fall time (C/C_o = 0.1 to 0.9) and flow velocity.

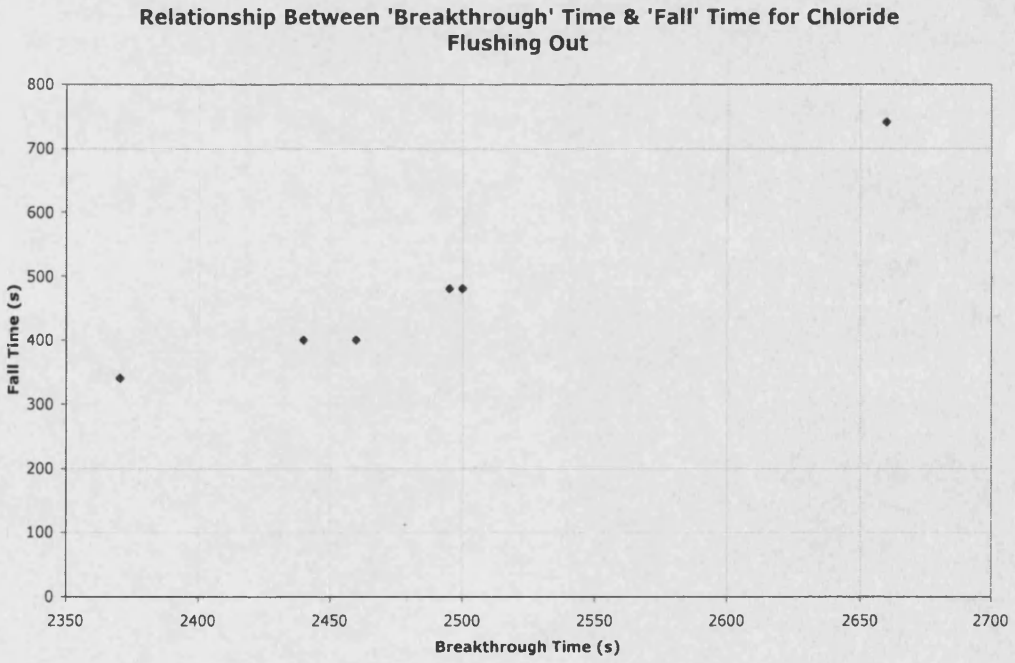

Figure 4.2.24. Positive relationship between the breakthrough time and fall time for the chloride effluent BTCs.

By contrast, the arsenic BTCs exhibit a degree of asymmetry, as shown by the greater fall time compared to the rise time; experiment I is shown as an example (Figure 4.2.25). The chloride BTCs demonstrate that the columns are in physical equilibrium and therefore the asymmetry observed in the As BTCs can be attributed to sorption irreversibility and chemical disequilibrium (Smedley and Kinniburgh, 2002 & Pang *et al.*, 2002). Arsenic, tightly bound to the goethite surfaces at the lower As concentrations, or trapped in porewater, can lead to asymmetrical BTCs (Fuller *et al.*, 1993, Puls & Powell, 1992 and Darland & Inskeep, 1997).

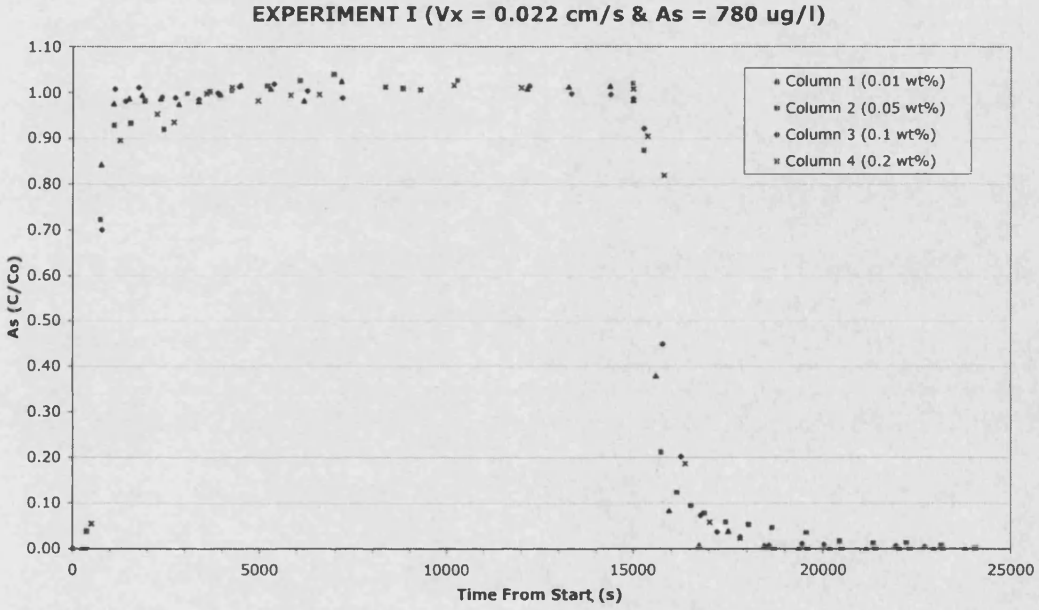

Figure 4.2.25. Experiment I arsenic adsorption and desorption experimental plots. The weight % values in brackets correspond to the mass % of goethite present within that column.

The column desorption experimental results tend to follow a similar pattern to the adsorption experiments. The order in which the columns desorb is the same as the order that arsenic is adsorbed; the column with the least goethite first, followed by those with greater goethite mass within the column fill. This is expected as, in the same way that the more available adsorption sites will take longer to fill, they are equally likely to take more time to desorb, especially if non-linear isotherms control partitioning of the arsenic from solution. Table 4.2.8 lists the observed 'breakthrough' and 'fall' times for the desorption of arsenic.

	COLUMN 3 (0.01 wt%)		COLUMN 2 (0.05 wt%)		COLUMN 1 (0.1 wt%)		COLUMN 4 (0.2 wt%)	
	BT (s)	FT (s)	BT (s)	FT (s)	BT (s)	FT (s)	BT (s)	FT (s)
EXPERIMENT A (870 µg/l & V_x = 0.027 cm/s)	150	560	280	1730	480	1260	575	1010
EXPERIMENT C (280 µg/l & V_x = 0.02 cm/s)	160	910	370	1060	485	1900	625	1190
EXPERIMENT I (750 µg/l & V_x = 0.022 cm/s)	290	780	390	1130	520	1320	640	1210
EXPERIMENT H (630 µg/l & V_x = 0.021 cm/s)	475	3000	300	930	520	1330	800	2800
EXPERIMENT J (630 µg/l & V_x = 0.019 cm/s)	375	1370	500	2010	575	2100	830	1790
EXPERIMENT B (600 µg/l & V_x = 0.018 cm/s)	490	1380	510	830	600	780	935	2210
EXPERIMENT D (57 µg/l & V_x = 0.018 cm/s)	490	1240	530	720	690	1410	1000	3150
EXPERIMENT E (780 µg/l & V_x= 0.013 cm/s)	500	440	540	1880	720	1440	1080	2120
EXPERIMENT G (540 µg/l & V_x= 0.013 cm/s)	515	2120	670	2890	745	1730	1085	2200

Table 4.2.8. The resulting breakthrough (BT) and fall times (FT) for desorption experiments A – J, and columns 1 – 4, in order of decreasing flow velocity.

An inverse relationship exists between the breakthrough time (BT) and flow velocity during the desorption phase (Figure 4.2.26), in a similar manner as observed for adsorption (Figure 4.2.18). This suggests that those experiments that show greater arsenic retardation during adsorption also demonstrate the greater As retention during desorption. The relationship between BT and influent As concentration (Figure 4.2.28) during desorption is not strong and is similar to that observed for the adsorption phase (Figure 4.2.14). Further investigation is required before the presence or absence of a distinctive trend can be confirmed. The fall time during desorption shows no relationship with respect to flow velocity or influent As concentration (Figures 4.2.27 and 4.2.29, respectively).

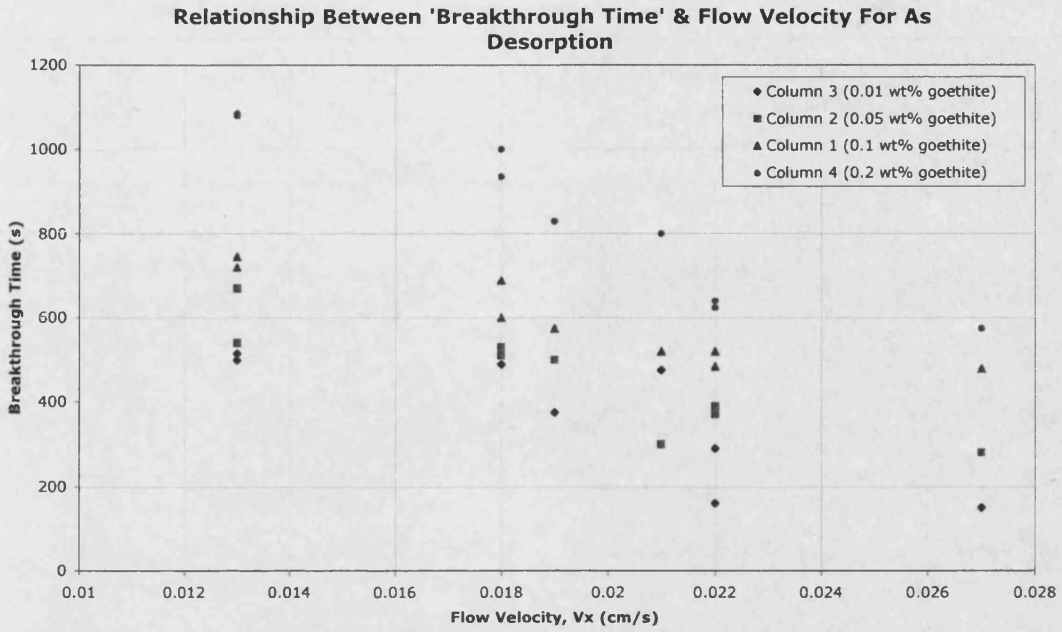

Figure 4.2.26. Plot illustrating the inverse relationship between breakthrough time during the desorption phase and the flow velocity.

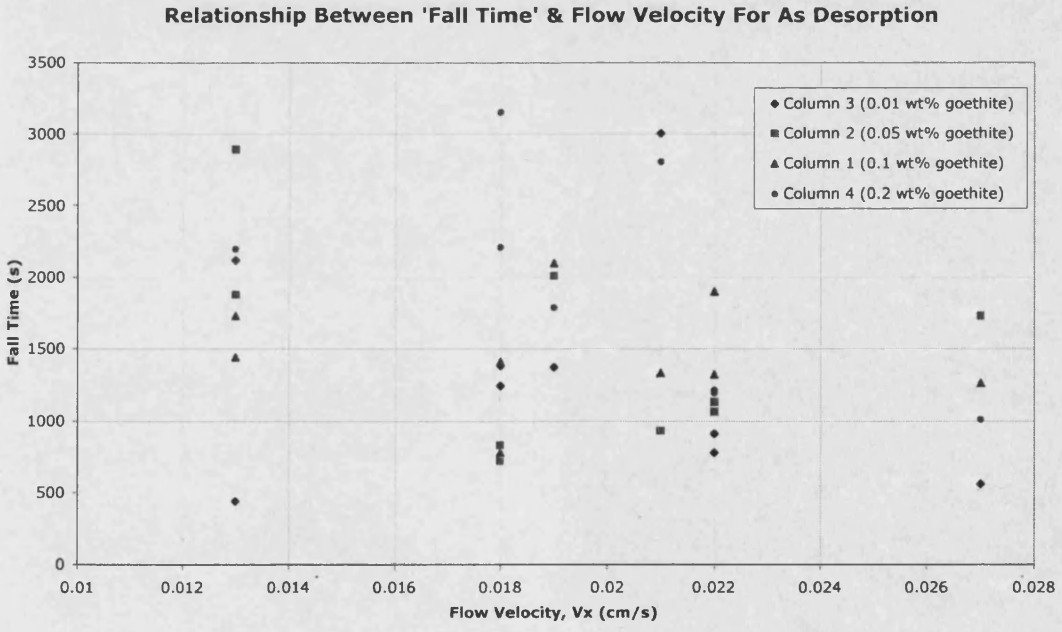

Figure 4.2.27. Plot illustrating no distinctive relationship between fall time during the desorption phase and the flow velocity.

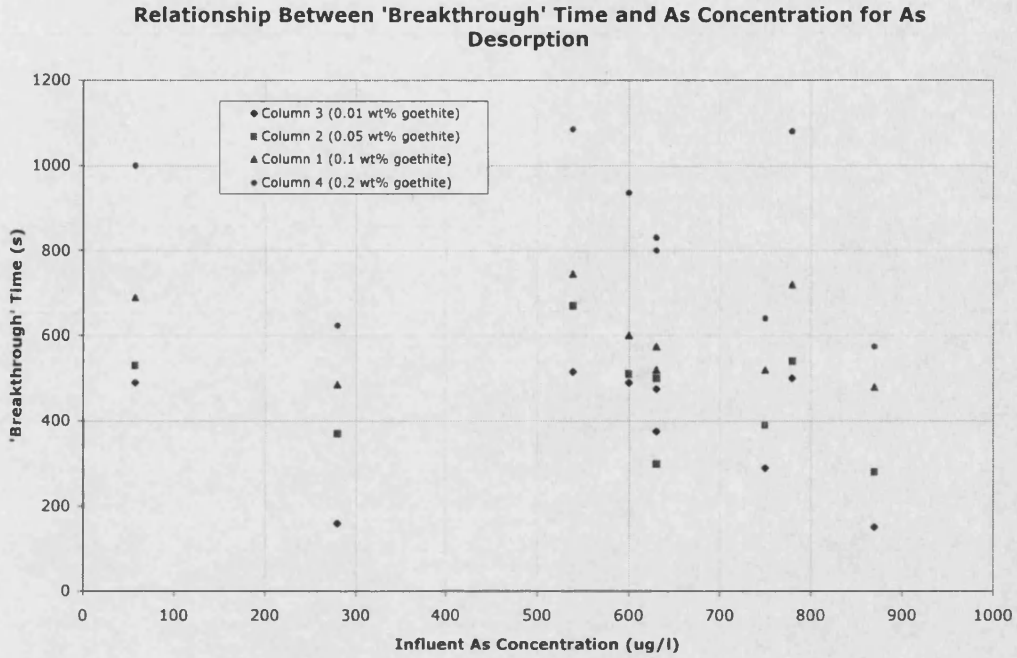

Figure 4.2.28. Plot illustrating no distinct relationship between breakthrough time during the desorption phase and influent As concentration.

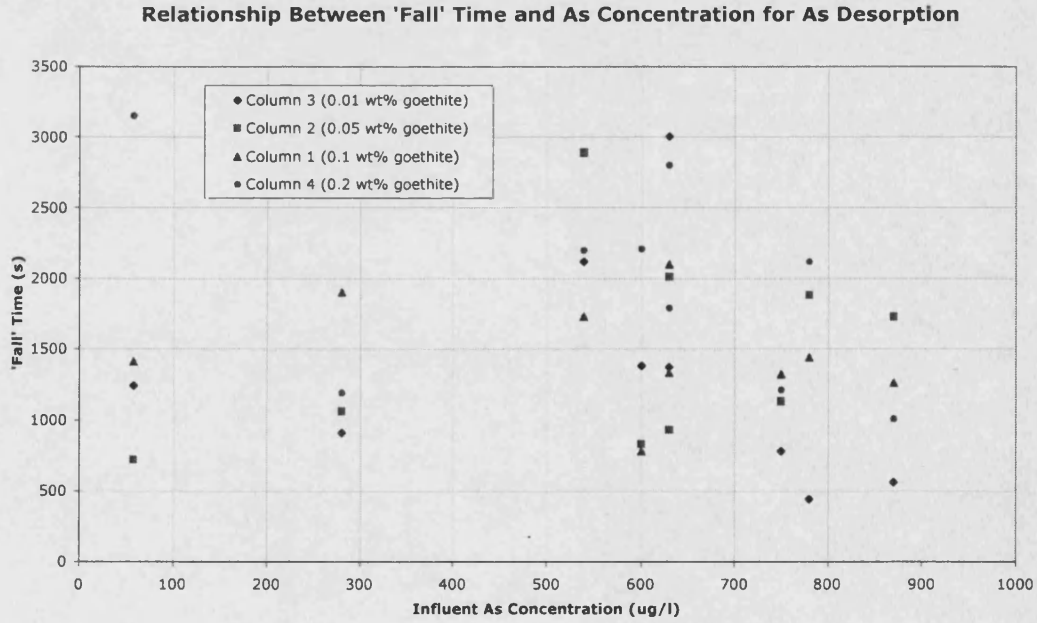

Figure 4.2.29. Plot illustrating no distinct relationship between fall time during the desorption phase and influent As concentration.

The rate of desorption (Q_d) is also a factor to consider, and is described by Appelo and Postma, 1994) as:

$$Q_d = k_d \cdot (S/S_m) \qquad \textit{Eqn. 4.2.3.}$$

With: S/S_m = representing the number of filled sites;
S_m = the maximum number of available sites; and
k_d = the proportionality rate constant.

Therefore, as the number of filled sites reduces, the rate of desorption decreases. Fuller *et al.* (1993) observed that slow arsenic diffusion from pore spaces was responsible for the prolonged equilibration time during batch experiments.

In testing for a mass balance between adsorption and desorption, Simpson's Rule is useful for integration under the BTC to determine the relative area under the curves.

Simpson's Rule (Bostock and Chandler, 1993):

$$A \approx {}^1/_3\, d\, [\{y_0 + y_n\} + 4\{y_1 + y_3 + \ldots\} + 2\{y_2 + y_4 + \ldots.\}] \qquad \textit{Eqn. 4.2.4.}$$

A = Area under the curve, between two points (x-axis)
d = Distance between uniform points (x-axis) at which the corresponding value for y is taken. In this case d is in pore volumes.
$\mathbf{y_m}$ = Corresponding value on the y-axis for x_m
$\mathbf{y_0}$ = Initial point
$\mathbf{y_n}$ = Final point

The mass balance calculation takes the form:

t = Time from the start of the experiment (t_0)
C/C_0 = Effluent concentration ratio with respect to the influent concentration (C_0)
m_o = Mass of influent As (mg) from $t_0 - t_1$ during adsorption phase
m_1 = Mass of effluent As (mg) from $t_0 - t_1$ during adsorption phase (area under BTC)
m_2 = $m_0 - m_1$ = Mass As remaining within column (mg) at t_1 ($C/C_0 = 1$)
m_3 = Mass of effluent As (mg) from $t_1 - t_2$ during desorption phase (area under BTC)

Table 4.2.9 summarises the results from the adsorption and desorption mass balance. The mean As recovery for all experiments is 88 %, compared with a mean recovery of 97 % for the chloride tests, suggesting that, on average, 12 % As remains adsorbed after the full duration of the experiment. The persistence of adsorbed arsenic may be due to retention of the more strongly-bound As and is a process best described using non-linear adsorption isotherms (Appelo and Postma, 1994). The apparent retention of As may also result from diffusion of some As into inaccessible pores, which lock the atoms and prevent easy release. Equation 4.2.3 shows how the release of As becomes slower as less As remains adsorbed, implying that kinetic effects may also cause prolonged As retention. The most retention was observed in the slower flow experiments (such as E and G), and may be due partly to the presence of concentration gradients within the column solution. For the faster flowing desorption experiments the arsenic released into solution will be more rapidly diluted and therefore the concentration gradient between the sorbed As and that in solution should be greater than for the slower flowing experiments. However, the combined effect of the rate of desorption and the concentration gradients tending to cancel one another may explain the apparent independence of the fall time relative to the flow velocity.

The accumulation of errors from experimental sampling, effluent concentration analysis and mathematical integration contribute 6 % error towards the overall mass balance. Allowing for these errors arsenic persistence is still demonstrated within the column material.

EXPERIMENT IDENTITY	m_0, INFLUENT MASS (mg)	m_1, ADSORPTION EFFLUENT MASS (mg)	$m_2 = m_0 - m_1$ (mg)	m_3 DESORPTION EFFLUENT MASS (mg)	AMOUNT RELEASED DURING DESORPTION PHASE (%)	AVERAGE RELEASE (%)
A3	0.0373	0.0190	0.0179	0.0150	84	
A2	0.0402	0.0247	0.0160	0.0126	81	
A1	0.0373	0.0226	0.0148	0.0139	94	
A4	0.0603	0.0378	0.0225	0.0199	88	87
B3	0.0238	0.00997	0.0138	0.0127	92	
B2	0.0370	0.0221	0.0149	0.0138	92	
B1	0.0264	0.0151	0.0113	0.00806	71	
B4	0.0264	0.0114	0.0150	0.0145	97	88
C3	0.00946	0.00437	0.00510	0.00506	99	
C2	0.0102	0.00589	0.00431	0.00427	99	
C1	0.00946	0.00575	0.00372	0.00427	115	
C4	0.0175	0.00991	0.00757	0.00650	86	100
D3	0.00401	0.00261	0.00140	0.00130	93	
D2	0.00251	0.00119	0.00132	0.00126	95	
D1	0.00176	0.000599	0.00116	0.000786	68	
D4	0.00376	0.00223	0.00153	0.00139	91	87
E3	0.0300	0.0153	0.0146	0.0126	86	
E2	0.0250	0.0114	0.0135	0.00915	68	
E1	0.0250	0.0115	0.0135	0.00696	52	
E4	0.0349	0.0175	0.0175	0.0157	90	74
G3	0.0164	0.00582	0.0106	0.00700	66	
G2	0.0276	0.0168	0.0108	0.00855	79	
G1	0.0225	0.0120	0.0105	0.00763	73	
G4	0.0294	0.0152	0.0142	0.00931	66	71
H3	0.0284	0.0153	0.0131	0.0141	108	
H2	0.0284	0.0170	0.0113	0.0101	89	
H1	0.0221	0.0116	0.0105	0.00796	76	
H4	0.0284	0.0144	0.0139	0.0130	93	92
I3	0.0312	0.0179	0.0133	0.0143	107	
I2	0.0273	0.0143	0.0130	0.0140	107	
I1	0.0254	0.0138	0.0116	0.0113	98	
I4	0.0410	0.0230	0.0180	0.0190	106	105
J3	0.0290	0.0152	0.0138	0.0121	88	
J2	0.0290	0.0160	0.0130	0.0119	92	
J1	0.0232	0.0130	0.0102	0.00949	93	
J4	0.0290	0.0141	0.0149	0.0135	91	91

Table 4.2.9. Summary of adsorption and desorption phase mass balance for each column experiment.

4.3. ANAEROBIC COLUMN EXPERIMENT

The column experiments described in preceding sections have been conducted in an aerobic environment but there are many examples of arsenic contaminated groundwater occurring as a result of anaerobic conditions, such as in Bangladesh, Vietnam, the Ashanti mining district in Ghana and parts of the USA (BGS & MML, 1999, Bowell, 1994, Stollenwerk, 2003 and Smedley & Kinniburgh, 2002). For completeness a set of column experiments were performed to determine the effect of reduction upon arsenic release.

The materials and procedures used are given in Chapter 2.4.3 and the results and discussions from the experiment and the relevance of different redox environments on describing adsorption partitioning are presented in Chapter 5.5.

5. INTERPRETATION OF EXPERIMENTS

5.1. INTRODUCTION

This chapter provides an analysis and interpretation of the batch and column experimental results with specific reference to adsorption parameters. The batch experiments focused on the effects of solution pH on adsorption using different concentrations of arsenic and goethite mass. The results presented in Chapter 3 are used here for the derivation of adsorption isotherms and partition coefficients. The best model for arsenic sorption is derived by fitting the experimental results to Linear, Freundlich and Langmuir sorption isotherms. Secondary information outlining the relationship between goethite mass, pH and the model coefficients is presented.

The column experiments were designed to be simplified analogues of a dynamic flow environment, and the results are used to interpret arsenic adsorption in flowing groundwater and to investigate the kinetics of adsorption. The breakthrough curves (BTCs) of As concentration as a function of time (Chapter 4) are used to obtain dynamic partition coefficients. A one-dimensional transport flow model BIO1D was used to interpret adsorption as a function of retardation and partition coefficients. The dynamic coefficients are compared to those derived from equilibrium batch experiments.

Finally, the results of desorption and the release of arsenic under chemical reduction with the calculation and comparison of aerobic and anaerobic partition coefficients conclude the chapter.

5.2. BATCH EXPERIMENTS – INTERPRETATION OF ADSORPTION ISOTHERMS AND SORPTION PARAMETERS

The amount of arsenic adsorbed (in mg) per unit mass sorbent (goethite (g)) is related to the amount of arsenic that remains in solution (mg/l) after equilibration using adsorption isotherms. For example, if the relationship is **linear**, the isotherm has the form:

$$S = K_d C \qquad \textit{Eqn. 5.2.1.}$$

Where: S = Amount arsenic sorbed per mass of goethite sorbent (mg/g)
K_d = Linear Partition coefficient (l/g)
C = Equilibrium arsenic concentration in solution (mg/l)

However, more realistic data are likely to have a non-linear relationship (Domenico & Schwartz, 1998). There are two commonly accepted non-linear isotherms: the Freundlich and the Langmuir isotherms.

The **Freundlich** isotherm describes the curve in which the amount of adsorption decreases asymptotically to zero as the solution concentration increases. The equation has the form:

$$S = K_f C^n \qquad \textit{Eqn. 5.2.2.}$$

Where: K_f = Freundlich coefficient (l/g)
n = Freundlich Isotherm Exponent

The **Langmuir** isotherm is more complex and includes a term to account for the maximum number of independent adsorption sites. Each site is assumed to have identical sorption characteristics (Appelo & Postma, 1994).

The Langmuir equation has the form:

$$S = Q_0 K_l C / (1 + K_l C) \qquad \textit{Eqn. 5.2.3.}$$
$$= \frac{Q_0}{[1 + 1/K_l C]}$$

Where: Q_0 **= Maximum surface sorption capacity of solid (mg/g) (Mass Solute Adsorbed / Mass Adsorbent for complete monolayer)**

K_l **= Langmuir coefficient, related to the enthalpy of adsorption (Srinivason & Mercer, 1987)**

K_l is related to two rate constants; k_a and k_d, which correspond to the flux inward to the surface and the flux outward from the surface, respectively. The total flux to the surface (Q_a) is related to the proportion of empty surface sites by the following expression:

$$Q_a = k_a C (1 - s/s_m) \qquad \textit{Eqn. 5.2.4.}$$

Where s represents those sites filled, s_m is the total number of available sites and C is the concentration in solution. The total flux from the surface (Q_d):

$$Q_d = k_d (s/s_m) \qquad \textit{Eqn. 5.2.5.}$$

However, when equilibrium is achieved and $Q_a = Q_d$, then the Langmuir coefficient becomes:

$$K_l = k_a / k_d \quad \text{and} \quad K_l = 1 / [C (1 - s/s_m)] \qquad \textit{Eqn. 5.2.6.}$$

(Appelo & Postma, 1994).

Appendix 3A summarises the batch experiment results and Figures 5.2.1, 5.2.2 and Appendix 5A show the experimentally derived adsorption isotherms in terms of arsenic adsorbed per unit mass goethite (mg/g) against the equilibrium arsenic concentration in solution (mg/l).

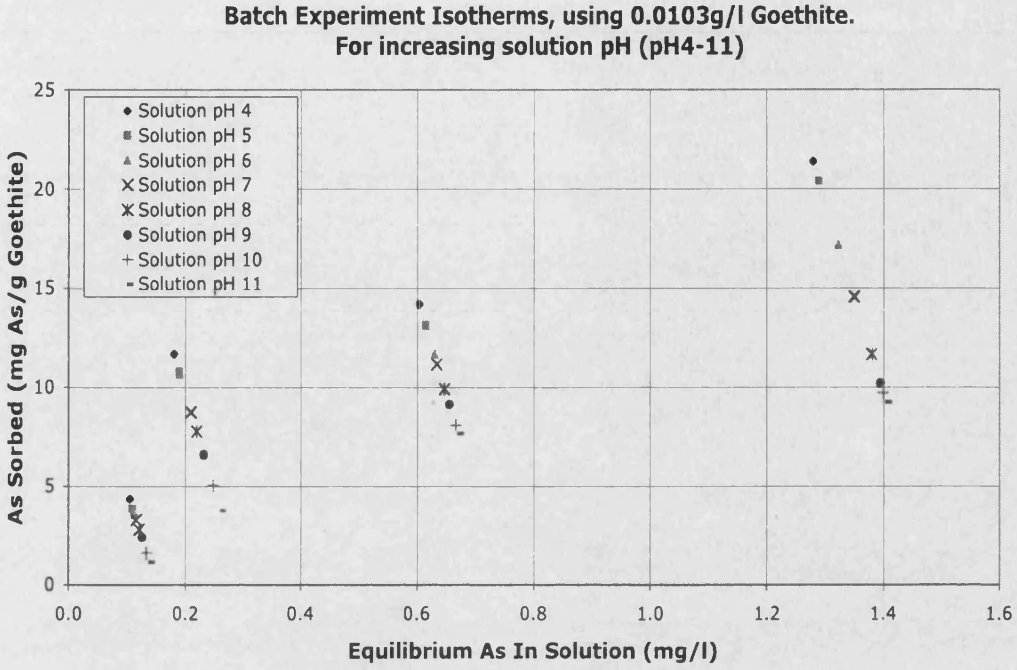

Figure 5.2.1. Batch experiment isotherm points, for goethite mass 0.0103 g/l and initial arsenic solution concentrations ranging from 150 μg/l to 1500 μg/l.

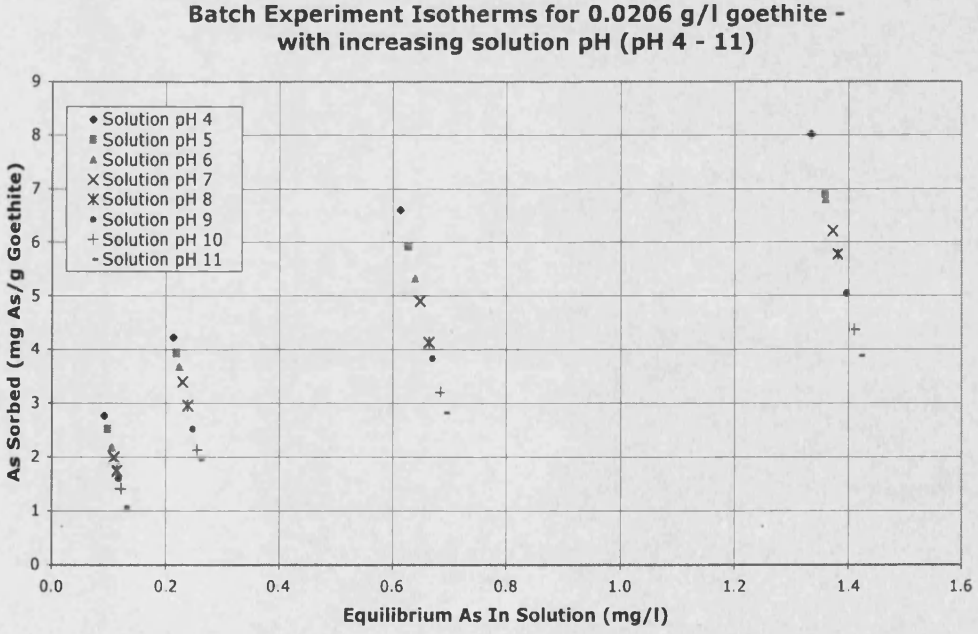

Figure 5.2.2. Batch experiment isotherm points, for goethite mass 0.0206 g/l and initial arsenic solution concentrations ranging from 150 μg/l to 1500 μg/l.

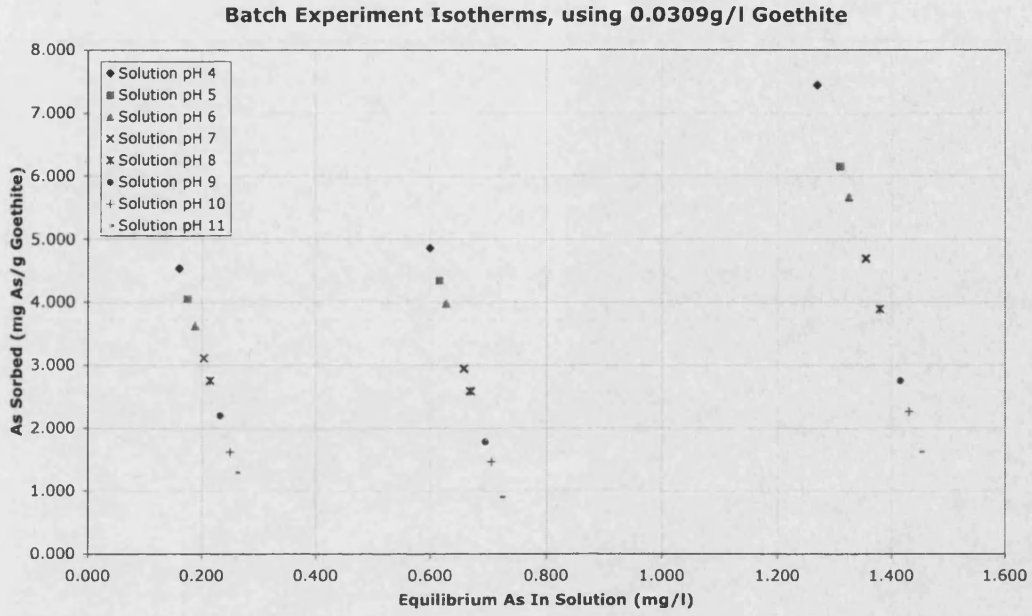

Figure 5.2.3. Batch experiment isotherm points, for goethite mass 0.0309 g/l and initial arsenic solution concentrations ranging from 300 μg/l to 1500 μg/l.

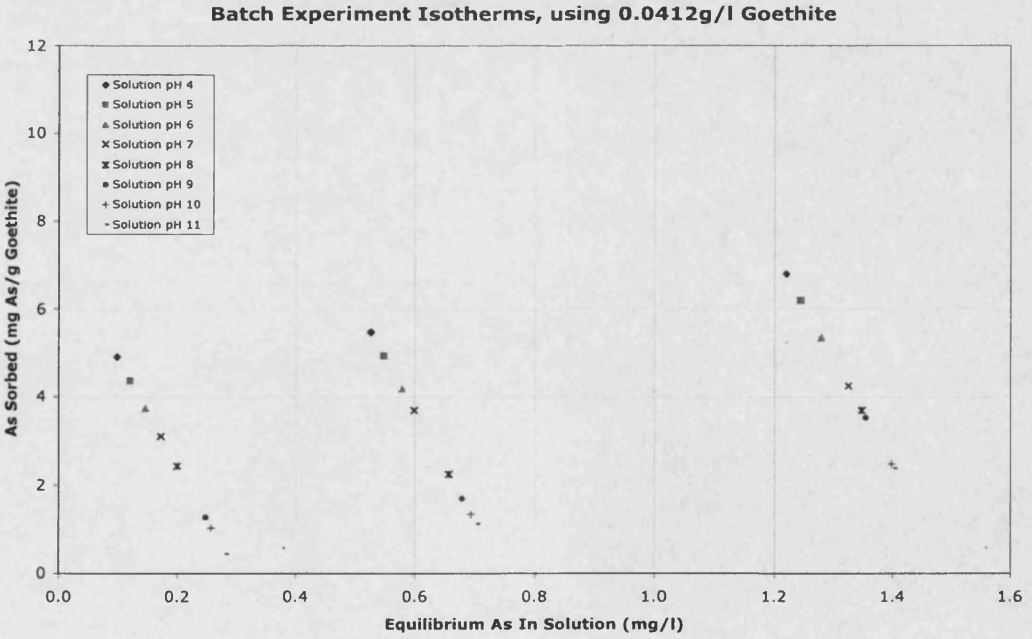

Figure 5.2.4. Batch experiment isotherm points, for goethite mass 0.0412 g/l and initial arsenic solution concentrations ranging from 300 μg/l to 1500 μg/l.

The isotherms show clearly that, as pH increases from 4 to 11, the amount of arsenic adsorbed per mass goethite decreases. An inverse pH dependence of adsorption was also demonstrated by the pH – adsorption envelopes in Chapter 3. The non-linear relationship between amount arsenic adsorbed and pH occurs for all values of goethite mass or equilibrium As concentration.

Comparing the isotherms for 0.0103 g/l goethite mass and 0.0206 g/l goethite mass (Figures 5.2.1 and 5.2.2, respectively) shows the effect of adsorbent mass on the amount of adsorbed arsenic mass. With increased goethite mass (M_g) the ratio of As adsorbed to As remaining in solution is lower. This phenomenon is best explained using the mathematics of the linear isotherm equation (equation 5.2.1). Provided the proportion of As sorbed (M_s, in mg) relative to the total initial As concentration (M_t, mg/l) remains constant, an increase in the goethite mass will result in a relative decrease in apparent sorption (S) and therefore the partition coefficient. This is summarised below, with V representing the volume of solution:

$$K_d = S/C = \frac{M_s / M_g}{(M_T - M_s) / V} = \left[\frac{M_s V}{M_T - M_s}\right] \frac{1}{M_g} = \left[\frac{V}{M_T/M_s - 1}\right] \frac{1}{M_g}$$

$$= \text{constant} \cdot \frac{1}{M_g} \qquad \textit{Eqn. 5.2.7.}$$

Two different approaches were used in the following to derive adsorption partition coefficients from the batch experimental data. The first approach used a least squares fitting technique between experimental and fitted data. The second approach was based on first order linear log-log graphical interpretations. The former permits an approximate mathematical description of the relationships.

5.2.1. The Freundlich Isotherm

The least-squares fitting approach used an Excel© 'Solver' algorithm. Its application established the parameters of the Freundlich equation from the observed data points. The equation parameters, K_f (the Freundlich isotherm coefficient) and n (which defines the shape of the curve) are thus ensured a best fit. The results of this fitting procedure are shown in Figure 5.2.5.

An initial observation of the fitted Freundlich isotherm shows a general fit (in form of $S = K_f C^n$) within the range of experimental plots. The fitted isotherm does not agree as well with the experimental points at lower equilibrium arsenic concentrations as at the higher arsenic concentrations. Also, the fit of the isotherm improves as the solution pH increases (Table 5.2.1).

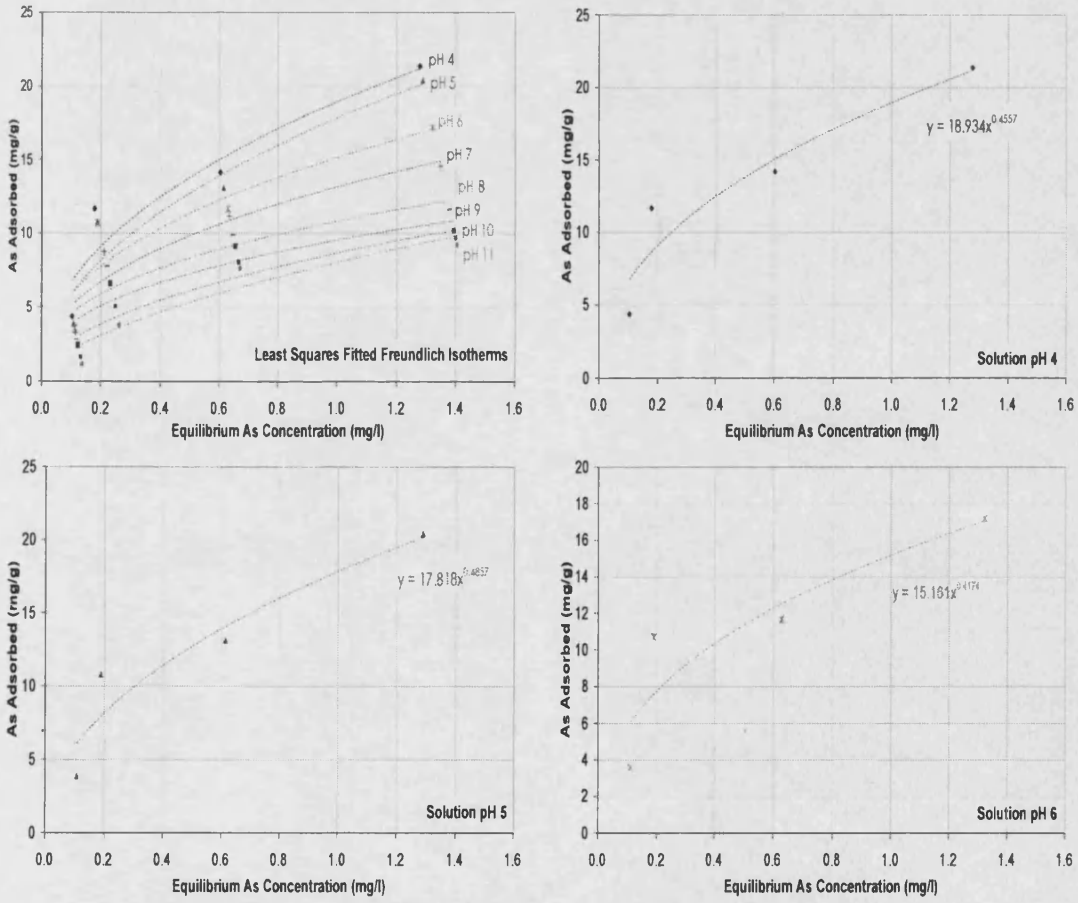

Figure 5.2.5a. Results from fitting using the Solver package in Excel©, and the Freundlich adsorption isotherm. Goethite mass is 0.0103 g/l. Solution pH 4 – 6.

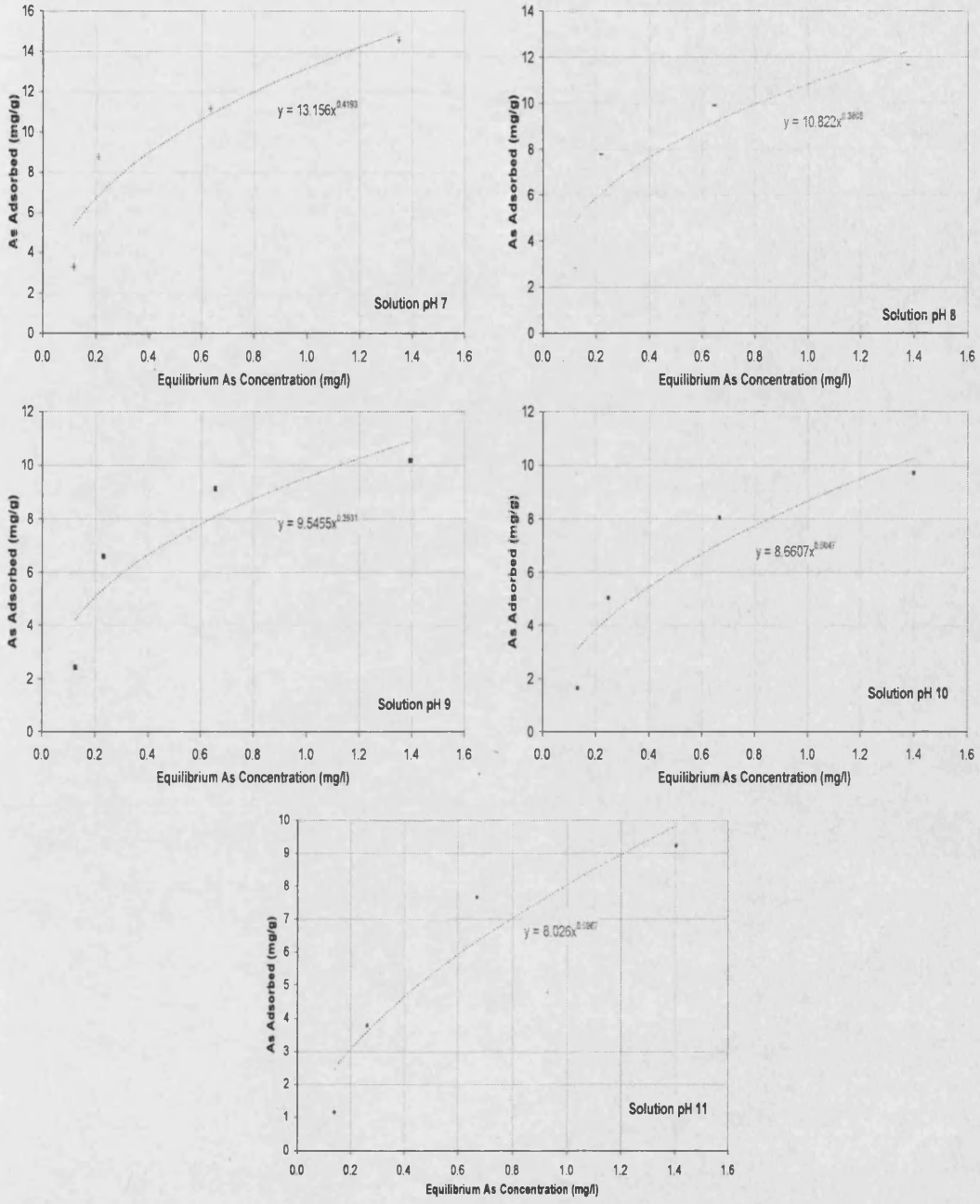

Figure 5.2.5b. Results from fitting using the Solver package in Excel©, and the Freundlich adsorption isotherm. Goethite mass is 0.0103 g/l. Solution pH 7 – 11.

The graphical approach was used also to determine the Freundlich isotherm parameters and for comparison with the statistical approach. Unlike the least-squares algorithm method, the graphical determination of partition parameters was applied to all batch experiment results (Appendix 5A). The Freundlich relationship is linear as a log-log plot. The gradient of the resulting plot defines

the parameter n, while the intercept on the log C* axis is used to find the partition coefficient (Log K_f) (Fetter, 1994).

From the Freundlich Log-Log plots (Appendix 5A), the 0.0206 g/l goethite mass experiment data show the strongest fit to this model (Figure 5.2.6).

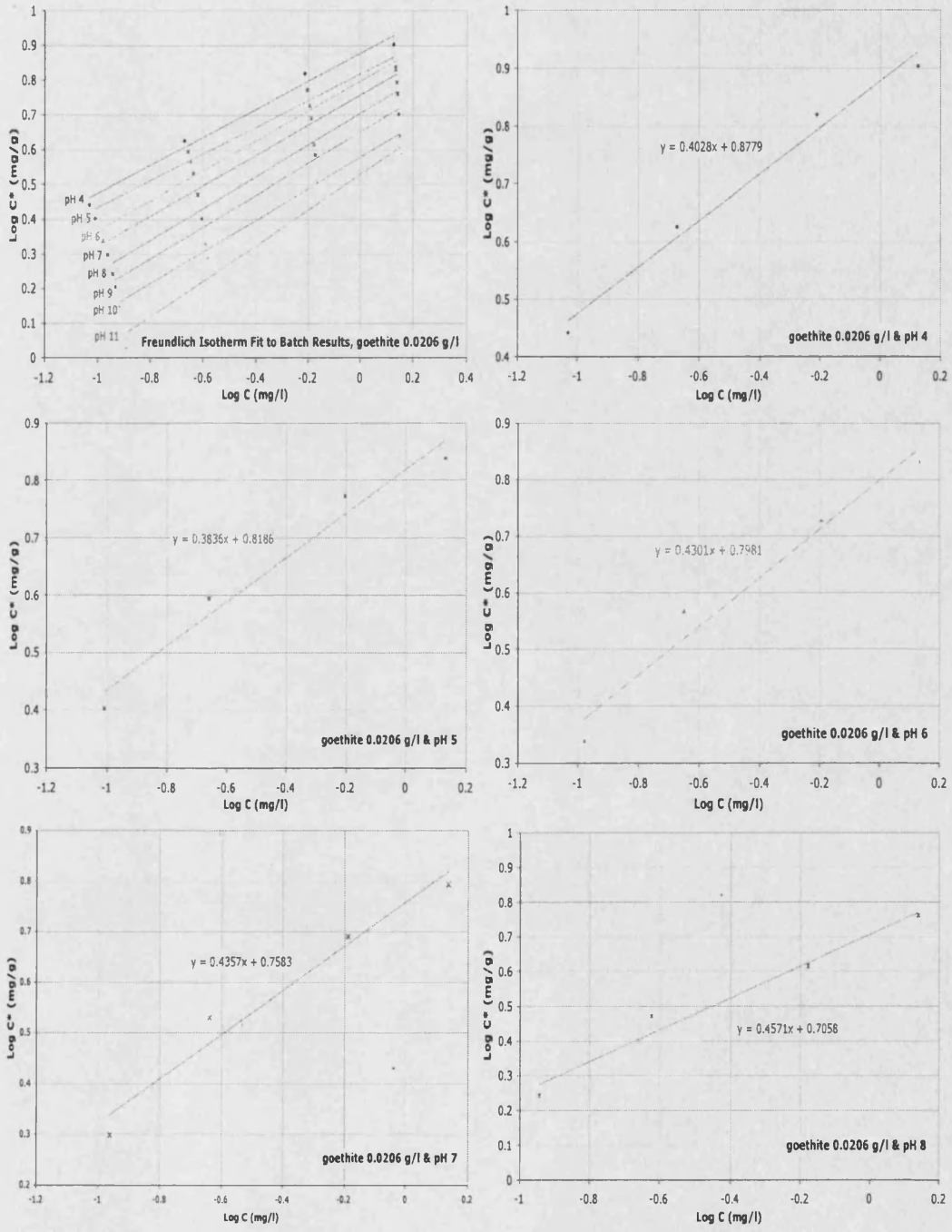

Figure 5.2.6a. Graphical approach to determining the Freundlich Isotherm coefficients, for the 0.0206 g/l batch experiments, pH 4 – 8.

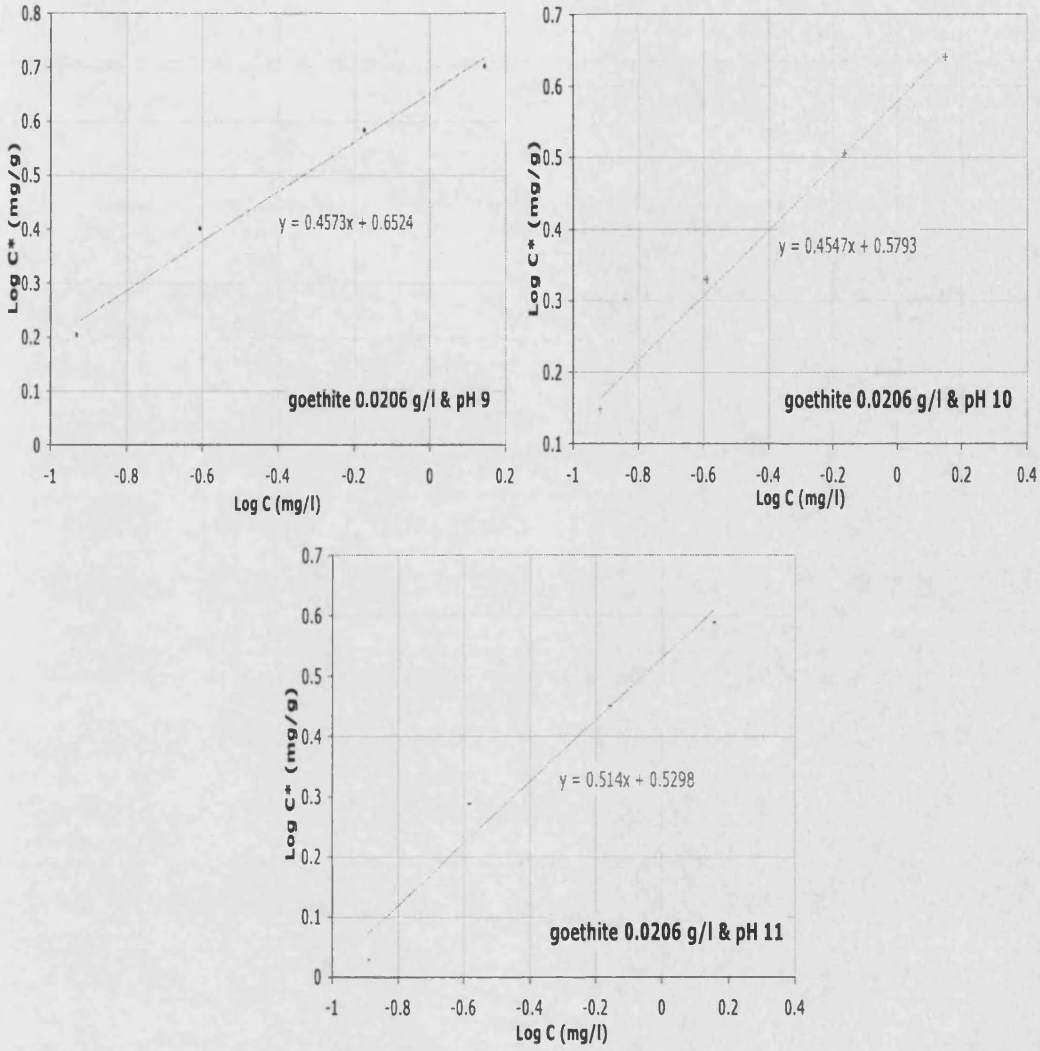

Figure 5.2.6b. Graphical approach to determining the Freundlich Isotherm coefficients, for the 0.0206 g/l batch experiments, pH 9 – 11.

Table 5.2.1 summarises the Freundlich parameters using both the Solver statistical method and the graphical approach, and Table 5.2.2 and Appendix 5B summarise all of the derived isotherm coefficients for the batch experiments.

Solution pH	K_f (l/g)	K_f (l/g)	n	n	Mean Squared Difference (Between Fitted and Experimental Data)
4	18.9	19.8	0.46	0.54	3.88
5	17.8	18.4	0.49	0.57	3.49
6	15.2	15.7	0.42	0.52	4.16
7	13.2	13.8	0.42	0.53	1.99
8	10.8	11.5	0.38	0.51	1.96
9	9.5	10.2	0.39	0.54	1.56
10	8.7	9.3	0.50	0.70	1.02
11	8.0	8.7	0.60	0.86	0.97

Table 5.2.1. Results of the fitted Freundlich isotherm using the Solver package within Excel (Black) and from the graphical interpretation (Red). Kf is the Freundlich partition coefficient, n is an isotherm parameter. Goethite mass used in experiment is 0.0103 g/l.

The derived partition coefficient (K_f) reduces as the solution pH is increased, varying from 19 at solution pH 4 to 8 at pH 11. Figure 5.2.7 demonstrates the quasi-linear trend between the derived K_f values and the solution pH for the range of interest. When the graphical derivations of Freundlich parameters were applied to all batch results (summarised in Table 5.2.2), again it was seen that there was a decrease in the K_f coefficient with increasing solution pH over all the batch experiments, but less so for those batches containing greater goethite mass.

Solution pH	0.0103 g/l goethite batches		0.0206 g/l goethite batches		0.0309 g/l goethite batches		0.0412 g/l goethite batches	
	K_f (l/g)	n	K_f (l/g)	n	K_f (l/g)	n	K_f (l/g)	n
4	19.6	0.53	7.5	0.40	6.4	0.22	6.3	0.12
5	18.4	0.57	6.6	0.38	5.4	0.19	5.7	0.14
6	15.7	0.52	6.3	0.43	5.0	0.21	4.9	0.16
7	13.8	0.53	5.7	0.44	3.9	0.19	4.0	0.15
8	11.5	0.51	5.1	0.46	3.3	0.16	3.0	0.19
9	10.2	0.54	4.5	0.46	2.3	0.10	2.6	0.58
10	9.3	0.70	3.8	0.46	1.9	0.17	1.9	0.51
11	8.7	0.86	3.4	0.51	1.3	0.10	1.6	1.06

Table 5.2.2. Freundlich parameters (K_f and n) derived for all batch experiments, using the graphical derivation.

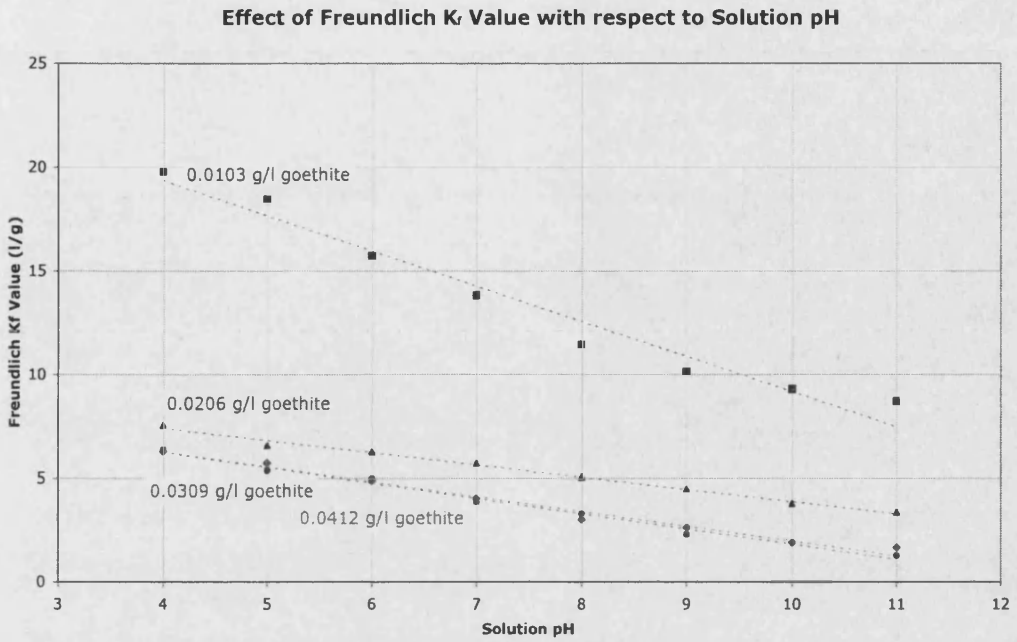

Figure 5.2.7. Plot illustrating the effect of solution pH upon the Freundlich K_f value. Using graphically derived parameters.

A first order linear approximation shows a good fit with the points plotted for K_f as a function of pH (Figure 5.2.7) and follows the general equation:

$$K_f = -\alpha(m)\,pH + \beta(m) \qquad \textit{Eqn. 5.2.8.}$$

Where α and β are parameters specific to the goethite mass, m, and are related to the adsorption mechanism describing the proportion of adsorption with respect to goethite mass.

Determination of the α and β are parameters for the batch experiments for different goethite mass require acknowledgement of their inverse power relationship with respect to goethite mass (Figures 5.2.8 and 5.2.9, respectively). More data points are needed to consolidate the α, β, model.

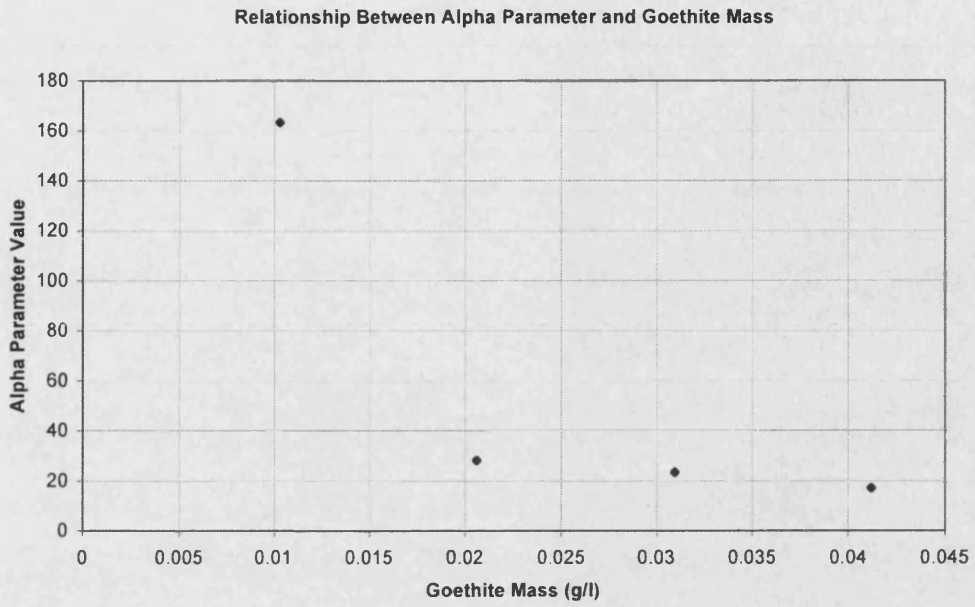

Figure 5.2.8. Function describing the relationship between α and the goethite mass.

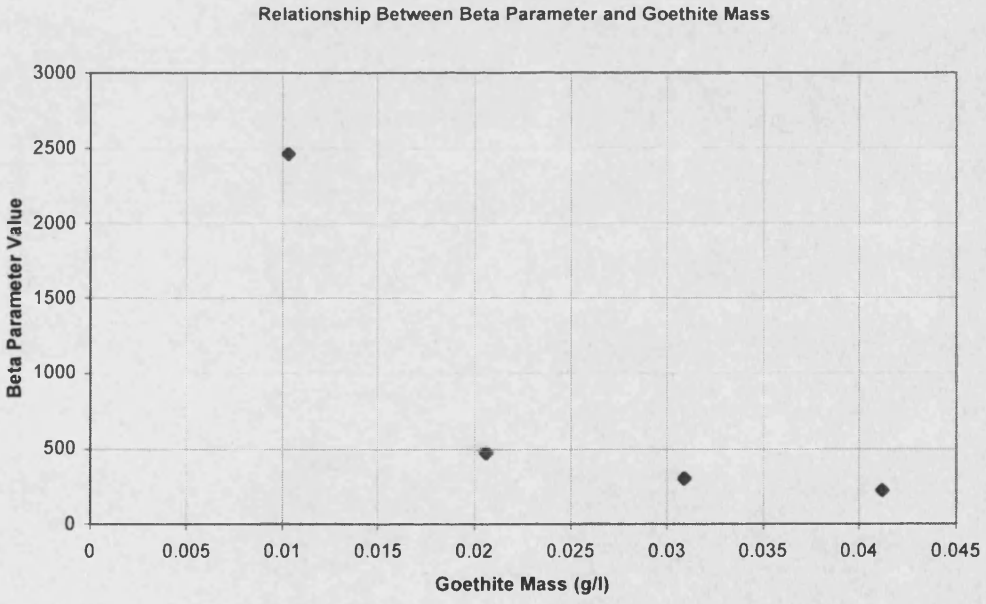

Figure 5.2.9. Function describing the relationship between β and the goethite mass.

The Freundlich isotherm exponent 'n' as a function of pH is shown in Figure 5.2.10 but shows no stable overall trend between n and the solution pH. The n values do, however, demonstrate a decrease with increasing goethite mass (Table 5.2.2). The value of n also becomes more variable with respect to pH in those experiments with the greatest amounts of goethite.

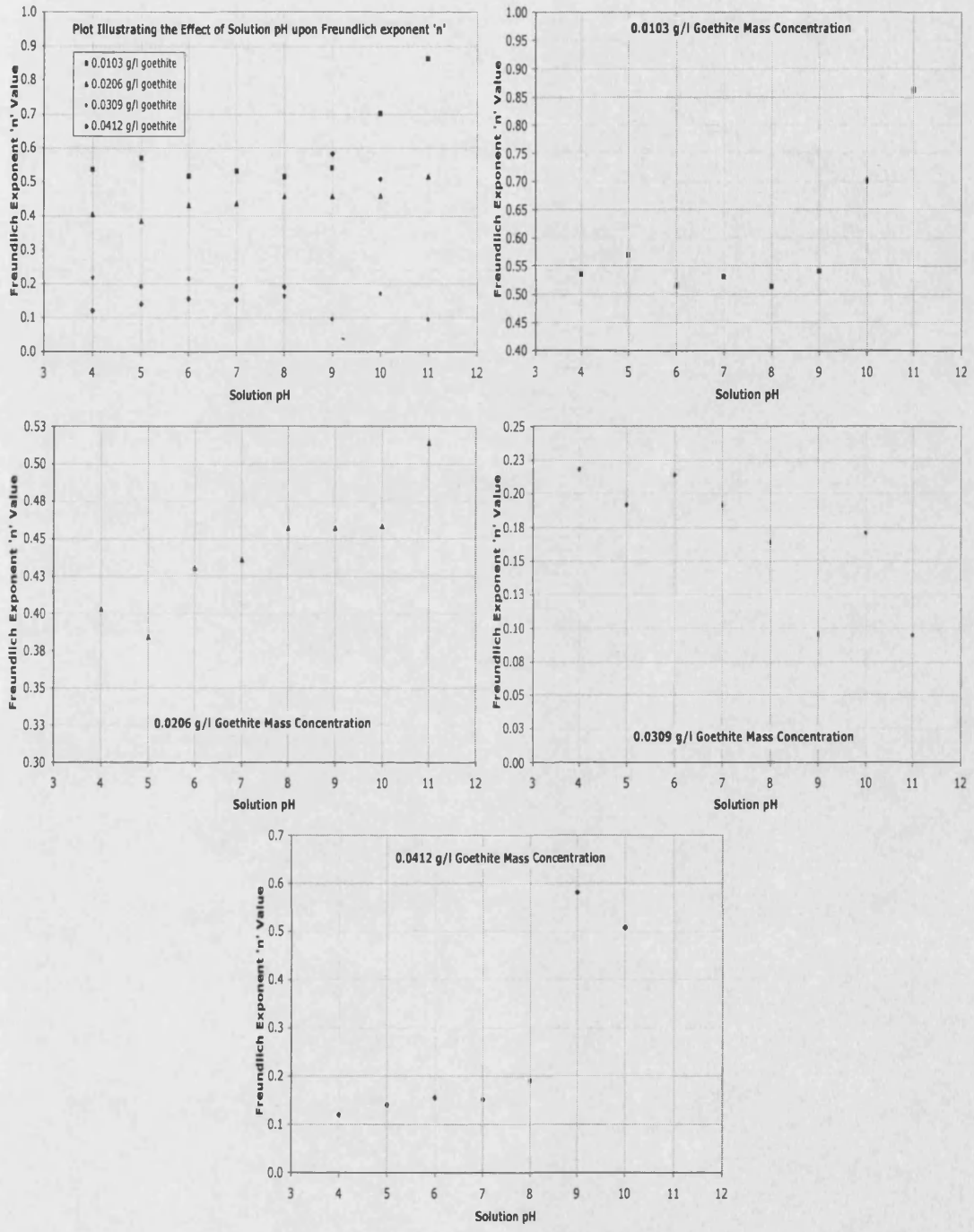

Figure 5.2.10. The effect of solution pH on the Freundlich n exponent.

It is also observed that, for the same solution pH, the K_f coefficient decreases non-linearly with goethite mass (average power function –1.02) (Figure 5.2.11). The inverse power relationship follows the general equation:

$$K_f = \chi(pH)\, m^{-\delta(pH)} \qquad \textit{Eqn. 5.2.9.}$$

Where χ and δ are coefficients related to the pH values. A similar inverse power function (power -1.06) describing As(V) adsorption partition coefficients onto increasing goethite mass was found by Matis *et al.* (1999).

In conclusion, the experimental observations follow closely to a Freundlich isotherm (Equation 5.2.2), in which the K_f value is a function of both a given goethite mass (m) and a given pH (Equations 5.2.8 and 5.2.9, respectively).

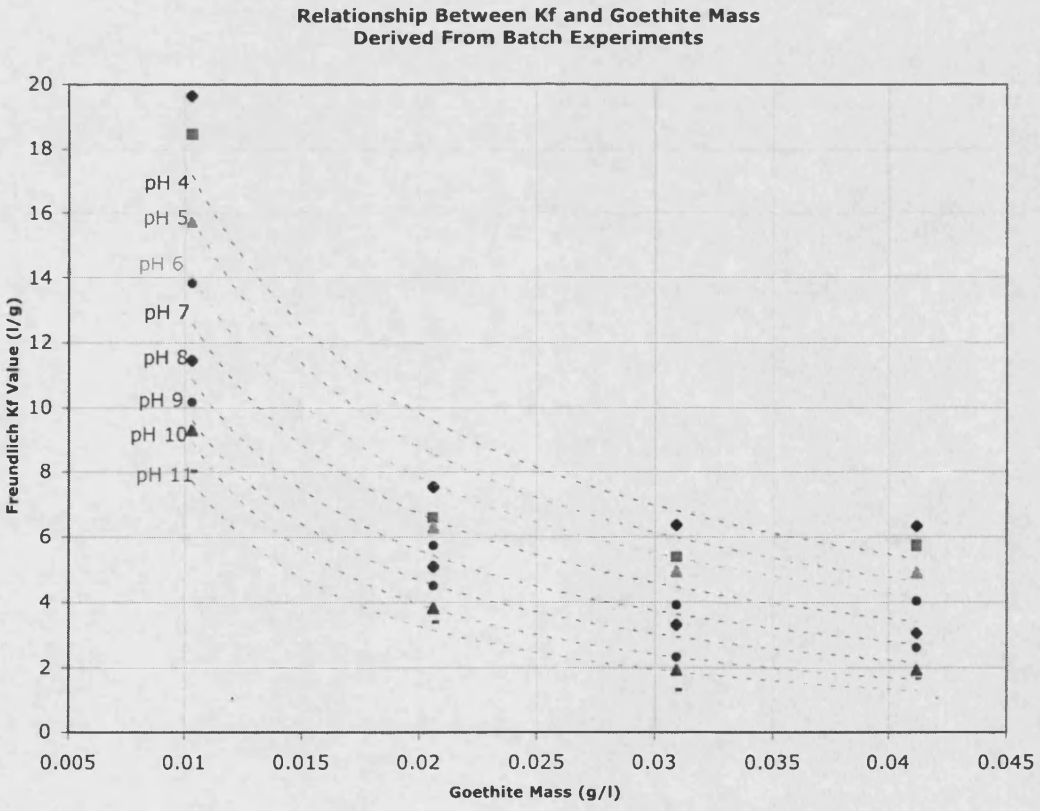

Figure 5.2.11. Graph showing the relationship between the derived K_f value (lg^{-1}) and the mass of goethite present within the experiment.

5.2.2. The Langmuir Isotherm

Results are shown with the experimental data fitted to the Langmuir isotherms using the method of minimisation of least square difference (Figure 5.2.12).

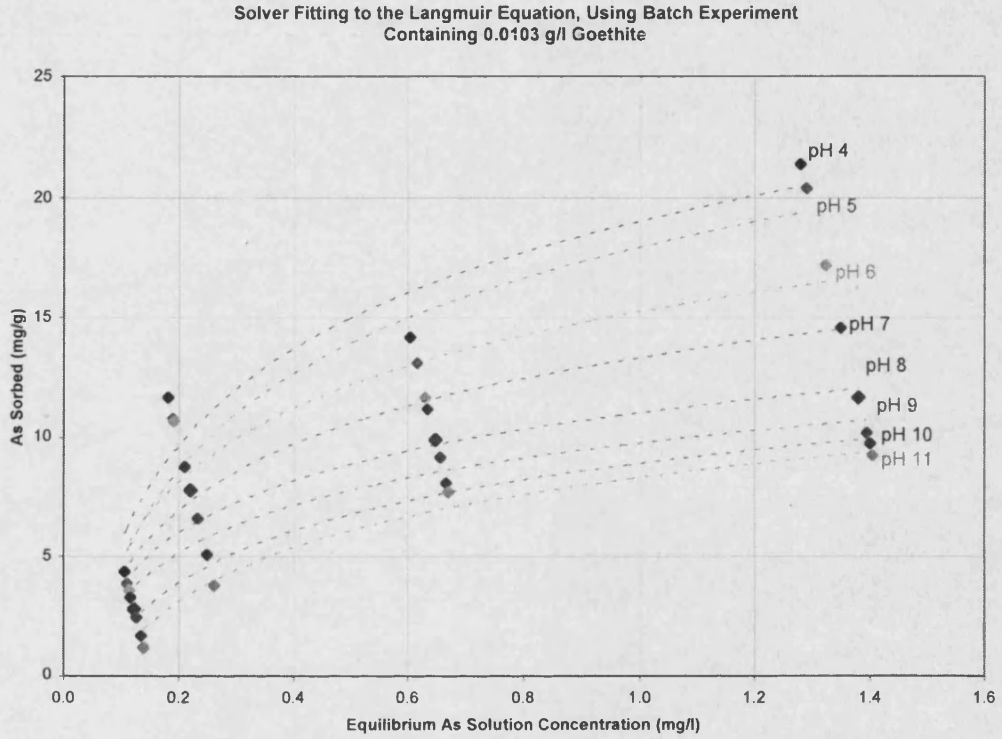

Figure 5.2.12. Langmuir adsorption Isotherm fitted to data. Goethite mass in solution is 0.0103g/l. The points represent experimental data and the curves the fitted isotherm.

The graphical approach for the Langmuir adsorption parameters used the plot of C/C* Vs. C (Appendix 5A). Table 5.2.4 and Appendix 5B show the results of the Langmuir model fitting for all batch experiments. The K_l parameters were derived from the gradient of the slope divided by the intercept, and the Q_o value from the reciprocal of the gradient (Fetter, 1994). More complex adsorption situations can also be modelled using such plots. For example, if the data on the C/C* Vs. C plot lie along two distinct straight lines of different gradient then this may indicate a two-site adsorption mechanism (Fetter, 1994). The isotherms for 0.0206 gl^{-1} goethite in Figure 5.2.13 more closely satisfy linearity

of C/C* function, and the batch results do not suggest the presence of a two-site mechanism.

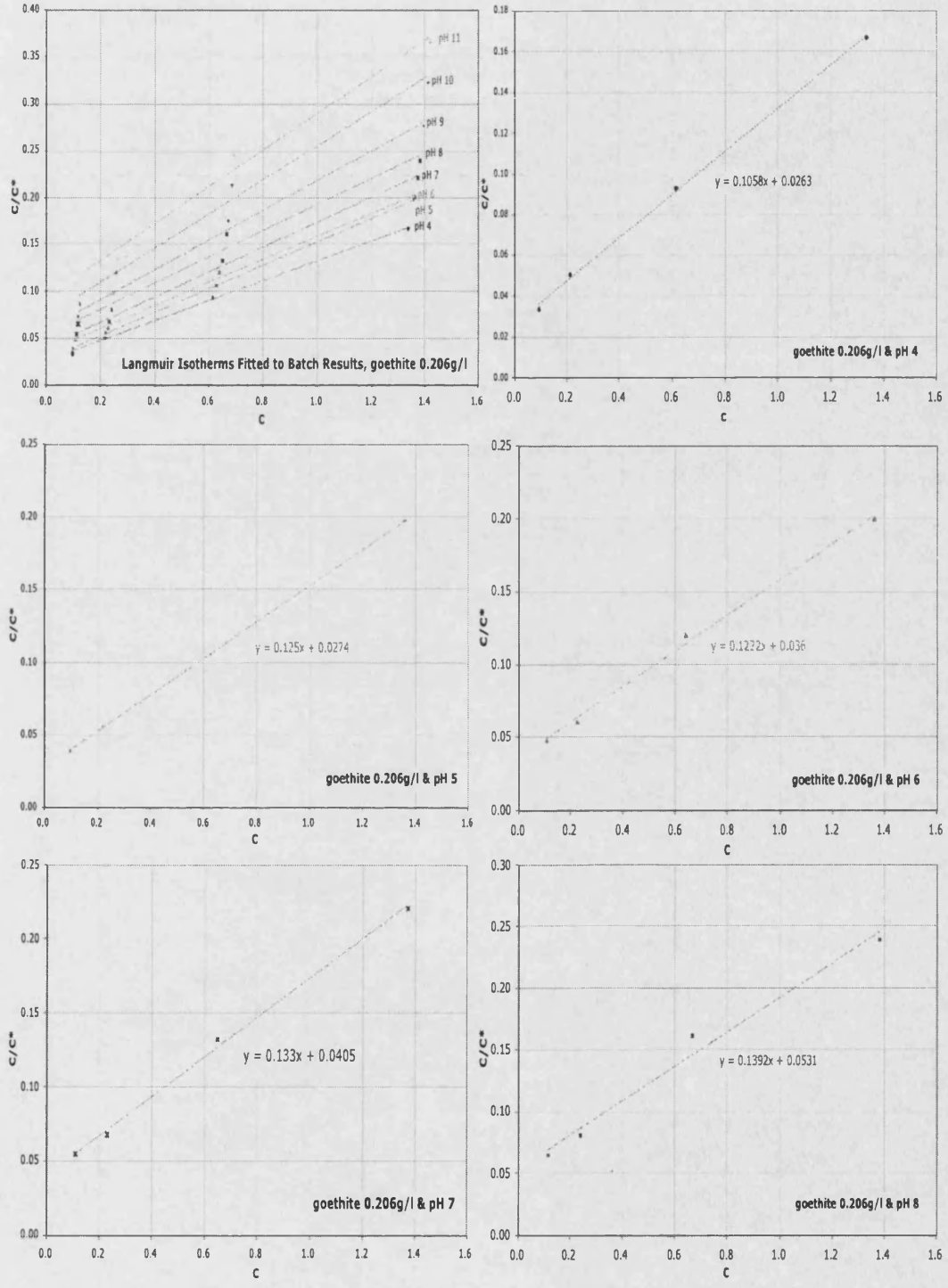

Figure 5.2.13a. Batch Experiment results plotted in terms of C/C* Vs. C, representative of the Langmuir adsorption model. Solution pH 4 – 8.

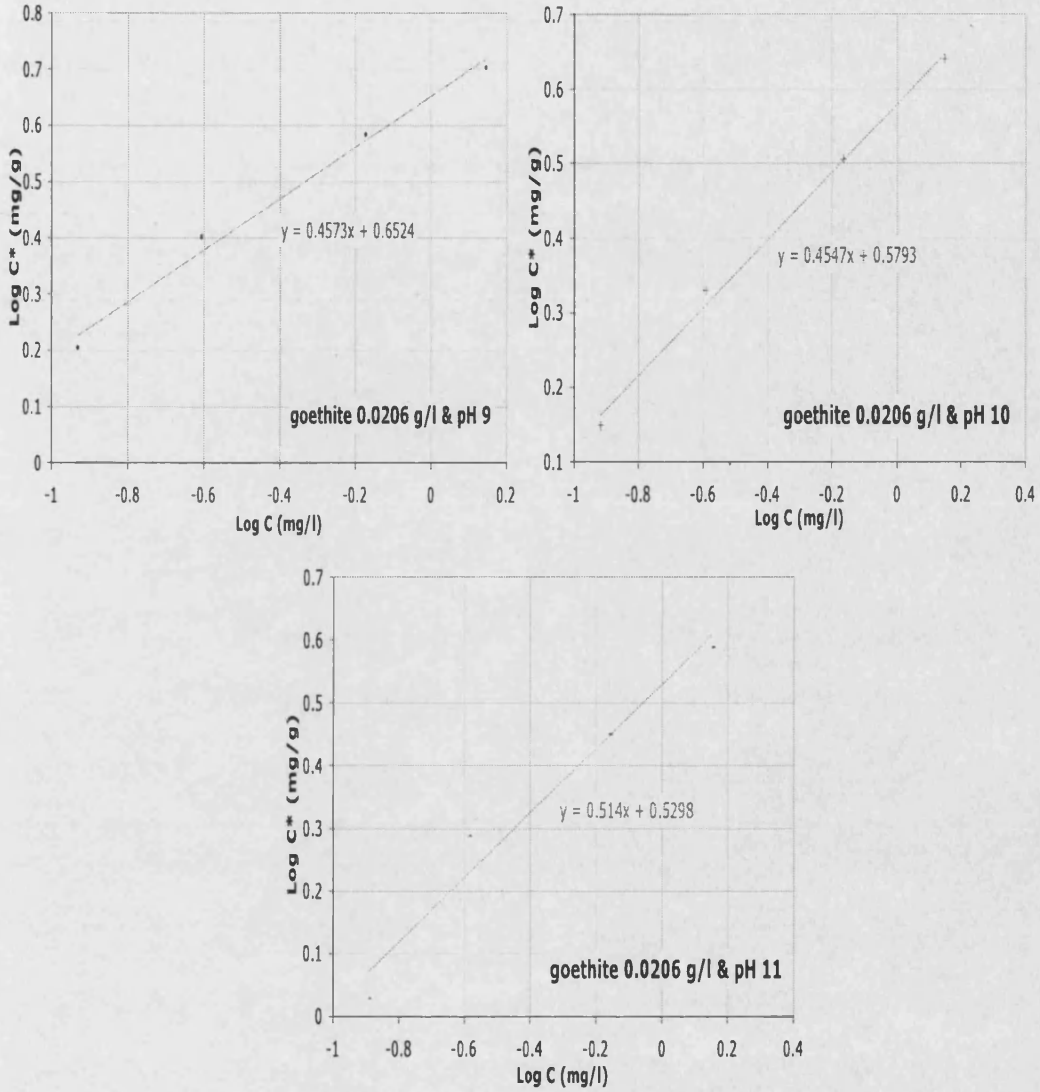

Figure 5.2.13b. Batch Experiment results plotted in terms of C/C* Vs. C, representative of the Langmuir adsorption model. Solution pH 9 – 11.

Similar to the Freundlich fitted isotherms, the degree of correlation between the observed data and the model fit improves as the equilibrium arsenic concentration and the solution pH increase. Table 5.2.3 shows the summary of the least squares fit.

Solution pH	K_l	K_l	Qo (mg/g)	Qo (mg/g)	Mean Squared Difference (Between Fitted and Experimental Data)
4	2.9	2.2	25.7	28.3	4.2
5	2.4	1.8	25.6	28.3	3.9
6	3.4	2.2	19.8	22.4	4.1
7	3.2	2.4	17.7	19.0	1.3
8	3.7	2.8	14.2	14.9	1.1
9	3.3	2.6	12.8	13.3	0.8
10	1.9	1.2	13.7	16.0	0.5
11	1.2	0.5	15.1	22.9	0.5

Table 5.2.3. Langmuir isotherm fitted parameters by least squares fitting, using Solver (black) and the graphical method (red), for solution Goethite mass of 0.0103 g/l.

Overall, the Langmuir coefficient (K_l) has a relatively constant value close to 3 up to pH 9 when it decreases sharply to below 2.

Solution pH	0.0103 g/l goethite batches		0.0206 g/l goethite batches		0.0309 g/l goethite batches		0.0412 g/l goethite batches	
	K_l	Q_o	K_l	Q_o	K_l	Q_o	K_l	Q_o
4	2.152	28.329	4.023	9.452	3.894	8.503	11.200	7.143
5	1.801	28.329	4.562	8.000	4.690	6.878	9.262	6.583
6	2.241	22.422	3.394	8.183	4.214	6.431	7.557	5.754
7	2.397	19.048	3.284	7.519	3.336	5.391	9.901	4.529
8	2.800	14.881	2.621	7.184	3.955	4.367	3.146	4.255
9	2.656	13.316	2.667	6.313	4.206	3.025	0.729	6.519
10	1.230	15.974	2.490	5.495	3.301	2.594	1.024	3.945
11	0.546	22.936	2.077	5.118	2.861	1.838		

Table 5.2.4. Summary of the Langmuir model parameters used to fit all batch experimental data.

Figure 5.2.14 illustrates the fundamental variation of the Langmuir K_l coefficient with respect to the solution pH, and Figure 5.2.15 shows the inverse relationship between the Q_o parameter and the solution pH. As the Q_o parameter relates to the number of available adsorption sites (Appelo and Postma, 1994), the general lowering of Q_o with increasing pH suggests competition from OH^-.

The relationships between K_l and Q_o and the solution pH are less regular than those of the Freundlich isotherm parameters, and generalised equations describing how these parameters vary with pH have not been determined. This

may be a consequence of the generally less well defined Langmuir isotherm parameters compared with the Freundlich isotherm. The Langmuir isotherm is therefore likely to be a less suitable model for the experimental results.

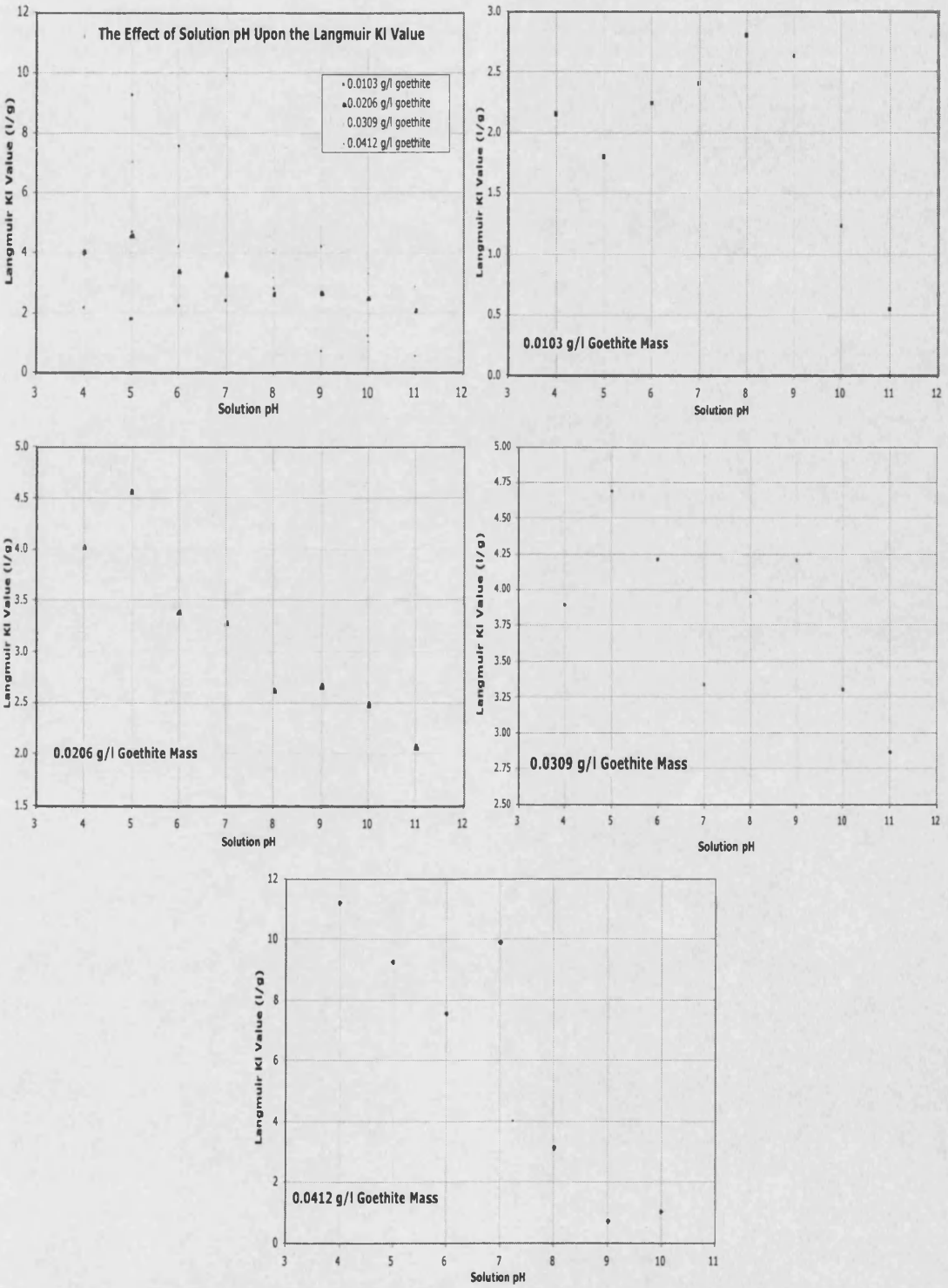

Figure 5.2.14. The effect of solution pH on the Langmuir K_l parameter, for all batch experiments (derived from C*/C Vs C plots).

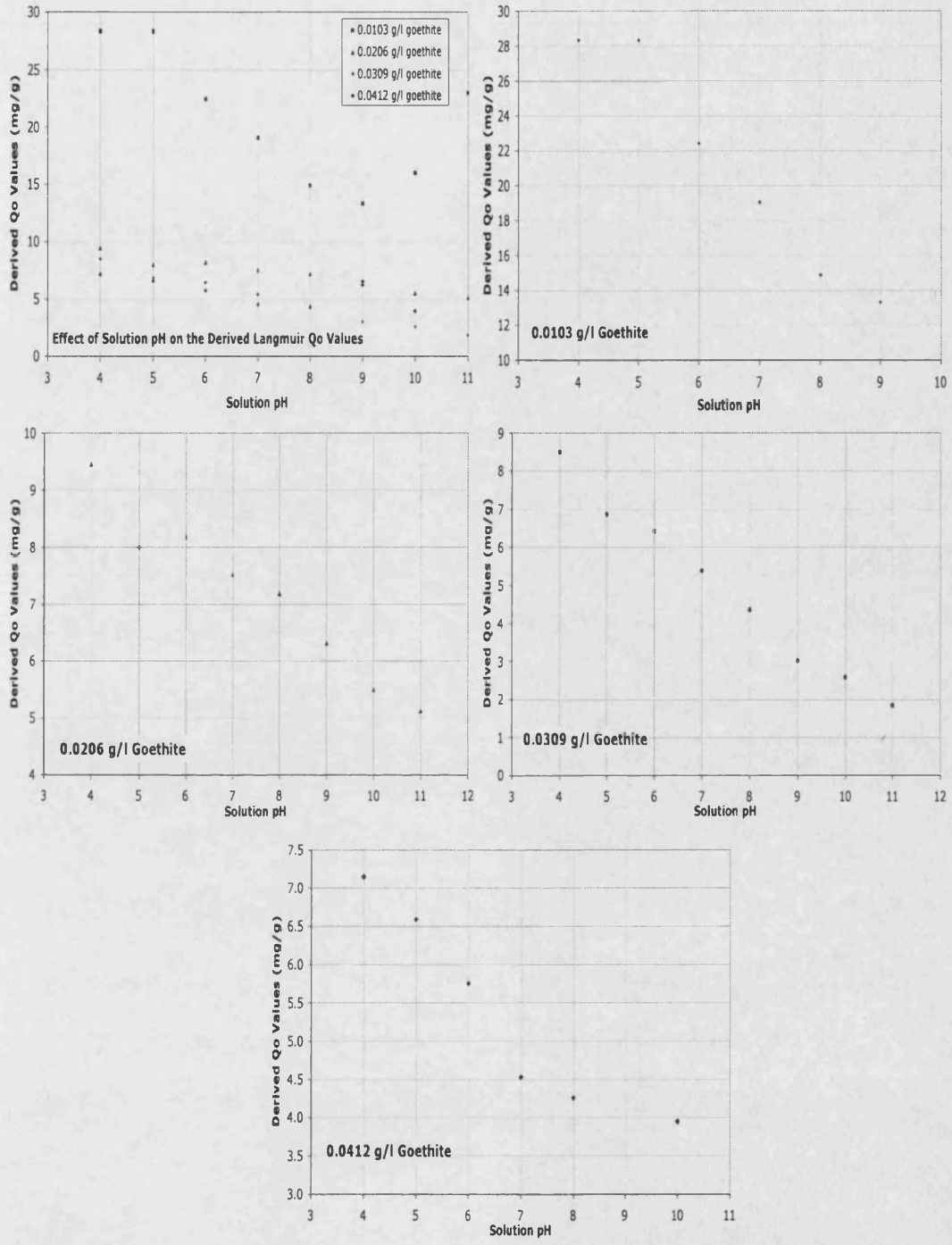

Figure 5.2.15. The effect of solution pH on the maximum available adsorption sites (Q_o), for all batch experiments (derived from C*/C Vs C plots).

In contrast to the Freundlich coefficient K_f value (Figure 5.2.11), the value for K_l increases with an increase in adsorbent mass present (Figure 5.2.16). In the

Langmuir model, Q_o gets smaller as the goethite mass increases and can be described with an inverse power relationship (average power is –1.01) (Figure 5.2.17). A logarithmic approximation is a useful fit for all solution pH points describing the relationship between K_l and goethite mass (m), with the general formula:

$$K_l = \alpha(pH) \log_e m + \beta(pH) \qquad \textit{Eqn. 5.2.10.}$$

Where α and β are coefficients related to the solution pH. The inverse power relationship between goethite mass and Q_o follows the general formula:

$$Q_o = \chi(pH)\, m^{-\delta(pH)} \qquad \textit{Eqn. 5.2.11.}$$

Where χ and δ are coefficients related to the solution pH.

From the available data there is not a strong enough variation in the α, β, χ and δ coefficient values and the solution pH to determine a functional relationship.

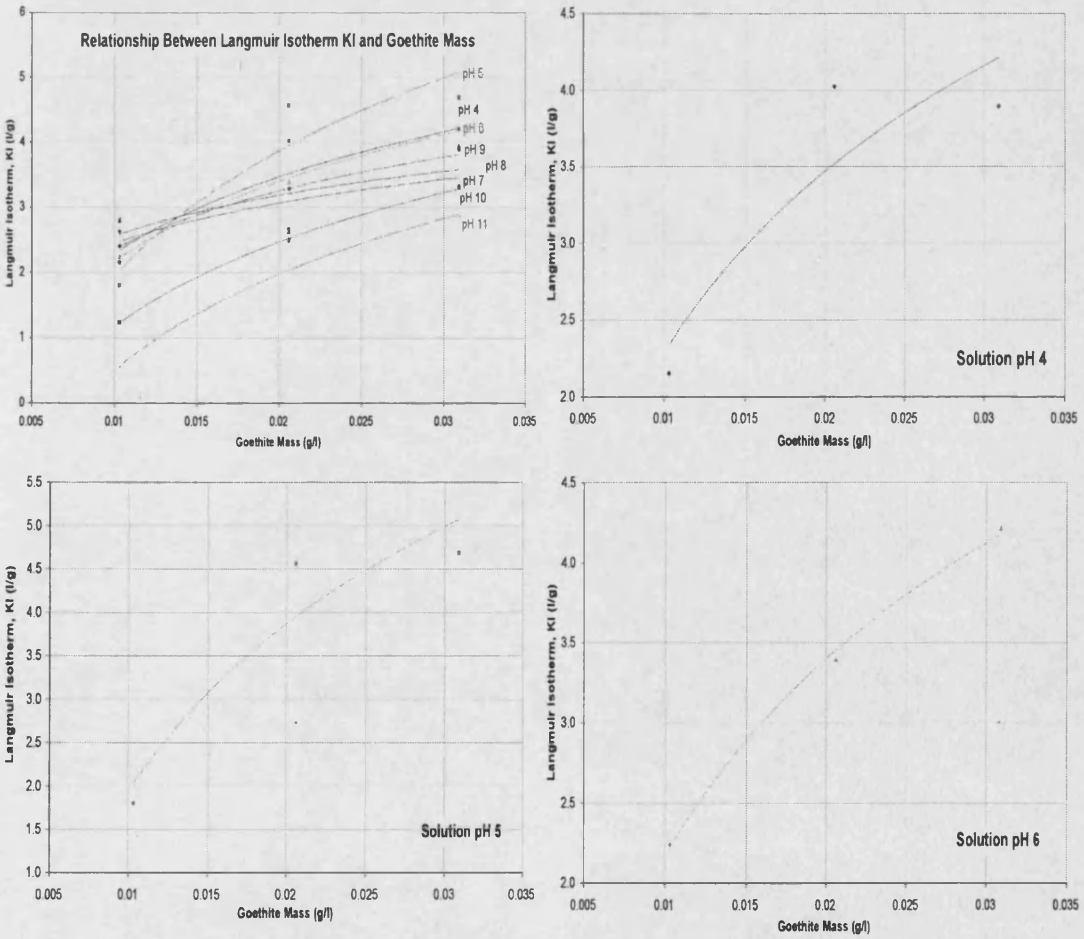

Figure 5.2.16a. The relationship between the batch experiment derived Langmuir K_l and the mass of goethite present within the experiment. Solution pH 4 – 6.

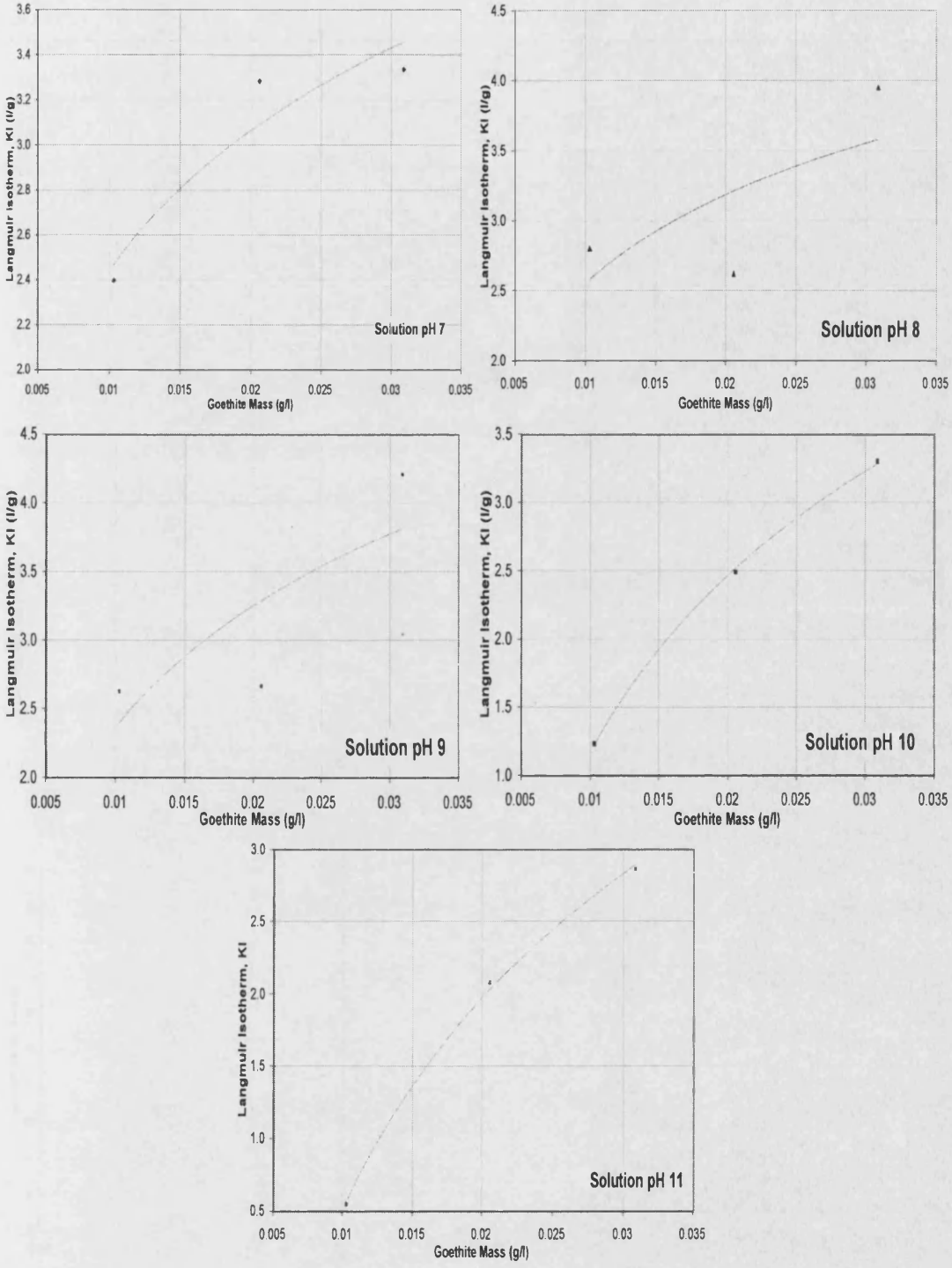

Figure 5.2.16b. The relationship between the batch experiment derived Langmuir K_l and the mass of goethite present within the experiment. Solution pH 7 – 11.

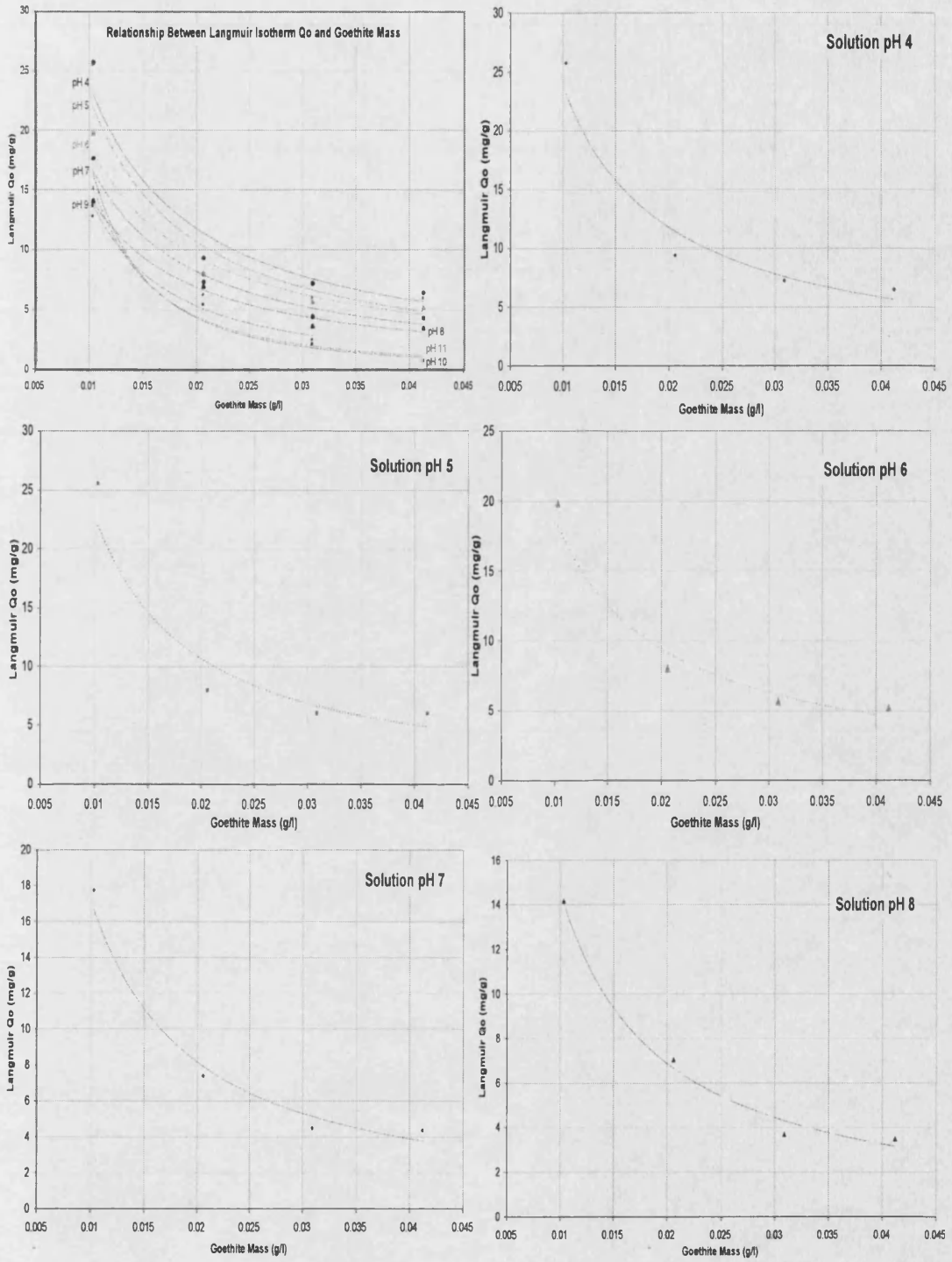

Figure 5.2.17a. The relationship between the batch experiment derived Langmuir Q_0 and the mass of goethite present within the experiment. Solution pH 4 – 8.

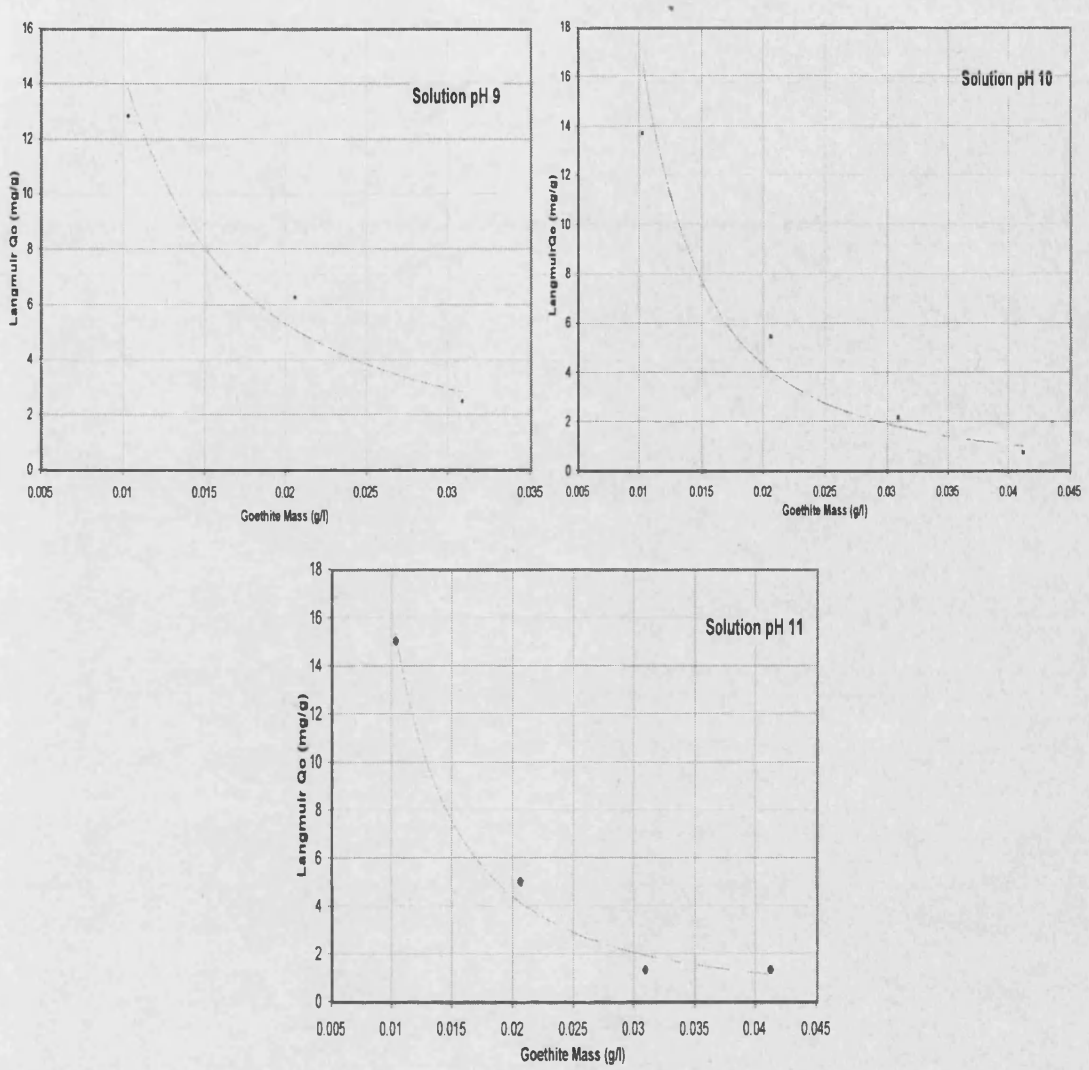

Figure 5.2.17b. The relationship between the batch experiment derived Langmuir Q_0 and the mass of goethite present within the experiment. Solution pH 9 – 11.

In comparing the correlation determinants (mean squared difference) between the Freundlich and Langmuir isotherm parameters (Tables 5.2.1 and 5.2.3) it is seen that both the Freundlich and Langmuir isotherm models are viable fits for the experimental data. However, the less well defined relationship between K_l and Q_o and solution pH may result from the poor suitability of the Langmuir model for the batch experiment data. Also, the inverse relationship between the maximum number of adsorption sites (Q_o) and goethite mass (Figure 5.2.17) is not easily defined and may result from the misuse of the Langmuir model.

5.2.3. The Linear Isotherm

Having explored the Freundlich and Langmuir isotherms as descriptive models for the batch data a linear isotherm model is included for comparison.

The data for all batch experiments were fitted to linear functions and given in Appendix 5A. The gradients of the linear function with zero as origin equates to the value of K_d (Figure 5.2.18).

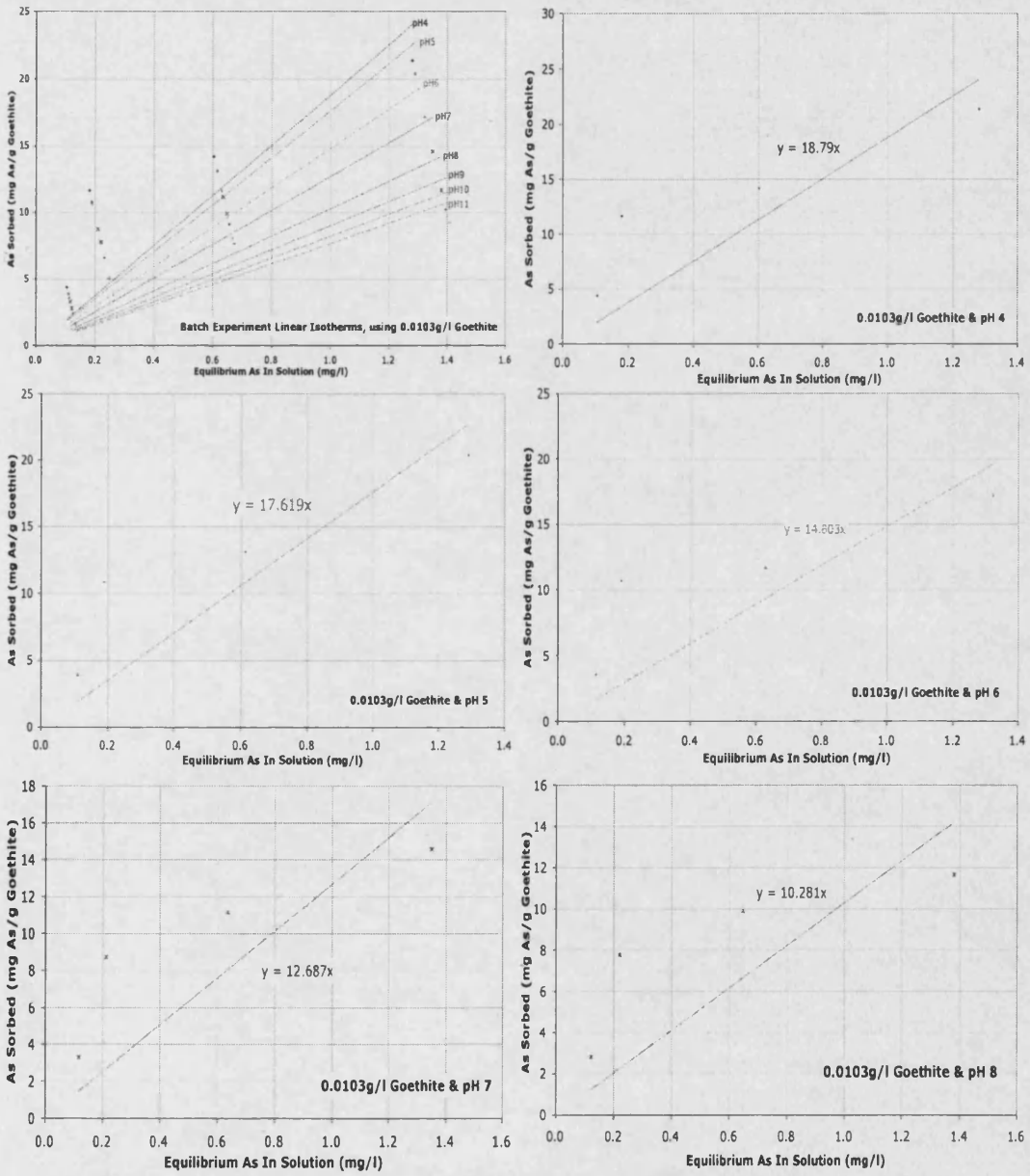

Figure 5.2.18a. Linear fitted isotherms to the batch experiment results for solution pH 4 – 8.

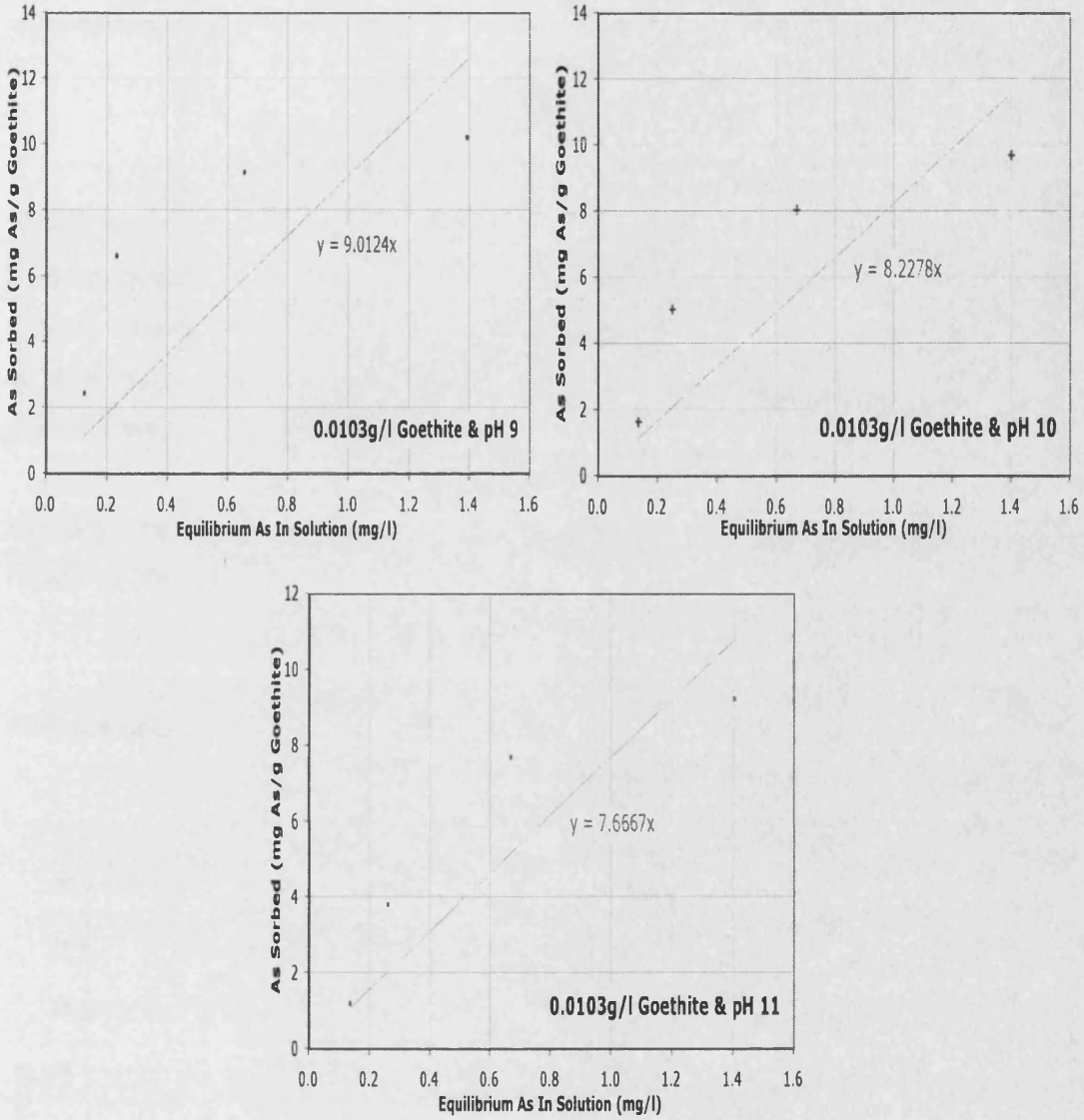

Figure 5.2.18b. Linear fitted isotherms to the batch experiment results for solution pH 9 – 11.

Figure 5.2.19 shows the relationship between K_d and the solution pH. The correlation between K_d and pH in this case is strong (with robust goodness of fit; R^2 ranges from 0.96 to 0.99). As the solution pH increases, the partition coefficient decreases linearly. Figure 5.2.20 illustrates an inverse power (average –0.96) function relationship between K_d and goethite mass, which is in agreement with the trends also observed by the Freundlich, K_f, and the Langmuir, Q_o parameters.

The linear approximation for K_d and the solution pH can be described with the general equation:

$$K_d = -\theta(m)\,pH + \omega(m) \qquad \textit{Eqn. 5.2.12.}$$

Where θ and ω are coefficients related to the goethite mass (m). Both show an inverse power relationship relative to the goethite mass (Figure 5.2.21 and 5.2.22). The power relationship that describes this correlation is nearly identical to that observed for the same relationship derived using Freundlich isotherm parameters.

Similarly, the inverse power relationship that describes K_d in terms of goethite mass has the general equation:

$$K_d = \phi(pH)\, m^{-\sigma(pH)} \qquad \textit{Eqn. 5.2.13.}$$

Where ϕ and σ are parameters of the fitted function and are related to the pH.

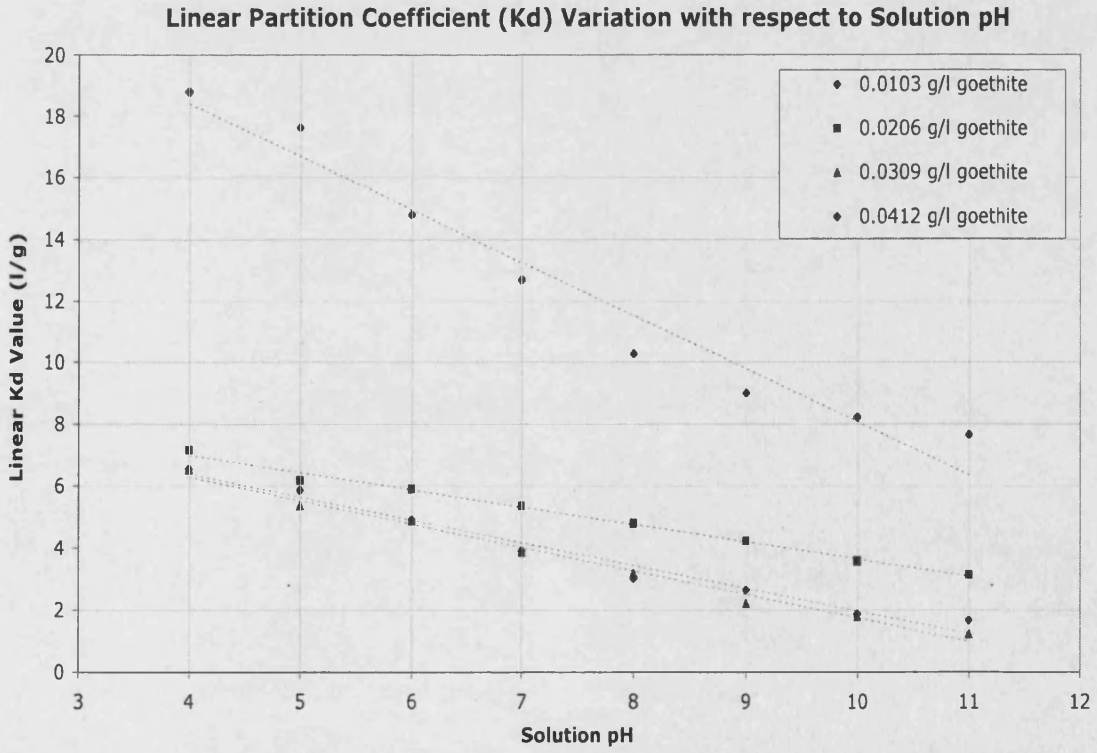

Figure 5.2.19. Correlation between Linear partition coefficient, K_d (l/g) and the solution pH, for all batch experiments.

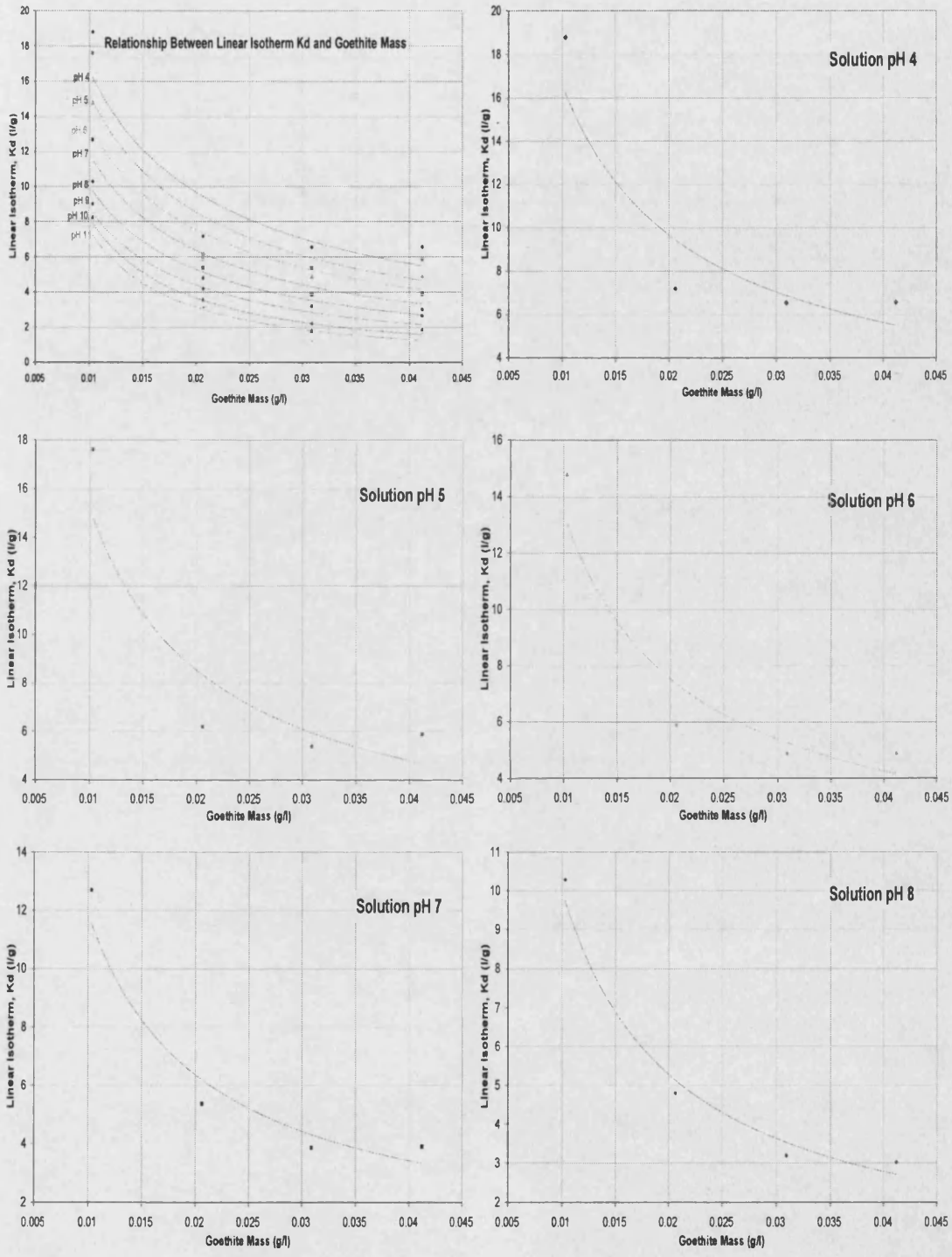

Figure 5.2.20a. The relationship between the derived K_d value and the mass of goethite present within the experiment. Solution pH 4 – 8.

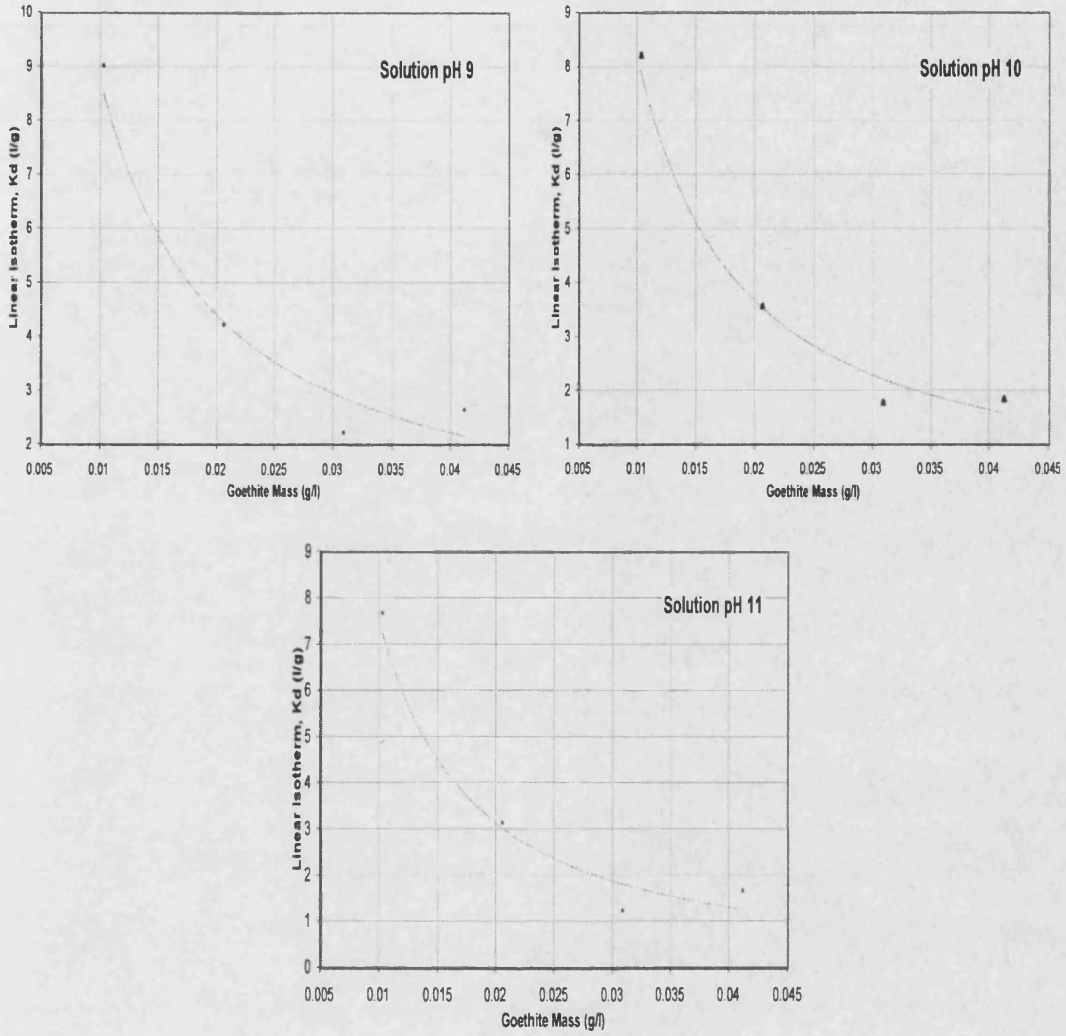

Figure 5.2.20b. The relationship between the derived K_d value and the mass of goethite present within the experiment. Solution pH 9 – 11.

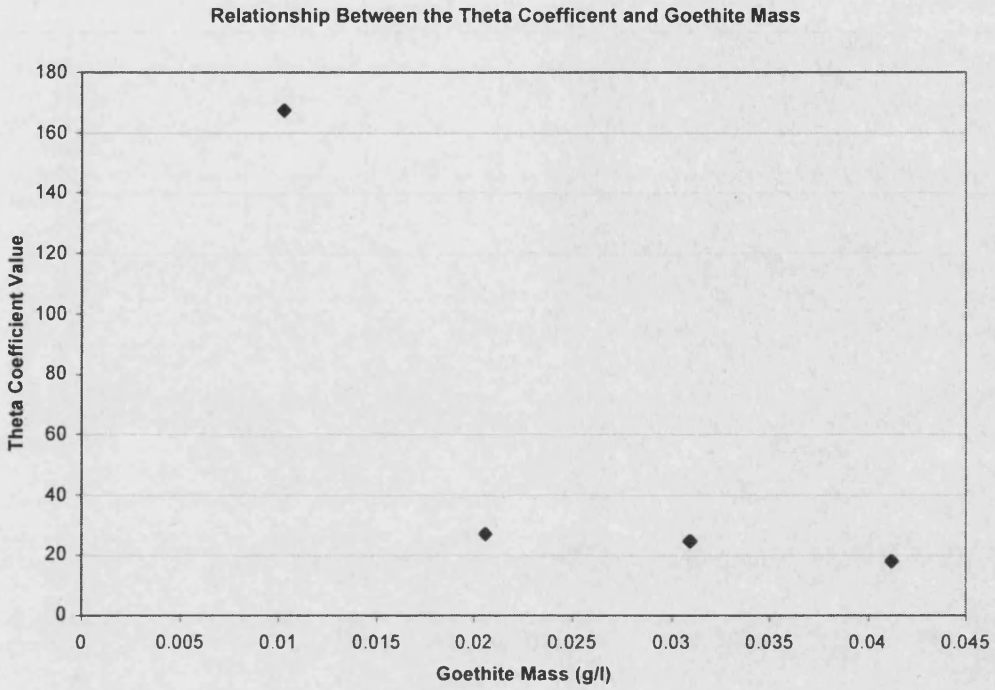

Figure 5.2.21. The function describing the relationship between the θ parameter and the goethite mass.

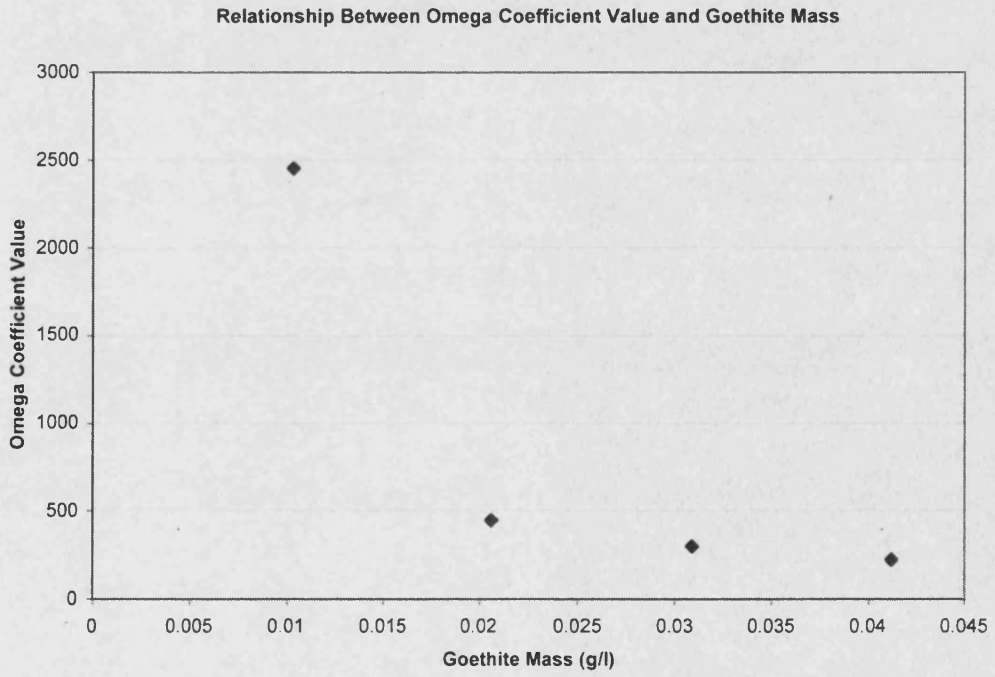

Figure 5.2.22. The function describing the relationship between the ω parameter and the goethite mass.

5.3. COLUMN EXPERIMENTS – INTERPRETATION OF ADSORPTION PARAMETERS AND MECHANISMS

5.3.1. The BIO1D Simulation Methodology

The breakthrough curves from the column experiments described in section 4.3. highlight the effects that goethite mass, arsenic concentration and flow rate have on the 'breakthrough' of arsenic. This section presents the results of using one-dimensional flow modelling with the BIO1D code (Srinivasan & Mercer, 1987) to simulate the breakthrough curves (BTCs) and hence determine the sorption parameters under equilibrium flow conditions. The BIO1D model uses the solute transport equation to simulate advection and dispersion as well as adsorption. Both linear and non-linear isotherms may be incorporated.

Solute Transport Equation (Srinivasan & Mercer, 1987):

$$D(\partial^2C/\partial x^2) - V_x(\partial C/\partial x) - [1+S(C)]\,(\partial C/\partial t) = 0 \qquad \textit{Eqn. 5.3.1.}$$

C = **Solute concentration in pore water (M/L^3)**
D = **Longitudinal hydrodynamic dispersion coefficient (L^2/T)**
x = **Distance (L)**
V_x = **Interstitial field velocity (L/T); assumed uniform**
S(C) = **Adsorption, function of C**
t = **Time (T)**

The set of starting parameters for initialising the model are:

The flux-averaged linear flow velocity (V_x, cms^{-1}), determined from the Cl BTCs (Chapter 4).

The dispersion coefficient (D) derived by fitting the chloride tracer breakthrough curves within the model separately, treating chloride as a conservative (unsorbed) ion.

The concentration of the solution species in the influent (C) (mgl^{-1}).

The total porosity (n_t) of the column fill was derived experimentally from measurements of saturated and dry material (see Chapter 2.2). As the values

were very similar for each column the average value of 21 % was used. The bulk density (p_b) of the column material was determined experimentally (Chapter 2.2). Table 5.3.1 summarises the derived n_t and p_b values required for modelling the adsorption term.

COLUMN IDENTITY	GOETHITE MASS (wt %)	n_t (%)	ρ_b (g/cm^3)
1	0.1	21.2	1.58
2	0.05	21.1	1.34
3	0.01	20.4	1.56
4	0.2	22.0	1.53
	Average =	**21.2**	**1.50**

Table 5.3.1. The total porosity (n_t) and bulk density of the column material for each of the experimental columns.

5.3.2. VIABILITY OF THE BIO1D MODEL – CHLORIDE FITTING

Chloride tracer experimental results demonstrate the conservative (non-reactive) behaviour of chloride transport in the columns. Table 5.3.2 shows the main parameters used for the chloride fitting together with the average linear flow velocities for the chloride breakthrough curves as determined from the breakthrough time and the length of the column. Section 2.4 described the individual experiment specifications.

The dispersion coefficient is related to the dispersivity (α) and the flow velocity (V_x) by:

$$D = \alpha V_x \qquad \textit{Eqn. 5.3.2.}$$

Where: D = Dispersion coefficient (cm^2/s)

α = Dispersivity (cm)

V_x = Average linear flow velocity (cm/s)

The effective porosity of the column material is found from Equation 5.3.3 and is shown in Table 5.3.2 for different experimental flow rates.

$$n_e = Q / (A \cdot V_x) \qquad \textit{Eqn. 5.3.3.}$$

Where: Q = Experimental volume flow rate (cm^3/s)

A = Cross-sectional area of column (cm^2)

V_x = Linear flow velocity determined from Cl BTCs (cm/s)

EXPERIMENT IDENTIFICATION	V_x (cm/s^{-1})	BREAKTHROUGH TIME, BT (s)	n_e (%)	D (cm^2/s)	α (cm)
E & G	0.013	670	13	0.011	0.846
B & D	0.018	520	13	0.016	0.889
J	0.019	490	14	0.017	0.914
H	0.021	460	14	0.018	0.857
C & I	0.022	450	14	0.020	0.909
A	0.027	390	26	0.024	0.889

Table 5.3.2. Experimental flow velocities (V_x), effective porosity (n_e) and BIO1D fitted dispersion coefficients (D) and dispersivity values (α).

The dispersivities (dispersion lengths) are on average 10.9 % of the flow lengths studied and therefore within the limits of scale dependence (Appelo and Postma, 1994). The dispersivity does not however, show any relationship with the flow velocity (Figure 5.3.1).

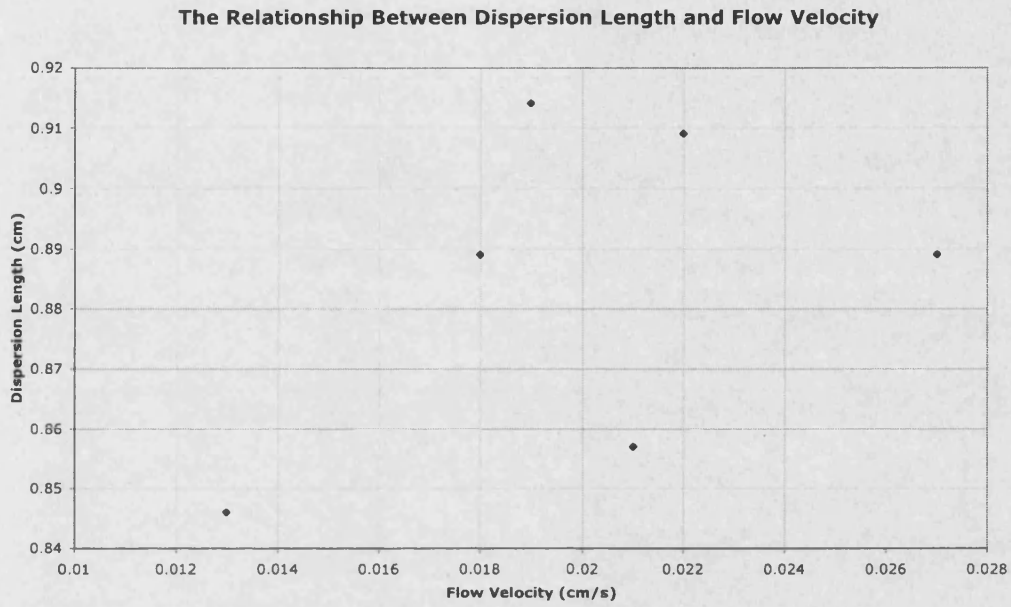

Figure 5.3.1. Graph illustrating no distinct relationship between the dispersion length (dispersivity) and the flow velocity.

Full results for both the experimental effluent chloride concentrations (in terms of C/Co) and the corresponding BIO1D simulations are given in Appendix 5C. These results are summarised in Figure 5.3.2 illustrating the different chloride transport through the columns with different flow velocities, and how well the BIO1D simulations fit the experimental data.

A 5 % mean difference, in terms of C/C_o at a given time, between the experimental and simulated BTC results was permitted in view of the possible scale of experimental and sampling error and including experimental flow perturbations. All BTCs were acceptable using BIO1D, with the simulations more accurate during early and latter times of breakthrough. However, individual column experiments occasionally exceeded the 5 % criterion around the

C/C_o = 0.5 breakthrough point (as shown in Appendix 5D). The 'goodness of fit' appears not to be related to flow velocity but may be explained to some degree by flow perturbations during the experiment. Table 5.3.3 summarises the 'closeness of fit' using the mean difference over the entire BTC for each experiment.

EXPERIMENT IDENTIFICATION	FLOW VELOCITY, V_x (cm/s)	MEAN % DIFFERENCE OVER ENTIRE BTC (SIMULATED Vs EXPERIMENTAL)
A	0.027	1.7
B & D	0.018	2.9
C & I	0.022	3.5
E & G	0.013	3.3
H	0.021	1.5
J	0.019	2.5

Table 5.3.3. The mean percentage difference between the simulated and experimental breakthrough curves, averaged over the entire BTC.

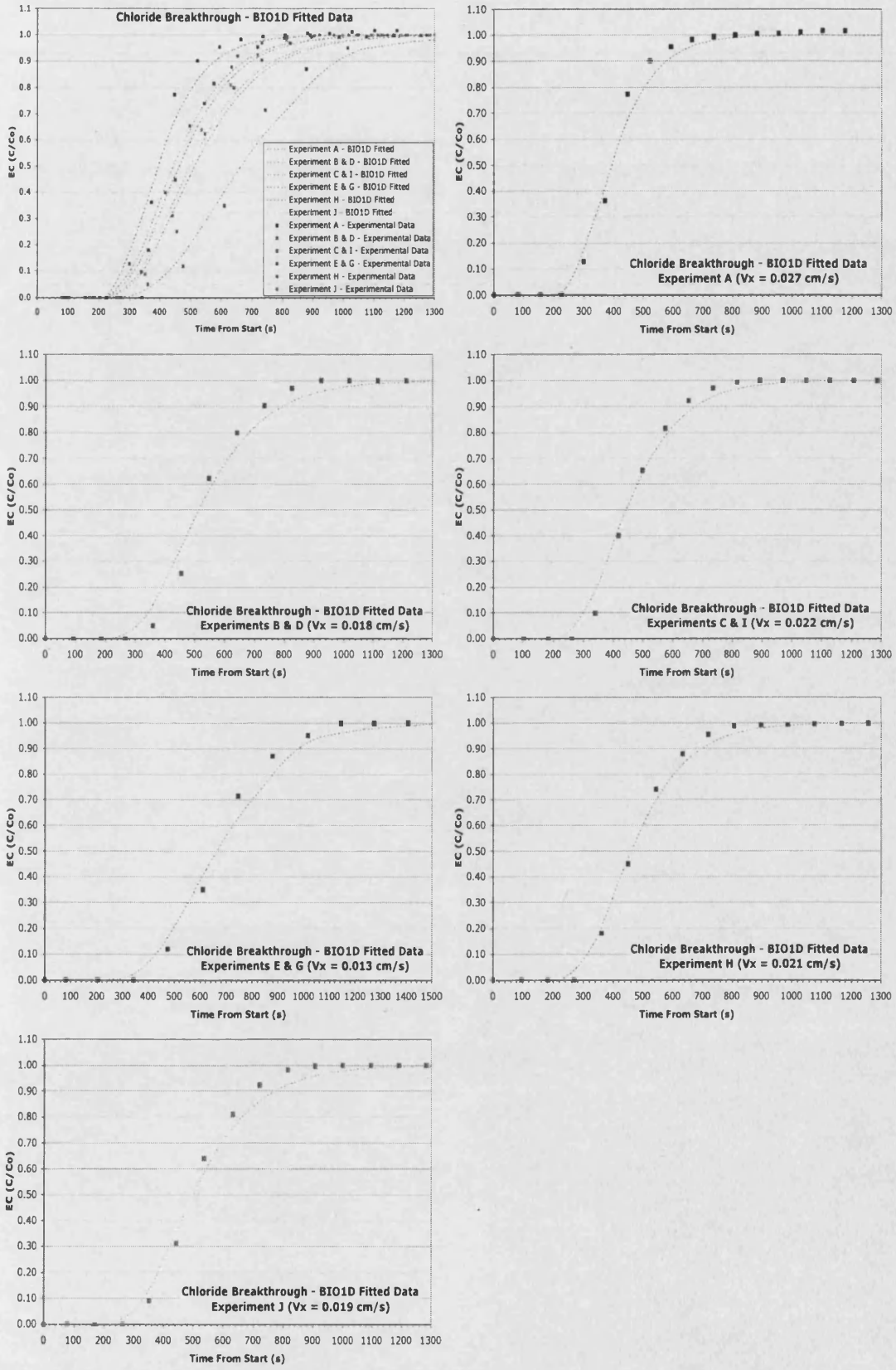

Figure 5.3.2. Chloride tracer breakthrough plots, both experimental and BIO1D simulated results.

5.3.3. BIO1D MODEL FITTING – LINEAR ISOTHERM FOR ARSENIC SORPTION

Arsenic Breakthrough Curves (BTCs) were fitted in a similar way to those for chloride, but they included adsorption terms within the one-dimensional solute transport equation (Equation 5.3.1).

The parameters required for initialising the models (V_x, C, D, n_t and ρ_b) were discussed in the previous section. The optimum adsorption terms K1 or R_f are defined in the linear adsorption equation and used in the BIO1D code (Srinivasan & Mercer, 1987) in the following way:

$$S(C) = K1/n_t = R_f - 1 = (\rho_b K_d') / n_t \qquad \textit{Eqn. 5.3.4.}$$

Where:

S(C)	**=**	**Adsorption term within the solute transport equation**
K1	**=**	**Linear Isotherm Coefficient**
n_t	**=**	**Total porosity (0.21)**
R_f	**=**	**Retardation Factor**
ρ_b	**=**	**Bulk Density of Matrix (g/cm^3)**
K_d'	**=**	**Linear Partition Coefficient (cm^3/g)**

K_d' is the Linear partition coefficient which is effective for the individual experiment column fill. The k_d' values for the column fill can be related to goethite K_d by correction of the goethite mass concentration within each column (Equation 5.3.5).

Appendix 5E contains all BTCs fitted to experimental data using the linear isotherm, and Figure 5.3.3 illustrates an example from experiment I. Table 5.3.4. shows the derived K1, R_f and K_d' values. The model uses only the K1 and R_f values and the partition coefficients (K_d') are derived directly from the linear adsorption equation 5.3.4 and equation 5.3.5. The bulk density used to determine K_d' for each column depends on the sediment within the column and, to compare partition coefficients specific to goethite, k_d' must be related to the goethite mass concentration within each column. The conversion factors from the initial derived K_d' to that accounting for adsorbent mass are derived as follows:

Column 1 Conversion Factor = 100 / 0.1 wt% goethite mass

Column 2 Conversion Factor = 100 / 0.05 wt% goethite mass

Column 3 Conversion Factor = 100 / 0.01 wt% goethite mass

Column 4 Conversion Factor = 100 / 0.2 wt% goethite mass

i.e. $K_d = K_d' \times$ Conversion Factor *Eqn. 5.3.5.*

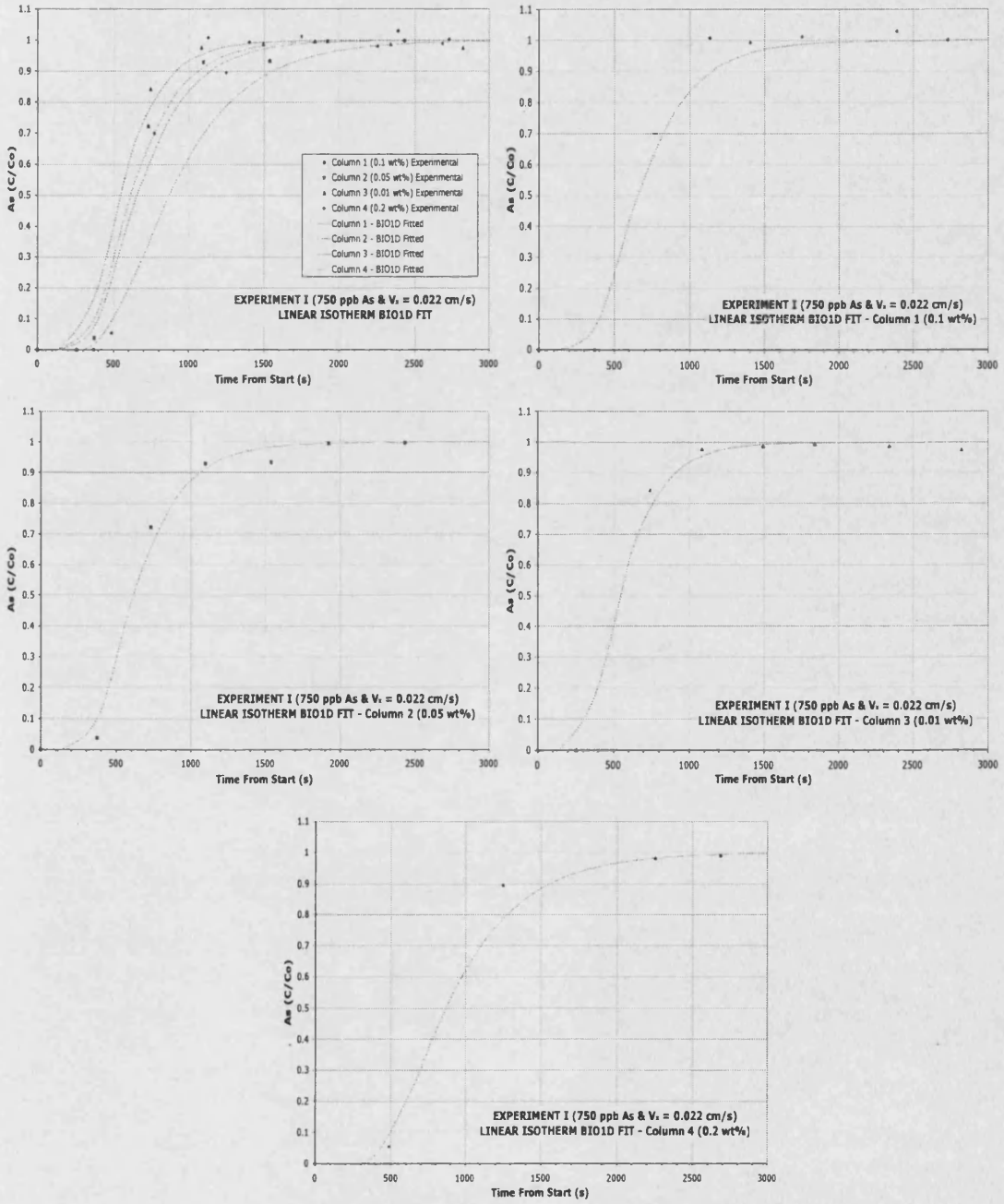

Figure 5.3.3. Experiment I Experimental breakthrough results and simulated BTCs using BIO1D and the Linear isotherm.

EXPERIMENT IDENTIFICATION	COLUMN IDENTIFICATION	BIO1D K1	BIO1D R_f	BIO1D Column K_d' (l/kg)	GOETHITE K_d (l/kg)
A (C_0 = 870 µg/l) V_x = 0.027 cm/s, D = 0.024 cm²/s	1 (0.1 wt%)	0.07	1.35	0.04	45
A	2 (0.05 wt%)	0.03	1.15	0.02	45
A	3 (0.01 wt%)	0.02	1.10	0.01	127
A	4 (0.2 wt%)	0.25	2.25	0.16	82
B (C_0 = 600 µg/l) V_x = 0.018 cm/s, D = 0.016 cm²/s	1	0.12	2.40	0.18	179
B	2	0.23	2.15	0.17	343
B	3	0.16	1.80	0.10	1013
B	4	0.31	2.55	0.20	101
C (C_0 = 280 µg/l) V_x = 0.022 cm/s, D = 0.02 cm²/s	1	0.12	1.60	0.08	77
C	2	0.085	1.425	0.06	127
C	3	0.01	1.05	0.01	63
C	4	0.21	2.05	0.14	69
D (C_0 = 57 µg/l) V_x = 0.018 cm/s, D = 0.016 cm²/s	1	0.29	2.45	0.19	186
D	2	0.25	2.25	0.19	373
D	3	0.215	2.075	0.14	1361
D	4	0.32	2.60	0.21	105
E (C_0 = 780 µg/l) V_x = 0.013 cm/s, D = 0.011 cm²/s	1	0.21	2.05	0.13	135
E	2	0.15	1.75	0.11	224
E	3	0.14	1.70	0.09	886
E	4	0.28	2.40	0.18	92
G (C_0 = 540 µg/l) V_x = 0.013 cm/s, D = 0.011 cm²/s	1	0.185	1.925	0.12	119
G	2	0.17	1.850	0.13	254
G	3	0.155	1.775	0.10	981
G	4	0.31	2.55	0.20	101
H (C_0 = 630 µg/l) V_x = 0.021 cm/s, D = 0.018 cm²/s	1	0.20	2.00	0.13	128
H	2	0.15	1.75	0.11	224
H	3	0.09	1.45	0.06	570
H	4	0.24	2.20	0.16	78
I (C_0 = 750 µg/l) V_x = 0.022 cm/s, D = 0.02 cm²/s	1	0.175	1.875	0.11	112
I	2	0.145	1.725	0.11	216
I	3	0.09	1.45	0.06	570
I	4	0.35	2.65	0.23	114
J (C_0 = 630 µg/l) V_x = 0.019 cm/s, D = 0.017 cm²/s	1	0.21	2.05	0.13	135
J	2	0.16	1.80	0.12	239
J	3	0.12	1.60	0.08	759
J	4	0.36	2.80	0.24	118

Table 5.3.4. BIO1D Results in terms of Linear Isotherm, for all the column experiments. The derived coefficient values are given, both column specific (K_d') and with respect to the goethite present (K_d).

The degree of fit between the simulations and the experimental data is compared in Table 5.3.5 and illustrated in Figure 5.3.4 as a function of the flow velocity. Figure 5.3.4 shows that the simulated BTCs fit the experimental BTCs the best at high flow velocities and may be the result of a better model description for the dispersion at high flow. BIO1D generally provides good

approximation to experimental methods. There is no observed correlation between the goodness of fit and the solute concentration (Appendix 5F). There may be kinetic effects that are not considered in the model and lead to the poorer simulations at low or extreme flow velocity and which are discussed further in section 5.3.3. Alternatively, flow variability may be an issue at the lower flow rates.

EXPERIMENT IDENTIFICATION	% DIFFERENCE (& R^2) COLUMN 1	% DIFFERENCE (& R^2) COLUMN 2	% DIFFERENCE (& R^2) COLUMN 3	% DIFFERENCE (& R^2) COLUMN 4
A	2.5 (0.98)	0.8 (1.00)	1.8 (0.99)	1.0 (1.00)
B	2.7 (0.99)	2.2 (0.99)	0.8 (1.00)	4.6 (0.97)
C	0.9 (1.00)	0.9 (1.00)	0.7 (1.00)	2.7 (0.98)
D	1.3 (1.00)	2.4 (0.99)	3.0 (0.98)	3.2 (0.98)
E	4.7 (0.97)	4.2 (0.97)	3.2 (0.98)	4.2 (0.98)
G	2.9 (0.99)	3.1 (0.98)	2.2 (0.99)	5.2 (0.97)
H	0.8 (1.00)	1.2 (1.00)	1.4 (0.99)	3.2 (0.98)
I	2.0 (0.99)	1.3 (0.99)	1.0 (1.00)	2.3 (0.99)
J	1.6 (1.00)	1.7 (0.99)	2.1 (0.99)	2.9 (0.99)

Table 5.3.5. Degree of fit between the modelled and experimental BTCs compared, using the mean difference for the entire BTC for each experiment. R^2 = regression or correlation coefficient.

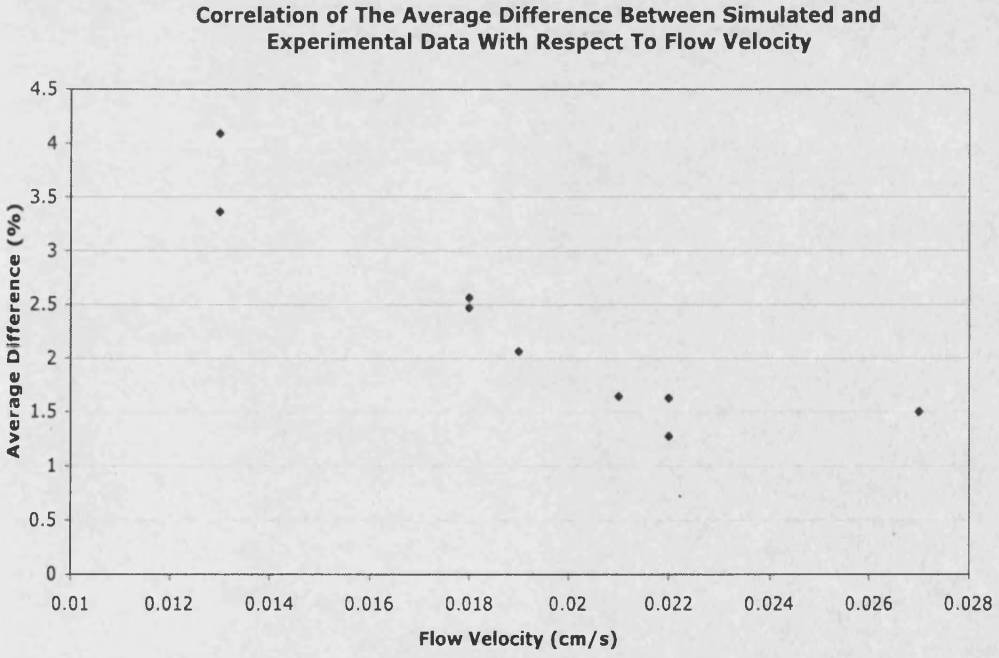

Figure 5.3.4. Plot demonstrating the difference between experimental and simulated data, as a mean percentage difference, for each experiment and the flow velocity (V_x).

The values of K_d for linear sorption of arsenic on goethite for the column experiments range from 44 to 1360 l/Kg. These are less than those derived for the equilibrium batch experiments, which lie between 3864 and 12687 l/Kg at solution pH 6, equating to the measured column effluent pH.

Figure 5.3.5 shows the relationship between the K_d values derived for the column experiments with respect to the flow velocity. The figure illustrates a general decrease of the goethite (corrected) partition coefficient with increasing flow velocity. The results also suggest a possible optimum velocity for adsorption at 0.018 cm/s for the masses used, which corresponds to a peak partition coefficient.

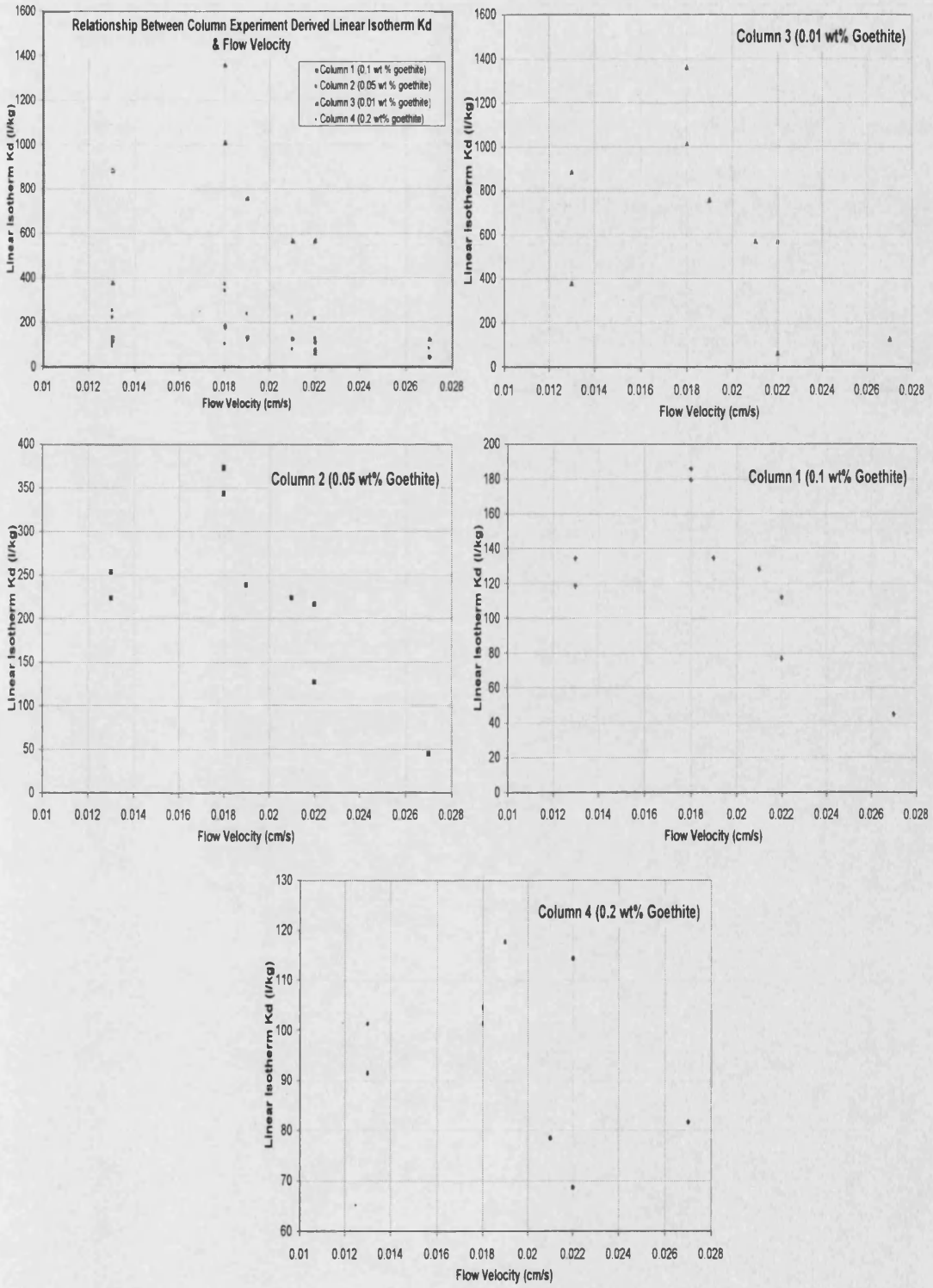

Figure 5.3.5. The relationship between K_d (corrected for goethite mass) and flow velocity (V_x).

A further relationship test was applied to the partition coefficient and the influent arsenic concentration (Figure 5.3.6) but the results do not show clear functionality. If adsorption is adhering strictly to the Linear isotherm description then the partition coefficients should not change with solution concentration.

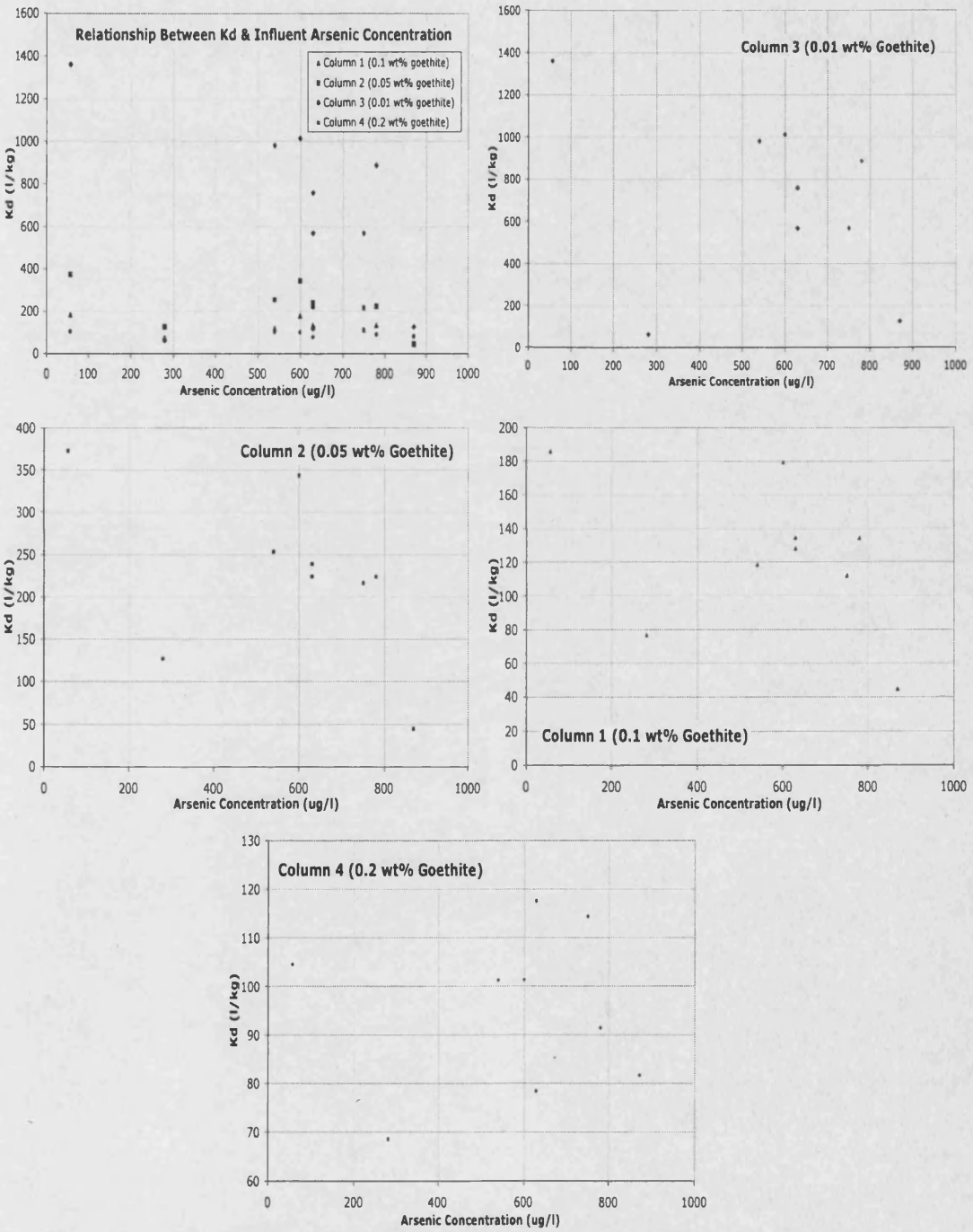

Figure 5.3.6. The relationship between K_d (corrected for goethite mass) and influent arsenic concentration.

An interesting inverse relationship between the corrected K_d values and the goethite mass within the columns is indicated in Figure 5.3.7, using discrete experimental results to discount effects from other experimental variables. The inverse relationship is better quantified for the experiments with lower flow velocity. Such a relationship can be represented by an inverse power function with a mean exponent of –0.72. The same trend was observed in the batch experiments, and can be explained by the mathematics of the isotherm coefficient as described in Section 5.2. However, column experiments A and C do not show the same inverse mass relationship (Table 5.3.4). This may be as a result of the relatively high flow velocities in these two experiments, suggesting that equilibrium adsorption has not been achieved as a consequence of kinetic disequilibrium. This is discussed further in Section 5.3.5.

In general, K_d is related to the goethite mass (m) by:

$$K_d = \alpha(C_0)\, m^{-\beta(v_x)} \qquad \textit{Eqn. 5.3.6.}$$

Where α and β represent functional parameters that are dependent on the arsenic concentration (C_0) and the flow velocity (v_x) respectively (Appendix 5G shows the functions used to describe α and β relationships).

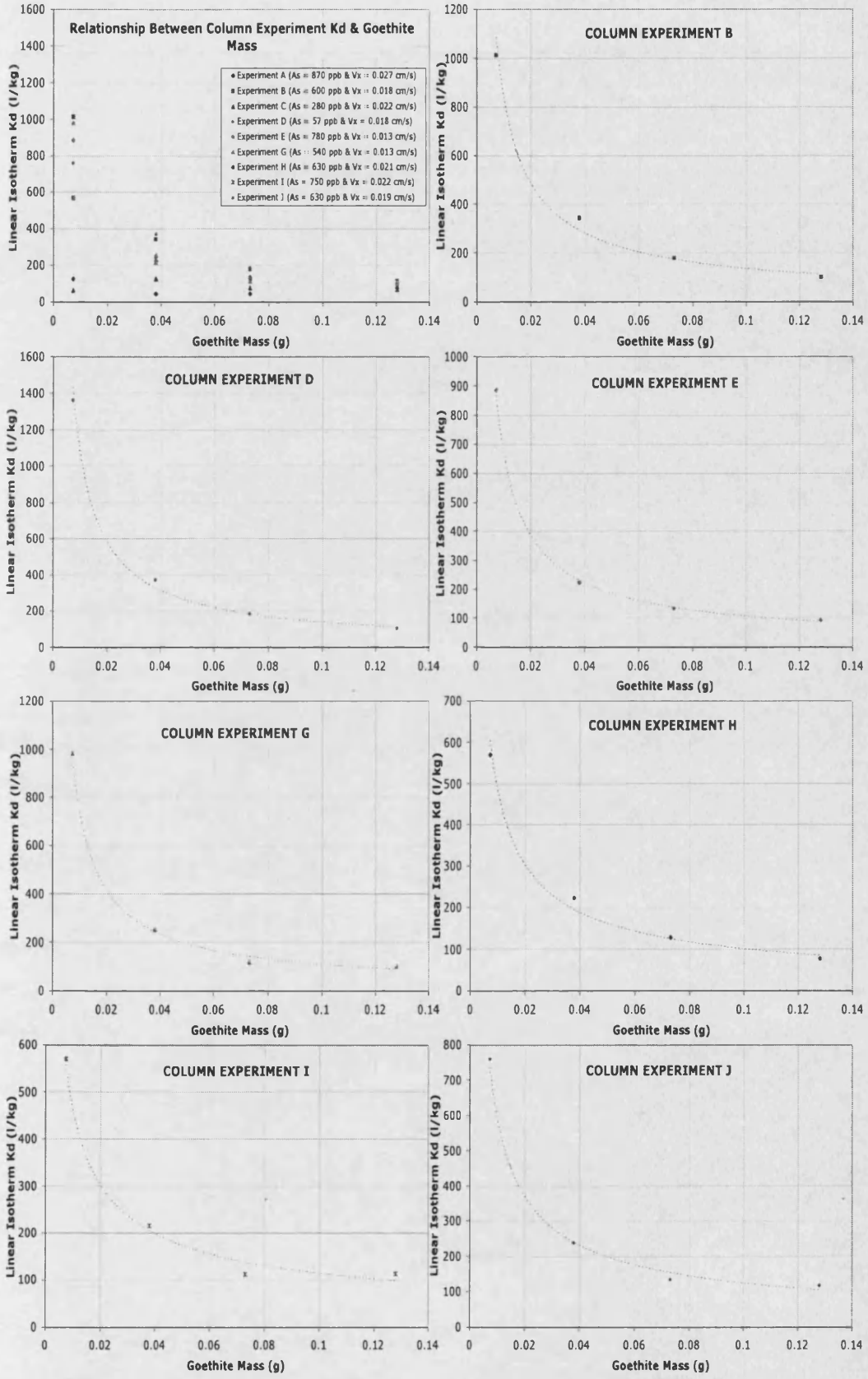

Figure 5.3.7. Illustration of the relationship between K_d (goethite corrected) and the mass of goethite within the column.

5.3.4. BIO1D MODEL FITTING – FREUNDLICH ISOTHERM

The BIO1D code was used also to fit BTCs to the experimental data incorporating the Freundlich isotherm adsorption term. All parameters for the simulations have been discussed in previous sections. The adsorption term, S(C) corresponds to the following Freundlich equation within the BIO1D code (Srinivasan & Mercer, 1987):

$$S(C) = [(K2\ n) / n_f]\ C^{n-1} = [(\rho_b\ K_f'\ n) / n_f]\ C^{n-1} \qquad \textit{Eqn. 5.3.7.}$$

$$\text{where} \quad K_f' = K2 / \rho_b$$

Where;

K2	**=**	**BIO1D Freundlich Isotherm Component**
n	**=**	**Freundlich exponent**
n_f	**=**	**Porosity (0.21)**
ρ_b	**=**	**Bulk Density of column material (g/cm³)**
C	**=**	**Solute concentration in pore fluid (g/cm³)**
K_f'	**=**	**Freundlich coefficient for column material (l/kg)**

Full experimental BTCs and the results simulated using the Freundlich isotherm are give in Appendix 5E. As an example, experiment I BTCs are shown in Figure 5.3.8. Table 5.3.6 summarises the Freundlich fitting parameter (K2) and the partition coefficient K_f for all simulated curves. As with the Linear K_d isotherm, the K_f values have been corrected to account for the proportion of goethite within the total bulk density (see Section 5.3.3). The 'n' exponent in the model was given a fixed value of 0.52, the average derived from the batch experiments over the pH range 5 – 7.

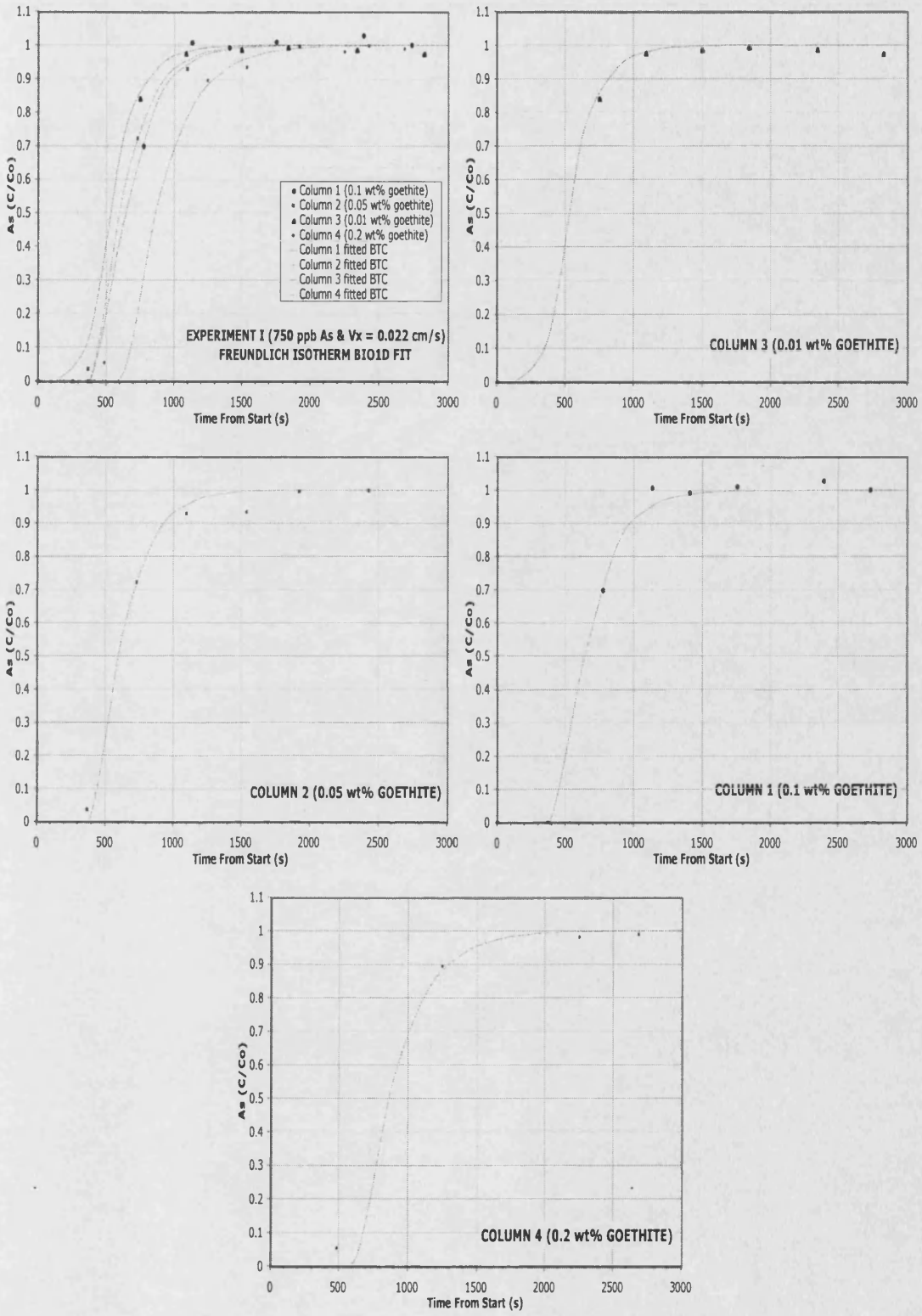

Figure 5.3.8. Experiment I breakthrough results and simulated BTCs using BIO1D and the Freundlich isotherm.

Table 5.3.7 summarises the difference between the BIO1D simulations and the experimental results for each column in terms of the mean difference over the entirety of the column experiment (Details are given in Appendix 5D). The degree of fit between simulations and the experimental data (Appendix 5F) does not vary significantly with flow velocity or arsenic concentration (Figures 5.3.9 and 5.3.10, respectively).

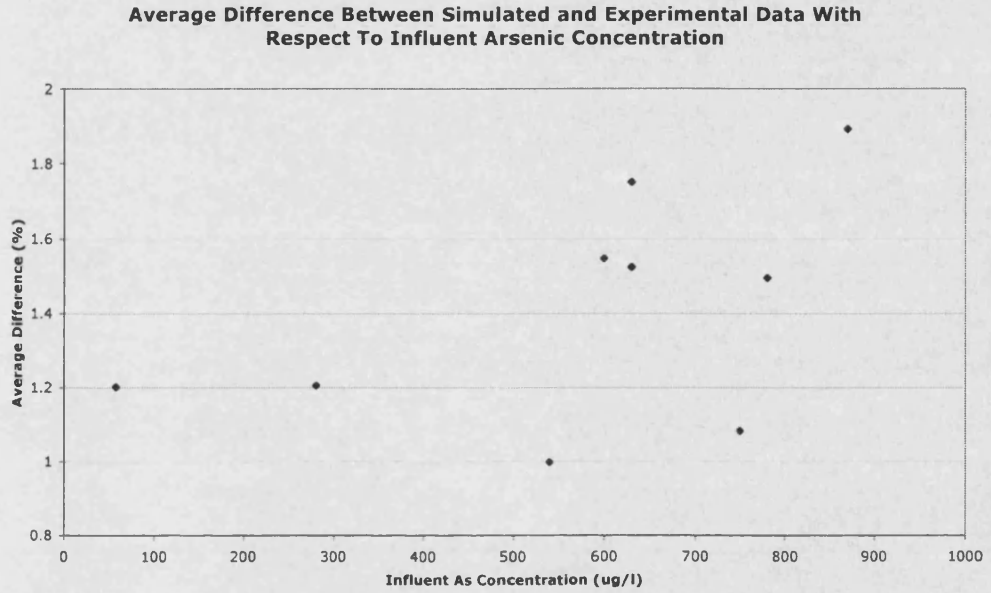

Figure 5.3.9. The 'goodness of fit' in terms of As concentration for the fitted BTCs, using the Freundlich adsorption term.

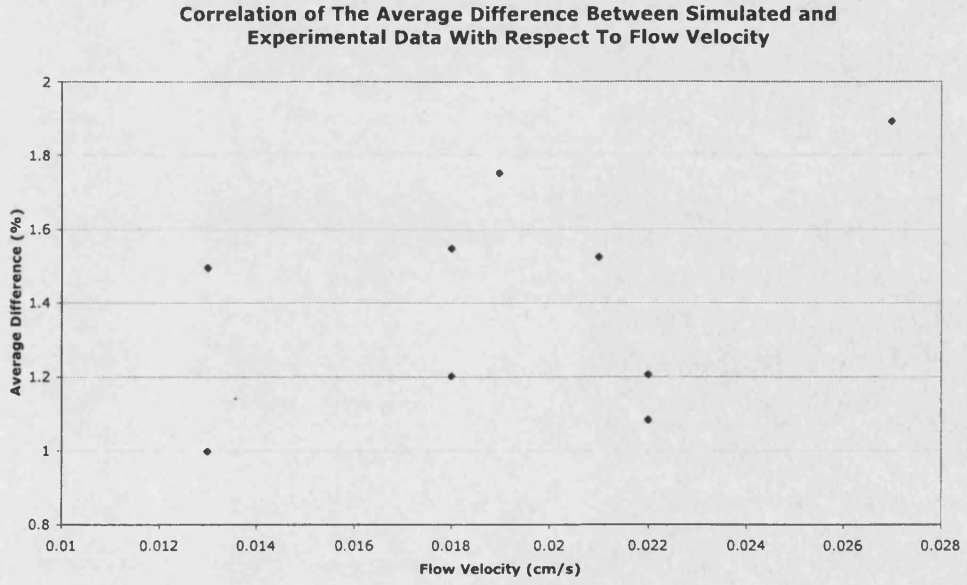

Figure 5.3.10. The 'goodness of fit' in terms of flow velocity (V_x) for the fitted BTCs, using the Freundlich adsorption term.

EXPERIMENT IDENTIFICATION	COLUMN IDENTIFICATION	BIO1D K2	BIO1D – Column Kf'	Goethite Kf ($l kg^{-1}$)
A (C_0 = 870 µg/l) V_x = 0.027 cm/s, D = 0.024 cm^2/s	1 (0.1 wt% goethite)	1.40	0.90	897
A	2 (0.05 wt%)	0.70	0.52	1045
A	3 (0.01 wt%)	0.50	0.32	3165
A	4 (0.2 wt%)	6.00	3.92	1961
B (C_0 = 600 µg/l) V_x = 0.018 cm/s, D = 0.016 cm^2/s	1	5.70	3.65	3654
B	2	4.50	3.36	6716
B	3	3.10	1.96	19620
B	4	6.60	4.31	2157
C (C_0 = 280 µg/l) V_x = 0.022 cm/s, D = 0.02 cm^2/s	1	1.60	1.03	1026
C	2	1.30	0.97	1940
C	3	0.10	0.06	633
C	4	4.20	2.75	1373
D (C_0 = 57 µg/l) V_x = 0.018 cm/s, D = 0.016 cm^2/s	1	1.90	1.22	1218
D	2	1.65	1.23	2463
D	3	1.45	0.92	9177
D	4	2.20	1.44	719
E (C_0 = 780 µg/l) V_x = 0.013 cm/s, D = 0.011 cm^2/s	1	4.90	3.14	3141
E	2	3.60	2.69	5373
E	3	3.00	1.90	18987
E	4	6.70	4.38	2190
G (C_0 = 540 µg/l) V_x = 0.013 cm/s, D = 0.011 cm^2/s	1	3.75	2.40	2404
G	2	3.40	2.54	5075
G	3	3.10	1.96	19620
G	4	6.20	4.05	2026
H (C_0 = 630 µg/l) V_x = 0.021 cm/s, D = 0.018 cm^2/s	1	4.13	2.65	2647
H	2	3.00	2.24	4478
H	3	1.90	1.20	12025
H	4	5.00	3.27	1634
I (C_0 = 750 µg/l) V_x = 0.022 cm/s, D = 0.02 cm^2/s	1	3.50	2.24	2244
I	2	3.22	2.40	4806
I	3	1.70	1.08	10759
I	4	7.00	4.58	2288
J (C_0 = 630 µg/l) V_x = 0.019 cm/s, D = 0.017 cm^2/s	1	4.20	2.69	2692
J	2	3.50	2.61	5224
J	3	2.50	1.58	15823
J	4	5.20	3.40	1699

Table 5.3.6. Freundlich parameters derived from the column experiments using BIO1D (n = 0.52).

EXPERIMENT IDENTITY	% DIFFERENCE (& R^2) COLUMN 1	% DIFFERENCE (& R^2) COLUMN 2	% DIFFERENCE (& R^2) COLUMN 3	% DIFFERENCE (& R^2) COLUMN 4
A	2.76 (0.9762)	0.91 (0.9946)	1.84 (0.9925)	2.06 (0.9856)
B	2.14 (0.9890)	1.08 (0.9969)	1.98 (0.9863)	0.99 (0.9989)
C	1.58 (0.9880)	1.65 (0.9881)	0.61 (0.9984)	0.98 (0.9985)
D	2.12 (0.9946)	0.78 (0.9992)	1.16 (0.9971)	0.75 (0.9995)
E	1.16 (0.9954)	1.94 (0.9933)	1.15 (0.9965)	1.73 (0.9942)
G	1.10 (0.9980)	1.00 (0.9983)	0.71 (0.9992)	1.17 (0.9990)
H	1.26 (0.9961)	1.80 (0.9910)	2.45 (0.9781)	0.58 (0.9987)
I	0.57 (0.9990)	1.27 (0.9964)	0.90 (0.9962)	1.59 (0.9907)
J	1.80 (0.9952)	2.13 (0.9913)	2.21 (0.9987)	0.87 (0.9987)

Table 5.3.7. Highlighting the differences between simulated and experimental breakthrough plots, in terms of % differences (in C/Co). R^2 = regression / correlation coefficients.

The relationship between K_f and flow velocity (V_x) is illustrated in Figure 5.3.11. This plot shows a weak inverse relationship between K_f and velocity. This trend is more strongly observed for those columns containing the least goethite. Figure 5.3.12 shows that the derived K_f values have no general relationship with the influent arsenic concentration. Section 5.3.5 discusses further the effect of flow velocity and influent As concentration. Another factor to consider is that the modelling was concerned only with adjustment of K_f and not the exponent n, which has been held constant throughout. The model may compensate for the K2 (modelling Freundlich component) value and give an over- or under-estimate of the true K_f value. For example, if the n value is too high or too low then K_f will be underestimated or overestimated, respectively (Appelo and Postma, 1994). Previously cited n parameters of 0.66 for ferric hydroxide and 0.78 for ferruginous manganese ore were derived by Thirunavukkarasu *et al.* (2003) and Chakravarty *et al.* (2002), respectively. These values suggest that an over-estimation of K_f may be expected. The relationship between K_f and goethite mass can be represented by an inverse power relationship with an average power exponent of –0.73, almost identical to that for the Linear K_d (Figure 5.3.13).

In general the relationship between K_f and the goethite mass (m) is described as:

$$K_f = \alpha(V_x, C_0)m^{-\beta(V_x, C_0)} \qquad \textit{Eqn. 5.3.8.}$$

$$\beta(V_x, C_0) \sim 0.73$$

Where α and β are coefficients that are determined by both the flow velocity (V_x) and the arsenic concentration (C_0) (Appendix 5G).

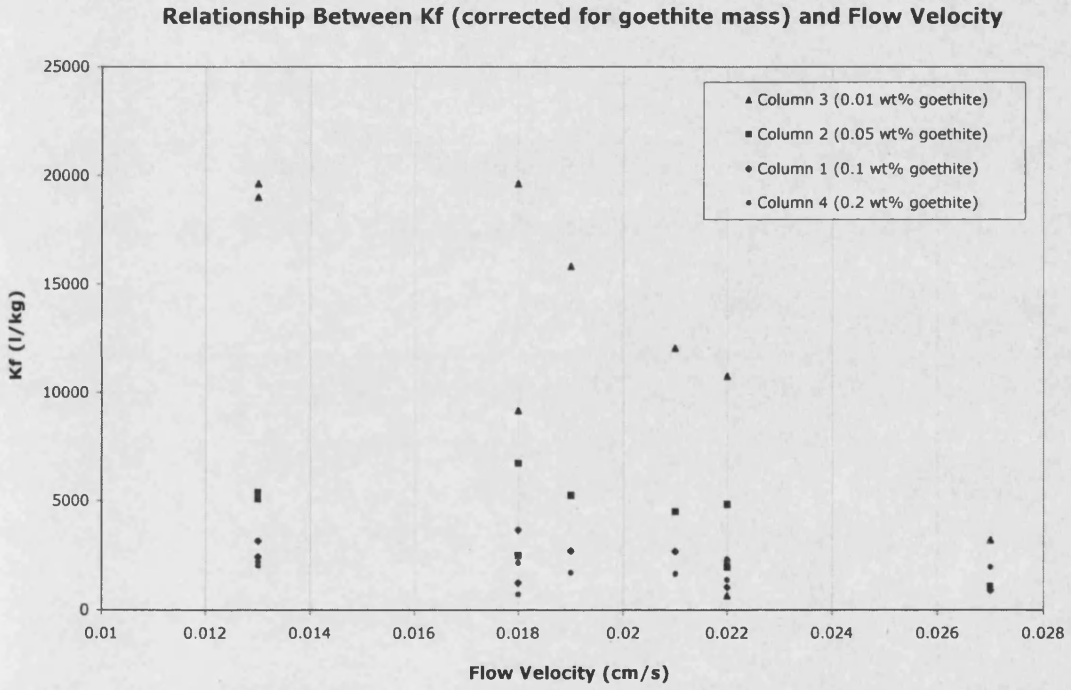

Figure 5.3.11. Relationship between K_f and the experimental flow velocity (V_x), for the individual columns containing different goethite mass.

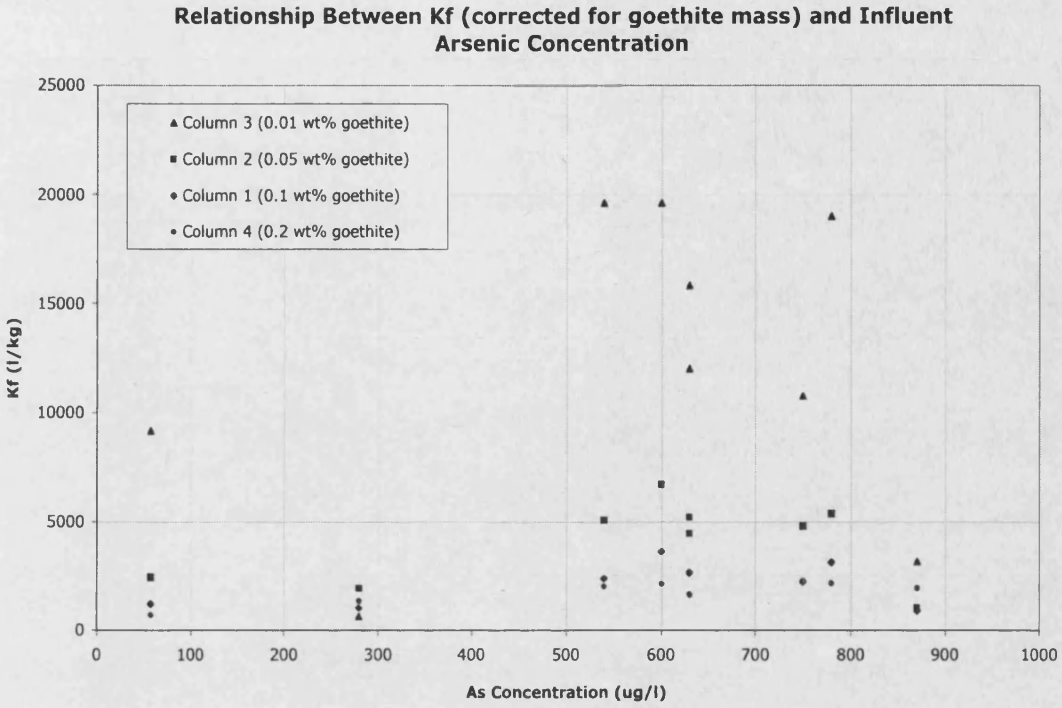

Figure 5.3.12. Relationship between K_f and the influent As concentration, for the individual columns containing different goethite mass.

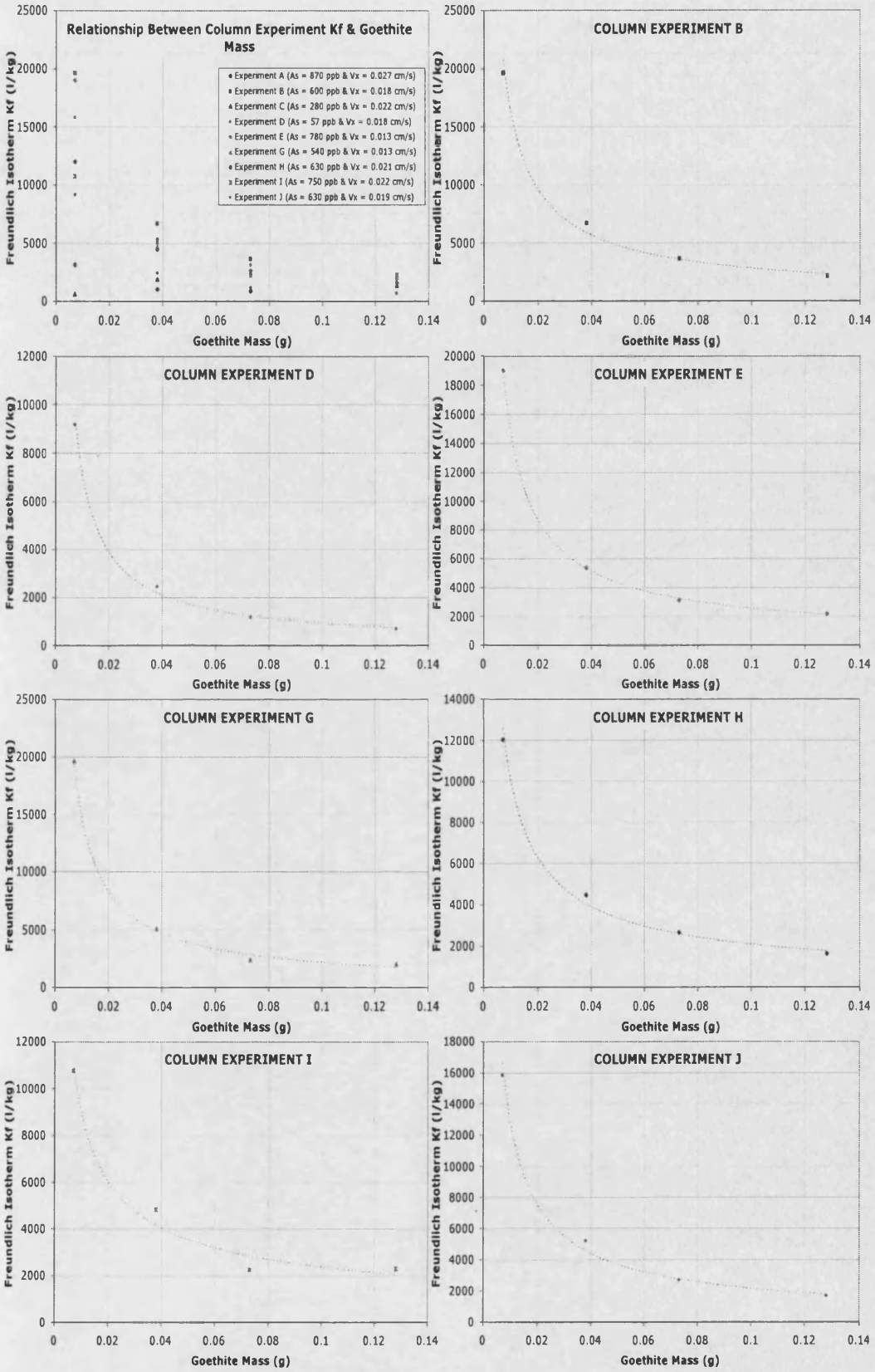

Figure 5.3.13. The relationship between the Freundlich K_f value and the goethite mass present within the column.

5.3.5. BIO1D RESULTS – Focus on Flow Velocity and Influent Concentration

It is possible to identify trends between the adsorption isotherm parameters and experimental flow velocity and arsenic concentration without interference from other experimental variables.

5.3.5.1. Flow Velocity Relationship

Two experiment groups were compared ({B,J,H} and {E,I}). Within each of these groups the influent arsenic concentration was constant with flow velocity the only variable. Table 5.3.8 summarises the Linear K_d and Freundlich K_f for the experiments, and the results are investigated in Figures 5.3.14 and 5.3.15.

EXPERIMENT & COLUMN IDENTITY	FLOW VELOCITY (V_x) cm/s	Linear K_d (l/kg)		Freundlich K_f (l/kg)	
B1	0.018	179	(3)	3654	(3)
J1	0.019	135	(2)	6716	(2)
H1	0.021	128	(1)	2647	(1)
B2	0.018	343	(3)	6716	(3)
J2	0.019	239	(1)	5224	(2)
H2	0.021	224	(2)	4478	(1)
B3	0.018	1013	(3)	19620	(3)
J3	0.019	759	(2)	15823	(2)
H3	0.021	570	(1)	12025	(1)
B4	0.018	101	(2)	2157	(3)
J4	0.019	118	(3)	1699	(2)
H4	0.021	78	(1)	1634	(1)
E1	0.013	135	(2)	3141	(2)
I1	0.022	112	(1)	2244	(1)
E2	0.013	224	(2)	5373	(2)
I2	0.022	216	(1)	4806	(1)
E3	0.013	886	(2)	18987	(2)
I3	0.022	570	(1)	10759	(1)
E4	0.013	92	(1)	2190	(1)
I4	0.022	114	(2)	2288	(2)

Table 5.3.8. Relationship between interpreted isotherm parameters and experimental flow velocity (V_x). The number in brackets shows the order of increasing partition coefficient.

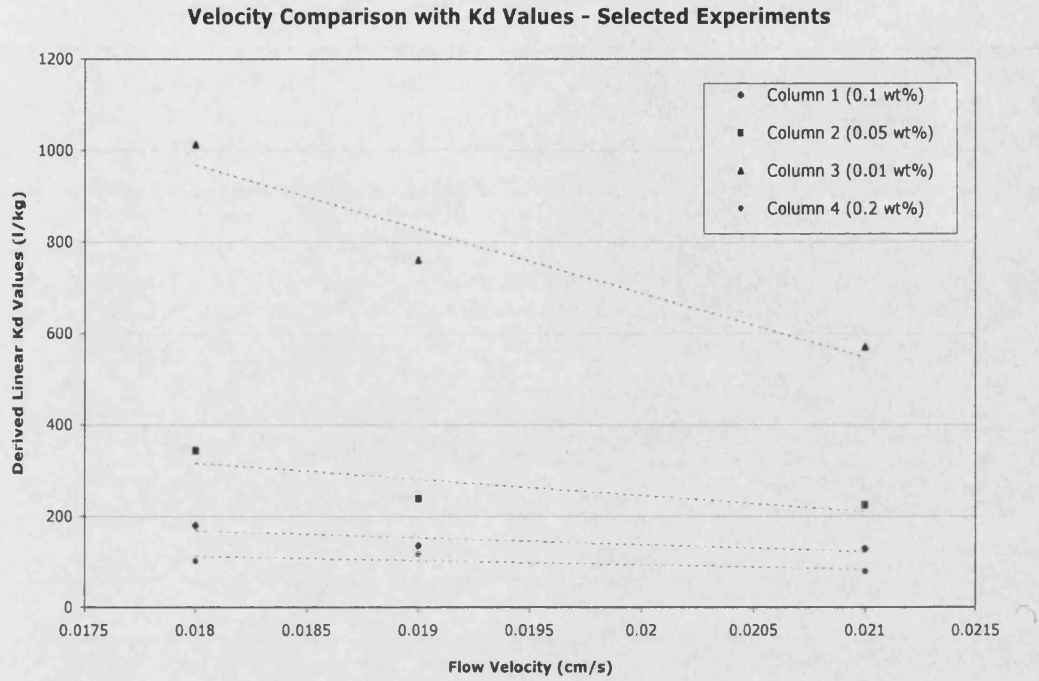

Figure 5.3.14. Linear partition coefficient (K_d) relationship with experimental flow velocity (V_x).

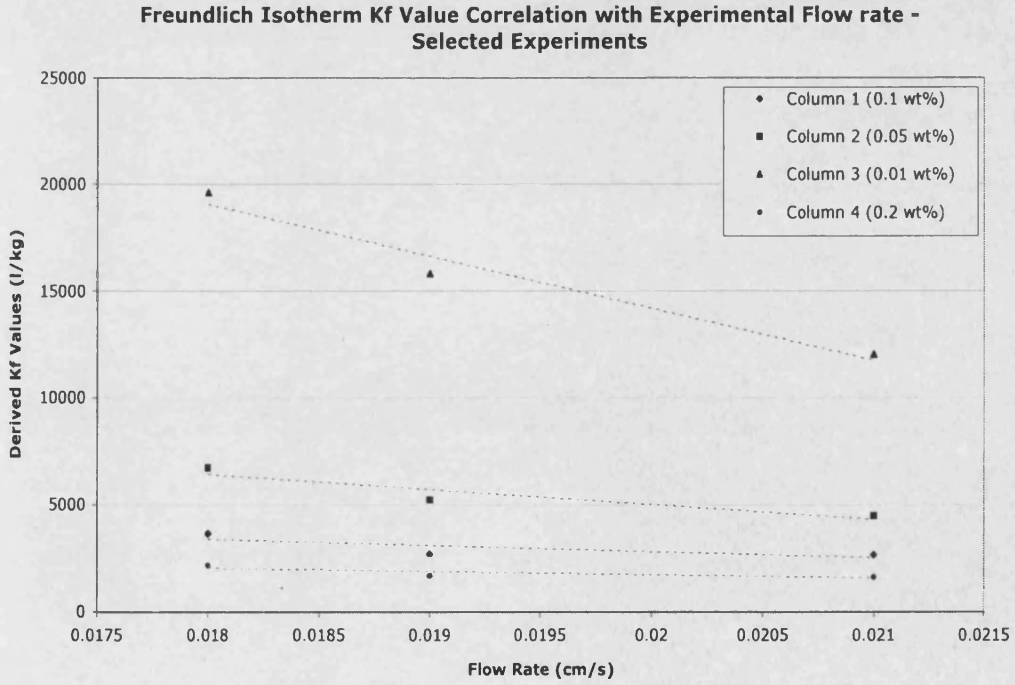

Figure 5.3.15. Freundlich coefficient (K_f) correlation with experimental flow velocity (V_x).

An inverse relationship exists between the flow velocity and K_d and K_f values. The Freundlich isotherm description has a marginally stronger relationship with the flow velocity than the Linear isotherm. In general the relationship between the partition coefficient (K_d or K_f) and the flow velocity (V_x) may be described approximately as:

$$K_d = \varepsilon(m)V_x + \phi(m) \qquad \textit{Eqn. 5.3.9.}$$

$$K_f = \gamma(m)V_x + \eta(m) \qquad \textit{Eqn. 5.3.10.}$$

Where ε, ϕ, γ, η are coefficients determined by the goethite mass (m).

The variation of isotherm parameter with respect to flow velocity suggests that kinetic effects are influential. For faster flow the adsorption of arsenic may be inhibited by reduced contact time and hence give lower derived isotherm adsorption coefficients. In addition, variations in the partition coefficients could result from variation in and multiplicity of flow paths. Under different flow rates different intergranular flow paths may be taken, and therefore, change the effective porosity of the column fill.

The variation in partition coefficient may reflect a change to the effective porosity of the column fill as the fluid velocity increases. Table 5.3.2 (Section 5.3) summarised the resulting effective porosity observed for the column experiments at different flow velocity. Figure 5.3.16 shows the relationship between the effective porosity and the flow velocities. This shows an almost constant effective porosity for the majority of flow velocities measured, but a sudden increase in effective porosity at the greatest flow. This suggests that there may be a capillary pressure barrier that is only overcome at high velocity. Therefore, the partition coefficients derived do not reflect changes to the effective porosity, which would result in an inverse trend. This lends support to the theory of kinetics affecting the partition coefficients during these experiments.

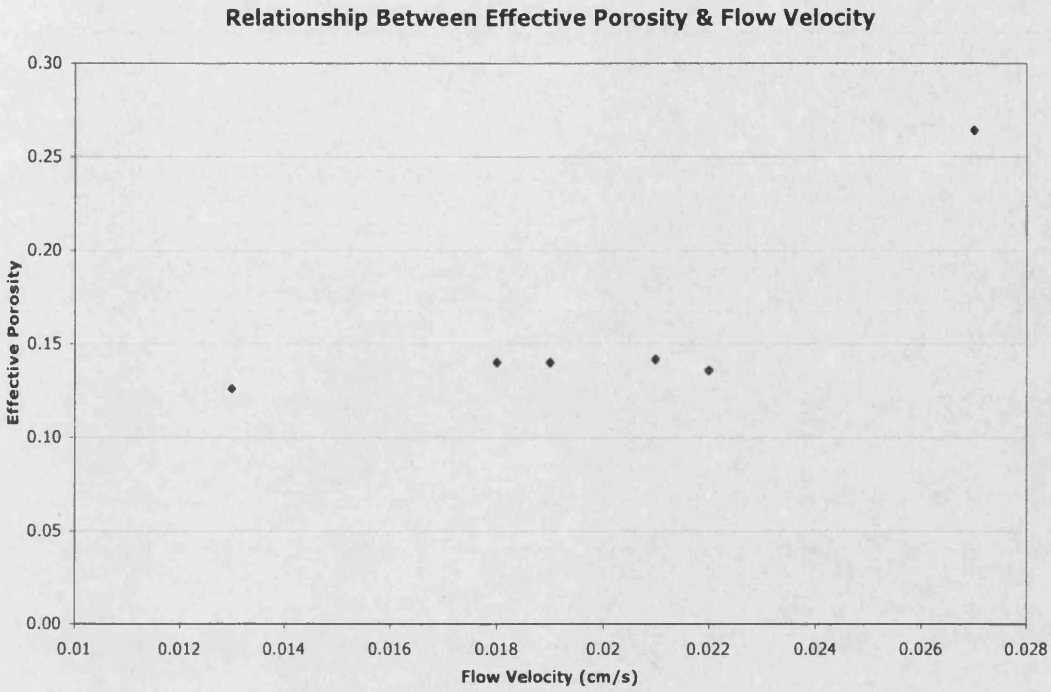

Figure 5.3.16. Illustration of the change in effective porosity (n_e) with increasing flow velocity.

5.3.5.2. *Arsenic Concentration Relationship*

The concentration of arsenic present within a solution and its relationship to the Linear and Freundlich isotherm coefficients is summarised in Table 5.3.9. Experiment groups {G,E}, {D,B}, and {C,I}, are used in the comparison. Each group has its flow velocity held as a constant but with different influent arsenic concentrations.

EXPERIMENT & COLUMN IDENTITY	As Solution Concentration (µg/l)	Linear K_d (l/kg)		Freundlich K_f (l/kg)	
G1	540	119	(1)	2409	(1)
E1	780	135	(2)	3141	(2)
G2	540	254	(2)	5075	(1)
E2	780	224	(1)	5373	(2)
G3	540	981	(2)	19620	(2)
E3	780	886	(1)	18987	(1)
G4	540	101	(2)	2026	(1)
E4	780	92	(1)	2190	(2)
D1	57	186	(2)	1218	(1)
B1	600	179	(1)	3654	(2)
D2	57	373	(2)	2463	(1)
B2	600	343	(1)	6716	(2)
D3	57	1361	(2)	9177	(1)
B3	600	1013	(1)	19620	(2)
D4	57	105	(2)	719	(1)
B4	600	101	(1)	2157	(2)
C1	280	77	(1)	1026	(1)
I1	500	112	(2)	2244	(2)
C2	280	127	(1)	1940	(1)
I2	500	216	(2)	4806	(2)
C3	280	63	(1)	633	(1)
I3	500	570	(2)	10759	(2)
C4	280	69	(1)	1373	(1)
I4	500	114	(2)	2288	(2)

Table 5.3.9. Comparison between the interpreted adsorption isotherm coefficients and the influent arsenic concentration. The number in brackets shows the order of increasing partition coefficient.

While the linear K_d values show a general decrease with increasing As concentration, the Freundlich K_f values increase. This discrepancy could be due to the constant value of 'n' used for the BTC simulations. This may force the K_f value to account for the apparent arsenic partitioning.

5.4. BATCH AND COLUMN EXPERIMENT ISOTHERM MODEL CONCLUSIONS & APPLICABILITY

5.4.1. Comparison of Mono-Mineral Partition Descriptions

The batch experiment adsorption is defined by a non-linear adsorption isotherm. The fitting of non-linear isotherms to the experimental data is more favourable towards the Freundlich model than that of the Langmuir. This is highlighted by the more substantial relationships observed between the Freundlich isotherm parameters and solution pH, and also the visually better fit of the Freundlich isotherm in the graphical interpretation of the experimental data. There is no significant statistical difference between the Linear and Freundlich model goodness of fit to the column data, although the Freundlich isotherm may not be as well represented as only the K_f coefficient was allowed to vary.

Solution pH	K_d (l/kg) 0.0103 g/l goethite	K_d (l/kg) 0.0206 g/l goethite	K_d (l/kg) 0.0309 g/l goethite	K_d (l/kg) 0.0412 g/l goethite
4	18790	7186	6550	6562
5	17619	6179	5378	5862
6	14803	5911	4891	4912
7	12687	5365	3864	3905
8	10281	4806	3203	3025
9	9012	4217	2221	2643
10	8228	3576	1793	1858
11	7667	3142	1240	1670

Table 5.4.1. Summary of K_d values for batch experiments.

Appendix 5B summarises the fitted isotherm parameters for the Linear, Freundlich and Langmuir models, and Table 5.4.1 summarises the Linear isotherm fitted partition coefficients for all batch experiments. These are compared in Table 5.4.2 with the partition coefficients derived from published experiments where equilibrium experiments were used. The partition coefficients derived from the current batch experiments in Table 5.4.1 are

generally larger than those of Hingston *et al.* (1971) and Bowell (1994), but within the range of those found by Matis *et al.* (1999). By contrast the Pierce and Moore (1982) values are significantly larger than the current batch experiment values. This can be attributed to the amorphous character of the Hydrous Ferric Oxide (HFO) used in their study, which has different adsorption mechanisms for the disordered crystal structure. The Hingston *et al.* (1971) coefficient is within the range of those determined from the current column experiments and the value derived by Bowell (1994) is generally an order of magnitude larger than the column values. The lower partition coefficients for the column experiments are of interest and may be the result of limited contact between arsenic and goethite. The flowing nature of the influent arsenic solution may not pass through all pore spaces or channels and hence less surface contact with the goethite. The kinetic interaction associated with adsorption processes may also limit complete adsorption, as previously discussed. The partition coefficients shown for goethite in Table 5.4.2 are for a wide range of As concentrations, from 57 μg/l used in the current experiments to 100000 μgl^{-1} used in the Matis *et al.* (1999) work. The range of goethite mass concentrations lies between 0.0103 g/l and 25 g/l. The range of partition coefficients shown in the table does not, however, seem to relate to the magnitude of the concentrations or the mass studied.

The Freundlich exponent 'n' derived herein ranges from 0.46 to 0.86 compares with those found for granular ferric oxide (0.66) and ferruginous manganese ore (0.78) by Thirunavukkarasu *et al.* (2003) and Chakravarty *et al.* (2002), respectively.

Table 5.4.2 also shows partition coefficients derived for other common soil minerals. Quartz does not significantly adsorb arsenic and this is reflected in the low partition coefficient. Goethite partition coefficients reflect the relatively high affinity for As(V) adsorption, although other minerals such as ferruginous manganese ore, birnessite and amorphous and granular ferric oxide have a much greater sorption capacity.

REFERENCE	K_d (l/kg)	As(V) Concentration (µg/l)	Adsorbent Mineral or Material
Xu *et al.* (1988)	2	71	Quartz
Bowell (1994)	25	45	Hematite (Fe_2O_3)
Xu *et al.* (1988)	34	48	Hematite
Hingston *et al.* (1971)	133	16000	Gibbsite [$Al(OH)_3$]
Hingston *et al.* (1971)	192	4900	Goethite
Anderson *et al.* (1976)	520	1200	Alumina [α-Al_2O_3]
Xu *et al.* (1988)	760	3.8	Kaolinite [$Al_2Si_2O_5(OH)_4$]
Matis *et al.* (1999)	483 – 9603	50000 – 100000	Goethite (0.1 – 2 g/l)
Bowell (1994)	1000	2.7	Lepidicrocite [χ-FeOOH)
Bowell (1994)	1800	749	Goethite (25 g/l)
Chakravarty *et al.* (2002)	7870	40 – 125	Ferruginous Manganese Ore (0.6 – 8 g/l)
Driehaus *et al.* (1995)	57500	75	Birnessite [δ-MnO_2]
Pierce and Moore (1982)	37000 – 460000	32 – 850	Amorphous – HFO (0.0045 g/l)
Thirunavukkarasu *et al.* (2003)	10.3×10^9	18.5	Granular Ferric Hydroxide (2 g/l)
Aragon and Thomson (2002)	28000 – 528000	100 – 5000	Granular Ferric Oxide (0.3 – 15 g/l)
Smedley *et al.* (2000)	1.0		Sandy Loess from Argentina: Fe = 0.0003 g/l (max = 0.00116 g/l)
Kuhlmeier (1997)	0.26 – 3.3		Sandy & Clayey contaminated soils from Texas
Smith *et al.* (2002)	3500 – 62000		Soils from Northern New South Wales, Australia (Fe = 1.3-157 g/kg)
Baes and Sharp (1983)	1.9 – 18 (av. 6.7)		Californian Soils
De Brouwere *et al.* (2004)	14 – 4430		Uncontaminated soils, Fe-rich
BGS/MML (1999)	5 – 1000		Modelled - Bangladesh Holocene aquifer sediments Fe total = 0.0003 – 0.3 g/l (as HFO)
Goldberg (2002)	660	1500	Modelled – Constant Capacitance Model (Fe = 0.5 g/l)
Vaishya and Gupta (2002)	11000 – 17000	As(III): 500 – 2000	Modelled – Active Available Site & chemical reaction rate models Fe-oxide coated sand (Fe = 20 g/l)
Current Batch Experiments	**1240 – 19790**	**150 – 1500**	**Goethite (0.0103 – 0.0412 g/l)**
Current Column Experiments	**44 – 1360**	**57 – 870**	**Goethite (0.0982 – 1.724 g/l)**

Table 5.4.2. Comparison of linear partition coefficients from previous studies with current experimental values.

5.4.2. Introducing Real Environments

5.4.2.1. Comparison with Soil Partition Descriptions

The table (5.4.2) also shows the results of natural soil partitioning of low partition coefficients and this may reflect the relatively low adsorbent mass concentrations, such as 0.00116 g/l Fe for the Argentina sandy loess or 0.003 – 0.3 g/l Fe in the Bangladesh sediments, compared to equilibrium adsorption to mono-minerals. The partition coefficients derived for the Bangladesh aquifer sediment (BGS and MML, 1999) generally lie within the range of those for the current column experiments, and also have similar adsorbent mass concentrations. The results from the batch and column experiments do not equate as well with the soil coefficients derived by Smedley *et al.* (2000), Baes and Sharp (1983) and Kuhlmeier (1997), which are much smaller than those for the current goethite sorption. Partition coefficients derived from the De Brouwere *et al.* (2004), Smith *et al.* (2002), and BGS and MML (1999) studies concerning As sorption to soils, are more in line with the values derived from the current experiments using similar As concentrations and Fe mass.

A number of factors may relate to the lower soil K_d, such as the lower adsorbent mass concentration within the natural soils, and the effect of other soil-groundwater constituents on As(V) sorption. For example, the BGS and MML (1999) study of As sorption onto the Bangladesh sediment found that As partition coefficients were much lower when in the presence of phosphate, which acts as a competing ion for available sorption sites. By contrast, Smith *et al.* (2002) determined K_d values similar to those derived for amorphous iron oxides, and they are within the same orders of magnitude as those from the current batch experiments. The higher partition coefficient may be due to the high iron content of the soils and this may not have been completely accounted for in calculating the coefficient.

5.4.2.2. *Goethite Mass within Natural Sediments*

The proportion of iron mass used within the column material (0.006 – 0.13 wt% Fe) is comparable to that of typical sediments. Bowell (1994) found that soils from the Ashanti mine area in Ghana contained 0.04 – 0.26 % Fe. Soils from New South Wales, Australia, contain 0.5 – 16 % Fe (Smith *et al.*, 2002) and the Holocene Bangladesh sediments contain 0.2 % Fe (BGS AND MML, 1999). Partition coefficients derived by all of the above studies compare well with those determined from the current experiments and therefore lend support to the validity of the parameters described by the current experiments.

5.4.2.3. *Predictive Modelling of Partitioning*

In some studies adsorption was simulated using modelling techniques, such as the Constant Capacitance Model (CCM) (Goldberg, 2002) or the Diffuse Double Layer surface complexation model (DDL) of Dzombak and Morel (1990), which was used within the BGS and MML (1999) partition prediction. These examples predict partition coefficients that are within the range of those from the current experiments, and would suggest that such methods of describing partitioning provide good descriptions. A study by Appelo and Postma (1999) who applied the DDL model in parallel with the geochemical PHREEQC model (Parkhurst, 1995) gave an excellent description of cation adsorption onto birnessite (δ-MnO_2) within a column experiment. Good model fits were also identified by Miller (2004) using PHREEQC to determine arsenic partitioning.

The application of models to predict As(III) partition coefficients for sulphate modified iron-oxide coated sand (Vaishya and Gupta, 2002) are much larger than expected. Similarly, Kent *et al.* (1995) observed that the Dzombak and Morel model over-predicted partition coefficients describing natural sediments, mostly caused by neglecting the effect of ion competition and under-estimating the Fe content within the natural sediments.

5.4.2.4. Hydraulic Conductivity Comparison with Real Sediments

Table 5.4.3 shows examples of hydraulic conductivities within various aquifer sediments where elevated levels of arsenic are known to exist.

Reference	Aquifer	Hydraulic Conductivity, K (cm/s)
Ravenscroft *et al.* (2001)	Bangladesh Holocene sediments	0.047 – 0.093
Schwartz *et al.* (1998)	Costa-Rica fine soils	0.0014
Smedley *et al.* (2002)	Argentina, La Pampa Quaternary loess	0.001
Current Column Experiments	**Quartz sand & goethite**	**0.006 – 0.03**

Table 5.4.3. Comparison of aquifer hydraulic conductivity with the current column material.

Comparison of the hydraulic conductivity shows that the column material used in the current work was comparable to previously studied As-rich aquifer sediments. Therefore, given the inverse relationship between the partition coefficient and the flow velocity observed, a similar relationship may also exist between the partition coefficient and the hydraulic conductivity within such aquifers. Therefore the partition coefficients derived from the column experiments would be applicable to aquifers with similar hydraulic conductivities. Thus, proportionally smaller partition coefficients may be expected in the marginally higher K Bangladesh sediments, and in the lower K sediments slightly larger partition coefficients are expected. These comparisons, however, do not consider the hydraulic gradient within the aquifer systems, which may induce far greater or smaller flow rates than those implied from the column model, but do provide an excellent indication of expected adsorption.

5.5. REDOX COLUMN EXPERIMENT

5.5.1. Experimental Breakthrough Curves (BTCs)

5.5.1.1. Arsenic Effluent Curves

An introduction to the redox column procedure was given in Section 2.2. The current section interprets the results arising from a change of the redox environment within a column experiment. The organic reductant used was 'Catechol'. The objective was to derive a partition coefficient under anaerobic conditions. A general investigation of the solid-phase material using Scanning Electron Microscopy (SEM) techniques was used to illustrate some of the processes occurring during reduction. Appendix 4B shows the results of a similar reducing column experiment (A).

Arsenic partitioning under the altered experimental conditions requires an estimate of the arsenic budget. This budget incorporates the following time schedule and progressive calculations:

(1) As mass influent ($t_0 - t_1$) = Calculated from As solution pumped into the column
(2) As mass effluent ($t_0 - t_1$) = Area under adsorption BTC
(3) As mass held (sorbed & in solution) within column at t_1 = (1) – (2)
(4) As mass effluent in dissolved phase, after 1 pore volume (PV) flush ($t_1 - t_2$) = Calculated from area under 1PV effluent curve.
(5) As mass remaining adsorbed or released to solution at t_2 = (3) – (4)
(6) As mass desorbed under reducing conditions ($t_2 - t_3$) = Calculated from area under reduced phase effluent curve.

Where: t_0 = Start of the complete experiment, when As in pumped into the column
t_1 = Time at which As effluent solution $C/C_0 = 1$, and the start of the DDW pore water flush.
t_2 = Time after which one pore volume DDW has been flushed through the column, and the start of the reducing phase.
t_3 = Time at the full duration of the experiment, after the reducing phase.

These terms have been highlighted on the effluent curve (Figure 5.5.1) and show the arsenic concentration in the column effluent for the full duration of the experiment. Appendix 5H shows the corresponding effluent curves for all sampling ports although for the purpose of the following description of arsenic budgeting only the Port E effluent is considered as it was the most consistent for monitoring. At the completion of the reduction experiment the arsenic concentration in the column effluent did not reach background or detection levels but remained at 10 μg/l. This suggests the establishment of a new redox equilibrium. Table 5.5.1 shows the calculation of each As mass budget term over the duration of the experiment.

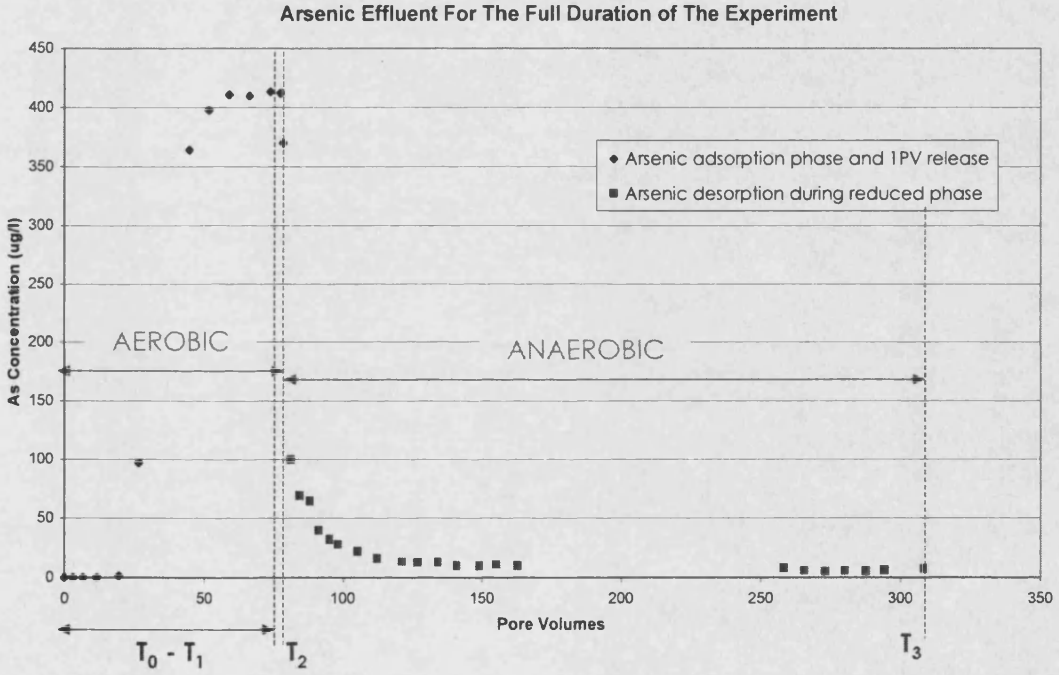

Figure 5.5.1. Effluent arsenic concentrations for the full duration of the experiment.

TERM		As MASS BUDGET (mg)
(1) As influent ($t_0 - t_1$)	(aerobic)	1.0601
(2) As effluent ($t_0 - t_1$)	(aerobic)	0.6604
(3) As held in column ($t_0 - t_1$)	(aerobic)	0.3997
(4) As effluent dissolved phase ($t_1 - t_2$)	(aerobic)	0.0160
(5) As adsorbed (t_2)	(aerobic)	0.3837
(6) As desorbed ($t_2 - t_3$)	(anaerobic)	0.1409
(7) As mass remaining sorbed (t_3)	(anaerobic)	0.2428

Table 5.5.1. Arsenic budget for the full duration of the experiment.

The integration required to determine areas at the various stages of the experimental effluent curve (Figure 5.5.1) is conveniently calculated using Simpson's Rule (Bostock and Chandler, 1993):

$$I = {}^1/_3\, d\, [\{y_0 + y_n\} + 4\{y_1 + y_3 + \ldots\} + 2\{y_2 + y_4 + \ldots.\}] \qquad \textit{Eqn. 5.5.1.}$$

Where: I = **Integrated area under the curve between x_0 and x_n (x_0 is the first point and x_n the final point along the x-axis).**
d = **Distance between uniform points x_0 and x_1**
y_m = **Corresponding value on y-axis for x_m.**

5.5.1.2. Effluent pH and Redox Potential, Eh

Figures 5.5.2 and 5.5.3 show the pH and Eh of the column effluent during the reducing phase of the experiment. As the experiment progressed the effluent pH decreased quasi-linearly from approximately 6.9 to 5.65, and the Eh increased non-linearly from approximately 104 to 212 mV. This increase may suggest that the influent solution has become contaminated with oxygen despite the care taken to minimise air ingress. Alternatively, it is possible that the catechol was exhausted by the reaction with the goethite in the column sediment. However, the Eh measurements should not be relied upon too heavily as the instrument of measurement used was not accurate and the measurement of effluent Eh was taken under aerobic conditions. The redox measurement is further complicated as the system is in disequilibrium and therefore a single redox potential cannot be accurately assigned to a particular redox species (Nordstrom and Wilde, 1998). Also, the presence of more than one redox element (Fe and As) within the system may obscure an individual Eh measurement and therefore under these dynamic conditions a single measurement may not be entirely representative (Nordstrom and Wilde, 1998).

Taking into account the difficulties associated with the redox measurements the actual species of arsenic and iron present cannot be accurately confirmed without further speciation analyses. A tentative suggestion as to the possible

species present has been made using the redox diagrams (Sections 1.4 and 1.5), although this must only be considered as a suggested speciation. The arsenic in the effluent throughout the reducing experiment was on the boundary between the As(V) acid species and the As(III) acid species (Section 1.4, Figure 1.4.1). The release of the acid series into solution may promote the apparent decrease in effluent pH. Therefore during the course of the anaerobic experiment the arsenic in solution is probably a mixture of As(V) and As(III), and the desorption of arsenic from the goethite is a consequence of both arsenic and iron reduction.

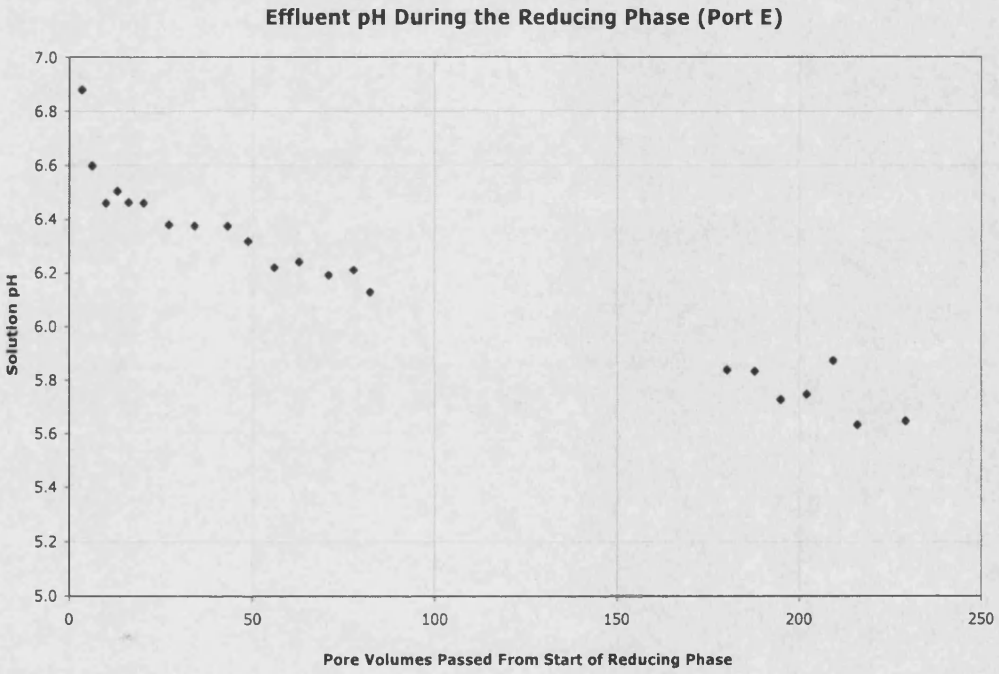

Figure 5.5.2. The effluent (port E) solution pH during the course of the reducing experiment.

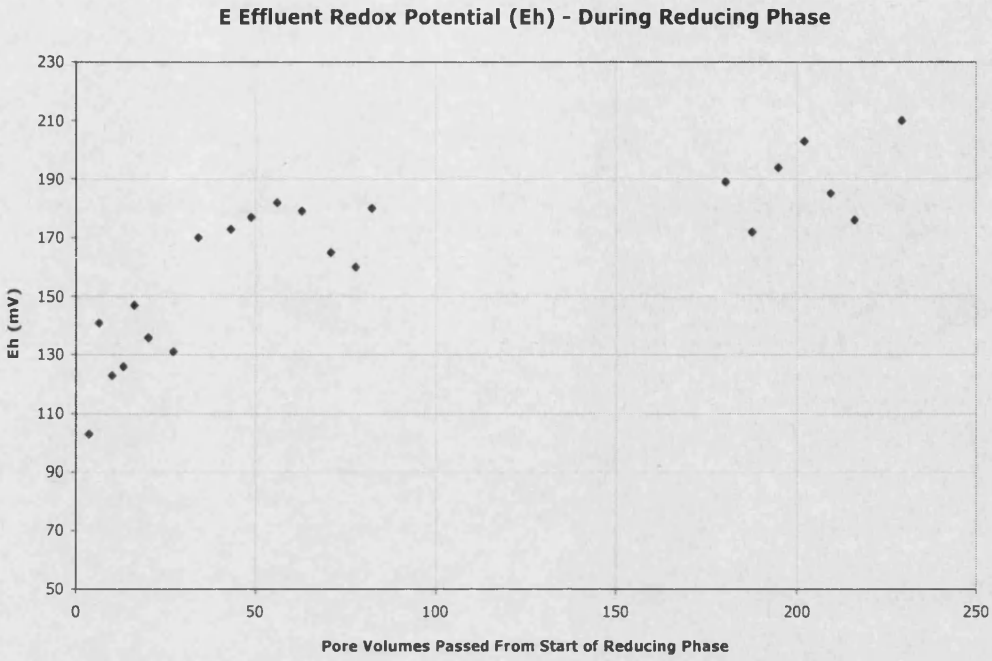

Figure 5.5.3. Redox potential (Eh) of the effluent solution during redox experiment 1.

5.5.1.3. Iron Effluent Curve

In considering the mechanism for arsenic release the dissolution of the solid-phase goethite must also be considered. Figure 5.5.4 shows the iron concentration determined from the column effluent during the reducing phase. This curve indicates that an initial high mass of iron is released into solution and the concentration thereafter decreases towards a long-term equilibrium value of 290 μg/l as the experiment continues to its full duration. This also suggests that a new equilibrium environment was achieved. With the use of the Eh-pH diagram for the Fe-O-C system (Section 1.4, Figure 1.4.4) the movement of iron species can be implied. However, it is important to note that there are limitations and difficulties relating to the measurement of redox potential. For example, the presence of mixed couples within the system could result in mixed Eh values that do not represent the true system. Also, the system is in disequilibrium and therefore it is difficult to assign the redox potential to the relevant redox species (Nordstrom and Wilde, 1998). At the start of the

reducing experiment the iron in the column effluent is in the oxidised form (Fe(III)) and as the experiment continues, the iron changes to the reduced form (Fe(II)). The Eh-pH relationships alone therefore suggest that arsenic in this experiment is released by both reductive dissolution of goethite and reduction of arsenic. The reduction of iron species within goethite by catechol has also been observed by Pracht *et al.* (2001) and Yoshida and Nakoshima (2000). Further evidence for this is described later in Section 5.5.2. The slow steady release of Fe(II) was also observed by Haury (2001) in column experiments similar to the current study (Figure 5.5.5). Haury (2001) attributes the overall release of arsenic from goethite to arsenic reduction at the iron hydroxide surfaces and to solid-phase reductive dissolution.

Figure 5.5.4 also shows a minor peak of iron concentration in the column effluent at about 65-70 pore volumes during the reducing phase, and comparison with the Eh variations (Figure 5.5.3) demonstrate that this corresponds to a minor decrease in the Eh. The slight change towards more reducing conditions encourages further reductive dissolution of iron. The iron effluent variation observed by Haury (2001) (Figure 5.5.5) also shows small perturbations in the solution concentration, but relate more closely to the variations in the effluent pH, which suggests that some iron reduction and dissolution occurs. The small dips in aqueous iron in the effluent solution may result from the formation of a secondary phase. Although SEM images taken after the reduction stage do not show evidence for this (Figure 5.5.8). It may also be possible that these dips represent periods where iron is re-incorporated into the goethite structure and this could be confirmed using geochemical or atomic-scale models. This could arise with reduction of sorbed arsenic and subsequent electron transfer from iron to arsenic resulting in oxidation of Fe(II) and re-sorption of Fe(III). This is a more likely reason for the apparent decline in released iron and was also observed in some previously published work (Stollenwerk, 2003).

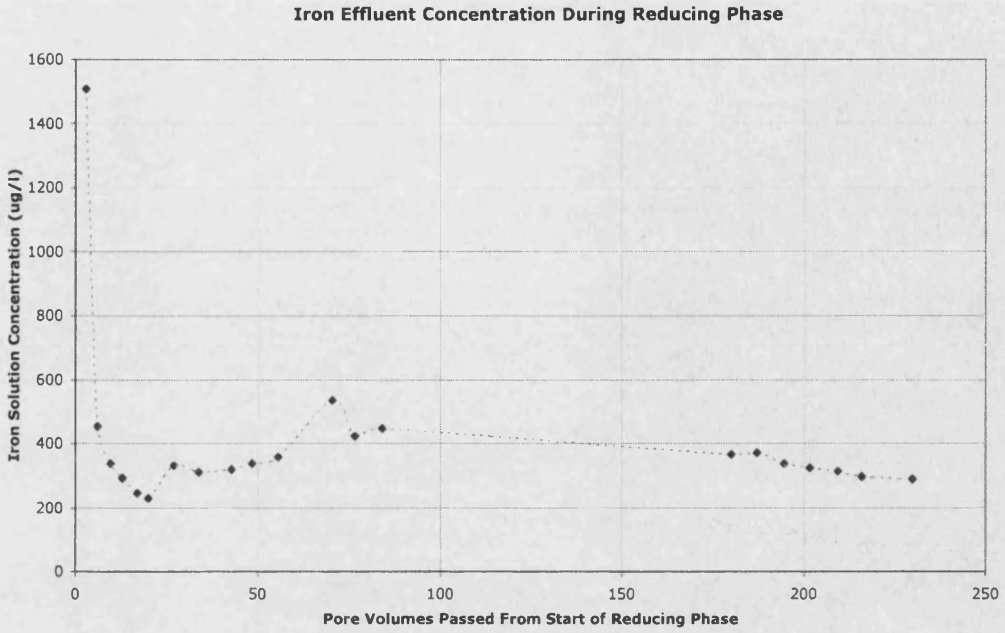

Figure 5.5.4. Iron released after the introduction of catechol, during the anaerobic phase.

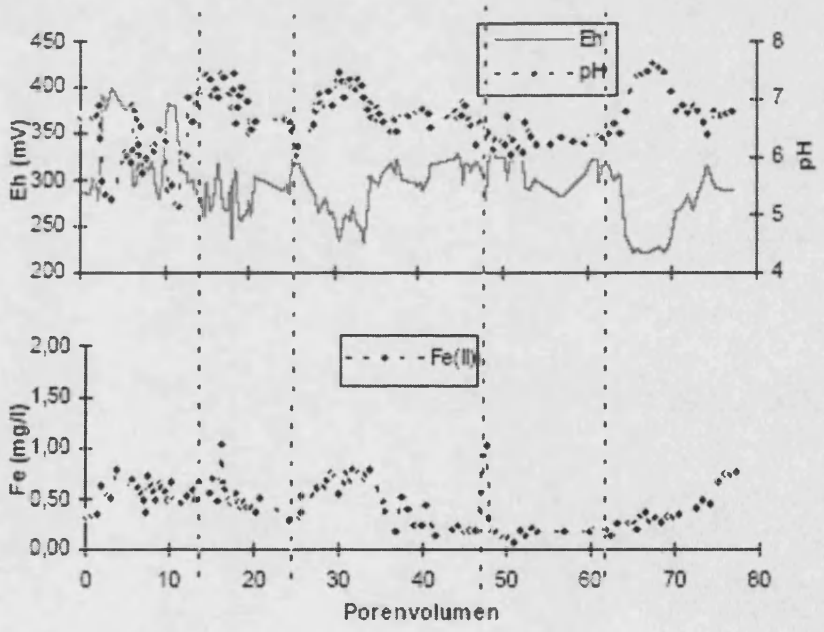

Figure 5.5.5. Iron release and the Eh and pH in the effluent of reducing column experiments with respect to pore volumes passed through the column. Taken from Haury (2001).

As goethite is dissolved during the progress of the experiment, it must be accounted for in the final determination of arsenic partitioning. Therefore an iron mass budget was calculated to account for the mass of goethite released during reduction. The results show that 0.32 g of Fe was released during the reducing phase. this corresponds to 55 % of the original iron mass (0.58 g of Fe within 0.92 g goethite) in the column sediment.

Although iron release had not ceased on completion of the experiment, the mass released during the reducing phase corresponds to similar proportions of iron reduction observed by Pracht *et al.* (2000). Pracht *et al.* (2000) found that for 10 μmol catechol solution 50-60 μmol Fe(III) was reduced. The present experiment used approximately 1000 μmol catechol and initially 10000 μmol of Fe(III) in goethite. Reduction was approximately half this amount on completion of the experiment, which closely corresponds to the relative proportions observed by Pracht *et al.* (2000).

5.5.2. Investigation of The Solid Phase

Microscopic methods were employed to observe physical changes in the solid phase material as a consequence of reduction. High magnification, good resolution photographs using a Phillips SEM aided the inspection of column material pre- and post-reduction. Figure 5.5.6 shows the column material before reduction. The large grains (~ 3 μm x 3 μm) are quartz and the acicular goethite crystals (~ 0.25 μm x 1.5 μm) are interspersed between them.

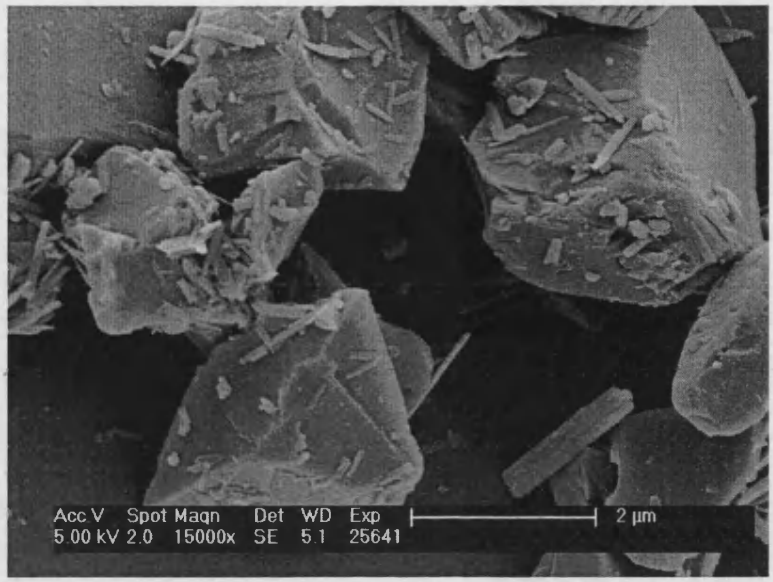

Figure 5.5.6. The column material before reduction.

Figure 5.5.7 shows a pre-reduction image of column material at a greater magnification to illustrate the relative abundance of goethite. This is compared with a similar image taken post-reduction (Figure 5.5.8).

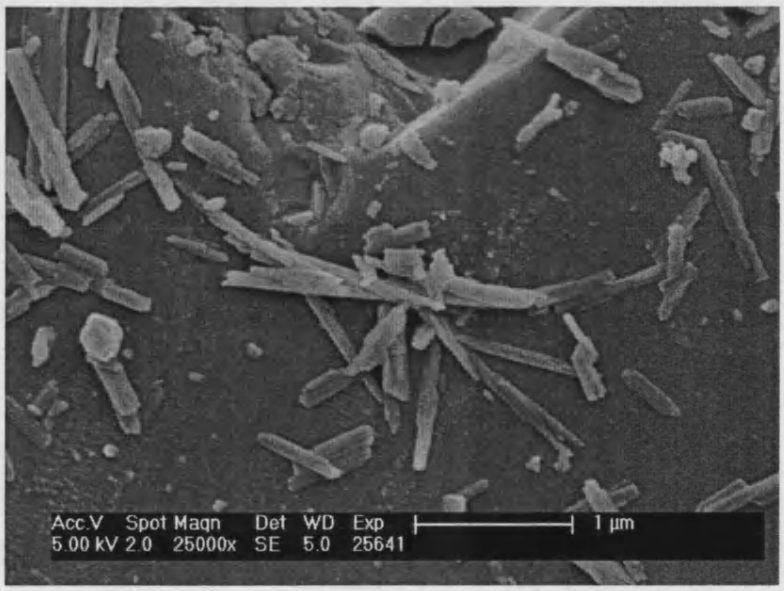

Figure 5.5.7. The column material before reduction at greater magnification.

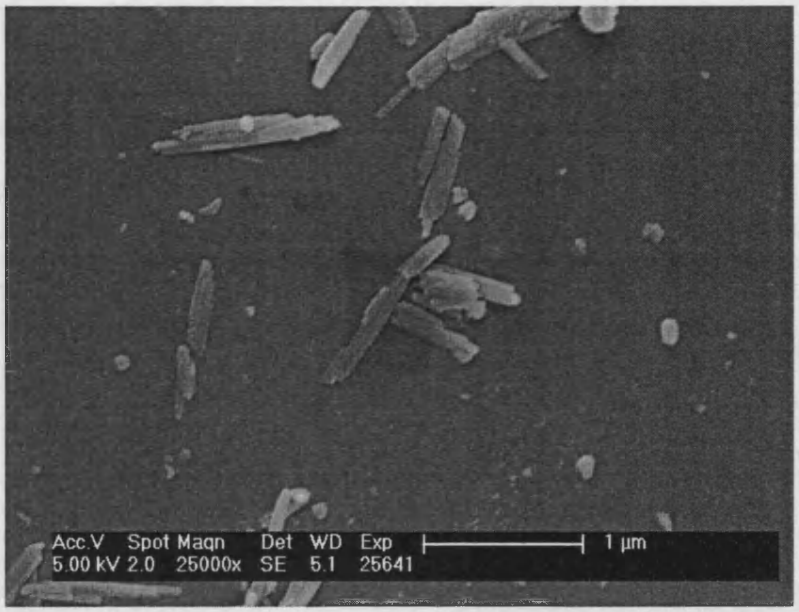

Figure 5.5.8. Column material after reduction.

The images do not quantitatively prove the decline of solid phase goethite resulting from reductive dissolution. However, they are illustrative of the Fe budgeting which demonstrated that in excess of 50 % of goethite was dissolved and also that dissolution was incomplete.

The JEOL SEM is able to scan small areas (10 x 10 µm) and perform spectral elemental analysis within that area to provide a tentative assessment of the presence of arsenic and iron before and after reduction. Examples of JEOL SEM images and spectra are shown in Figure 5.5.9 where typical clusters of goethite within the column material after the adsorption of arsenic but before reduction is shown. The corresponding elemental spectrum highlights the presence of silica within the underlying quartz particles, iron from the goethite on the particle surface and also the presence of small quantities of arsenic.

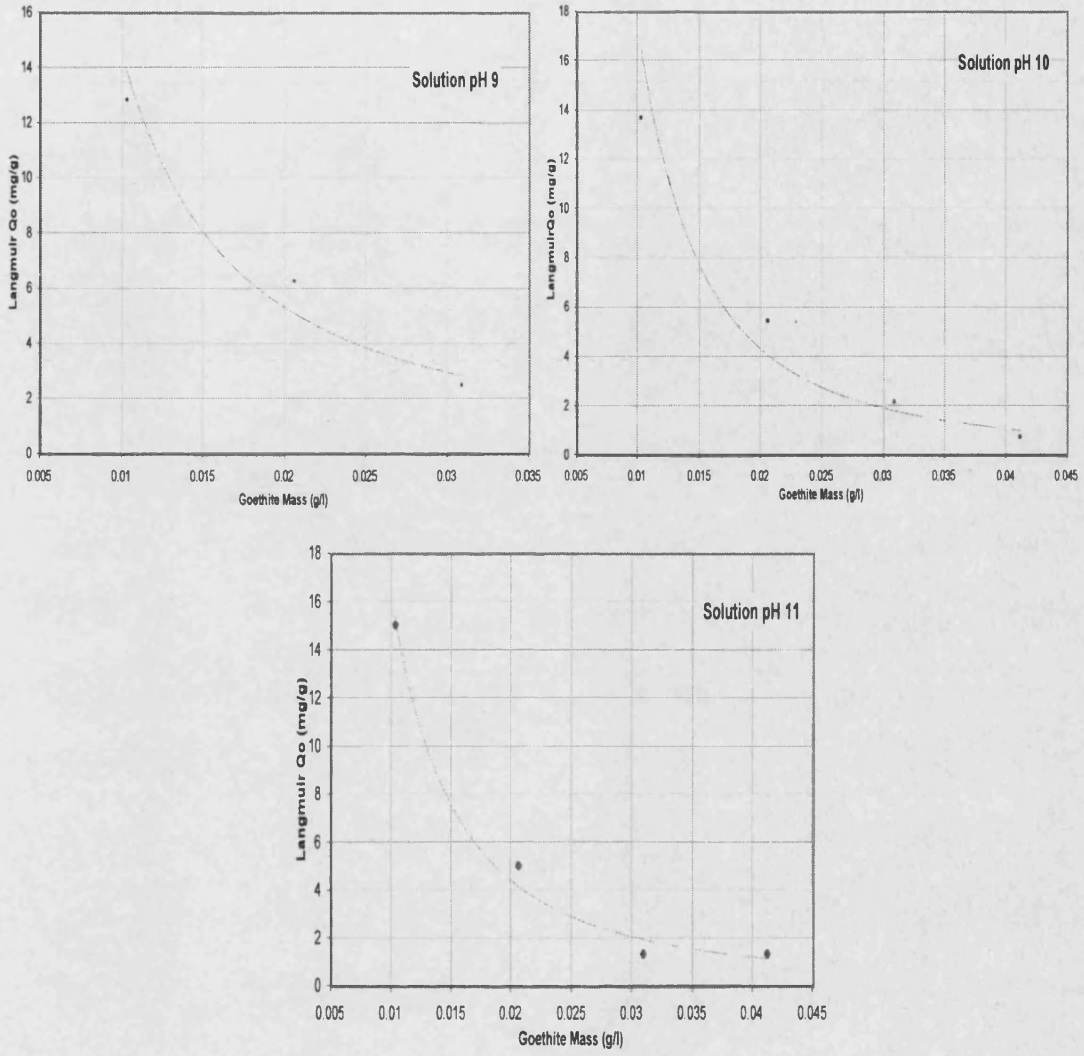

Figure 5.2.17b. The relationship between the batch experiment derived Langmuir Q_0 and the mass of goethite present within the experiment. Solution pH 9 – 11.

In comparing the correlation determinants (mean squared difference) between the Freundlich and Langmuir isotherm parameters (Tables 5.2.1 and 5.2.3) it is seen that both the Freundlich and Langmuir isotherm models are viable fits for the experimental data. However, the less well defined relationship between K_l and Q_o and solution pH may result from the poor suitability of the Langmuir model for the batch experiment data. Also, the inverse relationship between the maximum number of adsorption sites (Q_o) and goethite mass (Figure 5.2.17) is not easily defined and may result from the misuse of the Langmuir model.

5.2.3. The Linear Isotherm

Having explored the Freundlich and Langmuir isotherms as descriptive models for the batch data a linear isotherm model is included for comparison.

The data for all batch experiments were fitted to linear functions and given in Appendix 5A. The gradients of the linear function with zero as origin equates to the value of K_d (Figure 5.2.18).

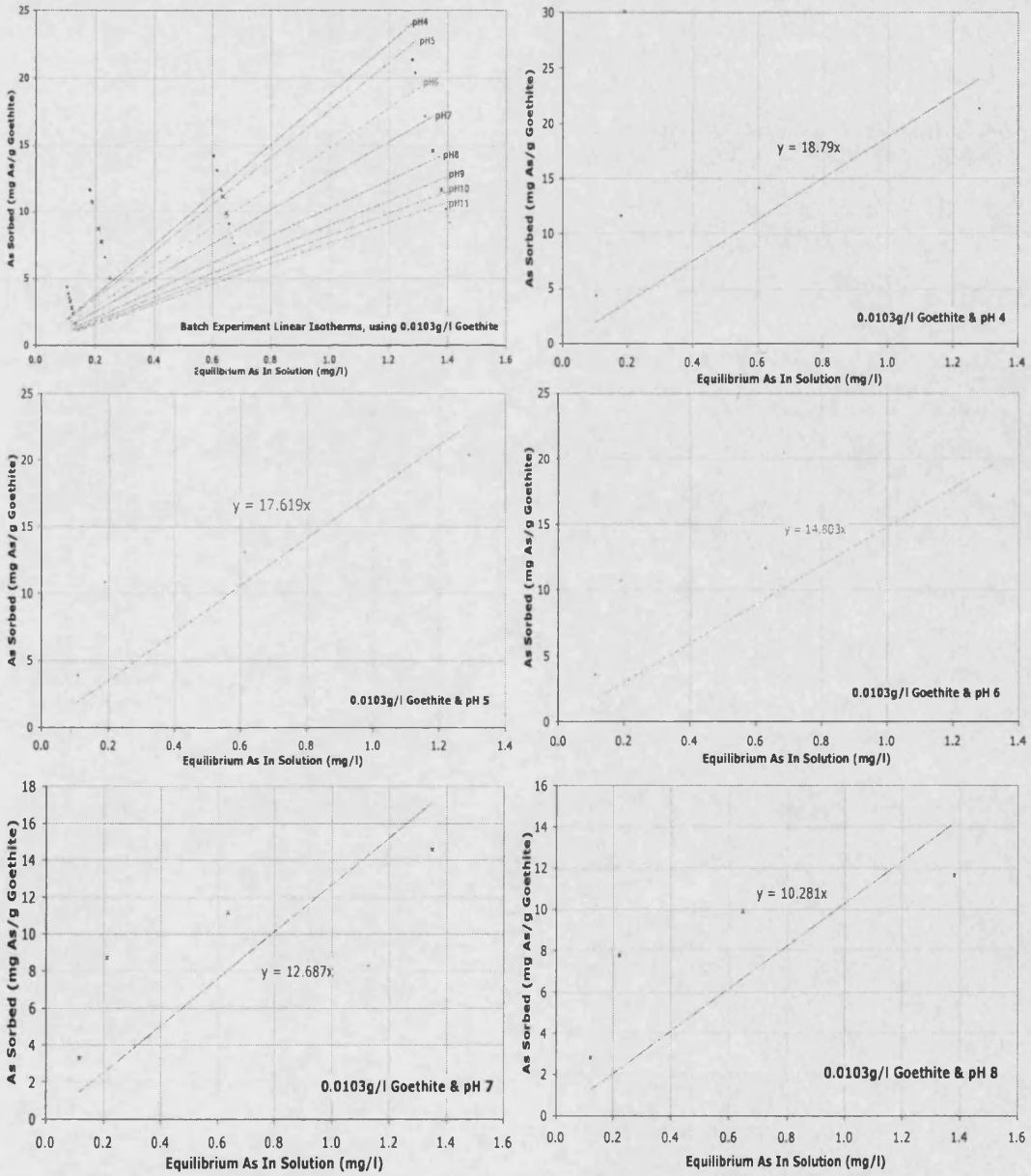

Figure 5.2.18a. Linear fitted isotherms to the batch experiment results for solution pH 4 – 8.

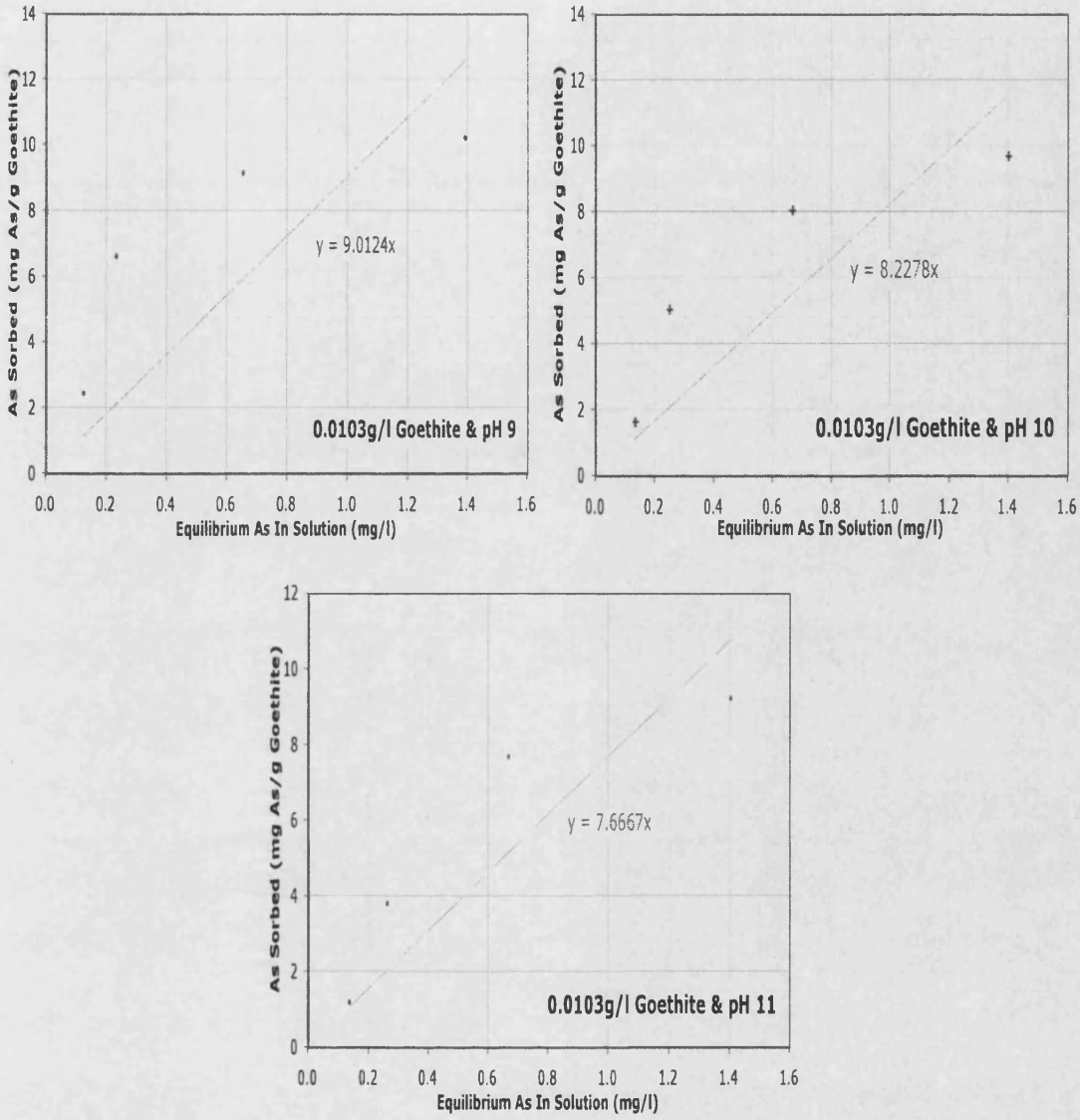

Figure 5.2.18b. Linear fitted isotherms to the batch experiment results for solution pH 9 – 11.

Figure 5.2.19 shows the relationship between K_d and the solution pH. The correlation between K_d and pH in this case is strong (with robust goodness of fit; R^2 ranges from 0.96 to 0.99). As the solution pH increases, the partition coefficient decreases linearly. Figure 5.2.20 illustrates an inverse power (average –0.96) function relationship between K_d and goethite mass, which is in agreement with the trends also observed by the Freundlich, K_f, and the Langmuir, Q_o parameters.

The linear approximation for K_d and the solution pH can be described with the general equation:

$$K_d = -\theta(m)\,pH + \omega(m) \qquad \textit{Eqn. 5.2.12.}$$

Where θ and ω are coefficients related to the goethite mass (m). Both show an inverse power relationship relative to the goethite mass (Figure 5.2.21 and 5.2.22). The power relationship that describes this correlation is nearly identical to that observed for the same relationship derived using Freundlich isotherm parameters.

Similarly, the inverse power relationship that describes K_d in terms of goethite mass has the general equation:

$$K_d = \phi(pH)\, m^{-\sigma(pH)} \qquad \textit{Eqn. 5.2.13.}$$

Where ϕ and σ are parameters of the fitted function and are related to the pH.

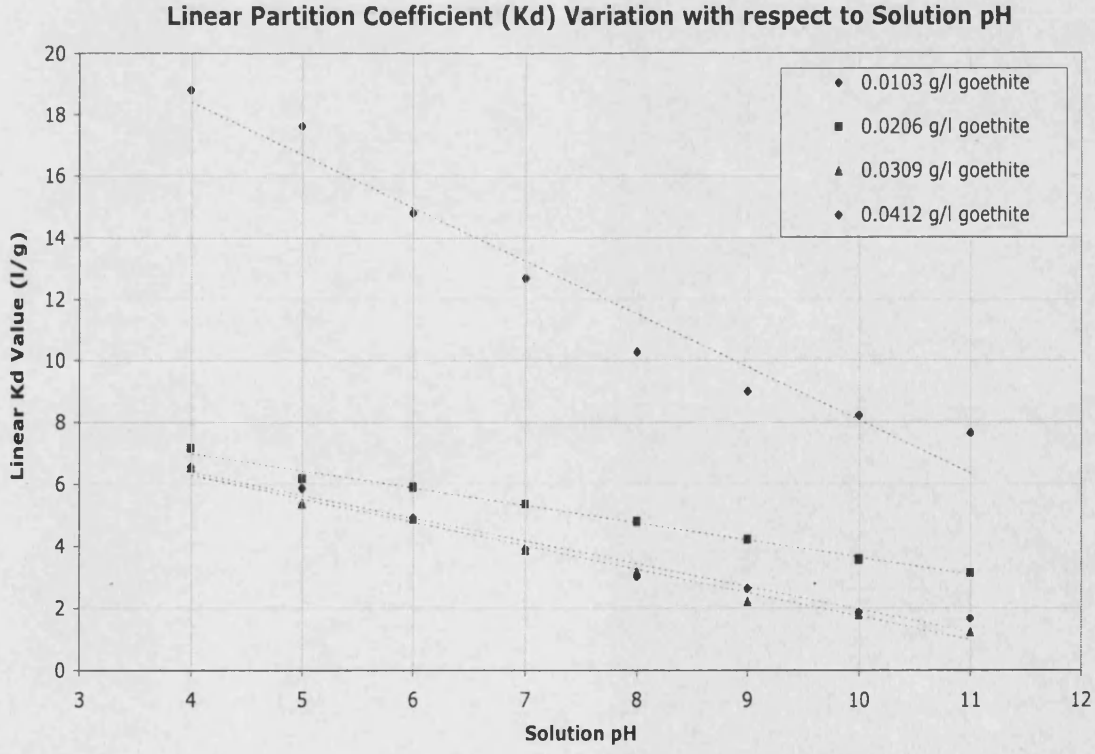

Figure 5.2.19. Correlation between Linear partition coefficient, K_d (l/g) and the solution pH, for all batch experiments.

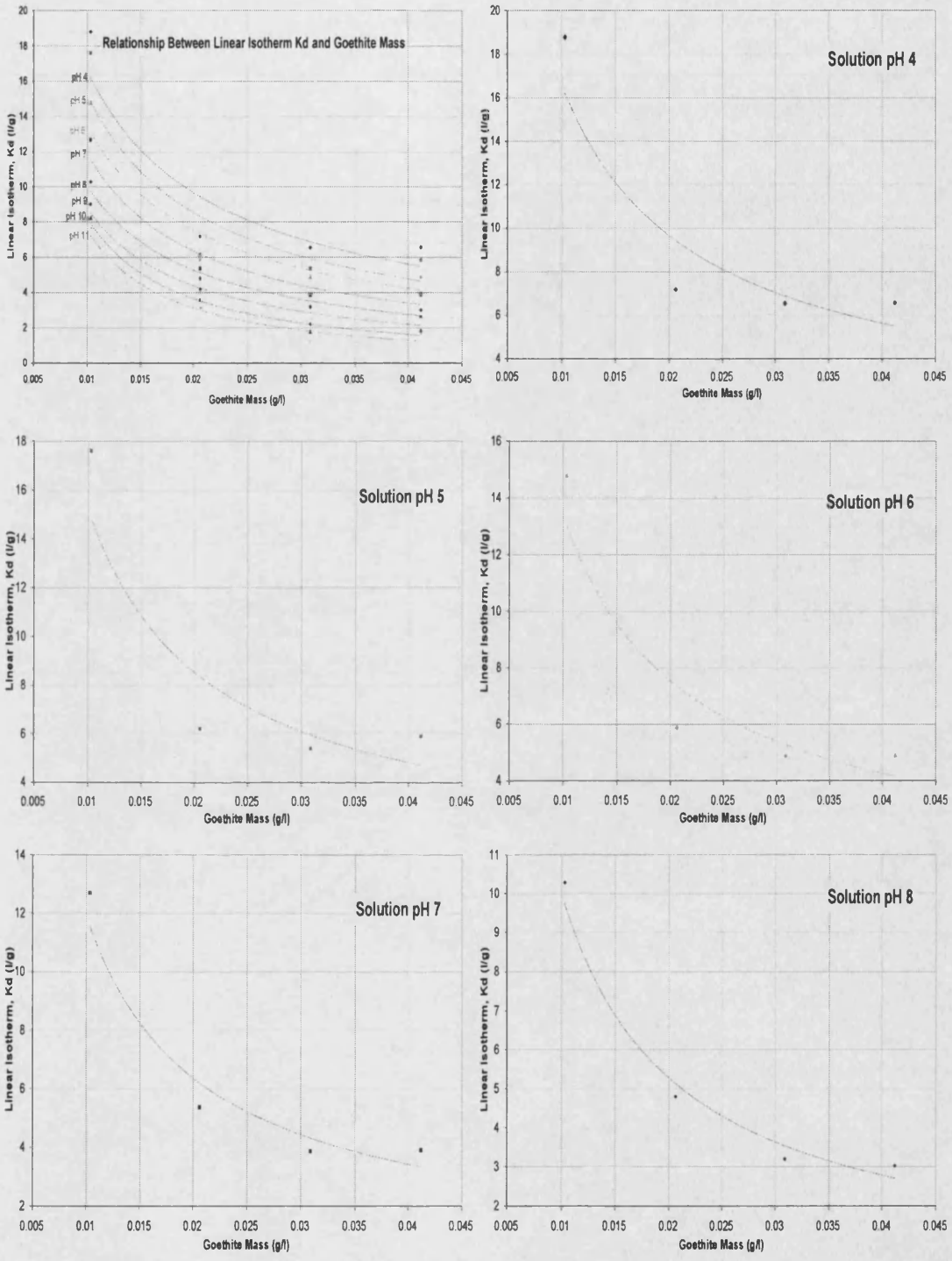

Figure 5.2.20a. The relationship between the derived K_d value and the mass of goethite present within the experiment. Solution pH 4 – 8.

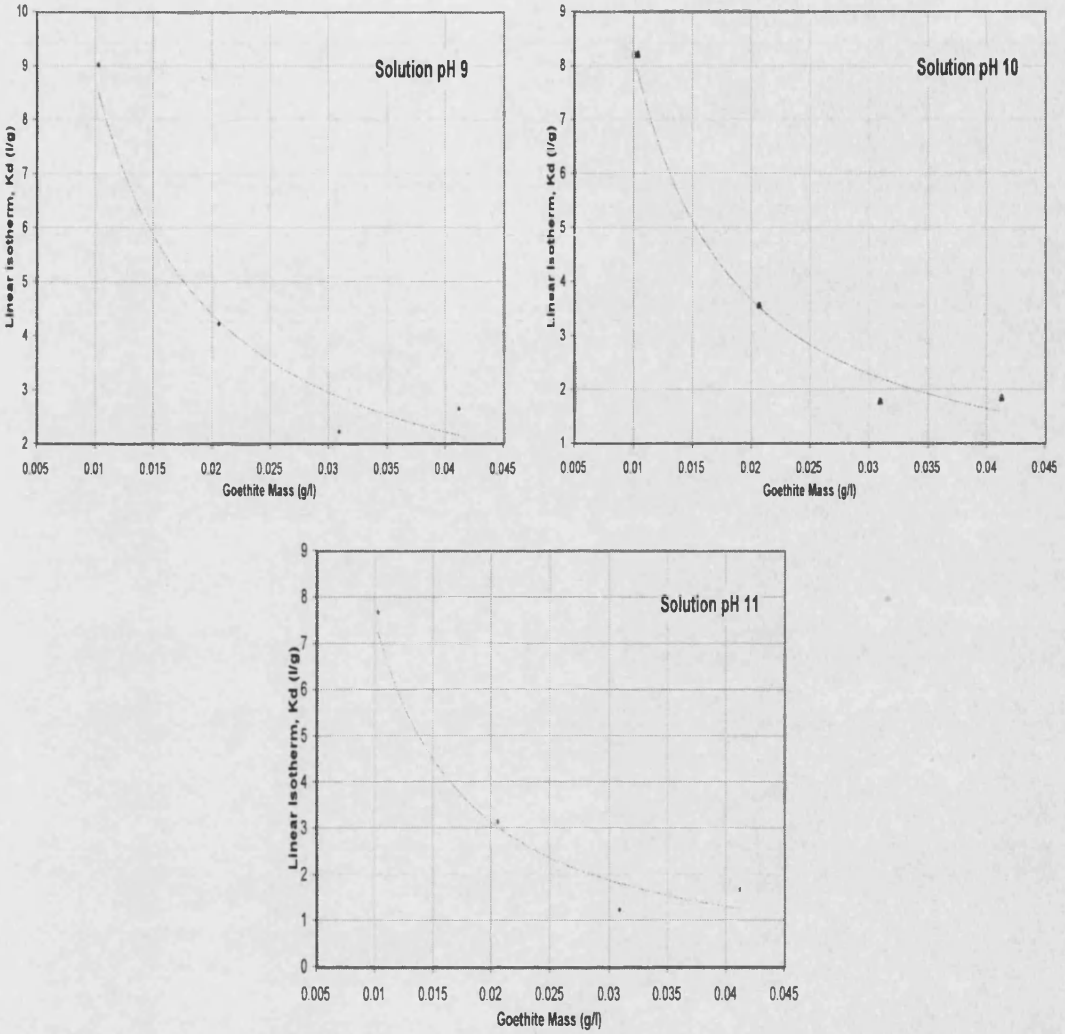

Figure 5.2.20b. The relationship between the derived K_d value and the mass of goethite present within the experiment. Solution pH 9 – 11.

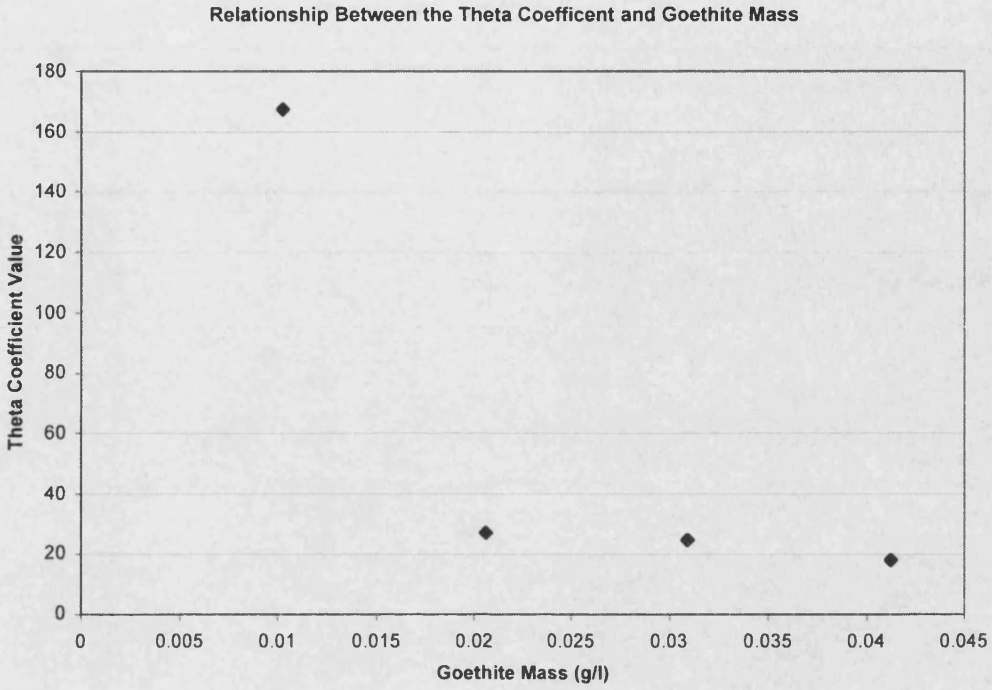

Figure 5.2.21. The function describing the relationship between the θ parameter and the goethite mass.

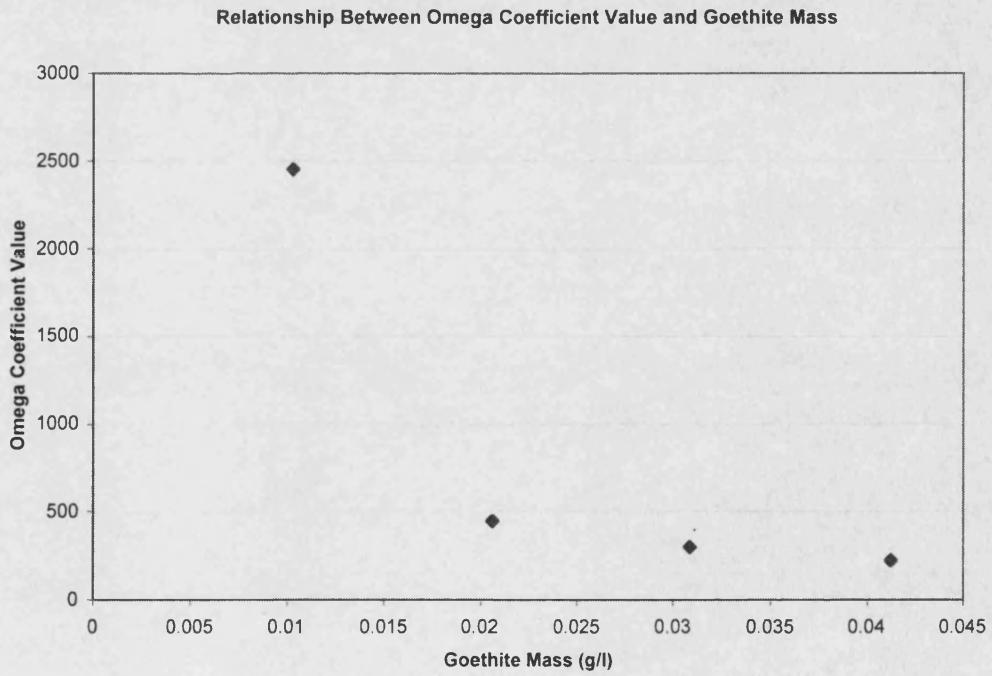

Figure 5.2.22. The function describing the relationship between the ω parameter and the goethite mass.

5.3. COLUMN EXPERIMENTS – INTERPRETATION OF ADSORPTION PARAMETERS AND MECHANISMS

5.3.1. The BIO1D Simulation Methodology

The breakthrough curves from the column experiments described in section 4.3. highlight the effects that goethite mass, arsenic concentration and flow rate have on the 'breakthrough' of arsenic. This section presents the results of using one-dimensional flow modelling with the BIO1D code (Srinivasan & Mercer, 1987) to simulate the breakthrough curves (BTCs) and hence determine the sorption parameters under equilibrium flow conditions. The BIO1D model uses the solute transport equation to simulate advection and dispersion as well as adsorption. Both linear and non-linear isotherms may be incorporated.

Solute Transport Equation (Srinivasan & Mercer, 1987):

$$D(\partial^2C/\partial x^2) - V_x(\partial C/\partial x) - [1+S(C)]\,(\partial C/\partial t) = 0 \qquad \textit{Eqn. 5.3.1.}$$

C = **Solute concentration in pore water (M/L^3)**
D = **Longitudinal hydrodynamic dispersion coefficient (L^2/T)**
x = **Distance (L)**
V_x = **Interstitial field velocity (L/T); assumed uniform**
S(C) = **Adsorption, function of C**
t = **Time (T)**

The set of starting parameters for initialising the model are:

The flux-averaged linear flow velocity (V_x, cms^{-1}), determined from the Cl BTCs (Chapter 4).

The dispersion coefficient (D) derived by fitting the chloride tracer breakthrough curves within the model separately, treating chloride as a conservative (unsorbed) ion.

The concentration of the solution species in the influent (C) (mgl^{-1}).

The total porosity (n_t) of the column fill was derived experimentally from measurements of saturated and dry material (see Chapter 2.2). As the values

were very similar for each column the average value of 21 % was used. The bulk density (p_b) of the column material was determined experimentally (Chapter 2.2). Table 5.3.1 summarises the derived n_t and p_b values required for modelling the adsorption term.

COLUMN IDENTITY	GOETHITE MASS (wt %)	n_t (%)	ρ_b (g/cm^3)
1	0.1	21.2	1.58
2	0.05	21.1	1.34
3	0.01	20.4	1.56
4	0.2	22.0	1.53
	Average =	**21.2**	**1.50**

Table 5.3.1. The total porosity (n_t) and bulk density of the column material for each of the experimental columns.

5.3.2. VIABILITY OF THE BIO1D MODEL – CHLORIDE FITTING

Chloride tracer experimental results demonstrate the conservative (non-reactive) behaviour of chloride transport in the columns. Table 5.3.2 shows the main parameters used for the chloride fitting together with the average linear flow velocities for the chloride breakthrough curves as determined from the breakthrough time and the length of the column. Section 2.4 described the individual experiment specifications.

The dispersion coefficient is related to the dispersivity (α) and the flow velocity (V_x) by:

$$D = \alpha V_x \qquad \textit{Eqn. 5.3.2.}$$

Where: D = Dispersion coefficient (cm^2/s)

α = Dispersivity (cm)

V_x = Average linear flow velocity (cm/s)

The effective porosity of the column material is found from Equation 5.3.3 and is shown in Table 5.3.2 for different experimental flow rates.

$$n_e = Q / (A \cdot V_x) \qquad \textit{Eqn. 5.3.3.}$$

Where: Q = Experimental volume flow rate (cm^3/s)

A = Cross-sectional area of column (cm^2)

V_x = Linear flow velocity determined from Cl BTCs (cm/s)

EXPERIMENT IDENTIFICATION	V_x (cm/s^{-1})	BREAKTHROUGH TIME, BT (s)	n_e (%)	D (cm^2/s)	α (cm)
E & G	0.013	670	13	0.011	0.846
B & D	0.018	520	13	0.016	0.889
J	0.019	490	14	0.017	0.914
H	0.021	460	14	0.018	0.857
C & I	0.022	450	14	0.020	0.909
A	0.027	390	26	0.024	0.889

Table 5.3.2. Experimental flow velocities (V_x), effective porosity (n_e) and BIO1D fitted dispersion coefficients (D) and dispersivity values (α).

The dispersivities (dispersion lengths) are on average 10.9 % of the flow lengths studied and therefore within the limits of scale dependence (Appelo and Postma, 1994). The dispersivity does not however, show any relationship with the flow velocity (Figure 5.3.1).

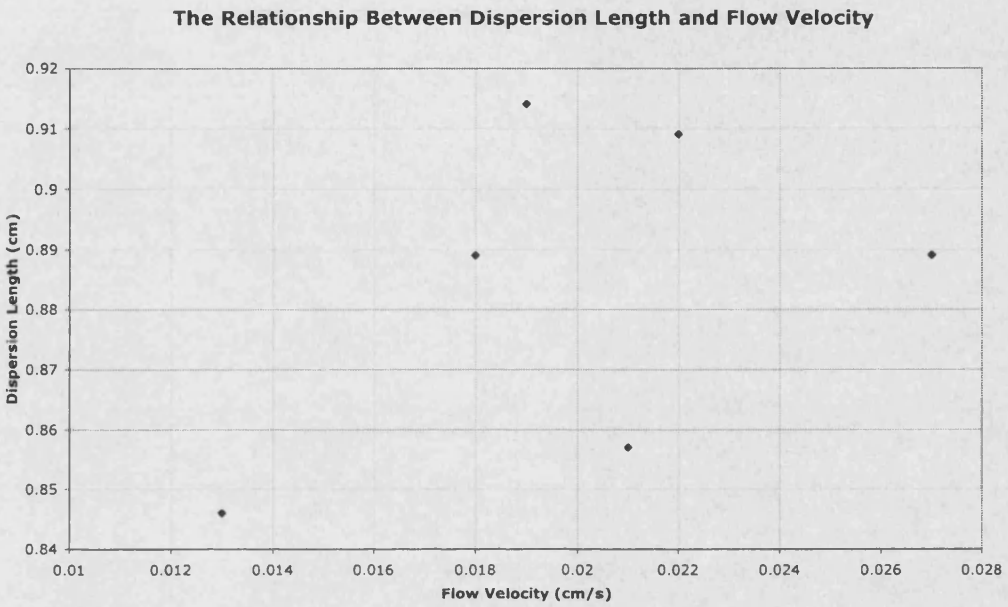

Figure 5.3.1. Graph illustrating no distinct relationship between the dispersion length (dispersivity) and the flow velocity.

Full results for both the experimental effluent chloride concentrations (in terms of C/Co) and the corresponding BIO1D simulations are given in Appendix 5C. These results are summarised in Figure 5.3.2 illustrating the different chloride transport through the columns with different flow velocities, and how well the BIO1D simulations fit the experimental data.

A 5 % mean difference, in terms of C/C_o at a given time, between the experimental and simulated BTC results was permitted in view of the possible scale of experimental and sampling error and including experimental flow perturbations. All BTCs were acceptable using BIO1D, with the simulations more accurate during early and latter times of breakthrough. However, individual column experiments occasionally exceeded the 5 % criterion around the

C/C_o = 0.5 breakthrough point (as shown in Appendix 5D). The 'goodness of fit' appears not to be related to flow velocity but may be explained to some degree by flow perturbations during the experiment. Table 5.3.3 summarises the 'closeness of fit' using the mean difference over the entire BTC for each experiment.

EXPERIMENT IDENTIFICATION	FLOW VELOCITY, V_x (cm/s)	MEAN % DIFFERENCE OVER ENTIRE BTC (SIMULATED Vs EXPERIMENTAL)
A	0.027	1.7
B & D	0.018	2.9
C & I	0.022	3.5
E & G	0.013	3.3
H	0.021	1.5
J	0.019	2.5

Table 5.3.3. The mean percentage difference between the simulated and experimental breakthrough curves, averaged over the entire BTC.

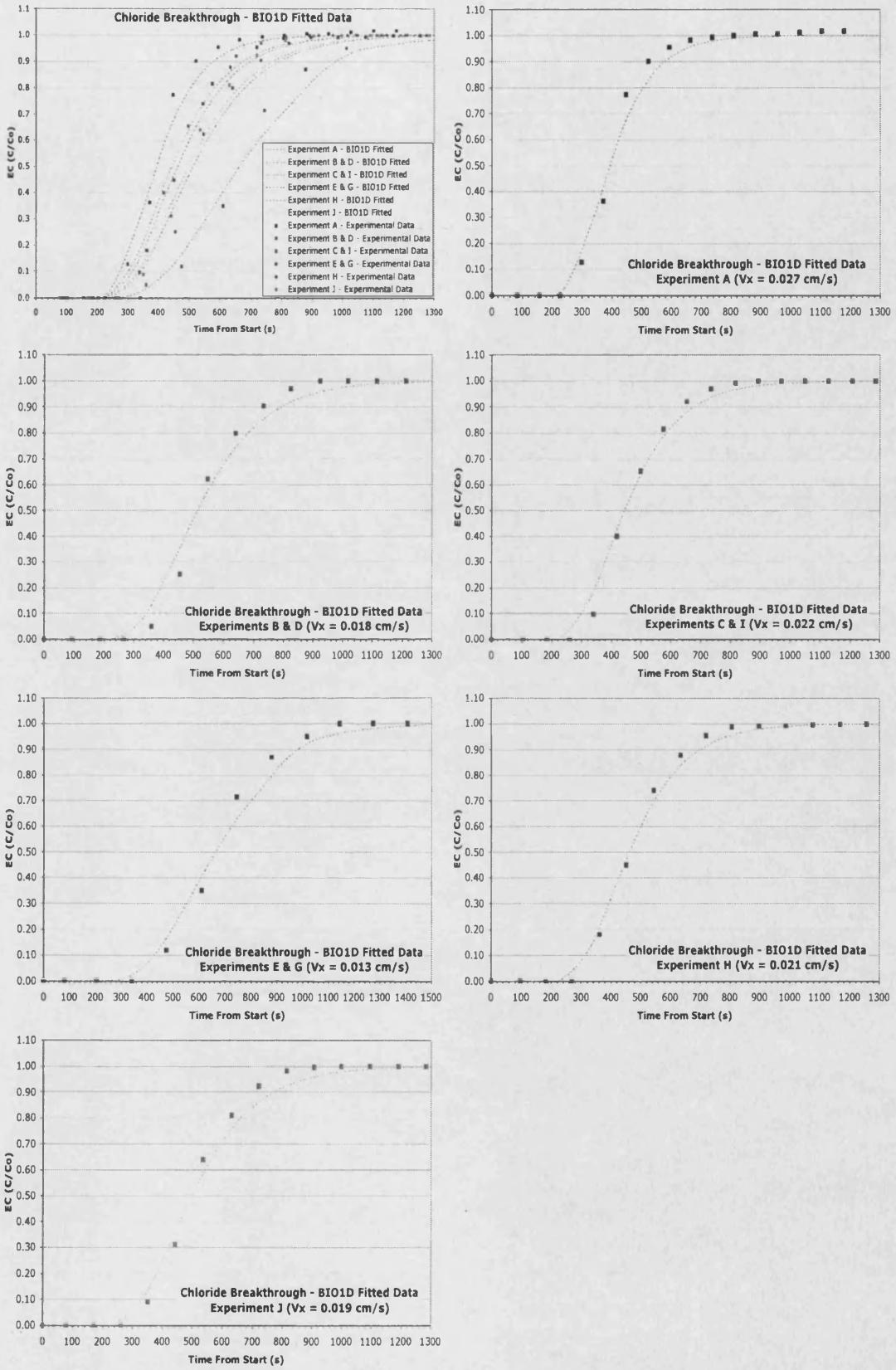

Figure 5.3.2. Chloride tracer breakthrough plots, both experimental and BIO1D simulated results.

5.3.3. BIO1D MODEL FITTING – LINEAR ISOTHERM FOR ARSENIC SORPTION

Arsenic Breakthrough Curves (BTCs) were fitted in a similar way to those for chloride, but they included adsorption terms within the one-dimensional solute transport equation (Equation 5.3.1).

The parameters required for initialising the models (V_x, C, D, n_t and ρ_b) were discussed in the previous section. The optimum adsorption terms K1 or R_f are defined in the linear adsorption equation and used in the BIO1D code (Srinivasan & Mercer, 1987) in the following way:

$$S(C) = K1/n_t = R_f - 1 = (\rho_b K_d') / n_t \qquad \textit{Eqn. 5.3.4.}$$

Where:

S(C)	**=**	**Adsorption term within the solute transport equation**
K1	**=**	**Linear Isotherm Coefficient**
n_t	**=**	**Total porosity (0.21)**
R_f	**=**	**Retardation Factor**
ρ_b	**=**	**Bulk Density of Matrix (g/cm³)**
K_d'	**=**	**Linear Partition Coefficient (cm³/g)**

K_d' is the Linear partition coefficient which is effective for the individual experiment column fill. The k_d' values for the column fill can be related to goethite K_d by correction of the goethite mass concentration within each column (Equation 5.3.5).

Appendix 5E contains all BTCs fitted to experimental data using the linear isotherm, and Figure 5.3.3 illustrates an example from experiment I. Table 5.3.4. shows the derived K1, R_f and K_d' values. The model uses only the K1 and R_f values and the partition coefficients (K_d') are derived directly from the linear adsorption equation 5.3.4 and equation 5.3.5. The bulk density used to determine K_d' for each column depends on the sediment within the column and, to compare partition coefficients specific to goethite, k_d' must be related to the goethite mass concentration within each column. The conversion factors from the initial derived K_d' to that accounting for adsorbent mass are derived as follows:

Column 1 Conversion Factor = 100 / 0.1 wt% goethite mass

Column 2 Conversion Factor = 100 / 0.05 wt% goethite mass

Column 3 Conversion Factor = 100 / 0.01 wt% goethite mass

Column 4 Conversion Factor = 100 / 0.2 wt% goethite mass

i.e. $K_d = K_d' \times$ Conversion Factor *Eqn. 5.3.5.*

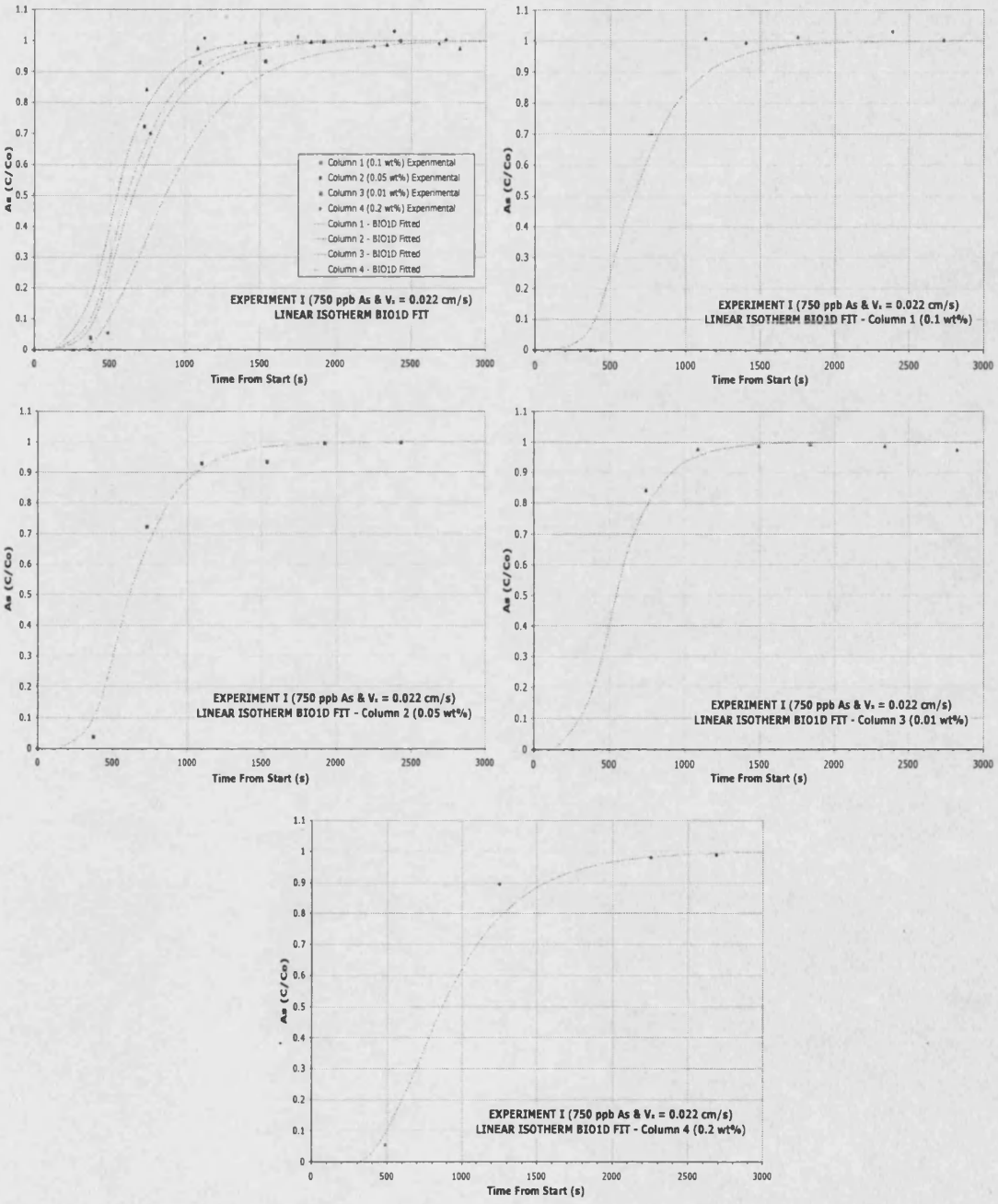

Figure 5.3.3. Experiment I Experimental breakthrough results and simulated BTCs using BIO1D and the Linear isotherm.

EXPERIMENT IDENTIFICATION	COLUMN IDENTIFICATION	BIO1D K1	BIO1D R_f	BIO1D Column K_d' (l/kg)	GOETHITE K_d (l/kg)
A (C_0 = 870 µg/l) V_x = 0.027 cm/s, D = 0.024 cm^2/s	1 (0.1 wt%)	0.07	1.35	0.04	45
A	2 (0.05 wt%)	0.03	1.15	0.02	45
A	3 (0.01 wt%)	0.02	1.10	0.01	127
A	4 (0.2 wt%)	0.25	2.25	0.16	82
B (C_0 = 600 µg/l) V_x = 0.018 cm/s, D = 0.016 cm^2/s	1	0.12	2.40	0.18	179
B	2	0.23	2.15	0.17	343
B	3	0.16	1.80	0.10	1013
B	4	0.31	2.55	0.20	101
C (C_0 = 280 µg/l) V_x = 0.022 cm/s, D = 0.02 cm^2/s	1	0.12	1.60	0.08	77
C	2	0.085	1.425	0.06	127
C	3	0.01	1.05	0.01	63
C	4	0.21	2.05	0.14	69
D (C_0 = 57 µg/l) V_x = 0.018 cm/s, D = 0.016 cm^2/s	1	0.29	2.45	0.19	186
D	2	0.25	2.25	0.19	373
D	3	0.215	2.075	0.14	1361
D	4	0.32	2.60	0.21	105
E (C_0 = 780 µg/l) V_x = 0.013 cm/s, D = 0.011 cm^2/s	1	0.21	2.05	0.13	135
E	2	0.15	1.75	0.11	224
E	3	0.14	1.70	0.09	886
E	4	0.28	2.40	0.18	92
G (C_0 = 540 µg/l) V_x = 0.013 cm/s, D = 0.011 cm^2/s	1	0.185	1.925	0.12	119
G	2	0.17	1.850	0.13	254
G	3	0.155	1.775	0.10	981
G	4	0.31	2.55	0.20	101
H (C_0 = 630 µg/l) V_x = 0.021 cm/s, D = 0.018 cm^2/s	1	0.20	2.00	0.13	128
H	2	0.15	1.75	0.11	224
H	3	0.09	1.45	0.06	570
H	4	0.24	2.20	0.16	78
I (C_0 = 750 µg/l) V_x = 0.022 cm/s, D = 0.02 cm^2/s	1	0.175	1.875	0.11	112
I	2	0.145	1.725	0.11	216
I	3	0.09	1.45	0.06	570
I	4	0.35	2.65	0.23	114
J (C_0 = 630 µg/l) V_x = 0.019 cm/s, D = 0.017 cm^2/s	1	0.21	2.05	0.13	135
J	2	0.16	1.80	0.12	239
J	3	0.12	1.60	0.08	759
J	4	0.36	2.80	0.24	118

Table 5.3.4. BIO1D Results in terms of Linear Isotherm, for all the column experiments. The derived coefficient values are given, both column specific (K_d') and with respect to the goethite present (K_d).

The degree of fit between the simulations and the experimental data is compared in Table 5.3.5 and illustrated in Figure 5.3.4 as a function of the flow velocity. Figure 5.3.4 shows that the simulated BTCs fit the experimental BTCs the best at high flow velocities and may be the result of a better model description for the dispersion at high flow. BIO1D generally provides good

approximation to experimental methods. There is no observed correlation between the goodness of fit and the solute concentration (Appendix 5F). There may be kinetic effects that are not considered in the model and lead to the poorer simulations at low or extreme flow velocity and which are discussed further in section 5.3.3. Alternatively, flow variability may be an issue at the lower flow rates.

EXPERIMENT IDENTIFICATION	% DIFFERENCE (& R^2) COLUMN 1	% DIFFERENCE (& R^2) COLUMN 2	% DIFFERENCE (& R^2) COLUMN 3	% DIFFERENCE (& R^2) COLUMN 4
A	2.5 (0.98)	0.8 (1.00)	1.8 (0.99)	1.0 (1.00)
B	2.7 (0.99)	2.2 (0.99)	0.8 (1.00)	4.6 (0.97)
C	0.9 (1.00)	0.9 (1.00)	0.7 (1.00)	2.7 (0.98)
D	1.3 (1.00)	2.4 (0.99)	3.0 (0.98)	3.2 (0.98)
E	4.7 (0.97)	4.2 (0.97)	3.2 (0.98)	4.2 (0.98)
G	2.9 (0.99)	3.1 (0.98)	2.2 (0.99)	5.2 (0.97)
H	0.8 (1.00)	1.2 (1.00)	1.4 (0.99)	3.2 (0.98)
I	2.0 (0.99)	1.3 (0.99)	1.0 (1.00)	2.3 (0.99)
J	1.6 (1.00)	1.7 (0.99)	2.1 (0.99)	2.9 (0.99)

Table 5.3.5. Degree of fit between the modelled and experimental BTCs compared, using the mean difference for the entire BTC for each experiment. R^2 = regression or correlation coefficient.

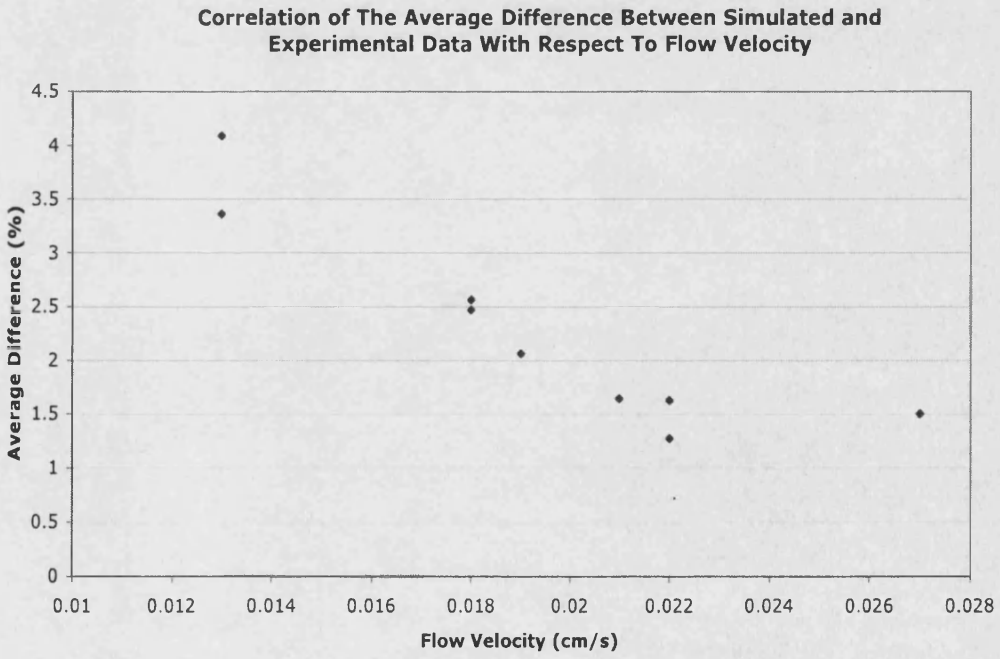

Figure 5.3.4. Plot demonstrating the difference between experimental and simulated data, as a mean percentage difference, for each experiment and the flow velocity (V_x).

The values of K_d for linear sorption of arsenic on goethite for the column experiments range from 44 to 1360 l/Kg. These are less than those derived for the equilibrium batch experiments, which lie between 3864 and 12687 l/Kg at solution pH 6, equating to the measured column effluent pH.

Figure 5.3.5 shows the relationship between the K_d values derived for the column experiments with respect to the flow velocity. The figure illustrates a general decrease of the goethite (corrected) partition coefficient with increasing flow velocity. The results also suggest a possible optimum velocity for adsorption at 0.018 cm/s for the masses used, which corresponds to a peak partition coefficient.

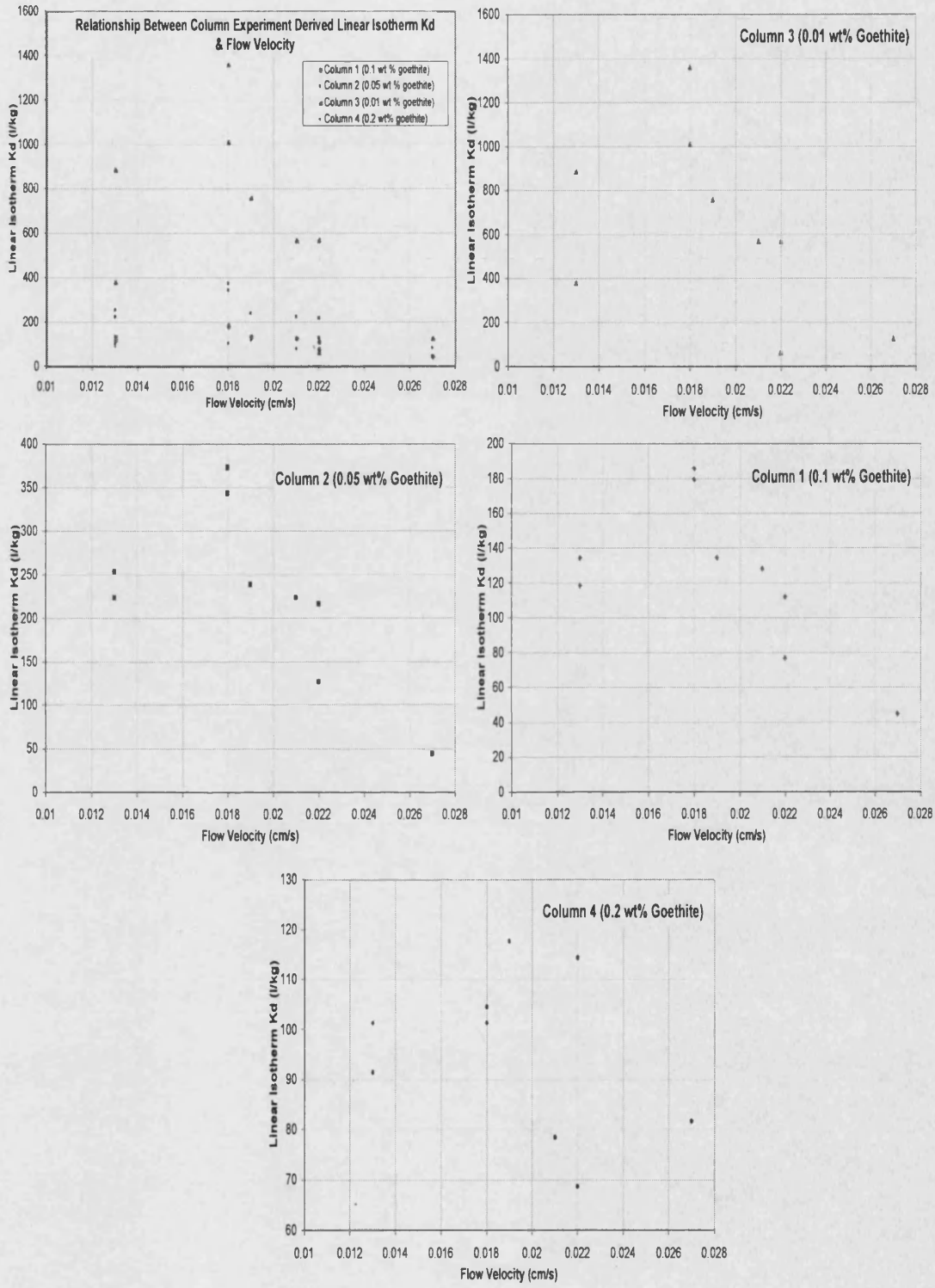

Figure 5.3.5. The relationship between K_d (corrected for goethite mass) and flow velocity (V_x).

A further relationship test was applied to the partition coefficient and the influent arsenic concentration (Figure 5.3.6) but the results do not show clear functionality. If adsorption is adhering strictly to the Linear isotherm description then the partition coefficients should not change with solution concentration.

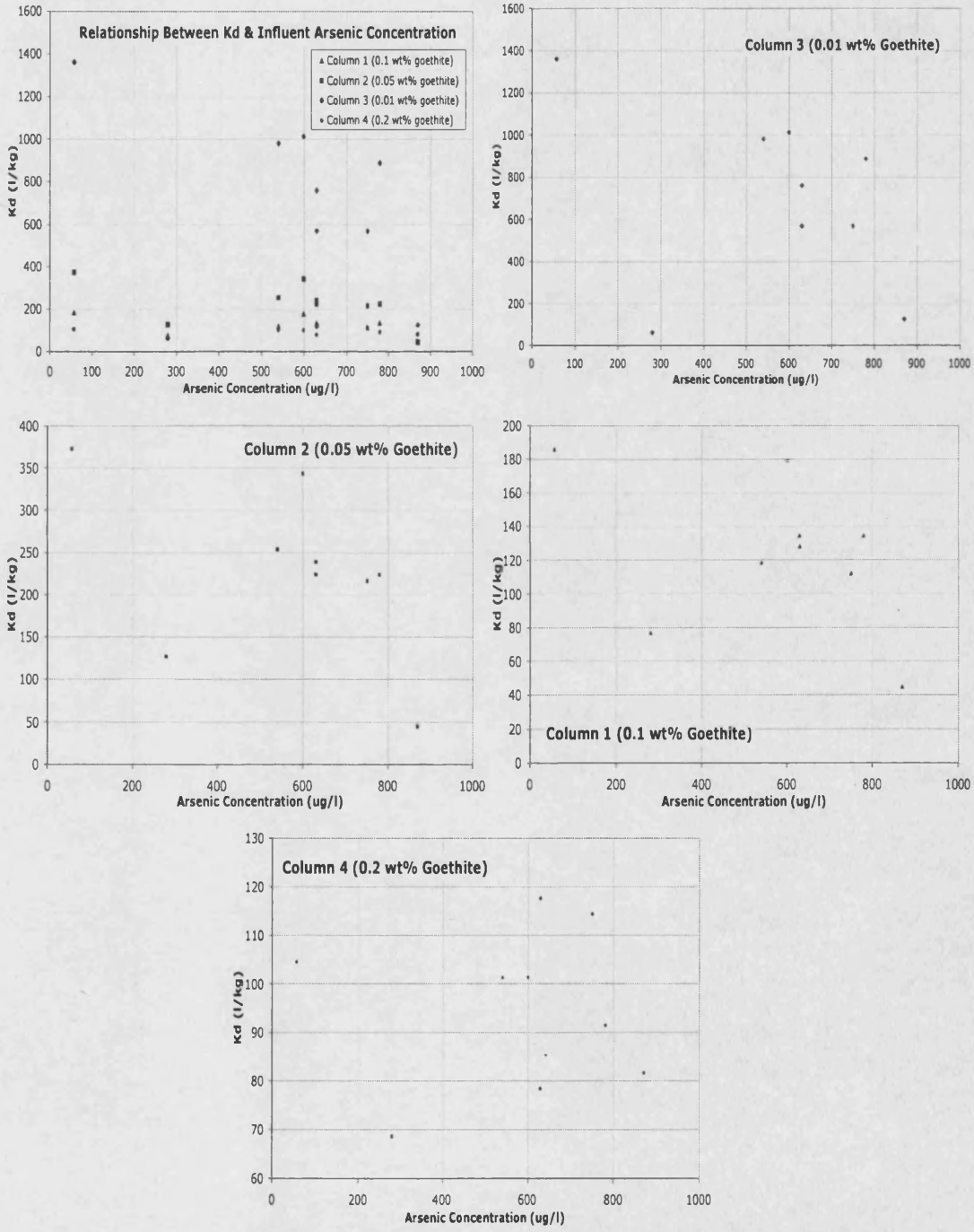

Figure 5.3.6. The relationship between K_d (corrected for goethite mass) and influent arsenic concentration.

An interesting inverse relationship between the corrected K_d values and the goethite mass within the columns is indicated in Figure 5.3.7, using discrete experimental results to discount effects from other experimental variables. The inverse relationship is better quantified for the experiments with lower flow velocity. Such a relationship can be represented by an inverse power function with a mean exponent of –0.72. The same trend was observed in the batch experiments, and can be explained by the mathematics of the isotherm coefficient as described in Section 5.2. However, column experiments A and C do not show the same inverse mass relationship (Table 5.3.4). This may be as a result of the relatively high flow velocities in these two experiments, suggesting that equilibrium adsorption has not been achieved as a consequence of kinetic disequilibrium. This is discussed further in Section 5.3.5.

In general, K_d is related to the goethite mass (m) by:

$$K_d = \alpha(C_0)\, m^{-\beta(v_x)} \qquad \textit{Eqn. 5.3.6.}$$

Where α and β represent functional parameters that are dependent on the arsenic concentration (C_0) and the flow velocity (v_x) respectively (Appendix 5G shows the functions used to describe α and β relationships).

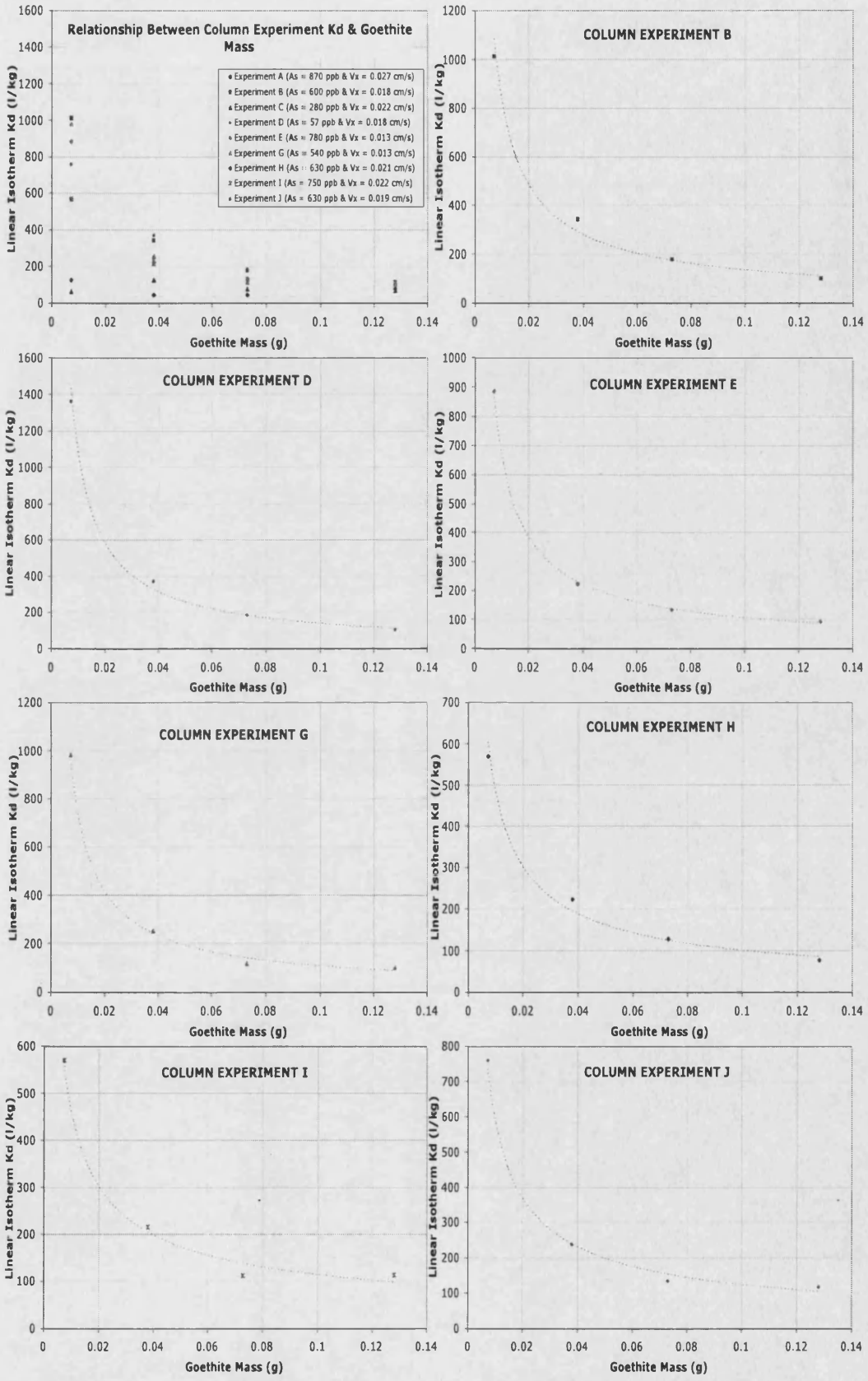

Figure 5.3.7. Illustration of the relationship between K_d (goethite corrected) and the mass of goethite within the column.

5.3.4. BIO1D MODEL FITTING – FREUNDLICH ISOTHERM

The BIO1D code was used also to fit BTCs to the experimental data incorporating the Freundlich isotherm adsorption term. All parameters for the simulations have been discussed in previous sections. The adsorption term, S(C) corresponds to the following Freundlich equation within the BIO1D code (Srinivasan & Mercer, 1987):

$$S(C) = [(K2\ n) / n_f]\ C^{n-1} = [(\rho_b\ K_f'\ n) / n_f]\ C^{n-1} \qquad \textit{Eqn. 5.3.7.}$$

$$\text{where} \quad K_f' = K2 / \rho_b$$

Where;

K2	**=**	**BIO1D Freundlich Isotherm Component**
n	**=**	**Freundlich exponent**
n_f	**=**	**Porosity (0.21)**
ρ_b	**=**	**Bulk Density of column material (g/cm³)**
C	**=**	**Solute concentration in pore fluid (g/cm³)**
K_f'	**=**	**Freundlich coefficient for column material (l/kg)**

Full experimental BTCs and the results simulated using the Freundlich isotherm are give in Appendix 5E. As an example, experiment I BTCs are shown in Figure 5.3.8. Table 5.3.6 summarises the Freundlich fitting parameter (K2) and the partition coefficient K_f for all simulated curves. As with the Linear K_d isotherm, the K_f values have been corrected to account for the proportion of goethite within the total bulk density (see Section 5.3.3). The 'n' exponent in the model was given a fixed value of 0.52, the average derived from the batch experiments over the pH range 5 – 7.

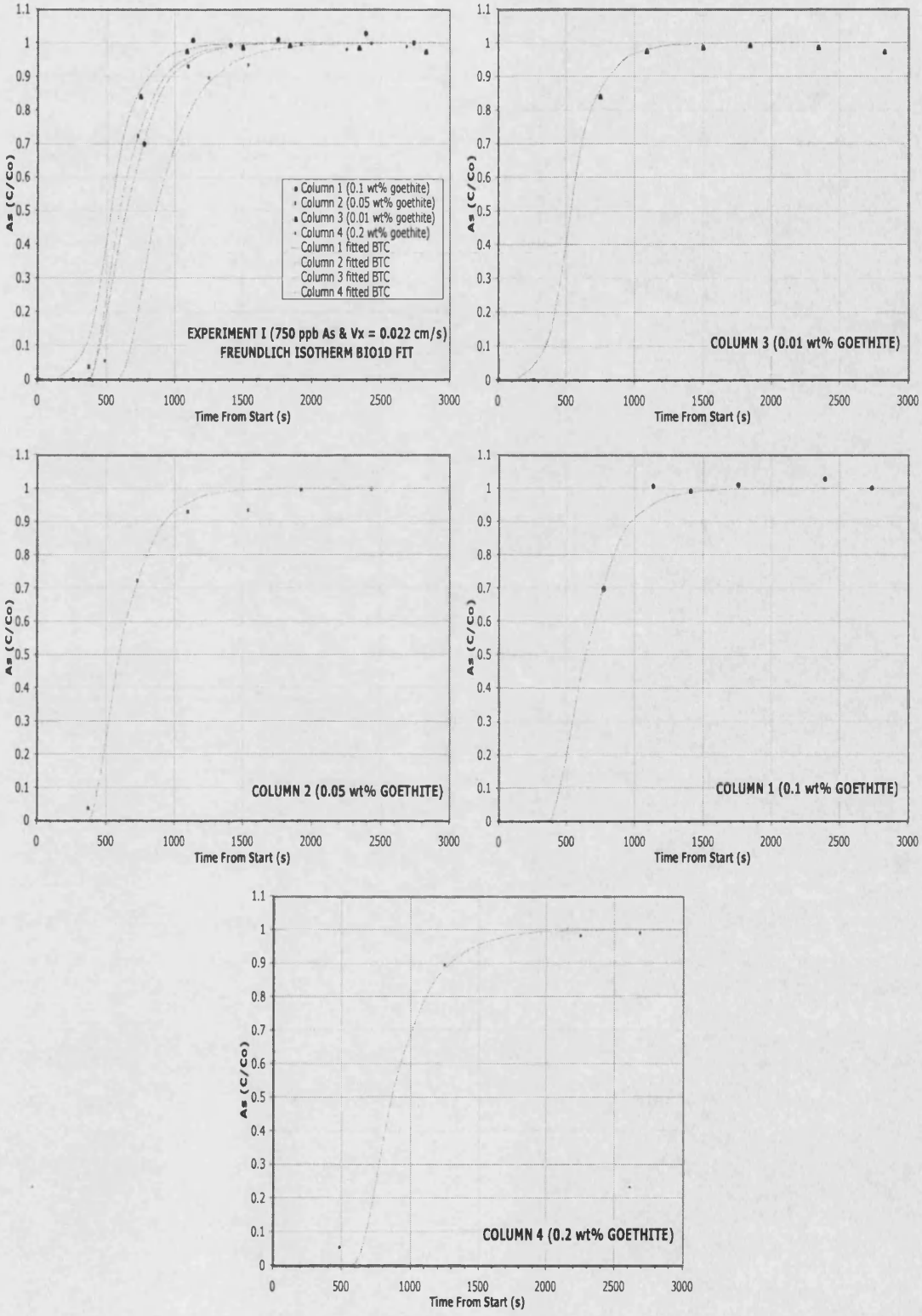

Figure 5.3.8. Experiment I breakthrough results and simulated BTCs using BIO1D and the Freundlich isotherm.

Table 5.3.7 summarises the difference between the BIO1D simulations and the experimental results for each column in terms of the mean difference over the entirety of the column experiment (Details are given in Appendix 5D). The degree of fit between simulations and the experimental data (Appendix 5F) does not vary significantly with flow velocity or arsenic concentration (Figures 5.3.9 and 5.3.10, respectively).

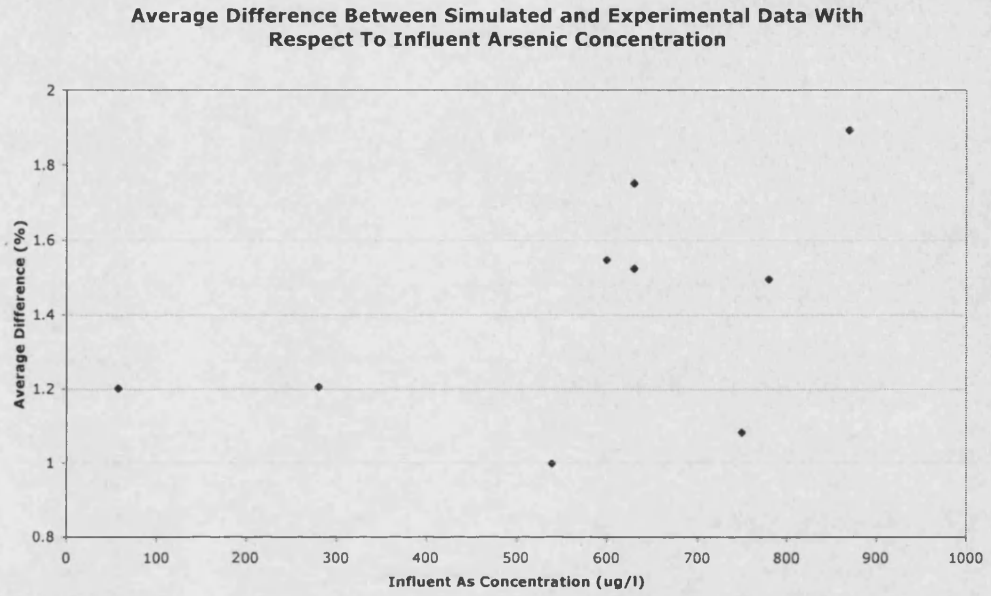

Figure 5.3.9. The 'goodness of fit' in terms of As concentration for the fitted BTCs, using the Freundlich adsorption term.

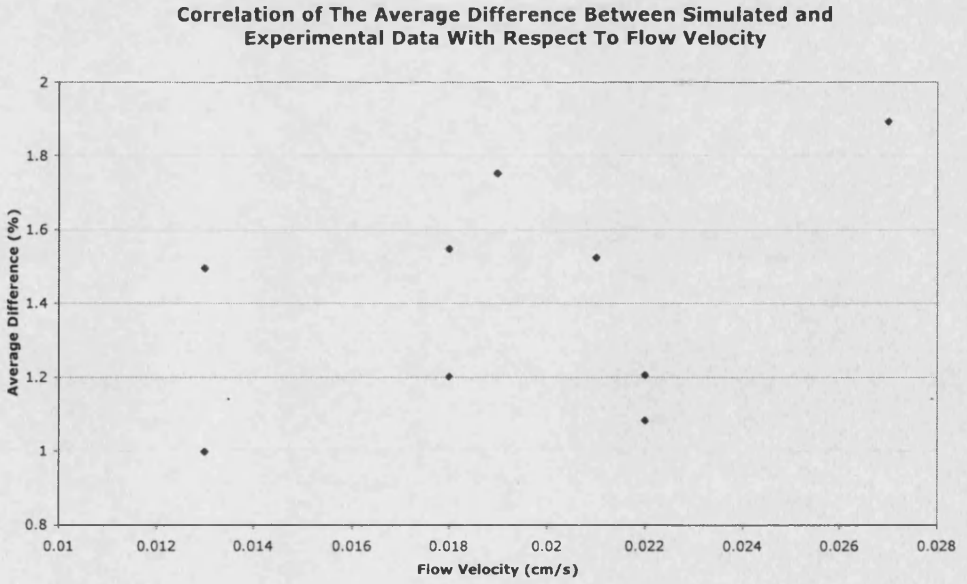

Figure 5.3.10. The 'goodness of fit' in terms of flow velocity (V_x) for the fitted BTCs, using the Freundlich adsorption term.

EXPERIMENT IDENTIFICATION	COLUMN IDENTIFICATION	BIO1D K2	BIO1D – Column Kf'	Goethite Kf (lkg^{-1})
A (C_0 = 870 µg/l) V_x = 0.027 cm/s, D = 0.024 cm^2/s	1 (0.1 wt% goethite)	1.40	0.90	897
A	2 (0.05 wt%)	0.70	0.52	1045
A	3 (0.01 wt%)	0.50	0.32	3165
A	4 (0.2 wt%)	6.00	3.92	1961
B (C_0 = 600 µg/l) V_x = 0.018 cm/s, D = 0.016 cm^2/s	1	5.70	3.65	3654
B	2	4.50	3.36	6716
B	3	3.10	1.96	19620
B	4	6.60	4.31	2157
C (C_0 = 280 µg/l) V_x = 0.022 cm/s, D = 0.02 cm^2/s	1	1.60	1.03	1026
C	2	1.30	0.97	1940
C	3	0.10	0.06	633
C	4	4.20	2.75	1373
D (C_0 = 57 µg/l) V_x = 0.018 cm/s, D = 0.016 cm^2/s	1	1.90	1.22	1218
D	2	1.65	1.23	2463
D	3	1.45	0.92	9177
D	4	2.20	1.44	719
E (C_0 = 780 µg/l) V_x = 0.013 cm/s, D = 0.011 cm^2/s	1	4.90	3.14	3141
E	2	3.60	2.69	5373
E	3	3.00	1.90	18987
E	4	6.70	4.38	2190
G (C_0 = 540 µg/l) V_x = 0.013 cm/s, D = 0.011 cm^2/s	1	3.75	2.40	2404
G	2	3.40	2.54	5075
G	3	3.10	1.96	19620
G	4	6.20	4.05	2026
H (C_0 = 630 µg/l) V_x = 0.021 cm/s, D = 0.018 cm^2/s	1	4.13	2.65	2647
H	2	3.00	2.24	4478
H	3	1.90	1.20	12025
H	4	5.00	3.27	1634
I (C_0 = 750 µg/l) V_x = 0.022 cm/s, D = 0.02 cm^2/s	1	3.50	2.24	2244
I	2	3.22	2.40	4806
I	3	1.70	1.08	10759
I	4	7.00	4.58	2288
J (C_0 = 630 µg/l) V_x = 0.019 cm/s, D = 0.017 cm^2/s	1	4.20	2.69	2692
J	2	3.50	2.61	5224
J	3	2.50	1.58	15823
J	4	5.20	3.40	1699

Table 5.3.6. Freundlich parameters derived from the column experiments using BIO1D (n = 0.52).

EXPERIMENT IDENTITY	% DIFFERENCE (& R^2) COLUMN 1	% DIFFERENCE (& R^2) COLUMN 2	% DIFFERENCE (& R^2) COLUMN 3	% DIFFERENCE (& R^2) COLUMN 4
A	2.76 (0.9762)	0.91 (0.9946)	1.84 (0.9925)	2.06 (0.9856)
B	2.14 (0.9890)	1.08 (0.9969)	1.98 (0.9863)	0.99 (0.9989)
C	1.58 (0.9880)	1.65 (0.9881)	0.61 (0.9984)	0.98 (0.9985)
D	2.12 (0.9946)	0.78 (0.9992)	1.16 (0.9971)	0.75 (0.9995)
E	1.16 (0.9954)	1.94 (0.9933)	1.15 (0.9965)	1.73 (0.9942)
G	1.10 (0.9980)	1.00 (0.9983)	0.71 (0.9992)	1.17 (0.9990)
H	1.26 (0.9961)	1.80 (0.9910)	2.45 (0.9781)	0.58 (0.9987)
I	0.57 (0.9990)	1.27 (0.9964)	0.90 (0.9962)	1.59 (0.9907)
J	1.80 (0.9952)	2.13 (0.9913)	2.21 (0.9987)	0.87 (0.9987)

Table 5.3.7. Highlighting the differences between simulated and experimental breakthrough plots, in terms of % differences (in C/Co). R^2 = regression / correlation coefficients.

The relationship between K_f and flow velocity (V_x) is illustrated in Figure 5.3.11. This plot shows a weak inverse relationship between K_f and velocity. This trend is more strongly observed for those columns containing the least goethite. Figure 5.3.12 shows that the derived K_f values have no general relationship with the influent arsenic concentration. Section 5.3.5 discusses further the effect of flow velocity and influent As concentration. Another factor to consider is that the modelling was concerned only with adjustment of K_f and not the exponent n, which has been held constant throughout. The model may compensate for the K2 (modelling Freundlich component) value and give an over- or under-estimate of the true K_f value. For example, if the n value is too high or too low then K_f will be underestimated or overestimated, respectively (Appelo and Postma, 1994). Previously cited n parameters of 0.66 for ferric hydroxide and 0.78 for ferruginous manganese ore were derived by Thirunavukkarasu *et al.* (2003) and Chakravarty *et al.* (2002), respectively. These values suggest that an over-estimation of K_f may be expected. The relationship between K_f and goethite mass can be represented by an inverse power relationship with an average power exponent of –0.73, almost identical to that for the Linear K_d (Figure 5.3.13).

In general the relationship between K_f and the goethite mass (m) is described as:

$$K_f = \alpha(V_x,C_0)m^{-\beta(V_x,C_0)} \qquad \textit{Eqn. 5.3.8.}$$

$$\beta(V_x,C_0) \sim 0.73$$

Where α and β are coefficients that are determined by both the flow velocity (V_x) and the arsenic concentration (C_0) (Appendix 5G).

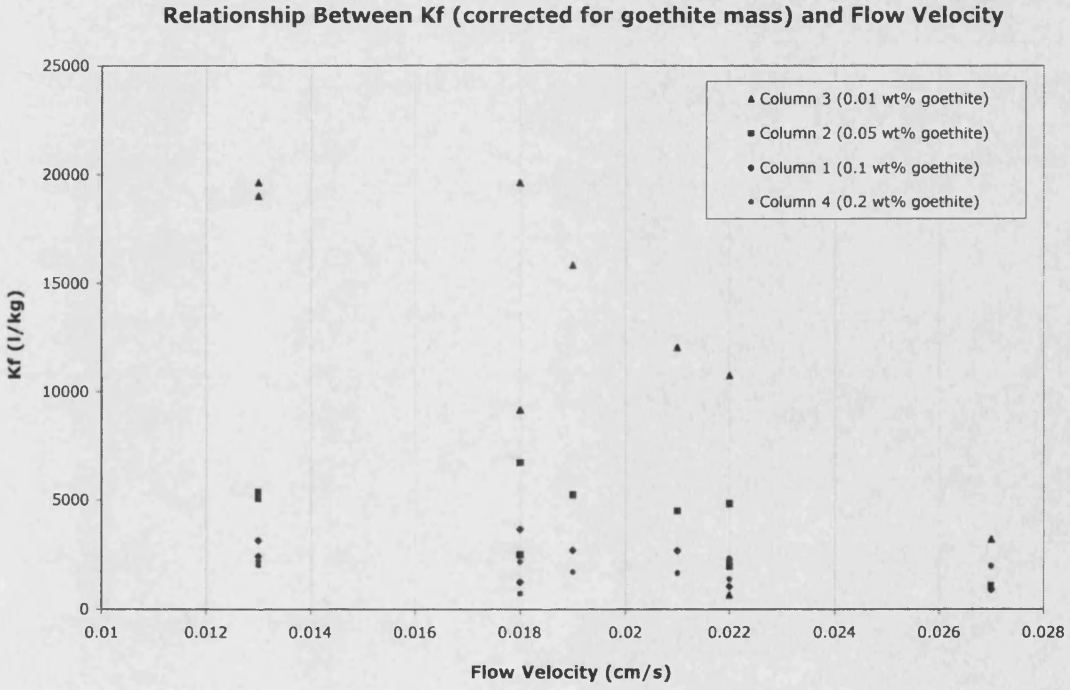

Figure 5.3.11. Relationship between K_f and the experimental flow velocity (V_x), for the individual columns containing different goethite mass.

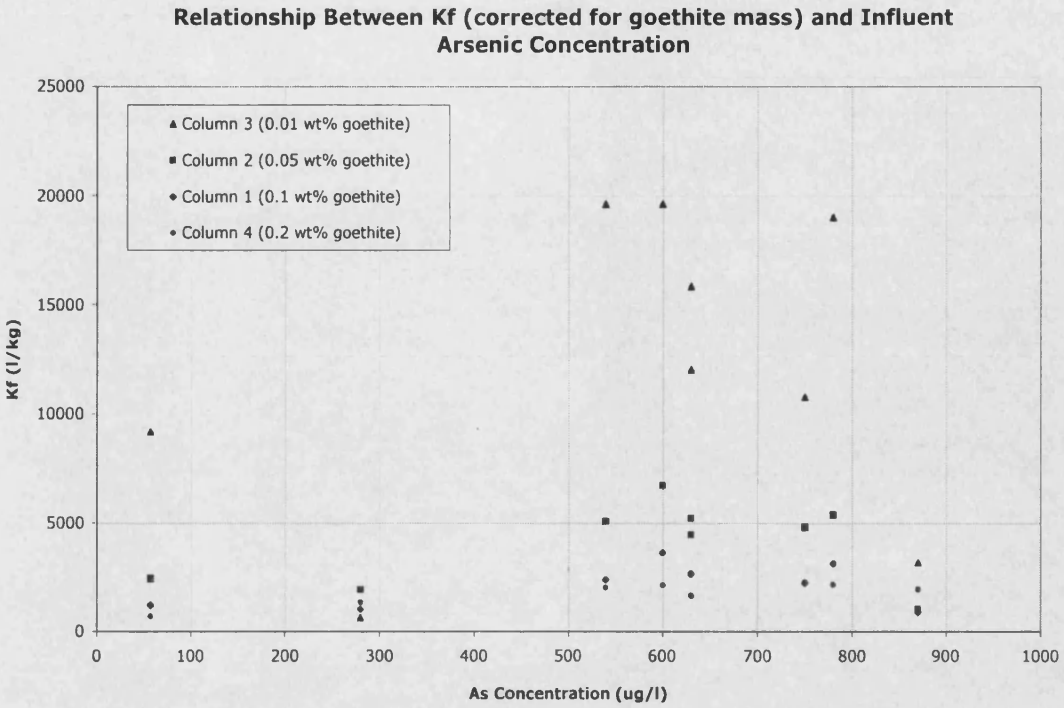

Figure 5.3.12. Relationship between K_f and the influent As concentration, for the individual columns containing different goethite mass.

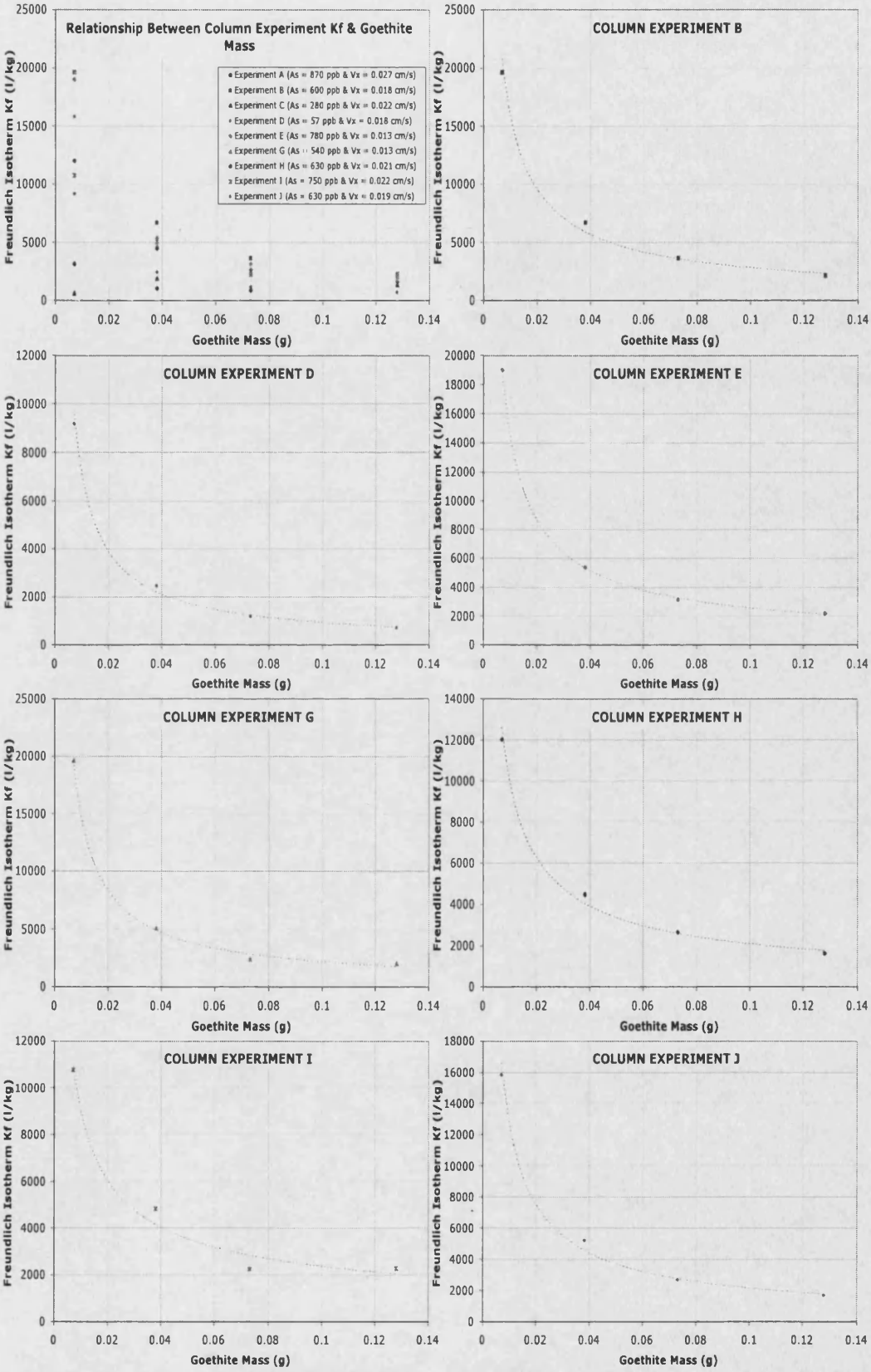

Figure 5.3.13. The relationship between the Freundlich K_f value and the goethite mass present within the column.

5.3.5. BIO1D RESULTS – Focus on Flow Velocity and Influent Concentration

It is possible to identify trends between the adsorption isotherm parameters and experimental flow velocity and arsenic concentration without interference from other experimental variables.

5.3.5.1. Flow Velocity Relationship

Two experiment groups were compared ({B,J,H} and {E,I}). Within each of these groups the influent arsenic concentration was constant with flow velocity the only variable. Table 5.3.8 summarises the Linear K_d and Freundlich K_f for the experiments, and the results are investigated in Figures 5.3.14 and 5.3.15.

EXPERIMENT & COLUMN IDENTITY	FLOW VELOCITY (V_x) cm/s	Linear K_d (l/kg)		Freundlich K_f (l/kg)	
B1	0.018	179	(3)	3654	(3)
J1	0.019	135	(2)	6716	(2)
H1	0.021	128	(1)	2647	(1)
B2	0.018	343	(3)	6716	(3)
J2	0.019	239	(1)	5224	(2)
H2	0.021	224	(2)	4478	(1)
B3	0.018	1013	(3)	19620	(3)
J3	0.019	759	(2)	15823	(2)
H3	0.021	570	(1)	12025	(1)
B4	0.018	101	(2)	2157	(3)
J4	0.019	118	(3)	1699	(2)
H4	0.021	78	(1)	1634	(1)
E1	0.013	135	(2)	3141	(2)
I1	0.022	112	(1)	2244	(1)
E2	0.013	224	(2)	5373	(2)
I2	0.022	216	(1)	4806	(1)
E3	0.013	886	(2)	18987	(2)
I3	0.022	570	(1)	10759	(1)
E4	0.013	92	(1)	2190	(1)
I4	0.022	114	(2)	2288	(2)

Table 5.3.8. Relationship between interpreted isotherm parameters and experimental flow velocity (V_x). The number in brackets shows the order of increasing partition coefficient.

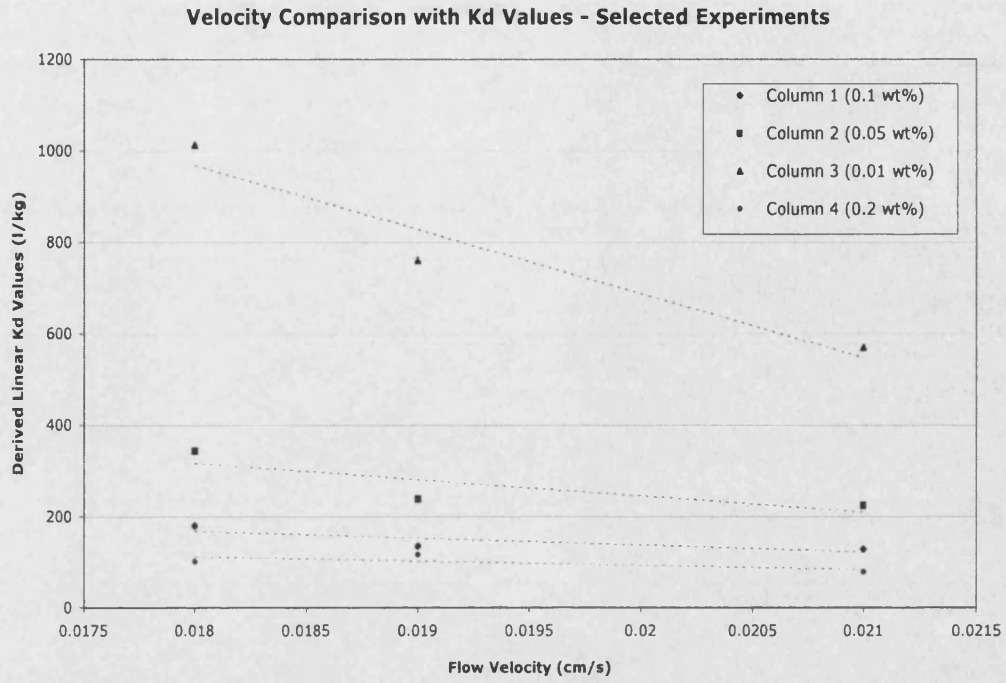

Figure 5.3.14. Linear partition coefficient (K_d) relationship with experimental flow velocity (V_x).

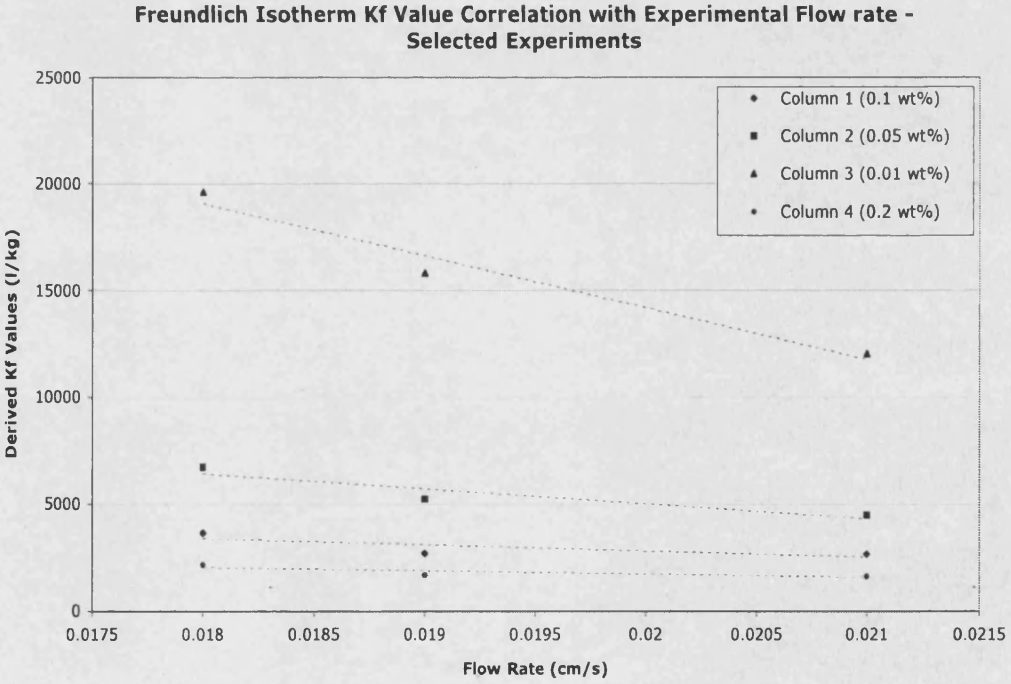

Figure 5.3.15. Freundlich coefficient (K_f) correlation with experimental flow velocity (V_x).

An inverse relationship exists between the flow velocity and K_d and K_f values. The Freundlich isotherm description has a marginally stronger relationship with the flow velocity than the Linear isotherm. In general the relationship between the partition coefficient (K_d or K_f) and the flow velocity (V_x) may be described approximately as:

$$K_d = \varepsilon(m)V_x + \phi(m) \qquad \textit{Eqn. 5.3.9.}$$

$$K_f = \gamma(m)V_x + \eta(m) \qquad \textit{Eqn. 5.3.10.}$$

Where ε, ϕ, γ, η are coefficients determined by the goethite mass (m).

The variation of isotherm parameter with respect to flow velocity suggests that kinetic effects are influential. For faster flow the adsorption of arsenic may be inhibited by reduced contact time and hence give lower derived isotherm adsorption coefficients. In addition, variations in the partition coefficients could result from variation in and multiplicity of flow paths. Under different flow rates different intergranular flow paths may be taken, and therefore, change the effective porosity of the column fill.

The variation in partition coefficient may reflect a change to the effective porosity of the column fill as the fluid velocity increases. Table 5.3.2 (Section 5.3) summarised the resulting effective porosity observed for the column experiments at different flow velocity. Figure 5.3.16 shows the relationship between the effective porosity and the flow velocities. This shows an almost constant effective porosity for the majority of flow velocities measured, but a sudden increase in effective porosity at the greatest flow. This suggests that there may be a capillary pressure barrier that is only overcome at high velocity. Therefore, the partition coefficients derived do not reflect changes to the effective porosity, which would result in an inverse trend. This lends support to the theory of kinetics affecting the partition coefficients during these experiments.

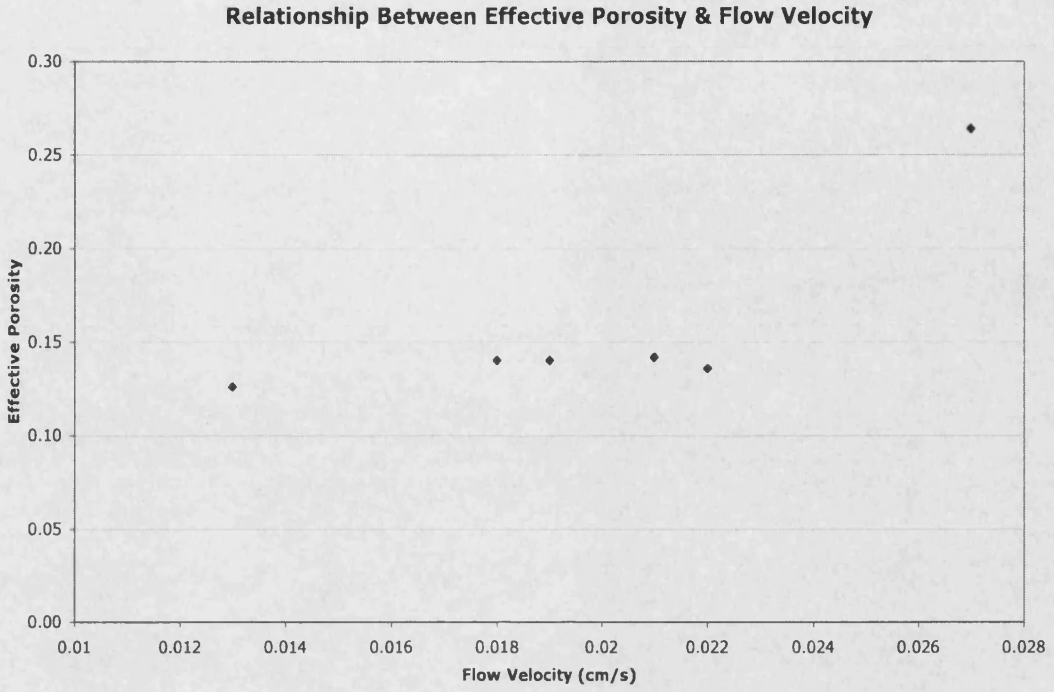

Figure 5.3.16. Illustration of the change in effective porosity (n_e) with increasing flow velocity.

5.3.5.2. *Arsenic Concentration Relationship*

The concentration of arsenic present within a solution and its relationship to the Linear and Freundlich isotherm coefficients is summarised in Table 5.3.9. Experiment groups {G,E}, {D,B}, and {C,I}, are used in the comparison. Each group has its flow velocity held as a constant but with different influent arsenic concentrations.

EXPERIMENT & COLUMN IDENTITY	As Solution Concentration (µg/l)	Linear K_d (l/kg)		Freundlich K_f (l/kg)	
G1	540	119	(1)	2409	(1)
E1	780	135	(2)	3141	(2)
G2	540	254	(2)	5075	(1)
E2	780	224	(1)	5373	(2)
G3	540	981	(2)	19620	(2)
E3	780	886	(1)	18987	(1)
G4	540	101	(2)	2026	(1)
E4	780	92	(1)	2190	(2)
D1	57	186	(2)	1218	(1)
B1	600	179	(1)	3654	(2)
D2	57	373	(2)	2463	(1)
B2	600	343	(1)	6716	(2)
D3	57	1361	(2)	9177	(1)
B3	600	1013	(1)	19620	(2)
D4	57	105	(2)	719	(1)
B4	600	101	(1)	2157	(2)
C1	280	77	(1)	1026	(1)
I1	500	112	(2)	2244	(2)
C2	280	127	(1)	1940	(1)
I2	500	216	(2)	4806	(2)
C3	280	63	(1)	633	(1)
I3	500	570	(2)	10759	(2)
C4	280	69	(1)	1373	(1)
I4	500	114	(2)	2288	(2)

Table 5.3.9. Comparison between the interpreted adsorption isotherm coefficients and the influent arsenic concentration. The number in brackets shows the order of increasing partition coefficient.

While the linear K_d values show a general decrease with increasing As concentration, the Freundlich K_f values increase. This discrepancy could be due to the constant value of 'n' used for the BTC simulations. This may force the K_f value to account for the apparent arsenic partitioning.

5.4. BATCH AND COLUMN EXPERIMENT ISOTHERM MODEL CONCLUSIONS & APPLICABILITY

5.4.1. Comparison of Mono-Mineral Partition Descriptions

The batch experiment adsorption is defined by a non-linear adsorption isotherm. The fitting of non-linear isotherms to the experimental data is more favourable towards the Freundlich model than that of the Langmuir. This is highlighted by the more substantial relationships observed between the Freundlich isotherm parameters and solution pH, and also the visually better fit of the Freundlich isotherm in the graphical interpretation of the experimental data. There is no significant statistical difference between the Linear and Freundlich model goodness of fit to the column data, although the Freundlich isotherm may not be as well represented as only the K_f coefficient was allowed to vary.

Solution pH	K_d (l/kg) 0.0103 g/l goethite	K_d (l/kg) 0.0206 g/l goethite	K_d (l/kg) 0.0309 g/l goethite	K_d (l/kg) 0.0412 g/l goethite
4	18790	7186	6550	6562
5	17619	6179	5378	5862
6	14803	5911	4891	4912
7	12687	5365	3864	3905
8	10281	4806	3203	3025
9	9012	4217	2221	2643
10	8228	3576	1793	1858
11	7667	3142	1240	1670

Table 5.4.1. Summary of K_d values for batch experiments.

Appendix 5B summarises the fitted isotherm parameters for the Linear, Freundlich and Langmuir models, and Table 5.4.1 summarises the Linear isotherm fitted partition coefficients for all batch experiments. These are compared in Table 5.4.2 with the partition coefficients derived from published experiments where equilibrium experiments were used. The partition coefficients derived from the current batch experiments in Table 5.4.1 are

generally larger than those of Hingston *et al.* (1971) and Bowell (1994), but within the range of those found by Matis *et al.* (1999). By contrast the Pierce and Moore (1982) values are significantly larger than the current batch experiment values. This can be attributed to the amorphous character of the Hydrous Ferric Oxide (HFO) used in their study, which has different adsorption mechanisms for the disordered crystal structure. The Hingston *et al.* (1971) coefficient is within the range of those determined from the current column experiments and the value derived by Bowell (1994) is generally an order of magnitude larger than the column values. The lower partition coefficients for the column experiments are of interest and may be the result of limited contact between arsenic and goethite. The flowing nature of the influent arsenic solution may not pass through all pore spaces or channels and hence less surface contact with the goethite. The kinetic interaction associated with adsorption processes may also limit complete adsorption, as previously discussed. The partition coefficients shown for goethite in Table 5.4.2 are for a wide range of As concentrations, from 57 μg/l used in the current experiments to 100000 μgl^{-1} used in the Matis *et al.* (1999) work. The range of goethite mass concentrations lies between 0.0103 g/l and 25 g/l. The range of partition coefficients shown in the table does not, however, seem to relate to the magnitude of the concentrations or the mass studied.

The Freundlich exponent 'n' derived herein ranges from 0.46 to 0.86 compares with those found for granular ferric oxide (0.66) and ferruginous manganese ore (0.78) by Thirunavukkarasu *et al.* (2003) and Chakravarty *et al.* (2002), respectively.

Table 5.4.2 also shows partition coefficients derived for other common soil minerals. Quartz does not significantly adsorb arsenic and this is reflected in the low partition coefficient. Goethite partition coefficients reflect the relatively high affinity for As(V) adsorption, although other minerals such as ferruginous manganese ore, birnessite and amorphous and granular ferric oxide have a much greater sorption capacity.

REFERENCE	K_d (l/kg)	As(V) Concentration (µg/l)	Adsorbent Mineral or Material
Xu *et al.* (1988)	2	71	Quartz
Bowell (1994)	25	45	Hematite (Fe_2O_3)
Xu *et al.* (1988)	34	48	Hematite
Hingston *et al.* (1971)	133	16000	Gibbsite [$Al(OH)_3$]
Hingston *et al.* (1971)	192	4900	Goethite
Anderson *et al.*(1976)	520	1200	Alumina [α-Al_2O_3]
Xu *et al.* (1988)	760	3.8	Kaolinite [$Al_2Si_2O_5(OH)_4$]
Matis *et al.* (1999)	483 – 9603	50000 – 100000	Goethite (0.1 – 2 g/l)
Bowell (1994)	1000	2.7	Lepidicrocite [χ-FeOOH)
Bowell (1994)	1800	749	Goethite (25 g/l)
Chakravarty *et al.* (2002)	7870	40 – 125	Ferruginous Manganese Ore (0.6 – 8 g/l)
Driehaus *et al.* (1995)	57500	75	Birnessite [δ-MnO_2]
Pierce and Moore (1982)	37000 – 460000	32 – 850	Amorphous – HFO (0.0045 g/l)
Thirunavukkarasu *et al.* (2003)	10.3×10^9	18.5	Granular Ferric Hydroxide (2 g/l)
Aragon and Thomson (2002)	28000 – 528000	100 – 5000	Granular Ferric Oxide (0.3 – 15 g/l)
Smedley *et al.* (2000)	1.0		Sandy Loess from Argentina: Fe = 0.0003 g/l (max = 0.00116 g/l)
Kuhlmeier (1997)	0.26 – 3.3		Sandy & Clayey contaminated soils from Texas
Smith *et al.* (2002)	3500 – 62000		Soils from Northern New South Wales, Australia (Fe = 1.3-157 g/kg)
Baes and Sharp (1983)	1.9 – 18 (av. 6.7)		Californian Soils
De Brouwere *et al.* (2004)	14 – 4430		Uncontaminated soils, Fe-rich
BGS/MML (1999)	5 – 1000		Modelled - Bangladesh Holocene aquifer sediments Fe total = 0.0003 – 0.3 g/l (as HFO)
Goldberg (2002)	660	1500	Modelled – Constant Capacitance Model (Fe = 0.5 g/l)
Vaishya and Gupta (2002)	11000 – 17000	As(III): 500 – 2000	Modelled – Active Available Site & chemical reaction rate models Fe-oxide coated sand (Fe = 20 g/l)
Current Batch Experiments	**1240 – 19790**	**150 – 1500**	**Goethite (0.0103 – 0.0412 g/l)**
Current Column Experiments	**44 – 1360**	**57 – 870**	**Goethite (0.0982 – 1.724 g/l)**

Table 5.4.2. Comparison of linear partition coefficients from previous studies with current experimental values.

5.4.2. Introducing Real Environments

5.4.2.1. Comparison with Soil Partition Descriptions

The table (5.4.2) also shows the results of natural soil partitioning of low partition coefficients and this may reflect the relatively low adsorbent mass concentrations, such as 0.00116 g/l Fe for the Argentina sandy loess or 0.003 – 0.3 g/l Fe in the Bangladesh sediments, compared to equilibrium adsorption to mono-minerals. The partition coefficients derived for the Bangladesh aquifer sediment (BGS and MML, 1999) generally lie within the range of those for the current column experiments, and also have similar adsorbent mass concentrations. The results from the batch and column experiments do not equate as well with the soil coefficients derived by Smedley *et al.* (2000), Baes and Sharp (1983) and Kuhlmeier (1997), which are much smaller than those for the current goethite sorption. Partition coefficients derived from the De Brouwere *et al.* (2004), Smith *et al.* (2002), and BGS and MML (1999) studies concerning As sorption to soils, are more in line with the values derived from the current experiments using similar As concentrations and Fe mass.

A number of factors may relate to the lower soil K_d, such as the lower adsorbent mass concentration within the natural soils, and the effect of other soil-groundwater constituents on As(V) sorption. For example, the BGS and MML (1999) study of As sorption onto the Bangladesh sediment found that As partition coefficients were much lower when in the presence of phosphate, which acts as a competing ion for available sorption sites. By contrast, Smith *et al.* (2002) determined K_d values similar to those derived for amorphous iron oxides, and they are within the same orders of magnitude as those from the current batch experiments. The higher partition coefficient may be due to the high iron content of the soils and this may not have been completely accounted for in calculating the coefficient.

5.4.2.2. *Goethite Mass within Natural Sediments*

The proportion of iron mass used within the column material (0.006 – 0.13 wt% Fe) is comparable to that of typical sediments. Bowell (1994) found that soils from the Ashanti mine area in Ghana contained 0.04 – 0.26 % Fe. Soils from New South Wales, Australia, contain 0.5 – 16 % Fe (Smith *et al.*, 2002) and the Holocene Bangladesh sediments contain 0.2 % Fe (BGS AND MML, 1999). Partition coefficients derived by all of the above studies compare well with those determined from the current experiments and therefore lend support to the validity of the parameters described by the current experiments.

5.4.2.3. *Predictive Modelling of Partitioning*

In some studies adsorption was simulated using modelling techniques, such as the Constant Capacitance Model (CCM) (Goldberg, 2002) or the Diffuse Double Layer surface complexation model (DDL) of Dzombak and Morel (1990), which was used within the BGS and MML (1999) partition prediction. These examples predict partition coefficients that are within the range of those from the current experiments, and would suggest that such methods of describing partitioning provide good descriptions. A study by Appelo and Postma (1999) who applied the DDL model in parallel with the geochemical PHREEQC model (Parkhurst, 1995) gave an excellent description of cation adsorption onto birnessite (δ-MnO_2) within a column experiment. Good model fits were also identified by Miller (2004) using PHREEQC to determine arsenic partitioning.

The application of models to predict As(III) partition coefficients for sulphate modified iron-oxide coated sand (Vaishya and Gupta, 2002) are much larger than expected. Similarly, Kent *et al.* (1995) observed that the Dzombak and Morel model over-predicted partition coefficients describing natural sediments, mostly caused by neglecting the effect of ion competition and under-estimating the Fe content within the natural sediments.

5.4.2.4. Hydraulic Conductivity Comparison with Real Sediments

Table 5.4.3 shows examples of hydraulic conductivities within various aquifer sediments where elevated levels of arsenic are known to exist.

Reference	Aquifer	Hydraulic Conductivity, K (cm/s)
Ravenscroft *et al.* (2001)	Bangladesh Holocene sediments	0.047 – 0.093
Schwartz *et al.* (1998)	Costa-Rica fine soils	0.0014
Smedley *et al.* (2002)	Argentina, La Pampa Quaternary loess	0.001
Current Column Experiments	**Quartz sand & goethite**	**0.006 – 0.03**

Table 5.4.3. Comparison of aquifer hydraulic conductivity with the current column material.

Comparison of the hydraulic conductivity shows that the column material used in the current work was comparable to previously studied As-rich aquifer sediments. Therefore, given the inverse relationship between the partition coefficient and the flow velocity observed, a similar relationship may also exist between the partition coefficient and the hydraulic conductivity within such aquifers. Therefore the partition coefficients derived from the column experiments would be applicable to aquifers with similar hydraulic conductivities. Thus, proportionally smaller partition coefficients may be expected in the marginally higher K Bangladesh sediments, and in the lower K sediments slightly larger partition coefficients are expected. These comparisons, however, do not consider the hydraulic gradient within the aquifer systems, which may induce far greater or smaller flow rates than those implied from the column model, but do provide an excellent indication of expected adsorption.

5.5. REDOX COLUMN EXPERIMENT

5.5.1. Experimental Breakthrough Curves (BTCs)

5.5.1.1. Arsenic Effluent Curves

An introduction to the redox column procedure was given in Section 2.2. The current section interprets the results arising from a change of the redox environment within a column experiment. The organic reductant used was 'Catechol'. The objective was to derive a partition coefficient under anaerobic conditions. A general investigation of the solid-phase material using Scanning Electron Microscopy (SEM) techniques was used to illustrate some of the processes occurring during reduction. Appendix 4B shows the results of a similar reducing column experiment (A).

Arsenic partitioning under the altered experimental conditions requires an estimate of the arsenic budget. This budget incorporates the following time schedule and progressive calculations:

(1) As mass influent ($t_0 - t_1$) = Calculated from As solution pumped into the column
(2) As mass effluent ($t_0 - t_1$) = Area under adsorption BTC
(3) As mass held (sorbed & in solution) within column at t_1 = (1) – (2)
(4) As mass effluent in dissolved phase, after 1 pore volume (PV) flush ($t_1 - t_2$) = Calculated from area under 1PV effluent curve.
(5) As mass remaining adsorbed or released to solution at t_2 = (3) – (4)
(6) As mass desorbed under reducing conditions ($t_2 - t_3$) = Calculated from area under reduced phase effluent curve.

Where: t_0 = Start of the complete experiment, when As in pumped into the column
t_1 = Time at which As effluent solution $C/C_0 = 1$, and the start of the DDW pore water flush.
t_2 = Time after which one pore volume DDW has been flushed through the column, and the start of the reducing phase.
t_3 = Time at the full duration of the experiment, after the reducing phase.

These terms have been highlighted on the effluent curve (Figure 5.5.1) and show the arsenic concentration in the column effluent for the full duration of the experiment. Appendix 5H shows the corresponding effluent curves for all sampling ports although for the purpose of the following description of arsenic budgeting only the Port E effluent is considered as it was the most consistent for monitoring. At the completion of the reduction experiment the arsenic concentration in the column effluent did not reach background or detection levels but remained at 10 μg/l. This suggests the establishment of a new redox equilibrium. Table 5.5.1 shows the calculation of each As mass budget term over the duration of the experiment.

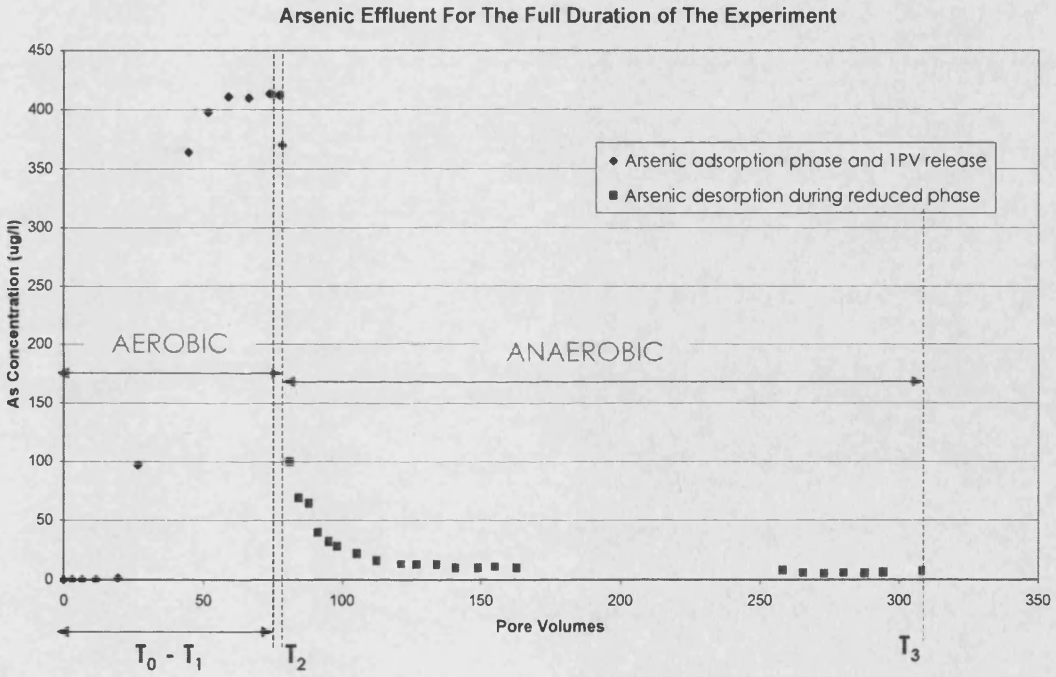

Figure 5.5.1. Effluent arsenic concentrations for the full duration of the experiment.

TERM		As MASS BUDGET (mg)
(1) As influent ($t_0 - t_1$)	(aerobic)	1.0601
(2) As effluent ($t_0 - t_1$)	(aerobic)	0.6604
(3) As held in column ($t_0 - t_1$)	(aerobic)	0.3997
(4) As effluent dissolved phase ($t_1 - t_2$)	(aerobic)	0.0160
(5) As adsorbed (t_2)	(aerobic)	0.3837
(6) As desorbed ($t_2 - t_3$)	(anaerobic)	0.1409
(7) As mass remaining sorbed (t_3)	(anaerobic)	0.2428

Table 5.5.1. Arsenic budget for the full duration of the experiment.

The integration required to determine areas at the various stages of the experimental effluent curve (Figure 5.5.1) is conveniently calculated using Simpson's Rule (Bostock and Chandler, 1993):

$$I = {}^1/_3\, d\, [\{y_0 + y_n\} + 4\{y_1 + y_3 + \ldots\} + 2\{y_2 + y_4 + \ldots.\}] \qquad \textit{Eqn. 5.5.1.}$$

Where: I = **Integrated area under the curve between x_0 and x_n (x_0 is the first point and x_n the final point along the x-axis).**
d = **Distance between uniform points x_0 and x_1**
y_m = **Corresponding value on y-axis for x_m.**

5.5.1.2. Effluent pH and Redox Potential, Eh

Figures 5.5.2 and 5.5.3 show the pH and Eh of the column effluent during the reducing phase of the experiment. As the experiment progressed the effluent pH decreased quasi-linearly from approximately 6.9 to 5.65, and the Eh increased non-linearly from approximately 104 to 212 mV. This increase may suggest that the influent solution has become contaminated with oxygen despite the care taken to minimise air ingress. Alternatively, it is possible that the catechol was exhausted by the reaction with the goethite in the column sediment. However, the Eh measurements should not be relied upon too heavily as the instrument of measurement used was not accurate and the measurement of effluent Eh was taken under aerobic conditions. The redox measurement is further complicated as the system is in disequilibrium and therefore a single redox potential cannot be accurately assigned to a particular redox species (Nordstrom and Wilde, 1998). Also, the presence of more than one redox element (Fe and As) within the system may obscure an individual Eh measurement and therefore under these dynamic conditions a single measurement may not be entirely representative (Nordstrom and Wilde, 1998).

Taking into account the difficulties associated with the redox measurements the actual species of arsenic and iron present cannot be accurately confirmed without further speciation analyses. A tentative suggestion as to the possible

species present has been made using the redox diagrams (Sections 1.4 and 1.5), although this must only be considered as a suggested speciation. The arsenic in the effluent throughout the reducing experiment was on the boundary between the As(V) acid species and the As(III) acid species (Section 1.4, Figure 1.4.1). The release of the acid series into solution may promote the apparent decrease in effluent pH. Therefore during the course of the anaerobic experiment the arsenic in solution is probably a mixture of As(V) and As(III), and the desorption of arsenic from the goethite is a consequence of both arsenic and iron reduction.

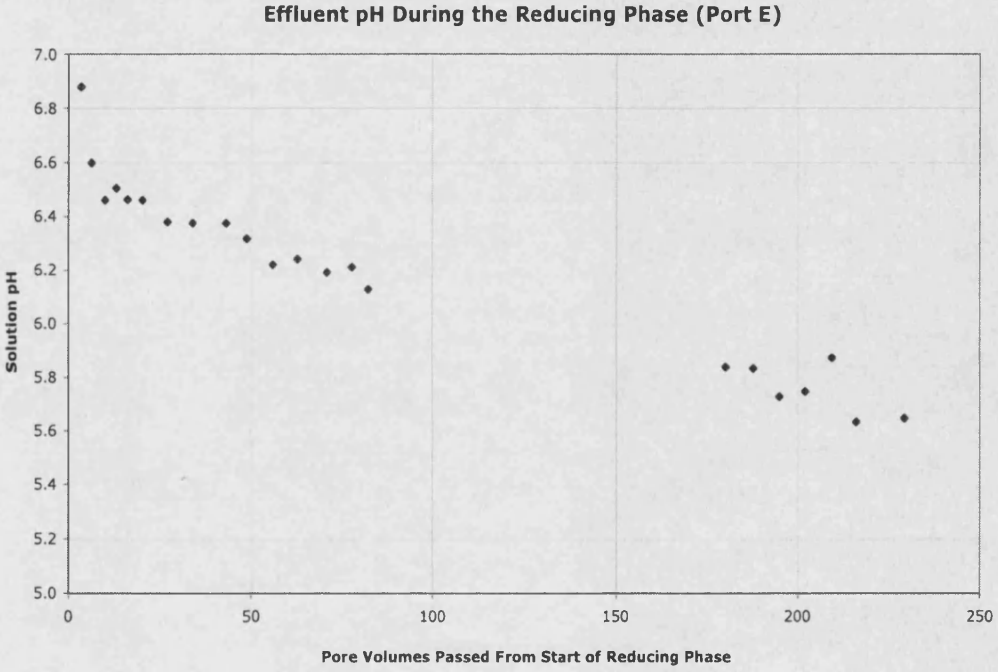

Figure 5.5.2. The effluent (port E) solution pH during the course of the reducing experiment.

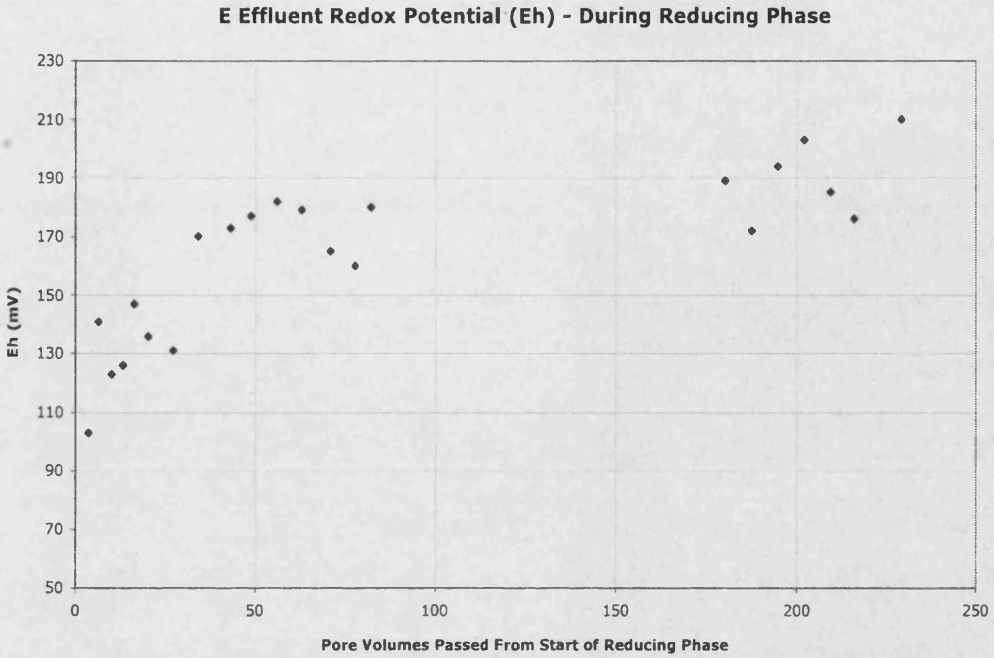

Figure 5.5.3. Redox potential (Eh) of the effluent solution during redox experiment 1.

5.5.1.3. Iron Effluent Curve

In considering the mechanism for arsenic release the dissolution of the solid-phase goethite must also be considered. Figure 5.5.4 shows the iron concentration determined from the column effluent during the reducing phase. This curve indicates that an initial high mass of iron is released into solution and the concentration thereafter decreases towards a long-term equilibrium value of 290 μg/l as the experiment continues to its full duration. This also suggests that a new equilibrium environment was achieved. With the use of the Eh-pH diagram for the Fe-O-C system (Section 1.4, Figure 1.4.4) the movement of iron species can be implied. However, it is important to note that there are limitations and difficulties relating to the measurement of redox potential. For example, the presence of mixed couples within the system could result in mixed Eh values that do not represent the true system. Also, the system is in disequilibrium and therefore it is difficult to assign the redox potential to the relevant redox species (Nordstrom and Wilde, 1998). At the start of the

reducing experiment the iron in the column effluent is in the oxidised form (Fe(III)) and as the experiment continues, the iron changes to the reduced form (Fe(II)). The Eh-pH relationships alone therefore suggest that arsenic in this experiment is released by both reductive dissolution of goethite and reduction of arsenic. The reduction of iron species within goethite by catechol has also been observed by Pracht *et al.* (2001) and Yoshida and Nakoshima (2000). Further evidence for this is described later in Section 5.5.2. The slow steady release of Fe(II) was also observed by Haury (2001) in column experiments similar to the current study (Figure 5.5.5). Haury (2001) attributes the overall release of arsenic from goethite to arsenic reduction at the iron hydroxide surfaces and to solid-phase reductive dissolution.

Figure 5.5.4 also shows a minor peak of iron concentration in the column effluent at about 65-70 pore volumes during the reducing phase, and comparison with the Eh variations (Figure 5.5.3) demonstrate that this corresponds to a minor decrease in the Eh. The slight change towards more reducing conditions encourages further reductive dissolution of iron. The iron effluent variation observed by Haury (2001) (Figure 5.5.5) also shows small perturbations in the solution concentration, but relate more closely to the variations in the effluent pH, which suggests that some iron reduction and dissolution occurs. The small dips in aqueous iron in the effluent solution may result from the formation of a secondary phase. Although SEM images taken after the reduction stage do not show evidence for this (Figure 5.5.8). It may also be possible that these dips represent periods where iron is re-incorporated into the goethite structure and this could be confirmed using geochemical or atomic-scale models. This could arise with reduction of sorbed arsenic and subsequent electron transfer from iron to arsenic resulting in oxidation of Fe(II) and re-sorption of Fe(III). This is a more likely reason for the apparent decline in released iron and was also observed in some previously published work (Stollenwerk, 2003).

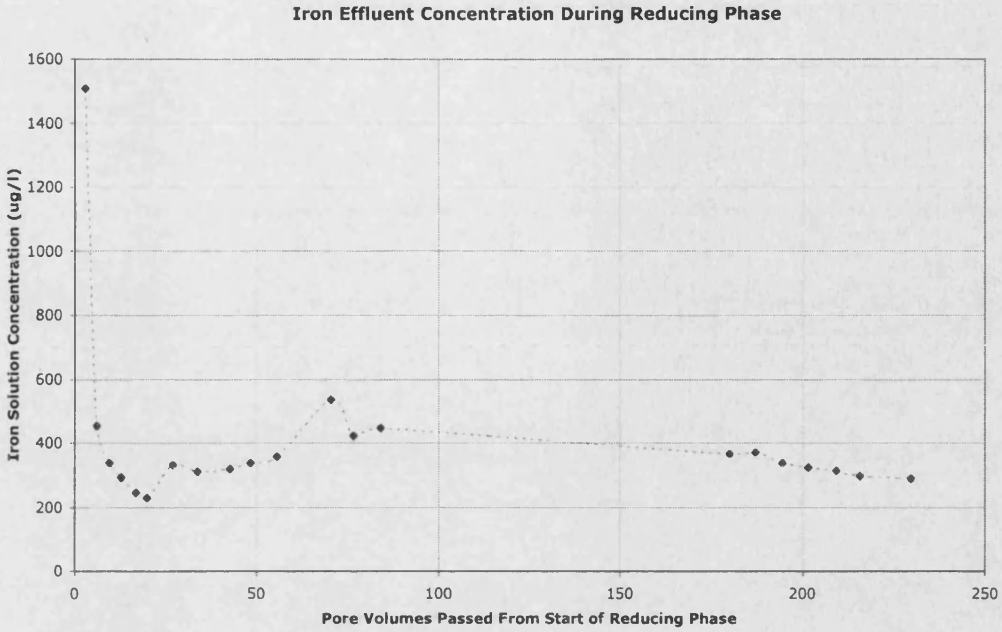

Figure 5.5.4. Iron released after the introduction of catechol, during the anaerobic phase.

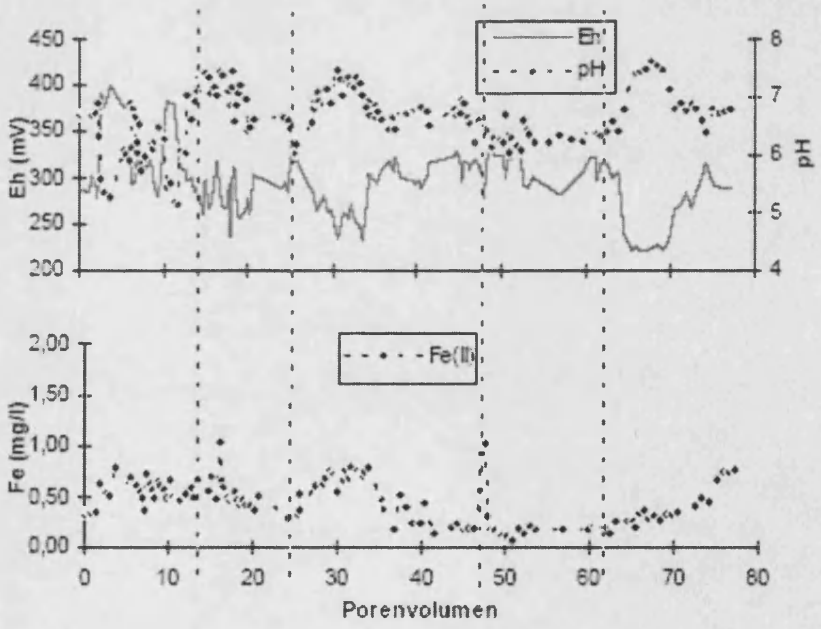

Figure 5.5.5. Iron release and the Eh and pH in the effluent of reducing column experiments with respect to pore volumes passed through the column. Taken from Haury (2001).

As goethite is dissolved during the progress of the experiment, it must be accounted for in the final determination of arsenic partitioning. Therefore an iron mass budget was calculated to account for the mass of goethite released during reduction. The results show that 0.32 g of Fe was released during the reducing phase. this corresponds to 55 % of the original iron mass (0.58 g of Fe within 0.92 g goethite) in the column sediment.

Although iron release had not ceased on completion of the experiment, the mass released during the reducing phase corresponds to similar proportions of iron reduction observed by Pracht *et al.* (2000). Pracht *et al.* (2000) found that for 10 μmol catechol solution 50-60 μmol Fe(III) was reduced. The present experiment used approximately 1000 μmol catechol and initially 10000 μmol of Fe(III) in goethite. Reduction was approximately half this amount on completion of the experiment, which closely corresponds to the relative proportions observed by Pracht *et al.* (2000).

5.5.2. Investigation of The Solid Phase

Microscopic methods were employed to observe physical changes in the solid phase material as a consequence of reduction. High magnification, good resolution photographs using a Phillips SEM aided the inspection of column material pre- and post-reduction. Figure 5.5.6 shows the column material before reduction. The large grains (~ 3 μm x 3 μm) are quartz and the acicular goethite crystals (~ 0.25 μm x 1.5 μm) are interspersed between them.

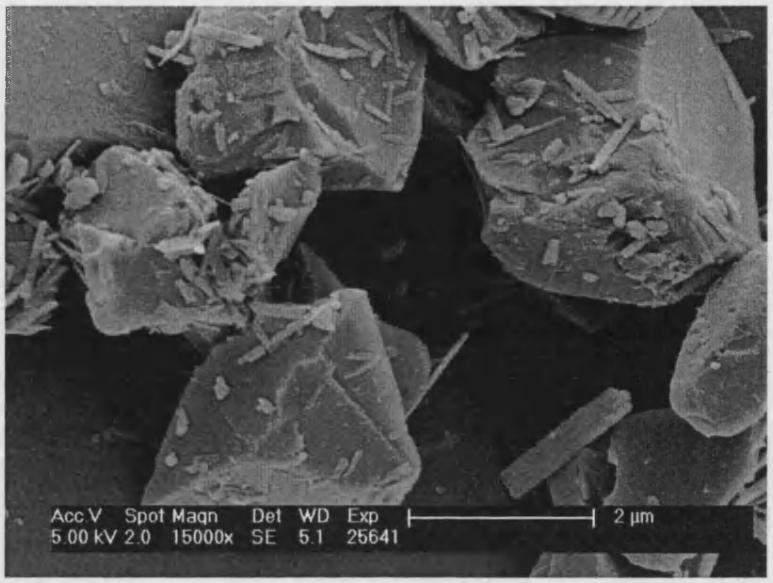

Figure 5.5.6. The column material before reduction.

Figure 5.5.7 shows a pre-reduction image of column material at a greater magnification to illustrate the relative abundance of goethite. This is compared with a similar image taken post-reduction (Figure 5.5.8).

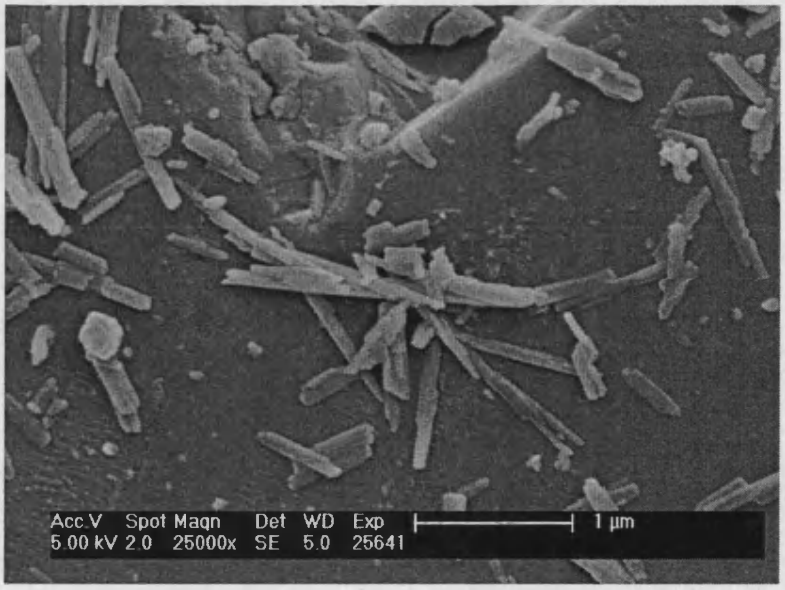

Figure 5.5.7. The column material before reduction at greater magnification.

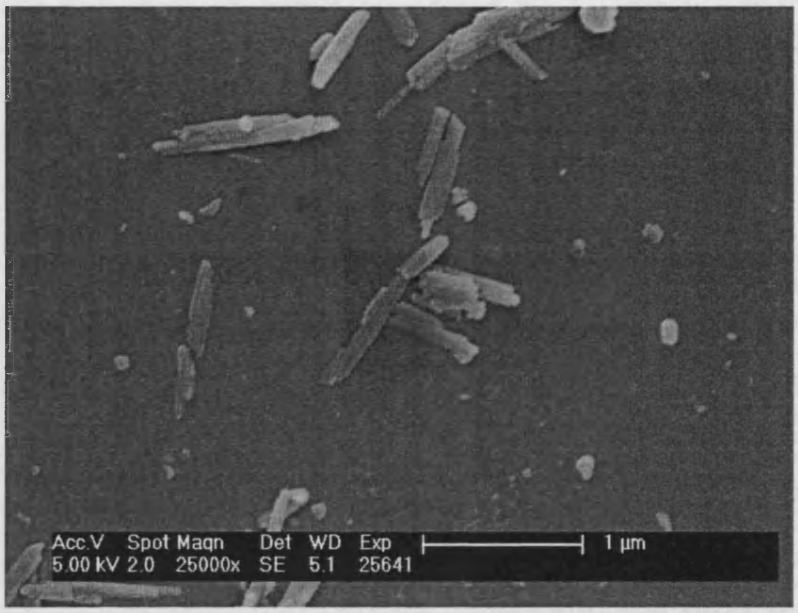

Figure 5.5.8. Column material after reduction.

The images do not quantitatively prove the decline of solid phase goethite resulting from reductive dissolution. However, they are illustrative of the Fe budgeting which demonstrated that in excess of 50 % of goethite was dissolved and also that dissolution was incomplete.

The JEOL SEM is able to scan small areas (10 x 10 µm) and perform spectral elemental analysis within that area to provide a tentative assessment of the presence of arsenic and iron before and after reduction. Examples of JEOL SEM images and spectra are shown in Figure 5.5.9 where typical clusters of goethite within the column material after the adsorption of arsenic but before reduction is shown. The corresponding elemental spectrum highlights the presence of silica within the underlying quartz particles, iron from the goethite on the particle surface and also the presence of small quantities of arsenic.

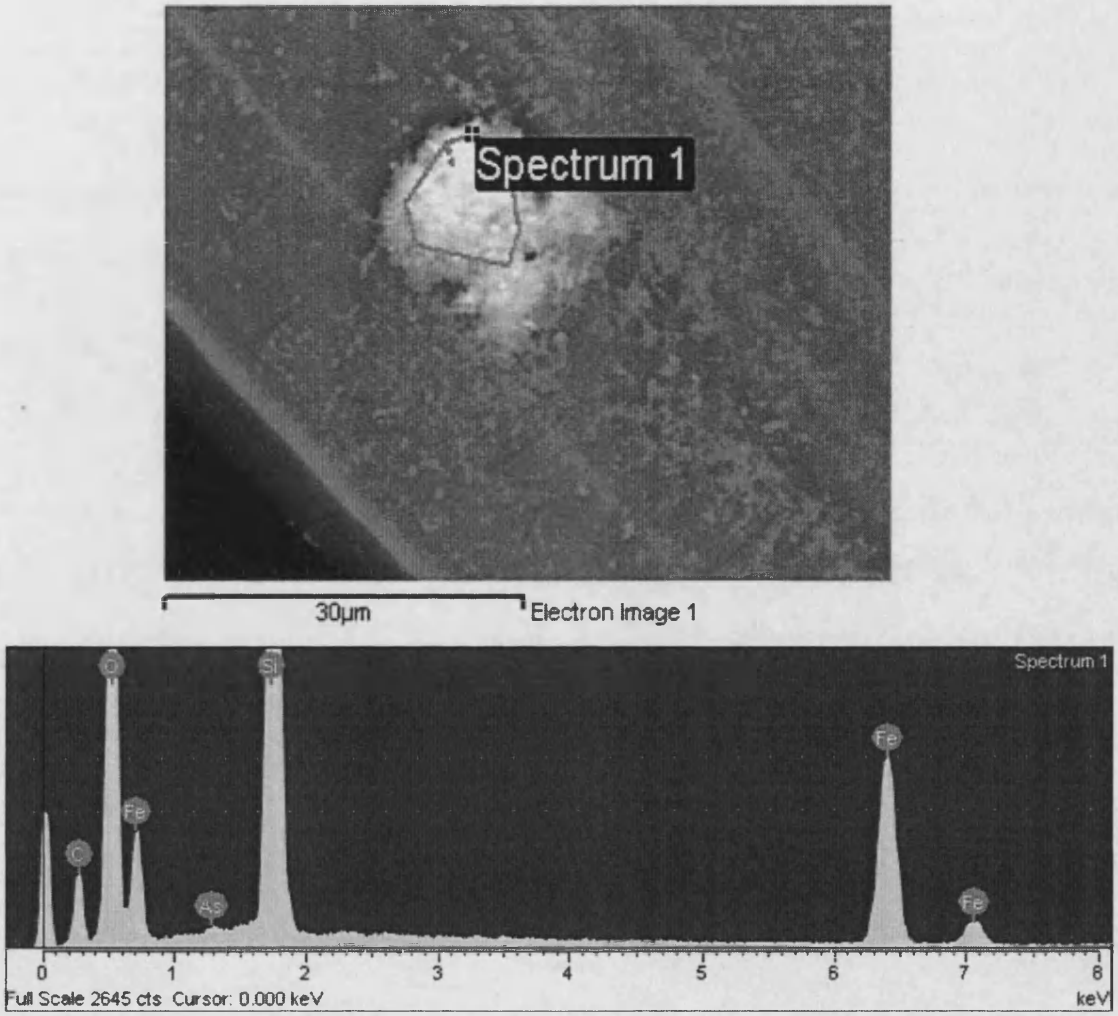

Figure 5.5.9. JEOL SEM spectra from a goethite cluster within the column material after arsenic adsorption and before the reducing phase. The As peak exists at 1.3 keV, Fe at 0.6, 6.4 and 7.1 keV and Si at 1.8 keV.

By contrast Figure 5.5.10 shows the spectrum obtained from the column material after reduction and illustrates the presence of silica and iron with the absence of arsenic. This technique requires collation of many results in order to build up a statistically accurate description of the elemental analysis, and this would require further study. Appendix 5I contains a selection of examples of the spectra measured including those of the column material before the

adsorption of arsenic to confirm the absence of arsenic before the experiment commenced.

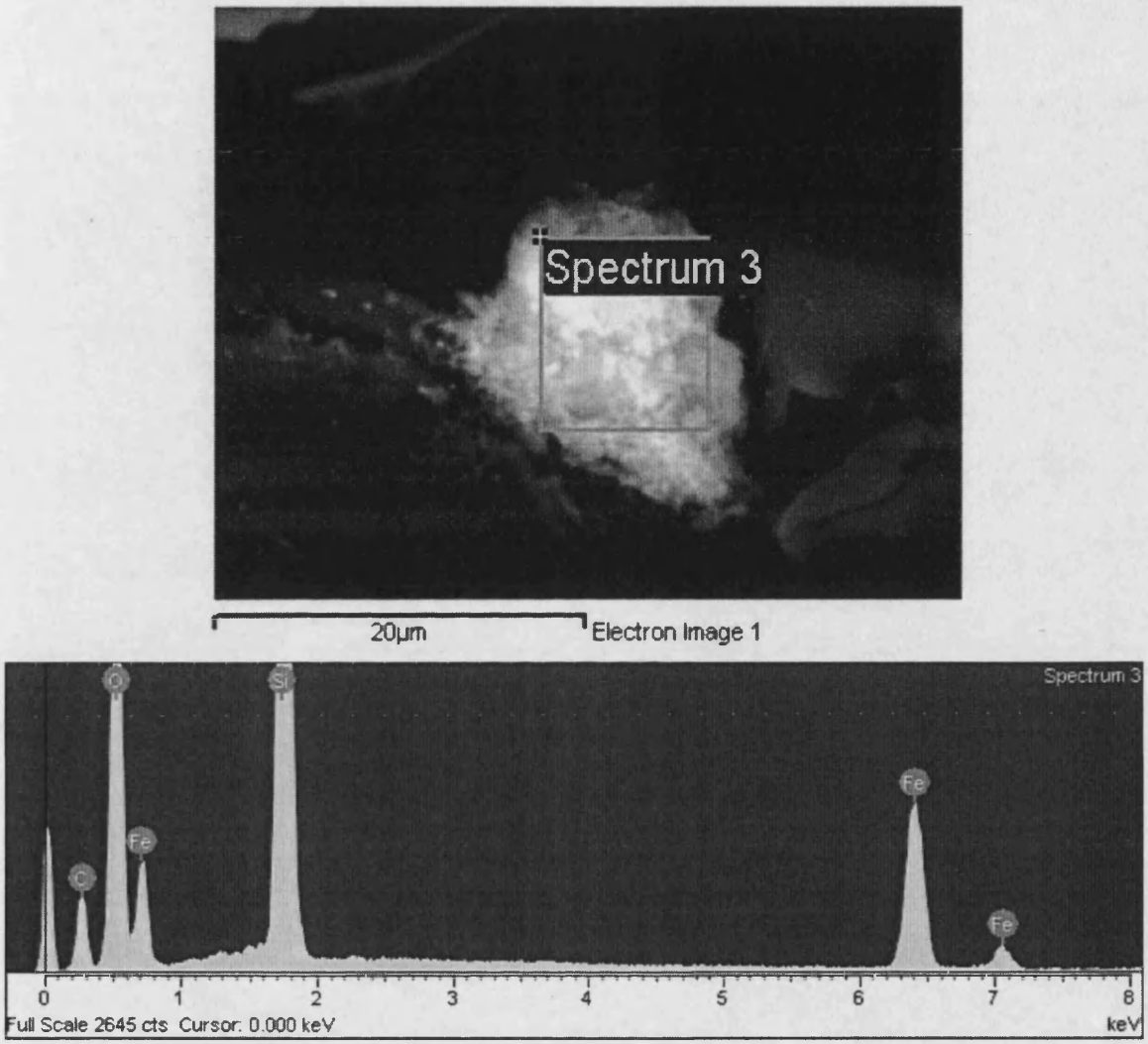

Figure 5.5.10. Elemental spectra of column material after reduction.

5.5.3. Anaerobic Arsenic Partitioning and Discussion

Partitioning of arsenic between the sorbed and solute phases with a pseudo-partition coefficient is presented below, using the arsenic and iron mass budgets for different stages of the experiment (Section 5.5.1). Although the adsorption of arsenic may in actuality be non-linear, it is only possible to describe the pseudo-coefficient in linear form and therefore the description is approximate and overestimation is expected. As a comparison the aerobic partition coefficient was derived for the arsenic adsorption column experiment using an integration method described by Appelo and Postma (1994):

$$S_1 - S_2 = \int_{C_2}^{C_1} V^* \, dC \qquad \text{Where } V^* = \frac{dS}{dC} \qquad \textit{Eqn. 5.5.2.}$$

S = Sorbed mass of arsenic per unit mass goethite (mgg^{-1})
C = Concentration of arsenic in effluent (mgl^{-1})
dS/dC = Gradient of adsorption isotherm

Therefore the pseudo-partition coefficient for aerobic adsorption of arsenic is:

$S_1 - S_2 = 0.3997$ mg As *(3)*

$$\therefore \text{ per g goethite} = \frac{0.3997 \text{ mg}}{0.92 \text{ g}} = 0.435 \text{ mg/g}$$

$C_1 - C_2 = 0.413 \text{ mg/l} - 0 = 0.413 \text{ mg/l}$

$$\therefore K_{ox} = \frac{0.435 \text{ mg/g}}{0.413 \text{ mg/l}} = 1.052 \text{ l/g}$$

$$= 1052 \text{ l/kg}$$

The number in brackets and italics relates to the arsenic budget term derived and presented in Table 5.5.1.

BIO1D was also used to fit a linear partition coefficient to the aerobic breakthrough curve. The derived coefficient was corrected for the bulk density

and relative proportion of goethite mass within the column as described in Section 5.3. The resulting partition coefficient K_d is 2041 l/kg and is approximately twice as large as the value determined from the integration method, but within the same order of magnitude.

The integration method was also applied to the reduction phase. Although in this case the reductive dissolution of solid-phase iron was considered and the remaining goethite mass was that used for derivation of the pseudo-partition coefficient.

$$S_1 - S_2 = \left\{ \begin{array}{c} \text{Area under reduced-phase curve between 0 and 0.370 mgl}^{-1} \text{ As concentration } (C_1) \end{array} \right\} - \left\{ \begin{array}{c} \text{Area under reduced-phase curve between 0 and 0.008 mgl}^{-1} \text{ As concentration } (C_2) \end{array} \right\}$$

$= \{0.1409\} - \{0.0609\}\ (6) = 0.08$ mg

$$\therefore \text{per g goethite} = \frac{0.08\ \text{mg}}{0.603\ \text{mg}} = 0.133\ \text{mg/g}$$

$C_1 - C_2 = 0.370 - 0.008 = 0.262$ mg/l

$$\therefore K_{red} = \frac{dS}{dC} = \frac{0.133\ \text{mgg}^{-1}}{0.262\ \text{mgl}^{-1}} = 0.508\ \text{l/g}$$

$$= 508\ \text{lkg}^{-1}$$

The redox K_{red} lies within the range of the partition coefficients derived for the aerobic column experiments described in Section 5.3. However, as other experimental variables such as flow velocity and goethite mass may interfere with the description of arsenic partitioning, a more useful comparison is between the aerobic and anaerobic pseudo-coefficients. The comparison between K_{ox} and K_{red} shows that K_{red} is half of the K_{ox} value. This could have a significant effect on macroscopic scale transport models used to simulate and predict arsenic transport in anaerobic aquifers such as Bangladesh. These

currently rely on partition coefficients derived in aerobic conditions and may be over-predict the actual adsorption (Cuthbert, 1999 & BGS and MML, 1999).

The lower anaerobic partition coefficient in this experiment is due to reductive dissolution of the solid-phase iron and the reduction of arsenic species. Further work should include imposing a range of reducing environments and investigate arsenic desorption following reduction of iron or arsenic only.

The partition coefficients derived for the current reduction experiment incorporate arsenic release under two modes, one owing to reduction of the goethite and subsequent arsenic release and the other due to desorption of As into the catechol solution (initially free of As). The derived pseudo-partition coefficient describes anaerobic partitioning of the sorbed mass as a result of goethite dissolution during the reduced phase. However, re-partitioning of the sorbed mass because of desorption was not considered and was expected to remain invariable throughout the experiment.

There are other complications that may affect the reduced phase partition description and some were identified by Haury (2001). Haury (2001) found that the mechanism for arsenic release within a reduced environment using catechol as the reductant was generally by arsenic reduction (As(V) to As(III)) and simultaneous goethite reduction and dissolution. However, further complications arise as some of the reduced arsenic was re-oxidised by goethite and re-adsorbed onto the remaining solid phase.

6. AN INTRODUCTION TO ATOMISTIC MODELLING

6.1. INTRODUCTION

Mathematical and computer models have a versatility and power that allows for an understanding and manipulation of real world environments. Combined with experimental information, the application of atomic scale models can achieve greater accuracy and insight into the chemical and physical processes. This chapter describes the foundations of atomistic models and their use for bulk, surface and interaction structure derivation.

Previous chapters investigated and described the quantitative and qualitative adsorption of arsenic onto goethite surfaces by experimental methods and explored the transport mechanisms involved. Although the results from the experimental work provide information about the sorption behaviour at the macroscopic level, they do not give an appreciative insight into the molecular scale interactions. Atomistic simulation allows for greater insight of these interactions. The combination of experimental and atomistic simulation results provides for a more comprehensive model to describe the interactions between arsenic and goethite mineral surfaces.

The atomistic modelling approach involves the description of atomic-scale interactions within crystalline systems and the determination of the energetics of such systems. These models are used in the prediction of properties of solids that cannot be ascertained otherwise than under extreme conditions, such as high pressures and extreme temperatures (Cygan, 2001). The models are also used to simulate structural and physical properties of solid materials leading to determination of their thermodynamic, kinetic and spectroscopic properties (Gale, 2003).

Computational techniques are based on *ab initio* quantum mechanics or on classical mechanics theory. The approach described in this chapter is based

on the Born model of solids (Born and Huang, 1954) using classical mechanics to describe the effective forces acting between atoms, and hence to calculate the lattice energy.

6.2. INTERATOMIC POTENTIALS

6.2.1. Total Energy

The Born model treats a solid as a number of point charges, separated by both short-range and long-range electrostatic forces (Cormack, 1999). It calculates the total energy of the system from the summation of many-body terms, of which there are a near infinite number; each term describing the atomic interactions with neighbours (Gale and Rohl, 2003).

Total Internal Energy within System (Gale and Rohl, 2003):

$$U = \sum_{i=1}^{N} U_i + 1/2\sum_{i=1}^{N}\sum_{j=1}^{N} U_{ij} + 1/6\sum_{i=1}^{N}\sum_{j=1}^{N}\sum_{k=1}^{N} U_{ijk} + ... \qquad \textit{Eqn. 6.2.1.}$$

U = Internal energy of the system (eV or kJ/mol)
i,j,k = Neighbourhood atoms positioned by vectors i, j and k
N = Total number of atoms

6.2.2. Two-Body Coulombic Term

The long-range term describes the coulombic (electrostatic) component of the two-body lattice energy contribution (Catlow, 2003):

$$U_{ij}(\mathbf{r_i},\mathbf{r_j}) = \frac{q_i q_j}{r_i r_j} + V_{ij}(\mathbf{r_{ij}}) \qquad \textit{Eqn. 6.2.2.}$$

$\mathbf{q_i}$,$\mathbf{q_j}$ = Electrostatic charge of two interacting ions i and j (eV)
$\mathbf{r_{ij}}$ = Distance between two ions (i and j) (Å)
$\mathbf{V_{ij}}$ = Non-coulombic two-body term

They do not encompass bonded interactions but describe charged particle force fields, which vary inversely with the distance (r_{ij}) between two particles i and j within ionic and semi-ionic compounds (Steele *et al.*, 2000). This is usually

the most dominant term within the calculation of total energy, especially in oxides where it can contribute up to 90 % of the total energy (Gale and Rohl, 2003).

Unless the structure to be modelled is very simple and highly symmetric, then the 1/r term within the coulombic energy function presents difficulty in the converging procedure. By application of the Ewald transformation (Ewald, 1921) that replaces the inverse distance term of the equation with a Laplace transform, dividing it into two series, one in real space and the other in reciprocal space, the series converges much faster (Leach, 2001).

6.2.3. Two-Body Non-Coulombic Term

The short-range components of the lattice energy summation account for bonded (for example O–H) and non-bonded interactions and include the effect of Van der Waals Forces (Steele *et al.*, 2000). The non-bonded pair-wise short-range potentials include repulsive and attractive contributions. The Lennard-Jones potential describes such reactions and is usually applied to models of rare gas and molecular crystals (Catlow, 2003).

The Lennard-Jones energy contribution (V_{ij})(Wimmer, 1996):

$$V_{ij} = \underbrace{(A_{ij}/r_{ij}^{m})}_{\text{Repulsive Term}} - \underbrace{(B_{ij}/r_{ij}^{n})}_{\text{Attractive Term}} \qquad \textit{Eqn. 6.2.3.}$$

A & B = Fitted parameters acting upon two atoms i and j(evÅ)
r_{ij} = Distance between two atoms i and j (Å).
m = Usually 12
n = Usually 9

Another short-range pair-wise potential frequently used with modelling ionic and semi-ionic materials is the Buckingham Potential (Collins and Catlow, 1992).

Buckingham Potential Equation (Gale, 1997):

$$V_{ij} = \underbrace{A_{ij} \exp(-r_{ij}/\rho)}_{\text{Repulsive Term}} - \underbrace{(C_{ij}/r_{ij}^{6})}_{\text{Attractive Term}} \qquad \textit{Eqn. 6.2.4.}$$

A_{ij} = Fitted parameter describing atom i and j interaction (eV)
r_{ij} = Distance between 2 atoms i & j (Å)
ρ = Potential Parameter related to the hardness of the ions (Å)
C_{ij} = Fitted parameter describing atom i and j interaction (eV Å)

Figure 6.2.1 shows an example of the effect of the Buckingham potential on the total energy for two-body interactions, using the Fe^{3+}–O^{2-} interaction described for the current simulations. The minimum point at 1.4 Å on the total energy curve defines the equilibrium separation between ions i and j. Repulsive forces are greatest when the inter-ionic distance are very small, usually less than 3 Å, and the Buckingham potential energy comprises mostly repulsive forces. At such distances the interaction energy between the atoms is mainly due to nuclear repulsion and is described as an exponential function of 1/r (Leach, 2001).

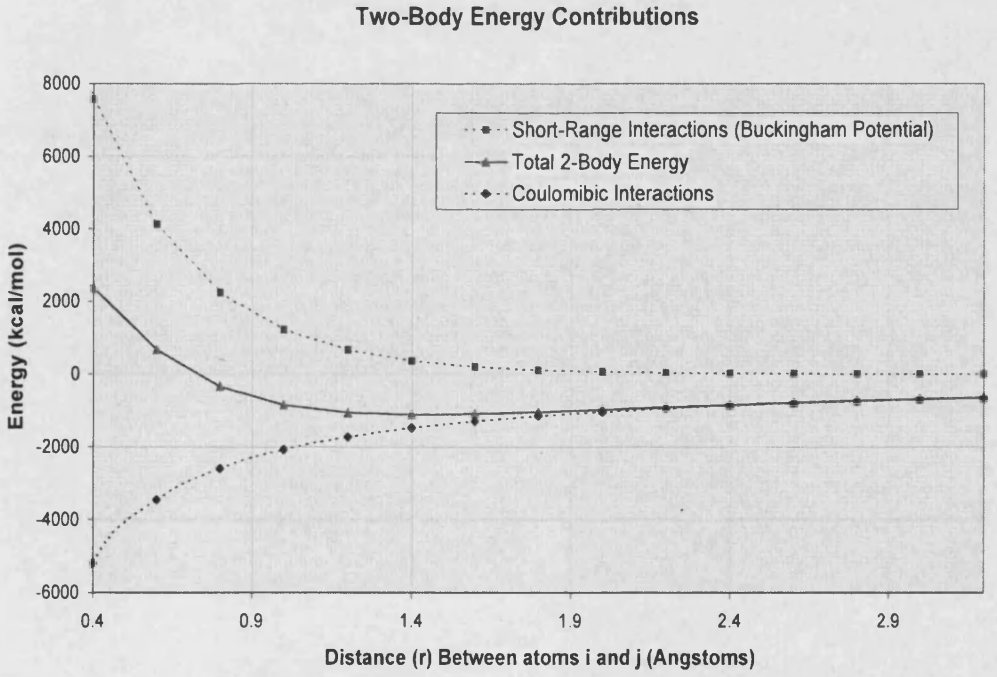

Figure 6.2.1. The effect of ionic forces contributing to two-body energy. This illustration uses the parameters for the Fe^{3+}–O^{2-} interactions used in subsequent modelling.

To describe the short-range interactions in covalently bonded systems the Morse potential is commonly used. This is an alternative two-body function that allows the molecular and partial covalent nature within materials to be modelled, and generally excludes the coulombic term (Gale and Rohl, 2003). This potential can be applied to diatomic molecules such as O–H and to molecular anionic species like carbonate ions (Gale, 2001).

The Morse potential energy contribution (Cygan, 2001):

$$V_{ij} = D_0 [1 - \exp\{1 - \alpha (r_{ij} - r_0)\}]^2 \qquad \textit{Eqn. 6.2.5.}$$

V_{ij}	=	Two-Body Morse potential energy (eV)
D_0	=	Equilibrium dissociation energy (eV)
r_0	=	Equilibrium distance between two atoms (i and j) (Å)
α	=	Parameter related to the vibrational stretching force constant ($Å^{-1}$).
r_{ij}	=	Distance between two atoms i and j (Å)

6.2.4. Ion Polarisability

To describe the polarisable nature of many ionic and amorphous materials, the two-body terms, such as the Lennard-Jones or the Buckingham potential, can be expanded to include a shell model. The polarisability should be included when modelling ionic materials, as the electrostatic term is more important and the partitioning between electron densities must be explained. The polarisation term describes the total ionic charge partitioning between the core and the shell of an atom ($q_{total} = q_{core} + q_{shell}$). The Dick and Overhauser (1958) 'Shell Model' is widely accepted as a suitable description of the polarising effects of ions. Their mechanical shell model treats a polarisable ion, such as oxygen, as comprising two parts: a core and a shell (Figure 6.2.2). The ion core is generally assigned a positive charge and consists of the nucleus and inner non-valence electrons and contains all of the ionic mass. The negatively charged shell, however, is considered mass-less and is built up of the valence electrons. The core and shell are screened from one another coulombically and their interaction is modelled by a harmonic spring.

The following equation describes the polarisability (α) (Gale, 2001).

$$\alpha = q_{shell} / (K_{cs} + F_{shell}) \qquad \textit{Eqn. 6.2.6.}$$

K_{cs} = Harmonic spring constant ($eV\text{Å}^{-2}$)
F_{shell} = Force constant, describing forces on shell resulting from the local environment.
q_{shell} = Ionic charge of shell (eV)

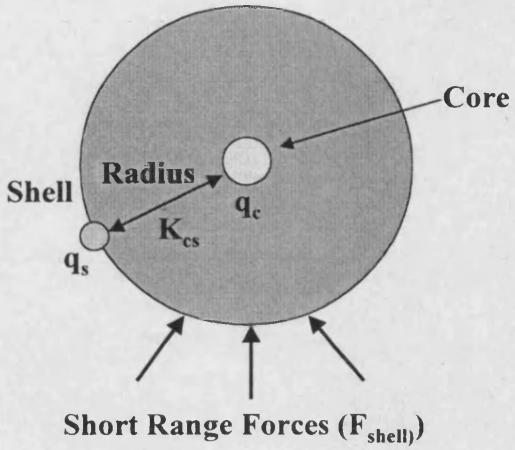

Figure 6.2.2. Illustration describing the shell model for polarisability (reproduced from Gale, 2001).

Application of the shell model allows a number of detailed structural properties to be assessed, such as the elastic, dielectric and diffusion coefficients (Cygan, 2001). The application of the ionic polarisation has proven to be more effective for atomic interaction descriptions than a point dipole approach (Catlow, 1977).

6.2.5. Three-Body Term

In structures that are not entirely ionic, a three-body term is included within the lattice energy calculation and gives directionality to the bonding:

Three Body Energy Term (Harmonic & Exponential) (Gale, 1997):

$$U_{ijk} = {}^1/_2\, k_2 (\theta_{jik} - \theta_0)^2 \exp(-r_{ij}/\rho) \exp(-r_{ik}/\rho) \qquad \textit{Eqn. 6.2.7.}$$

k_2	=	Potential parameter (eVrad^{-2})
θ_0	=	Equilibrium angle (Rad)
ρ	=	Potential parameter (Å)
r_{ij} or r_{ik}	=	Distance between 2 atoms (i & j or i & k) as a vector
θ_{ijk}	=	Angle between two inter-atomic vectors i-j & j-k (Rad)

The three-body term has been used extensively to describe bond bending that occurs around tetrahedral cations, for example O–Si–O within silicate and aluminosilicate minerals. Sanders *et al.* (1984) found that using two-body terms within the model of α-SiO_2 resulted in poor structure representation. The three-body bond-bending term was required to account for the partial covalency within the crystal. Other examples where the inclusion of a three-body term has significantly improved the simulations include feldspar lattice energy minimisations (Purton and Catlow, 1990), magnesium silicates (Parker and Price, 1985) and uranium dioxide (Steele *et al.*, 2002). The three-body term is currently used to model most tetrahedral ions that display both ionic and covalent bonding.

6.3. POTENTIAL FITTING

The variable potential parameters such as A, B, C and ρ in the Lennard-Jones and Buckingham two-body potentials are derived through a least-squares fitting procedure and the Root Mean Square Distance (RMSD) d_{RMS} equation (Leach, 2001):

$$d_{RMS} = \sqrt{\frac{\sum_{i=1}^{N} d_i^2}{N}} \qquad \textit{Eqn. 6.3.1.}$$

N = Number of atoms included within the RMSD calculation
d_i = Distance between co-ordinates of atom i in both the simulated structure and the known structure.

In essence the fitting procedure allows the potential parameters to reach a value in which the theoretically derived structure corresponds closely to an experimentally observed structure. Incorporation of elastic constants and vibrational spectra can also be used to enhance the fit of the potentials.

An important intrinsic requirement for the potential parameters is to define the range over which they are valid. Increased distance between two atoms leads to weaker interactions between them and essentially invalidates the potentials used to describe the interactions. Limiting the distance over which the potentials can act leads to simplification of the simulation and therefore a reduction in the computational time and effort required. This distance is known as the 'cut-off' and is applied mainly to radial distances. The potential is constrained to be omni-directional within the maximum distance. It is also possible to define a minimum radial distance for which the potential can act and hence enabling multiple cut-off ranges within that potential and so allowing overlap between potentials (Gale and Rohl, 2003).

6.4. BULK STRUCTURE MODELLING

In order to successfully simulate the bulk structure of any material it is fundamental for a minimisation procedure to reach a stable structure. Geometrical optimisation provides one method for obtaining stable structural configurations and is achieved with repeated sampling of the PES (potential energy surface) until a potential energy minimum is obtained (Cygan, 2001). Altering the energy of the system by changing the position of the atoms allows movement along the potential energy surface to occur, until a conclusion is reached when the minimum energy, or stationary points are found corresponding to stable structures (Leach, 2001).

The minimum energy is obtained when there are no longer any differential forces acting upon the atoms. Initial tolerances for the energy difference and derivatives need to be specified, and when these are satisfied the minimisation method is complete. Sometimes the true global minimum and most stable structure is not found and the minimisation leads to a local minimum (Cygan, 2001).

Usually minimisation of bulk structures is performed at constant pressure as simulated by allowing variation of the cell parameters until no net forces act upon the simulation cell boundaries (Cygan, 2001). For the most successful type of minimisation or optimisation no constraints should be applied, although this is not common, and usually constraints such as the symmetry are fixed.

A number of algorithms are used for the minimisation, including line searches, steepest gradient methods, conjugate gradients and the Newton-Raphson method. The Newton-Raphson algorithm calculates the first and second derivatives of the energy in order to define a suitable path along the potential energy surface on route towards the minimum energy configuration. It does this by using a Hessian approximation in order to establish the search direction (x) during the minimisation procedure (Gale, 2001):

$$(x = -H^{-1}\mathbf{g}) \qquad \textit{Eqn. 6.4.1.}$$

H = Hessian matrix
g = Gradient vector

The Newton-Raphson algorithm has been used comprehensively within such calculations. Another algorithm that is often used, especially to accelerate minimisation towards the end of an optimisation, is the RFO (Rational Functional Optimisation) (Gale and Rohl, 2003). The RFO method applies the Newton-Raphson approach to find minimum points and then locates the various possible routes for change (transition states) on the PES for any given position. The step sizes chosen are small enough to promote convergence to transition states.

6.5. SURFACE SIMULATIONS

Surface simulations are either two dimensional, with a periodic repeat in x and y, or three-dimensional where repeating slabs are separated by a vacuum gap (Gay and Rohl, 1994). In the two-dimensional approach the surface is considered as a 'block' divided into two regions (Figure 6.5.1a). The first, upper region (IA) is made up of the surface atoms that are allowed to relax during the simulation until there are no longer forces acting upon them. Those atoms within the lower region (IIA) are held fixed at their optimised positions and reproduce the effect that the bulk has upon the surface (Gay and Rohl, 1994). Regions IB and IIB similarly describe interactions with other crystal surfaces or with molecules whereby region IIB remains empty (Figure 6.5.1b). The thickness (or region size) of these two regions is important. Region (II) must be large enough to ensure that the bulk potential is reproduced while region (I) must be of an appreciable size so that the surface energy can converge.

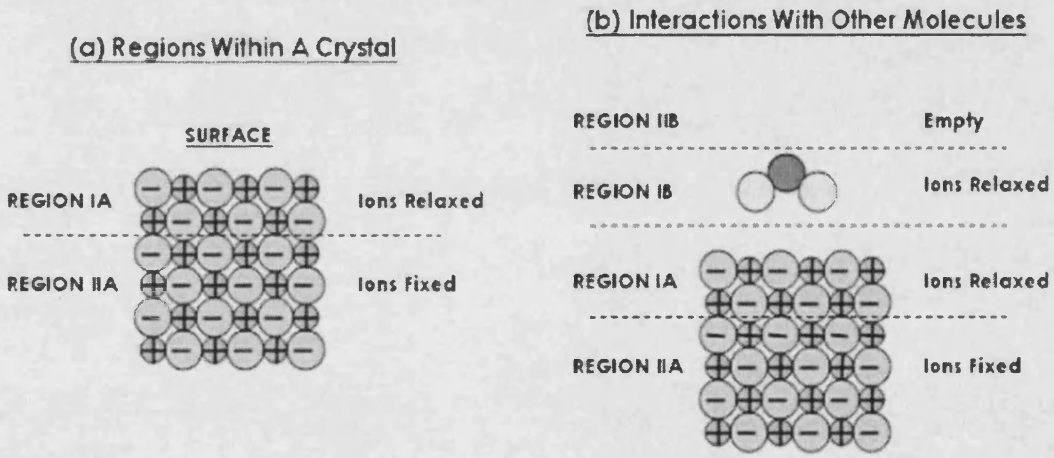

Figure 6.5.1. Illustration of the two region surface model (reproduced from Gay and Rohl, 1994).

When the structure is cleaved to obtain a particular plane the resulting surface may not always be charge neutral. Sometimes a dipole arises across the crystal as a result of the atomic configuration of the surface terminations. Tasker (1979)

defined three types of surface (I, II, III) that can form during the cleavage process (Figure 6.5.2).

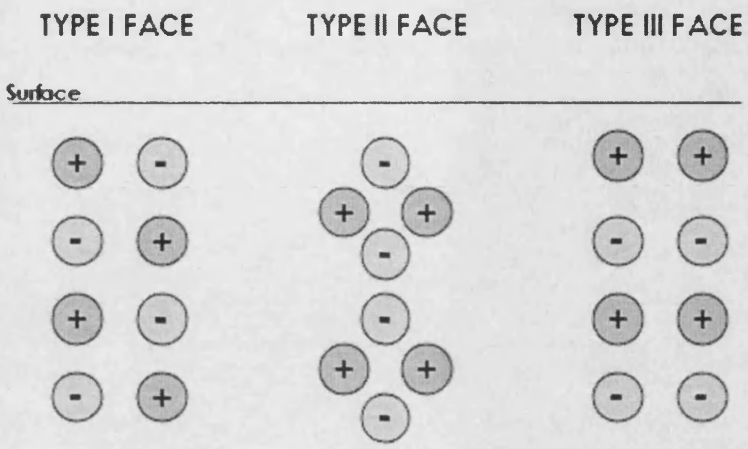

Figure 6.5.2. Schematic illustration of the three types of faces that can arise on crystal cleavage (reproduced from Wright *et al.*, 1998)

The first type of surface (I) shown in Figure 6.5.2 is one where no dipole arises and the particular arrangement of anions and cations gives rise to a net neutral surface charge. With the Type (I) surfaces it is possible to cleave the crystal at any depth along the plane and always encounter a neutral surface. The Type (II) surfaces comprise of charged planes, which can be cleaved at particular depths to obtain no charge in the repeat unit with neutral surfaces. The depth at which the surface is cut is described as the 'shift'. The third type of surface (III) can be cut at any depth and all planes will be either positively or negatively charged and so will always have a dipole. The magnitude of the dipole and therefore the surface energy is a function of the depth of the simulation cell. Within the natural environment such surfaces are facetted and expose essentially stable planes, or they contain defects (Steele *et al.*, 2002). In the case of many oxide materials, dipolar surfaces will also protonate to remove charge effects.

To remove the dipole within the simulations requires cleaving the crystal at specific depths and translating an appropriate number of ions from the top layer to the bottom of the simulation region to achieving charge neutrality

across the region. The amount of charge to be removed (q_r) is given by the relationship:

$$q_r = q_d / d \qquad \textit{Eqn. 6.5.1.}$$

q_d = Magnitude of the dipole
d = Depth of the simulation region.

This effectively leads to the formations of vacancies on the surface.

Once the surfaces have been appropriately cleaved they must then be 'relaxed' in order to obtain the relative energetics for the optimised structure. The surface energy is a measure of the stability of the surface and is defined as the work required to cleave the surface (Wright *et al.*, 1998):

$$\gamma = \frac{U_s - U_b}{A} \qquad \textit{Eqn. 6.5.2.}$$

γ = Surface Energy (Jm^{-2})
U_s = Energy of 'n' atoms at the surface (J)
U_b = Energy of 'n' atoms in the bulk (J)
A = Surface area (m^2)

6.5.1. Attachment Energy and Crystal Morphology

Like the surface energy, the attachment energy is a thermodynamic property and relates to the kinetics of surface growth occurring in a crystal. The attachment energy (U_A) is defined as the energy released when a stoichiometric layer is added to a crystallographic surface (Gale and Rohl, 2003):

$$U_A = U_{Tot}^{n+1} - U_{Tot}^{n} - U_{Tot}^{1} \qquad \textit{Eqn. 6.5.3.}$$

U_A = Attachment energy (eV)
U_{Tot}^{n} = Total energy within surface model for n growth layers (eV)
U_{Tot}^{1} = Energy of growth for a single layer (eV).

The Hartman-Perdok technique uses the attachment energy as a method of determining the 'Growth morphology' and hence the macroscopic shape of the crystal. Those faces with higher absolute values of attachment energy have faster growth rates and as a result will form relatively small surfaces on the crystal (Verma *et al.*, 2000). The largest faces on a crystal are those with the lowest growth rate and smallest absolute attachment energy (Figure 6.5.3).

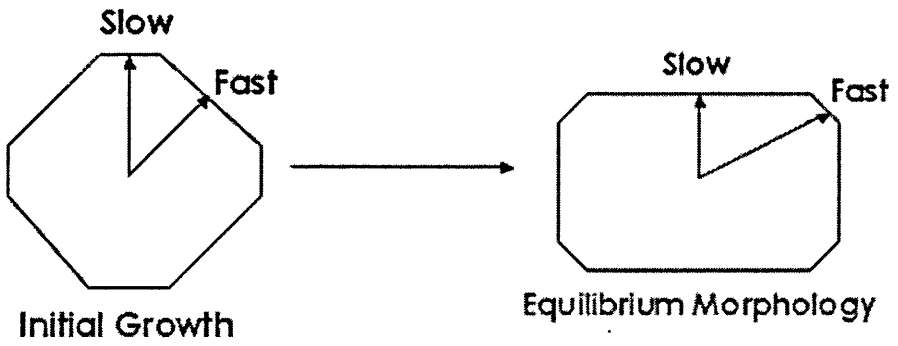

Figure 6.5.3. Schematic illustration of the effect of kinetics upon surface morphology (From De Leeuw *et al.*, 2003).

Using the attachment energy to determine crystal morphology is only one method. The 'Equilibrium morphology' is determined using Wulff's Theorem, and employs the lowest total surface free energy to predict the crystal shape which is determined by calculation of perpendicular distance between the origin and the face (Gadewar *et al.*, 2002). The theorem states that for all γ_i and h_i the ratio is constant as follows:

$$\text{Constant} = \frac{\gamma_i}{h_i} \qquad \textit{Eqn. 6.5.4.}$$

γ_i	=	Specific free energy of face i (Jm^{-2})
h_i	=	Perpendicular distance between origin and face i (m)
i	=	$1 \rightarrow N$
N	=	Number of faces.

Using the equilibrium approach eliminates the inclusion of unstable surfaces on the morphology, and the surface energy of the remaining stable faces contributes inversely to the total surface area of a specific plane (Gale and Rohl, 2003). Therefore those surfaces with high surface energy and are less stable only account for a small surface area of the equilibrium morphology.

Another commonly applied method of morphology prediction is the Bravais-Friedel-Donnay-Harker (BFDH) law which uses the assumption that the binding energies between crystal planes are larger for small interplanar distances. Hence, those planes with larger interplanar distances and lower binding energies are morphologically more important. This method is usually used for a fast initial determination of the important growth faces but is less accurate (Lu and Ulrich, 2003).

6.6. THE GENERAL UTILITY LATTICE PROGRAM (GULP)

The atomistic simulations used in the current research employ the GULP code developed by Julian Gale (Gale, 1997) and subsequently updated to its current format GULP 3.0 (Gale and Rohl, 2003). It was used to simulate both the bulk and surface structures of goethite and the subsequent adsorption of arsenic.

The GULP code requires an initial input file (See Appendix 7A for examples) to define the initial atomic positions of all atoms in the unit cell. The input file also requires assigned atomic charges as well as the potential parameters that combine to describe the total lattice energy of the modelled system. The type of simulation to be modelled can be specified by introducing keywords that control the type of calculation required, such as 'opti' for an optimisation procedure and 'conp' to simulate constant pressure conditions.

The algorithm for the minimisation is also definable although the GULP code automatically assigns the Newton-Raphson function. Others can be used, provided they are assigned within the input file. GULP also allows the minimiser to be changed at particular instants within the optimisation. For example, by adding the line 'switch rfo gnorm 0.005' implies that when the gradient of the potential energy surface becomes 0.005, the minimising algorithm will switch from Newton-Raphson to the RFO (Rational Functional Optimisation) minimiser. Gale and Rohl (2003) suggest that using such switches in the algorithm can accelerate optimisations, especially when used towards the end of a simulation.

The GULP code has been successfully applied to a variety of systems, from the determination of aluminium solubility into lower mantle perovskite ($MgSiO_3$) (Akber-Knutson and Bukowinski, 2004) to crystal structure defects and interactions with other elements (van Westrenen *et al.*, 2003, Wright *et al.*, 2002 and Steele *et al.*, 2000).

A visualisation and manipulation package called GDIS interfaces to the GULP code. The GDIS software was developed to provide visual representation of

manipulated molecules and periodic systems (GDIS, 2003). The interface is compatible with GULP files and therefore can be used to provide pictorial images of the modelled structures. GDIS consists of several tools for structural manipulations and in this study was used to obtain pictorial evidence of the bulk, surface structures and adsorbed structures. It also provided representation of the electrostatic surface energies in the form of contour maps. Alongside the visualisation capacity of GDIS it allows cleavage of the crystal surface at specific Miller indices and permits those surfaces to be minimised subsequently using GULP.

7. ATOMIC AND CRYSTAL STRUCTURE SIMULATIONS

7.1. INTRODUCTION

The previous chapter introduced the theoretical basis of and variety of atomistic modelling and crystal system simulations. In this chapter the criteria for selecting the parameters for interatomic potentials used in modelling goethite and neutrally charged arsenate molecule $AsO(OH)_3$ are explored. The simulated goethite bulk structure and surfaces are compared and confirmed with experimental structures. Preliminary calculations on the surface structure are presented. Their relevance to sorption properties of goethite is developed in Chapter 8.

The modelling of the arsenate molecule, $AsO(OH)_3$ is new. This chapter demonstrates the sequence of actions required for derivation of the molecule potential set and the acquisition of a reasonable molecule structure.

7.2. MODELLING THE BULK GOETHITE STRUCTURE

The crystal structure and physical properties of goethite were described in Chapter 2 (Section 2.2). Several important investigations have been published on goethite structures using experimental methods to determine the bulk cell parameters and atomic positions. From the cell parameters cited by Pivovarov (2002), Klein and Hurlbut (1993), Lima-De-Faria (1963), Steele *et al.* (2002) and Nagai *et al.* (2003) the a, b and c lengths are shown to vary by an insignificant amount up to a maximum of 0.5 %. Their structures used the space group pbnm to describe the symmetry, and therefore the unit cell as c-a-b instead of the conventional a-b-c. Studies by Szytula *et al.* (1968), Gualtieri and Venturelli (1999), Jones *et al.* (2000) and the current simulations used the pnma space group and the unit cell configuration a-b-c. Gualtieri and Venturelli (1999) found that by increasing the sample temperature from 25 to 156 C the overall unit cell dimensions remained unchanged although the atom positions varied up to 7 %. Investigation into the effect of pressure showed a greater variation in the cell parameters and atom positions. As the pressure ranged from 0 to 9 GPa a significant difference was observed in the 'a' length (3.2 % increase) with atomic position differences of up to 7 % of the starting zero GPa positions (Nagai *et al.*, 2003). For the purpose of this study the calculations are fixed at 0 K and 0 GPa.

To successfully simulate the surface structure of goethite, it is important to confirm that the model is able to reproduce the bulk properties. The potential parameters used in the current study are given in Table 7.2.1. As a starting point, existing parameters describing interactions between Fe–O and O–O for a range of Fe-oxides (Schroder *et al.*, 1992) were used. The Morse potential of Baram and Parker (1996) was added to describe the O–H molecule. The Buckingham parameters for the $O_{hydroxyl}$–Fe interaction were derived in the current study by the fitting procedure outlined in section 6.3. The simulated and experimental bulk structure of goethite is given in Table 7.2.2. Potential methods have also been used by Jones *et al.* (2000) and Steele *et al.* (2002) to

study the bulk and surface properties of goethite. The structures reported by these workers are included in Table 7.2.2 for comparison.

Buckingham Potential Pair	A (eV)	ρ (Å)	C (eV Å^{-6})	Cut-off Distances (Å)
$O2_{shell}$ – $O2_{shell}$	22764.00	0.1490	27.88	0.00 – 12.00
$O1_{shell}$ – $O1_{shell}$	22764.00	0.1490	6.97	0.00 – 12.00
$Fe3_{core}$ – $O2_{shell}$	1102.40	0.3299	0.00	0.00 – 12.00
$Fe3_{core}$ – $O1_{shell}$	901.52	0.3299	0.00	0.00 – 12.00
$H1_{core}$ – $O2_{shell}$	208.11	0.2500	0.00	0.00 – 12.00
$H1_{core}$ – $O1_{shell}$	311.97	0.2500	0.00	1.40 – 12.00

Spring Constants	K (eV Å^{-2})	γ |e|
O2	74.92	0.60
O1	74.92	0.60

Morse Potential Pair	D_e (eV)	β (Å^{-1})	R_e (Å)	Cut-off Distances (Å)
$H1_{core}$ – $O1_{shell}$	7.0525	3.1749	0.9485	0.00 – 1.40

Atom Charges	Core Charge (eV)	Shell Charge (eV)
Fe3	3.00	-
O2	0.86902	-2.86902
O1	0.89502	-2.29502
H1	0.40	-

Table 7.2.1. The potential parameters used in the current calculations.

REFERENCE	a (Å)	b (Å)	c (Å)
Szytula *et al.* (1968) – Experimentally Derived	9.95	3.01	4.62
Gualtieri & Venturelli (1999) – Experimentally Derived	9.913	3.013	4.580
Steele *et al.* (2002) – Calculated	10.015 (+ 2.0 %)	3.169 (+ 5.3 %)	4.57 (- 1.1 %)
Jones *et al.* (2000) – Calculated	10.405 (+ 4.6 %)	3.085 (+ 2.5 %)	4.874 (+ 5.5 %)
Current Simulations – Calculated	9.816 (- 1.3 %)	3.172 (+ 5.4 %)	4.748 (+ 2.8 %)

Table 7.2.2. Comparison of unit cell lattice parameters obtained with experiments and using potentials. The percentages in brackets represent the % difference from the Szytula *et al.* (1968) parameters.

Using the Jones *et al.* (2000) potential set, the difference of 2.5 to 5.5 % between the simulated cell parameters and the experimental counterpart is relatively large. With the Steele *et al.* (2002) potentials the derived cell parameters for 'a' and 'c' are within 2.5 % of the experimental, with the 'b' length 5.3 % larger.

Although the Steele *et al.* (2002) potential set compare better with the experimental cell parameters, the model is not stable as negative phonon frequencies, indicative of instabilities, appear during the simulation suggesting that the structure wants to reduce its symmetry. Comparison of the current simulated cell parameters in Table 7.2.2 with the experimental set show the best overall fit compared with the other modelled parameters. This ensured that in the current model all cell lengths were within 5.4 % of the experimental.

Figure 7.2.1 shows the optimised goethite unit cell obtained by the simulation using the chosen potential set. The Fe^{3+} ion (Fe3) is in six-fold co-ordination (octahedral) with surrounding oxygen ions, three of which are hydroxyl oxygen (denoted O1) and three are oxygen anions (denoted O2).

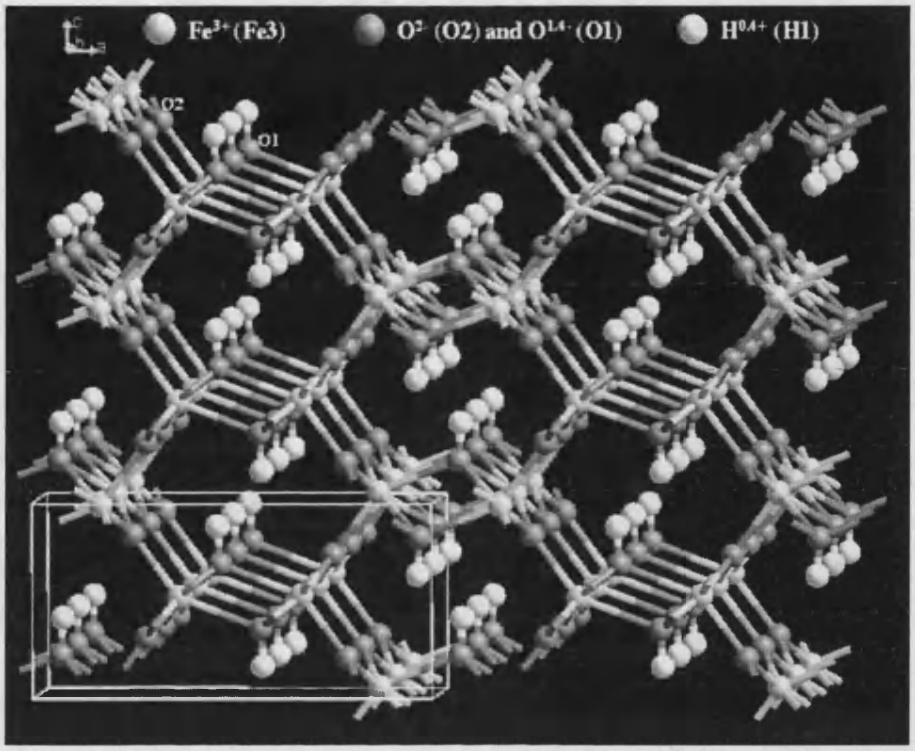

Figure 7.2.1. Goethite bulk structure showing double rows of iron octahedra and double rows of vacancies. The highlighted box indicates the unit cell.

The double rows of Fe^{3+} octahedra can be seen in Figure 7.2.1 connected to other double rows by sharing oxygen (O2) atoms. This structure has also been described by Cornell and Schwertmann (1996) from experimental work. They summarise the structure as double chains of octahedra alternating with double chains of vacant sites or tunnels. The simulated bulk structure compares well with other experimentally derived structures (Weckler and Lutz (1998), Suzuki *et al.* (2001) and Manceau *et al.* (2000)).

Table 7.2.3 highlights the difference in the bond lengths in the optimised goethite structure based on the chosen potentials and also those from other models and experimentally derived distances. Although bond lengths ideally should not differ maximally more than 5 % of the experimental, the majority of simulated lengths comply with this. When the other potential sets were used the simulated bond lengths showed significantly greater differences compared to the experimental. Therefore, although the H1 – O2 bond length was not

simulated to within 5 % using the current potentials, the overall simulation produces more accurate bond lengths than those incorporating the Steele *et al.* (2002) and Jones *et al.* (2000) potential sets.

BONDING ATOMS	Weckler & Lutz (1998) – Experiment Bond Lengths (Å)	Suzuki *et al.* (2001) – Experiment Bond Lengths (Å)	Current Simulation Bond Lengths (Å)
H1 – O1	0.987	Not available	1.009 **(+ 2.2 %)**
H1 – O2	1.793	Not available	1.942 **(+ 8.3 %)**
Fe3 – O1	2.095	2.07/2.09	2.193 **(+ 4.5 %)**
Fe3 – O2	1.926/1.957	1.95	1.902/1.906 **(- 1.1 %)**

Table 7.2.3. Simulated bond lengths within goethite compared with experimentally derived lengths. The percentages in brackets represent the % difference from the experimental lengths derived by Weckler & Lutz (1998).

With the goethite structure successfully simulated (Appendix 7A shows the simulated structure positions), the bulk structure was cleaved in various planes to derive important bonding surfaces as described in the following section.

7.3. GOETHITE SURFACE CONFIGURATIONS

The goethite surfaces were constructed by the GDIS interface which allows cleavage along chosen planes at various depths. GDIS was used to search for those surface depths associated with given cleavage planes that result in charge neutrality. Table 7.3.1 gives a comprehensive list of all the relaxed cleavage faces and cleavage depths with zero charge.

By comparing the relaxed surface energies for cleavage planes using the most stable cut (Table 7.3.1), it can be seen that the most stable surface, with the lowest relaxed surface energy, is the (100), whereas the least stable surface is the (111). Some surfaces show considerable change between the un-relaxed and relaxed surface energy (Table 7.3.1), up to an 87 % decrease. This magnitude of relaxation is not uncommon, and suggests that the stability of a surface can be greatly increased with relaxation of the surface ions (Read *et al.*, 2001). Results of the Steele *et al.* (2002) calculations also show relaxations of up to 83 % (Table 7.3.2). The surfaces that show the least relaxation are those that do not involve bond breaking and forming as part of the rearrangement, for example the (111) surface (Figure 7.3.1). The majority of relaxed surfaces terminate with an OH group, and the unrelaxed surfaces that undergo the least relaxation generally terminate in a mixture of Fe, O and OH. By contrast, those surfaces that experience the greatest relaxation do not terminate with hydroxyl groups before relaxation, but attain this upon the rearrangement of surface atoms, for example the (110) surface (Figure 7.3.2). Almost all of the surface hydroxyl terminations, irrespective of the amount of relaxation, point upwards away from the surface. This is probably because the surface is simulated in a vacuum, which may not occur in the presence of water.

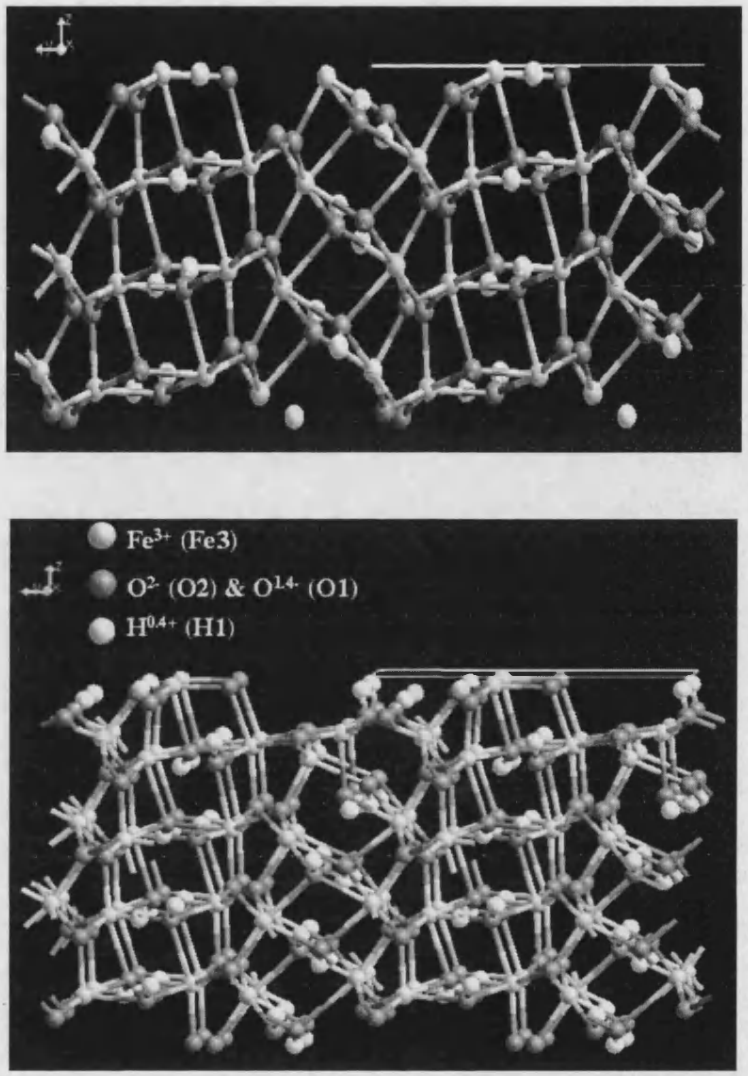

Figure 7.3.1. The unrelaxed (above) and relaxed (below) modelled (111)_2 surface with hydroxyl terminations. The unit cell has been repeated for a more enhanced surface illustration.

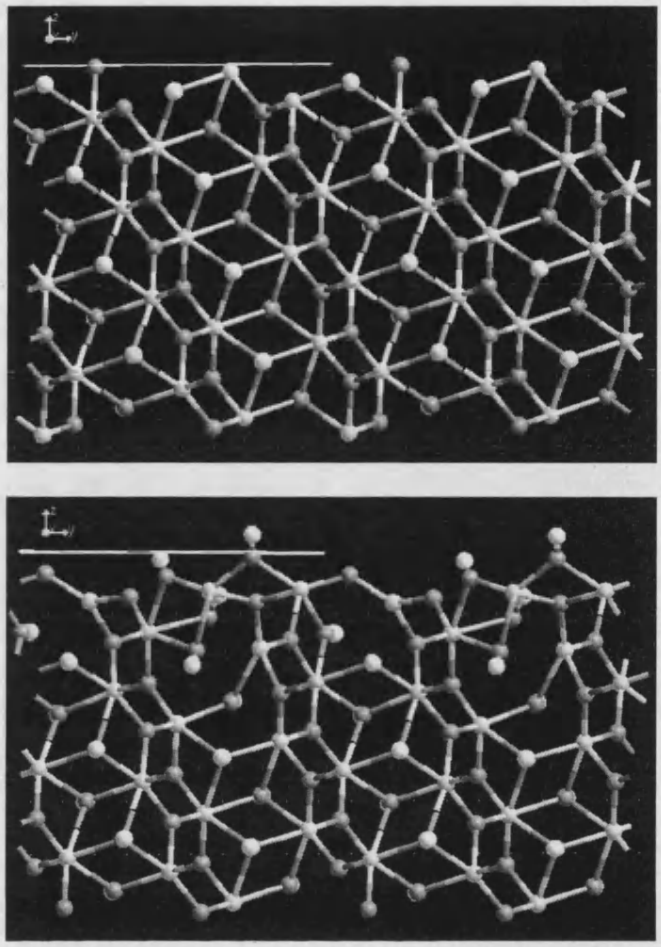

Figure 7.3.2. The (110)_1 surface before (above) and after (below) relaxation, showing significant rearrangement.

Using the relaxed surface energies as a guide to the order of stability, the order from the most stable surface to the least stable is as follows:

(100)< (101)< (301)< (201)< (210)< (012)< (001)< (211)< (021)< (110)< (010)< (011)< (120)< (102)< (111)

The most stable (100) surface is terminated by hydroxyl ions bonded to under co-ordinated Fe atoms (5-fold co-ordination) (Figure 7.3.3). The termination occurs at the mid-point of the 'tunnel ring' structures, which give rise to large vacant areas between the surface hydroxyls. On relaxation the (100) surface hydroxyl ions take a more 'upright' position almost perpendicular to the surface, compared with the pre-relaxation position of parallel to the surface. The least stable (111) surface terminates with an assembly of hydroxyl groups and under-coordinated oxygen and iron ions (Figure 7.3.1). On relaxation the

position of the surface hydroxyls is more upright, pointing away from the other surface ions. The pre-relaxation surface comprises gaps that widen after relaxation, due to the surface iron atoms being pulled into the bulk structure to attain a higher co-ordination by bonding to two neighbouring oxygen ions. In general, the more stable surfaces terminate with few hydroxyl groups or oxygen anions and the less stable surfaces have a greater proportion of under-coordinated ions at the surface.

Face	Cleavage Depth (unit cell fractions)	Dhkl (Å)	Surface Energies (Jm^{-2})			Attachment Energies (eV)		Region Sizes (R1 & R2)
			Un-relaxed	Relaxed	Energy Change (%)	Un-relaxed	Relaxed	
(100)_1	0.00	4.91	1.28	0.61	53	-1.19	-1.20	1 : 1
(100)_2	0.25	4.91	3.68	1.89	49	-3.43	-3.31	1 : 1
(101)_1	0.00	4.26	6.46	2.04	68	-6.77	-5.42	4 : 4
(101)_2	0.50	4.26	2.84	1.15	60	-2.93	-3.12	4 : 4
(301)_1	0.00	2.69	4.11	1.18	71	-6.60	-5.16	10 : 10
(301)_2	0.50	2.69	10.63	4.62	57	-17.99	-24.72	10 : 10
(201)_1	0.00	3.41	11.02	1.59	86	-14.69	-16.49	8 : 8
(201)_2	0.50	3.41	4.64	1.22	74	-5.88	-5.34	7 : 7
(210)_1	0.00	2.66	2.38	1.32	44	-3.96	-4.09	4 : 4
(210)_2	0.50	2.66	5.56	1.89	66	-9.55	-9.32	4 : 4
(012)_1	0.00	0.95	3.50	1.34	62	-13.48	-16.47	7 : 7
(012)_2	0.28	0.95	8.83	3.66	59	-38.15	-47.26	9 : 9
(012)_3	0.50	0.95	3.50	1.34	62	-13.48	-16.47	7 : 7
(012)_4	0.72	0.95	8.83	3.66	59	-38.15	-47.27	9 : 9
(001)_1	0.00	2.36	7.71	1.48	81	-10.95	-11.44	4 : 4
(001)_2	0.50	2.36	7.71	2.07	73	-10.95	-9.46	4 : 4
(211)_1	0.00	2.32	9.91	4.34	56	-20.02	-18.04	6 : 6
(211)_2	0.50	2.32	5.92	1.64	72	-9.86	-8.09	9 : 9
(021)_1	0.00	0.75	1.74	1.67	4	-57.96	-57.77	12 : 12
(021)_2	0.50	0.75	1.74	1.67	4	-57.98	-57.74	12 : 12
(110)_1	0.00	1.51	12.61	1.80	86	-60.16	-47.49	7 : 7
(110)_2	0.25	1.51	6.64	1.99	70	-30.05	-16.42	6 : 6
(010)_1	0.00	1.58	3.26	1.89	42	-12.02	-9.96	3 : 3
(010)_2	0.25	1.58	3.26	1.89	42	-12.02	-9.96	3 : 3
(011)_1	0.00	2.63	13.46	7.57	44	-20.48	-19.34	7 : 7
(011)_2	0.50	2.63	15.22	1.91	87	-18.97	-25.30	8 : 8
(120)_1	0.00	0.78	2.26	2.17	4	-25.37	-26.56	18 : 18
(120)_2	0.50	0.78	2.26	2.17	4	-25.35	-26.55	18 : 18
(102)_1	0.00	2.30	15.63	4.28	73	-23.58	-19.76	12 : 12
(102)_2	0.50	2.30	8.17	4.06	50	-15.53	-17.90	14 : 14
(111)_1	0.00	2.54	4.40	4.38	0	-11.65	-11.75	7 : 7
(111)_2	0.50	2.54	4.48	4.24	5	-15.33	-15.12	5 : 5

Table 7.3.1. Summarising the un-relaxed and relaxed surface and attachment energies of the simulated surfaces, and the percentage reduction in surface energy on relaxation.

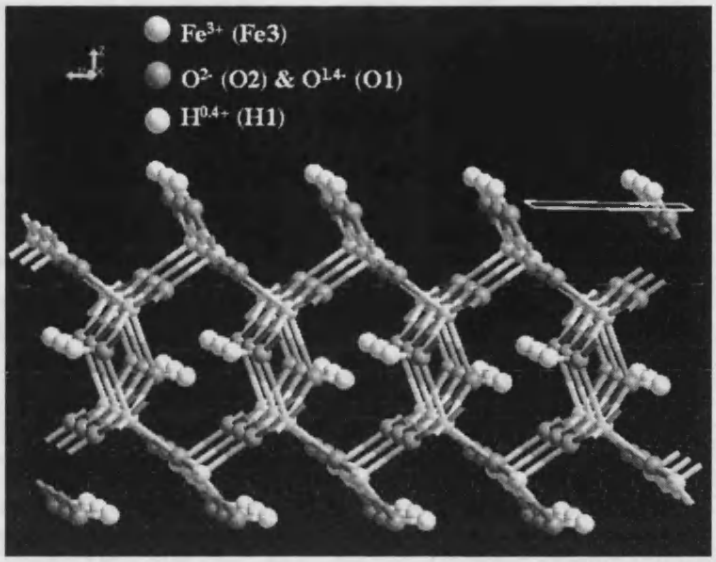

Figure 7.3.3. The relaxed modelled (100)_1 surface with hydroxyl terminations. The unit cell has been repeated for a more enhanced surface illustration.

The simulation study of Steele *et al.* (2002) found that the (010) cleavage surface was the most stable and the (100) was the least stable, and both surfaces were important surfaces. Comparison between the surface energy for the Steele *et al.* (2002) study and the current simulations has taken into account the different symmetry group used by Steele *et al.* and Table 7.3.2 reflects this. The relaxed energies between the two calculations are similar, with an average difference of +0.51 Jm^{-2}. The differences also highlight the sensitivity of surface energies to the potential set used.

Face	Steele *et al.*, 2002				Current Simulations	
	Cleavage Depth (unit cell fractions)	Surface Energies (Jm^{-2})			Surface Energies (Jm^{-2})	
		Un-relaxed	Relaxed	Energy Change (%)	Relaxed	Energy Change (%)
(001)	0.000	3.17	1.89	40	1.48 (-0.41)	81
	0.500	1.26	0.81	36	2.07 (+1.26)	73
(110)	0.500	2.93	1.55	47	1.80 (+0.25)	70
(012)	0.500	4.69	1.50	68	1.34 (-0.16)	62
(011)	0.500	3.36	1.40	58	1.91 (+0.51)	87
(100)	0.250	3.40	2.15	37	1.85 (-0.30)	49
(111)	0.000	6.03	2.08	66	4.38 (+2.30)	0
	0.500	5.62	1.96	65	4.24 (+2.28)	5
(010)	0.250	11.63	1.99	83	1.89 (-0.10)	42
	0.500	8.02	2.42	70	1.89 (-0.53)	42

Table 7.3.2. Calculated surface energies derived by Steele *et al.* (2002) using pbnm symmetry and comparison with the current study with pnma symmetry. The closest cleavage depth has been taken for comparison if that particular depth is unavailable. The numbers in brackets show the difference between the current model and the Steele *et al.* Model.

To validate the surface simulations the analysis of the derived morphological structure was compared with structures determined experimentally. Relaxed surfaces were used in construction of the crystal morphology using the GDIS interface package.

Methods of determining crystal morphology are described in Chapter 6 using the surface energy, attachment energy and the BFDH (Bravais-Friedel-Donnay-Harker) technique (Gale and Rohl, 2003). The BFDH morphology (Figure 7.3.4) is based on the inter-planar spacing and is usually a crude first-order estimation (Lu and Ulrich, 2003).

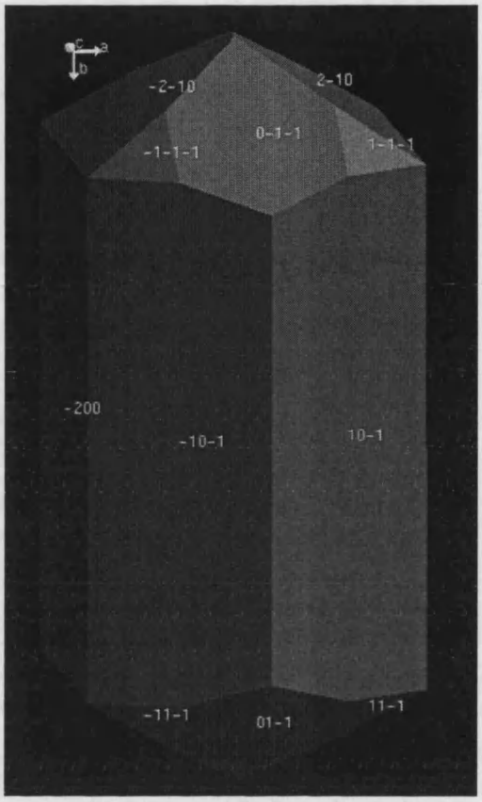

Figure 7.3.4. BFDH method of morphology determination of the goethite surfaces, using the GDIS interface. (200) surface is the same as the (100)

The predicted crystal is almost acicular with two predominantly large long surfaces: the (100) and (101) that are terminated by the (210), (111) and (011) planes. All of the surfaces observed in this structure as cited previously are important growth surfaces.

Figures 7.3.5 and 7.3.6 are the simulated growth and equilibrium morphologies respectively. In contrast to the BFDH method, the growth morphology (Figure 7.3.5) is based on the un-relaxed attachment energy. Large crystal surfaces result from relatively slow growth rates and are indicative of smaller absolute energy values. This simulated morphology also shows the dominance of stable (100) and (101) faces with a small contribution from (210) terminating faces. The prominence of the (100) face is overestimated relative to the experimental morphology (Figure 2.2.1, Chapter 2.2), while the expressed (110) and (010) are not, highlighting the differences between real and ideal crystal structures

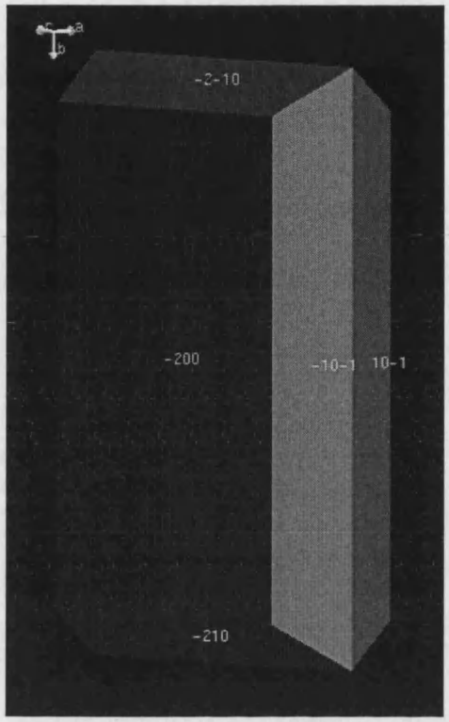

Figure 7.3.5. Relaxed growth morphology of goethite, derived using the GDIS interface and the current simulated surfaces.

The equilibrium morphology (Figure 7.3.6) is based on relaxed surface energies and those faces with high energy are less stable and hence account for only a small portion of the morphological form. The simulated structure is similar to the growth morphology with the addition of the (012) faces and more contribution from the (101) faces.

7.3.6. Relaxed Equilibrium Morphology, from the simulated surfaces.

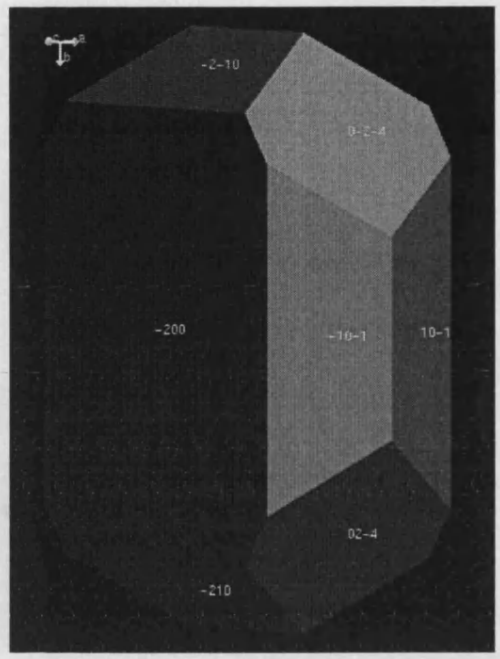

Several experimental studies have identified the (010) group of planes as forming the perfect cleavage surface (for example; Rakovan *et al.* (1999), Klein and Hurlbut (1993), Duda and Rejl (1990)). Ostergren *et al.* (2000[i]) observed that in both natural and synthetic goethite the most common crystal faces are the (110) and (021), with oxygen singly, doubly and triply co-ordinated to the structural iron. Other experimental studies have also described several important goethite surfaces, and Figure 2.2.1 (Chapter 2.2) shows the morphology of typical goethite crystals, comprising (110) surfaces running parallel to the long-axis and bounded by (021) faces, with a small contribution from (100) and (010) (Randall *et al.* (1999), Manceau *et al.* (2000) and Barrón *et al.* (1997)). Microscopy studies by Rakovan *et al.* (1999) determine the growth faces as (010), (110) and (111) and Cornell and Schwertmann (1996) cite the important surfaces as (101), (001) and (210). It is important to note that the above surfaces were obtained with respect to the pbnm symmetry group, whereas the current simulations have used pmna symmetry. Therefore, with this in mind, the calculated morphology is very similar to those determined previously by experiment, lending support to the validity of the model.

Discrepancies between the experimental and calculated morphology, for example the absence of the (001) and (010) surfaces in the calculated

morphology, can be explained as follows. The natural crystal growth depends on several factors, such as the kinetics of surface growth. For example, the (001) surface growth rate is much longer than the (101) surface, and therefore small crystals have a higher proportion of (001) faces, which are superseded by the (101) surfaces as the crystal grows (Gaboriaud and Ehrhardt, 2003). Another cause for the differences in morphology may be due to physical and chemical effects acting upon the real crystal, for instance the pH, temperature, presence of water and the occurrence of defects on the crystal surfaces, all of which were absent in the zero pressure – zero K models.

The effect of solvation on the surfaces of model morphology was observed by De Leeuw *et al.* (2003) in the analyses of metal and metal oxides. For example, they found that by using the BFDH method only the (10T1) and (10T0) surfaces existed, and it was only by hydrating the crystal surface that a 'true' morphological structure could be simulated and the expected (0001) cleavage plane obtained. Similarly a more accurate description of the surface stabilities of goethite and therefore the morphological character may be attained with hydration (De Leeuw *et al.*, 2003), which is a more realistic situation for goethite found under natural conditions.

7.4. MODELLING MOLECULAR ARSENIC

In the search for surface sites that are most likely to adsorb arsenic, a preliminary step is to derive potentials that can model As–oxides. Two structures were modelled:

(a) Arsenic trioxide (known as claudetite, $As_2^{3+}O_3^{2-}$, As denoted As3)

(b) Arsenic pentoxide ($As_2^{5+}O_5^{2-}$, As denoted As5).

Both are comparatively simple and adaptable to the use of a least-square fitting procedure to obtain As–O potentials. The O^{2-}–O^{2-} (denoted O4) potentials and O4 spring constants for the model are those from Schroder *et al.* (1992) and are in keeping with the goethite bulk inter-atomic description. The optimised structures are given in Appendix 7B and the fitted inter-atomic potentials describing the As – O interactions are in Table 7.4.1.

INTER-ATOMIC INTERACTION	A (eV)	*P* (Å)	C (eVÅ^6)	Cut-off Distances (Å)
$O4_{shell}$ – $O4_{shell}$	22764.00	0.1490	27.88	0 – 12.00
$As3_{core}$ – $O4_{shell}$	1455.8324	0.3455	0.00	0 – 15.00
$As5_{core}$ – $O4_{shell}$	1301.7025	0.3366	0.00	0 – 15.00

Table 7.4.1. Buckingham potentials used to describe the arsenic – trioxide and - pentoxide structures (See Equation 6.2.4 in Chapter 6).

No experimental data for bond lengths were available for the arsenic pentoxide structure. However, the bond lengths obtained from the claudetite simulations compared well with those derived by x-ray crystallography (Pertlik, 1978) and are within 2.5 % (Table 7.4.2).

ATOMIC BOND LENGTHS	Pertlik (1978) – Experimental (Å)	Current Simulations (Å)	% Difference
As – O	3.450	3.367	- 2.4

Table 7.4.2. Bond length difference between simulated and experimentally derived claudetite structures.

The As3–O4 potentials derived by the simulation were used subsequently in the exchange simulations reported in Chapter 8.4. The As5–O4 potentials were further modified to more accurately describe these interactions within the arsenate $AsO(OH)_3$ molecule. This molecule was chosen as it is neutral and therefore can be added to a goethite surface while maintaining the charge neutrality constraints of the GULP code. No previous experimental studies for this molecule could be found and hence a construction was estimated using the neutral arsenite molecule ($As(OH)_3$) as a frame of reference.

The visualisation of the arsenic molecule was achieved by the cerius^2 (Accelrys, 2004) interface software designed to allow users to 'draw' molecular structures with given bond lengths and bond angles. Although the precise structure of the molecule was uncertain, an initial formulation of the molecule was created using bond lengths and vibrational energies currently available for a similar structure. The reference structure chosen was that cited by Tossel (1997) for the arsenite molecule, $As(OH)_3$ (Figure 7.4.1).

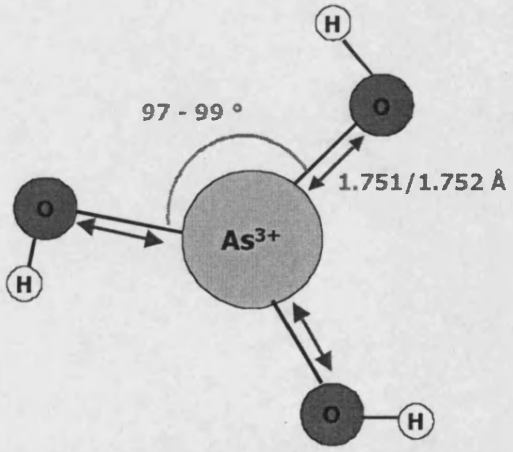

Figure 7.4.1. Schematic representation of the arsenite molecule ($As(OH)_3$) cited by Tossel (1997). The oxygen atoms are not planar as illustrated, and bond angles & lengths are universal.

The significant advantage of this information about arsenite was that the bond lengths, angles and frequencies accompanying the paper were more detailed than any other available data for arsenic molecules. From the initial $As(OH)_3$ structure the molecule was enhanced with a double bonded oxygen to establish the charge neutrality, hence creating $AsO(OH)_3$. The addition of oxygen to the molecule is a reasonable step as oxygen and hydroxyl groups often attach to charge deficient assemblages within aqueous environments. A double bond was used to connect the oxygen atom as it compensates for all free outer electrons.

Gale (unpublished data, 2002) was able to produce a viable structure for $AsO(OH)_3$ using electronic structure methods. Once the molecule had form it was possible to use GULP (Gale, 2003) to obtain inter-atomic potentials. Table 7.4.3 lists the derived potentials that were used in the subsequent modelling of $AsO(OH)_3$. The O4–O4 interactions were described with the potential derived by Schroder *et al.* (1992), as previously used in the bulk simulations of goethite. The O – H interactions use the Baram and Parker (1996) potentials and the other interactions were parameterised using the GULP fitting procedure.

The final molecular co-ordinates (Cartesian form) that resulted from the relaxed optimisation of the $AsO(OH)_3$ molecule are in Appendix 7B. Figure 7.4.2 shows the optimised molecule with bond lengths and bond angles.

(a)

Buckingham Potential Pair	Potentials References	A (eV)	P (Å)	C (eVÅ^6)	Cut-off Distances (Å)
$O4_{shell}$–$O4_{shell}$	Schroder *et al.* (1992)	22764.00	0.1490	27.88	0.00 – 12.00
$O3_{shell}$–$O4_{shell}$	Schroder *et al.* (1992)	22764.00	0.1490	13.94	0.00 – 12.00
$O3_{shell}$–$O3_{shell}$	Schroder *et al.* (1992)	22764.00	0.1490	6.97	0.00 – 12.00
$H3_{ore}$–$O4_{shell}$	Baram & Parker (1996)	311.97	0.2500	0.00	0.00 – 12.00
$H3_{ore}$–$O3_{shell}$	Baram & Parker (1996)	311.97	0.2500	0.00	1.40 – 12.00
$As5_{ore}$–$O4_{shell}$	Fitted During Current Study	1755.8324	0.3455	0.00	0.00 – 12.00
$As5_{core}$–$O3_{shell}$	Fitted During Current Study	1209.3670	0.3307	0.00	0.00 – 12.00

(b)

Spring Constants	References	K (eV Å^{-2})	γ |e|
O4	Schroder *et al.* (1992)	74.92	0.60
O3	Schroder *et al.* (1992)	74.92	0.60

(C)

Morse Potential Pair	References	D_e (eV)	β (Å^{-1})	R_e (Å)	Cut-off Distances (Å)
$H3_{core}$ – $O3_{shell}$	Baram & Parker (1996)	7.1525	3.1749	0.9285	0.00 – 1.40

(d)

Three Body Term (Exponential)	References	K (eV rad^{-2})	θ ( )
O3s – H3c – As5c	Fitted During Current Study	30.1525	109.47

(e)

Atom	References	Core Charge (eV)	Shell Charge (eV)
As5	Used in current study	5.00	-
O4	Schroder *et al.* (1992)	0.86902	-2.86902
O3	Baram & Parker (1996)	0.89502	-2.29502
H3	Baram & Parker (1996)	0.40	-

Table 7.4.3 (a – e). Interatomic potentials used for the $AsO(OH)_3$ molecule simulation. The O3 and H3 refer to the hydroxyl group, O4 to O^{2-} anion and As5 to As^{5+}.

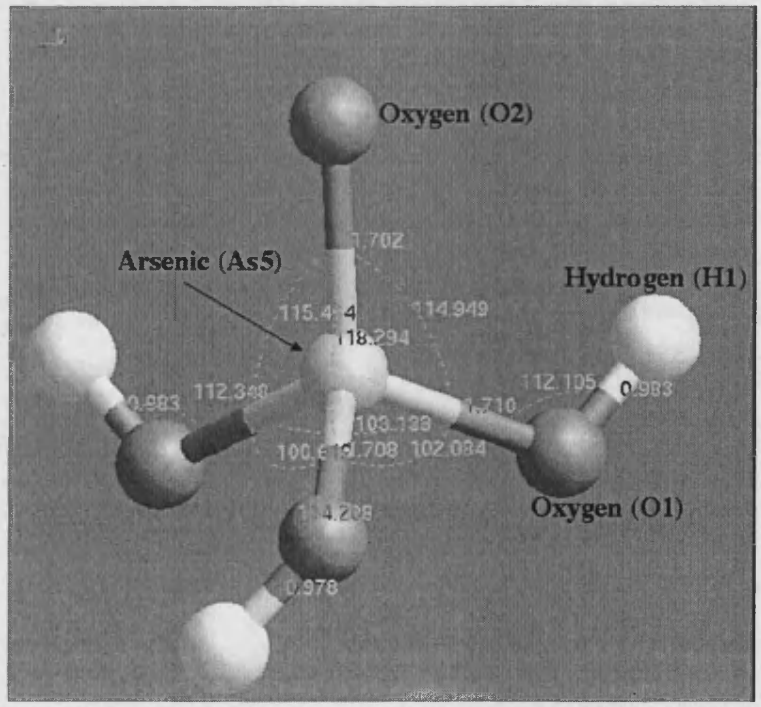

Figure 7.4.2. $AsO(OH)_3$ molecule relaxed in GULP. Illustrates bond lengths and angles.

In the validation of the simulated molecule, the modelled bond lengths were compared with those of the neutral arsenite molecule ($As(OH)_3$) as derived by Tossel (1997). A first observation is that the As–O bond lengths for the arsenate molecule are slightly shorter, by an average of 0.04 Å (Table 7.4.4). The average As–O bond length within the modelled arsenate molecule compares well with those cited by Tossel (1997) and is within 2.5 %. The As5–O lengths are shorter than the As3–O owing to the slight difference between molecular structures and the greater electrostatic attraction between As^{5+} and O^{2-} compared with the As^{3+} ion. The arsenate molecule incorporates double bonding to the oxygen anion and these usually have higher bond energies and corresponding shorter bond lengths than single bonds. The simulated As5 = O4 bond length is in fact only 0.4 % shorter than the single bonded As5 – OH bond lengths. Table 7.4.4 also shows the bond angles in the modelled molecule, which are higher than the O – As – O angles of between 97 and 99° that Tossel (1997) found in the arsenite molecule because of the added oxygen anion in the arsenate structure.

(a)

Atoms	Bond Lengths (Å)	Average (Å)
As5 = O4	1.702	
As5 – O3	1.710	
As5 – O3	1.708	
As5 – O3	1.714	**1.710**
O3 – H3	0.983	
O3 – H3	0.978	
O3 – H3	0.983	**0.981**
As3 – O	1.751 / 1.752	**Tossel Study (1997)**

(b)

Atoms	Bond Angles (°)	Average (°)
H3 – O3 – As5	112.105	
H3 – O3 – As5	114.208	
H3 – O3 – As5	112.348	**113**
O3 – As5 – O3	106.619	
O3 – As5 – O3	103.133	
O3 – As5 – O3	102.084	**104**
O4 – As5 – O3	115.464	
O4 – As5 – O3	118.294	
O4 – As5 – O3	114.949	**116**
O – As – O	**97 – 99**	**Tossel Study (1997)**

Table 7.4.4. $AsO(OH)_3$ simulated bond lengths and bond angles.

It is also important to compare the vibrational frequencies of arsenite and arsenate molecules. Table 7.4.5 illustrates the stretching frequencies derived by Tossel (1997), using quantum mechanical models of the arsenite molecule, in comparison with the frequencies obtained for the current simulated arsenate molecule using GULP. The frequencies show good agreement with those derived by Tossel (1997) and are within 5 % of the arsenite frequencies.

In summary, a viable charge neutral arsenate molecule was modelled using unique potential sets. The molecule was then used to simulate As(V) interactions with goethite surfaces (Chapter 8).

Tossel (1997) Modelled Frequencies (cm^{-1})	This study Frequencies Derived for $AsO(OH)_3$ (cm^{-1})	Percentage Difference From Tossel Frequencies
675	645	– 4.5 %
698	669	– 4.2 %
716	723	+ 1.0 %

Table 7.4.5. Comparison of calculated vibrational (stretching) frequencies for As – O and As – OH between the Tossel (1997) study and the current simulations.

8. SURFACE INTERACTIONS

8.1. INTRODUCTION

This chapter uses the outcome from the simulation models, introduced previously to further elucidate possible adsorption mechanisms of As (V) onto goethite surfaces. The interaction between goethite and molecular As is described in terms of the complexes introduced in Section 2.5.4.

The simulation models were used to determine the electrostatic charge distribution on goethite surfaces. Such surface charge distribution maps show areas of positive and negative charge and therefore possible sites for anion and cation attraction respectively (Section 8.2). By calculating the energetics of adsorption of the arsenate molecule ($AsO(OH_3)$) onto goethite surfaces, different surface sites and adsorption complexes are compared (Section 8.3). As well as adsorption surface reactions, substitution models provide some information about the energetics of this process with respect to different goethite surfaces (Section 8.4). Using the results from simulated adsorption complexes, comparisons are made with referenced As–Fe distances (as measured by spectroscopic methods (Section 8.5)). Finally the simulation results and those derived from the current batch and column experiments of previous chapters were combined to describe the mechanisms of arsenate adsorption onto goethite.

Reviews of As adsorption at mineral surfaces, especially for oxides and hydroxides including goethite, have been based on spectroscopic methods of analysis. For example, Farquhar *et al.* (2002) identified the bonding mechanisms for both As (V) and As (III) on goethite and Lepidicrocite (γ-FeOOH). The evidence from EXAFS (Extended X-ray Absorption Fine Structure) spectroscopy, demonstrated that inner-sphere complexes are created by bidentate bridging between the As (V) and As (III) and oxygen on the hydroxide surfaces.

8.2. SURFACE ELECTROSTATIC MAPS

The electrostatic forces on metal oxide surfaces are important for the attraction of oppositely charged ionic aqueous species. The surface of a metal oxide will have localised sites of positive and negative electrostatic charge depending on the co-ordination state of the surface atoms. For example, under co-ordinated surface cations define sites of positive electrostatic charge and under co-ordinated anions define negative electrostatic charge. It is the positively charged sites that are important for the attraction of aqueous arsenic species such as: H_3AsO_4, $H_2AsO_4^-$, $HAsO_4^{2-}$ for the arsenate species; and H_3AsO_3, $H_3AsO_3^-$ and $HAsO_3^{2-}$ for arsenite (Ferguson and Gavis, 1972).

This section describes the electrostatic charges on simulated goethite surfaces using a map produced with the GDIS visualisation package. Although the overall simulation block is neutrally charged, small scale variation in charges exist on the surfaces and these are the indicators of likely adsorption sites. The goethite surfaces are therefore at PZC and in this study the effect of solution pH on the goethite surface and on adsorption mechanisms has not been considered.

The (110) surface displays a large difference between positive and negative electrostatic charges. Figure 8.2.1 illustrates the electrostatic (es) map of the surface. The undulating map surface follows the contours of the surface atom positions, while the colours correspond to the magnitude of the surface es charge, as illustrated in the legend. From this it is shown that the positive areas are derived from two under co-ordinated Fe(III). In the bulk structure Fe(III) is in octahedral co-ordination, whereas the surface Fe(III) is only bonded to three and four other ions. The negative areas result from six under co-ordinated oxygen atoms; four O2 (O^{2-}) atoms with a co-ordination number (CN) of 1 and 2 (corresponding to CN 3 in the bulk) and two O1 ($O^{1.426-}$) hydroxyl oxygen with CN 3 (corresponding to CN 4 in the bulk). The large variation in the electrostatic charge of this surface indicates the potential affinity for attracting the arsenic molecule to specific sites.

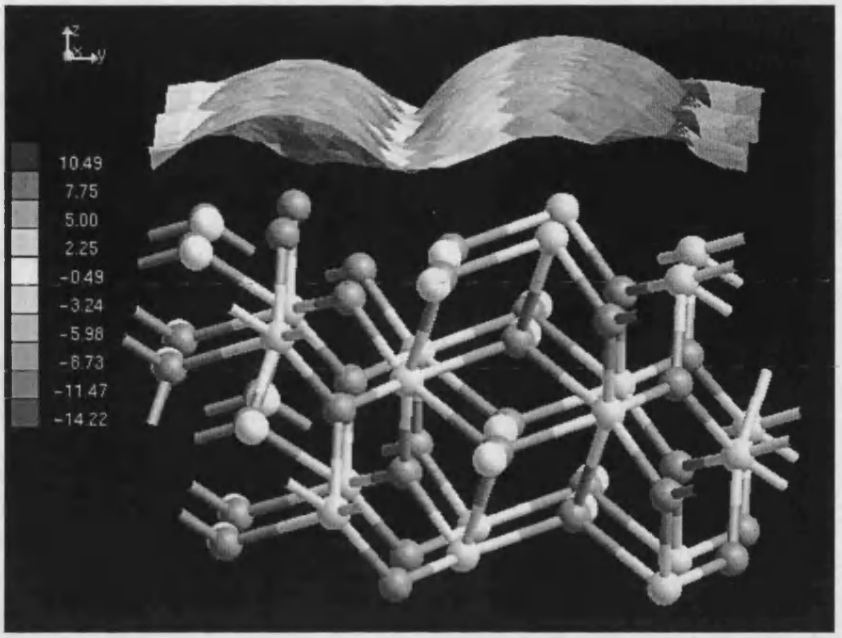

Figure 8.2.1. Simulated (110) surface and corresponding es-map (2 unit cells). Green atoms are Fe, red atoms are O1 and O2 and white atoms are H.

Figure 8.2.2 illustrates the es map of the (100) surface, which was the most stable of the simulated surfaces with the lowest surface energy. The map shows smaller variation in the es charge field on the surface and therefore less potential attraction for ionic arsenic species. This surface shows only one under co-ordinated surface Fe(III) ion that creates the positive charge and one under co-ordinated surface oxygen (O1) creating the negative areas.

The (010) surface similarly shows smaller es variability and the zero charge field is more prevalent and spread over the majority of the surface (Figure 8.2.3) although the relaxed surface energy is much larger than for the (100) surface. The (010) surface has two under co-ordinated Fe(III) ions and two under co-ordinated oxygen ions (two O2 anions).

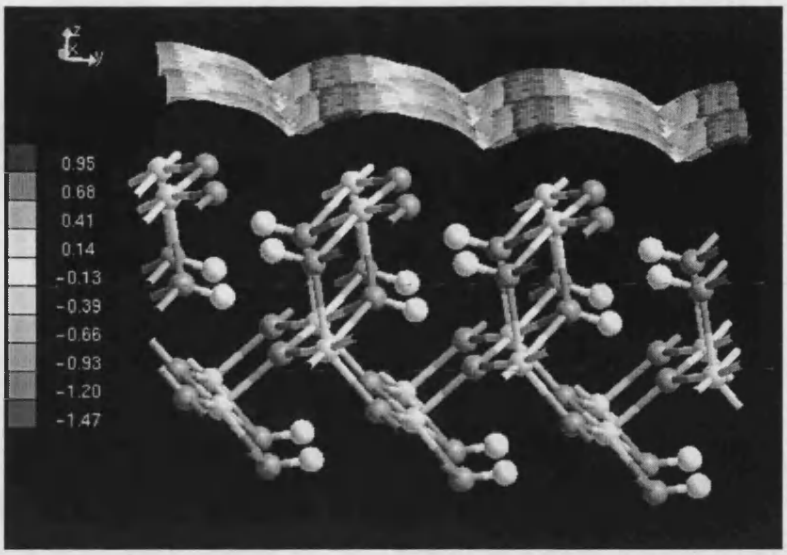

Figure 8.2.2. Electrostatic map of the simulated (100) surface.

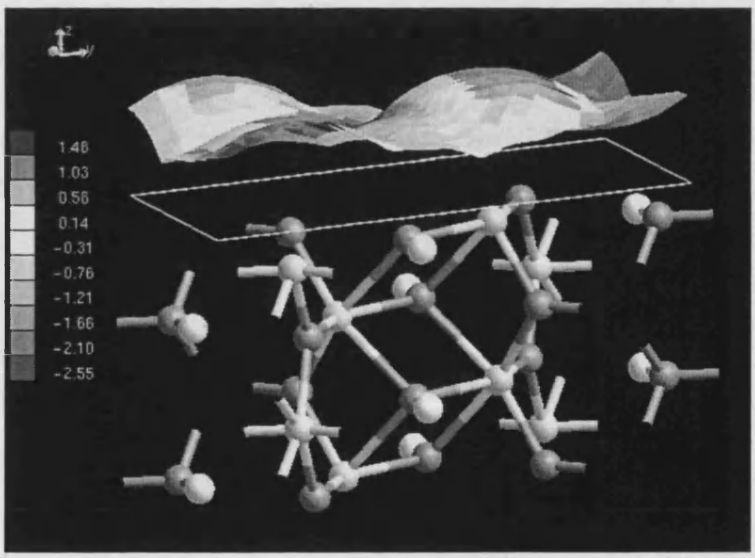

Figure 8.2.3. Electrostatic map of the simulated (010) surface.

The number of under co-ordinated surface ions was used as indicators of the relative site density for each type of site, such as Fe with CN 3, 4 and 5. Table 8.2.1 summarises the site densities for the most important morphological surfaces. These were used in subsequent adsorption calculations to establish those surfaces with the greatest adsorption potential. Only the Fe site densities

are given, as it is the positive electrostatic charges that will attract the negative arsenic anions common to natural groundwaters (See Chapter 2.1).

SURFACE	POSITVE CHARGE – (ATOM COORDINATION)	NEGATIVE CHARGE – (ATOM COORDINATION)	ADSORPTION SITE DENSITY ($Å^{-2}$)			
			Fe(3)	Fe(4)	Fe(5)	Total
(201)	2xFe(4) & 2xFe(5)	2xO1(2) & 2xO2(2)		0.05	0.05	0.10
(301)	2xFe(4) & 2xFe(5)	2xO1(2) & 2xO2(2)		0.04	0.04	0.08
(100)	Fe(5)	O1(3)			0.07	0.07
(210)	3xFe(5)	O1(3) & 2xO2(2)			0.06	0.06
(011)	2xFe(5)	2xO2(2)			0.04	0.04
(110)	2xFe(3) & 2xFe(4)	2xO1(3), 2xO2(1) & 2xO2(2)	0.02	0.02		0.04
(120)	2xFe(3) & 2xFe(4)	4xO1(2) & 4xO2(2)	0.02	0.02		0.04
(012)	2xFe(4)	O1(3) & O2(2)		0.03		0.03
(001)	3xFe(3)	3xO1(2) & 3xO2(2)	0.03			0.03
(211)	2xFe(3)	2xO2(2)	0.03			0.03
(101)	2xFe(5)	2xO1(3) & 2xO2(2)			0.02	0.02
(010)	2xFe(4)	2xO2(2)		0.02		0.02
(111)	Fe(3)	O1(3) & O2(2)	0.01			0.01

Table 8.2.1. Potential surface adsorption sites. The adsorption site density represents the number of under-coordinated surface Fe ions per unit surface area.

The results in table 8.2.1 are sorted to show the surfaces in order of decreasing adsorption site density. Those surfaces with the greatest site density have the potential for more arsenic to adsorb.

8.3. ARSENATE MOLECULE ADSORPTION SIMULATIONS

8.3.1. Introduction

Using the es maps for goethite surfaces (Section 8.2) the likely adsorption sites were identified and the 'docking' of the arsenate molecule ($AsO(OH)_3$) onto goethite, using potentials derived in Chapter 7, was simulated. The physical nature of adsorption of the arsenate molecule onto the goethite structure indicates the likely adsorption mechanisms and of the most important surfaces for sorbing arsenic.

The arsenate molecule was 'adsorbed' onto the different goethite surfaces by physically placing it above appropriate sites and then relaxing both the molecule and the surface. From the results of these exercises, it is clear that the complex formed depends on the surface structure. For example, the lowest energy configuration for the adsorption of $AsO(OH)_3$ onto the (011) surface involves the formation of an **As – O – Fe** monodentate–mononuclear (MM) complex. However the most stable configuration, with the lowest energy for the (110) surface involves two hydroxyl oxygens bonding to two surface Fe(III) in the following arrangement (bidentate–binuclear (BB) complex):

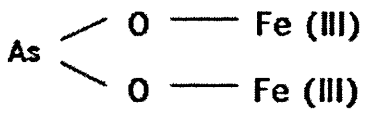

The adsorption interaction of the As molecule was simulated for the (100), (101), (210), (011), (012) and (111) surfaces. These represent the more stable surfaces of the simulated morphological structure (Chapter 7). The (010) and (110) surfaces have also been modelled, representing the cleavage plane and another dominant surface not shown on the simulated morphology, respectively.

As well as using the es map to suggest sites to 'dock' or 'adsorb' the arsenate molecule, other adsorption sites were studied and include physical gaps within

the surface structure where the arsenate molecule might be physically placed. The arsenate molecule was placed in two different starting orientations:

(1) In its upright position, with the three hydroxyl groups pointed towards the goethite surface, and the oxygen anion pointing directly away from the surface.
(2) The 180° image position, with the oxygen anion pointing towards the goethite surface.

The whole assembly was then relaxed to find the lowest energy sorption configuration.

The following sections describe the adsorption model energetics for the formation of surface complexes, the different complexes formed and the initial adsorption sites chosen.

8.3.2. The Energetics of Complexation

The results of the adsorption simulations are given in Table 8.3.1 and more comprehensively in Appendix 8A. The table shows the complexation energies, which, in this study, are defined as the difference between the lattice energy of the final adsorbed arsenate-goethite structure and the sum of the relaxed energy of the goethite surface and the arsenate molecule:

$$E_{molecule} + E_{surface} \rightarrow E_{(surface + molecule)} \quad \textit{Eqn. 8.3.1.}$$
after adsorption

$$E_{(surface + molecule)} - [E_{surface} + E_{molecule}] \rightarrow E_{complexation} \quad \textit{Eqn. 8.3.2.}$$
summation of individual energies

SURFACE	ADSORPTION SITE DENSITY ($Å^{-2}$)	LOWEST SIMULATED COMPLEXATION ENERGY (eV)	ARSENIC COORDINATION FOR MOST STABLE COMPLEX	LOWEST ENERGY COMPLEX
(011)	0.04	-14.82	5	MM
(111)	0.01	-14.46	5	BB
(120)	0.04	-6.98	5	BB
(010)	0.02	-6.23	6	TT
(012)	0.03	-5.62	6	TT
(110)	0.04	-5.14	6	BB
(100)	0.07	-4.50	5	MB
(210)	0.06	-4.36	5	BB
(101)	0.02	-1.89	5	BB

Table 8.3.1. Summary of the arsenate molecule adsorption simulations onto various goethite surfaces, and the surface adsorption site density (i.e. the total number of Fe under co-ordinated sites per surface area). MM = Monodentate Mononuclear complexes, BB = Bidentate Binuclear, MB = Monodentate Binuclear and TT = Tridentate Trinuclear.

The co-ordination of As(V) usually changes from tetrahedral co-ordinate bonding in the $AsO(OH)_3$ molecule to five co-ordinate in the adsorbed structures. The additional bonded ion is either an oxygen anion (O2) or hydroxyl oxygen (O1) from the goethite surface, with the subsequent loss of the double

bond between As(V) and the molecular oxygen anion. The average co-ordination of the As(V) in the adsorbed complexes was compared with results from previous EXAFS studies (Table 8.3.2). The As-O co-ordination number of the simulated structures corresponds well with those derived from spectroscopic analysis and lie within acceptable errors for spectroscopic analysis. The pH of the experiments does not greatly affect the co-ordination of As–O (O'Reilly *et al.*, 2001).

REFERENCE	Experiment pH	AVERAGE As-O CO-ORDINATION	ERROR LIMITS (%)
Farquhar *et al.* (2002)	5.5 – 6.5	4.0 (± 1.1)	27.8
Waychunas *et al.* (1993)	8.0	4.7 (± 0.5)	5 – 10
Sherman & Randall (2003)	4.0	4.0 (± 0.8)	20
O'Reilly *et al.* (2001)	4.0 & 6.0	4.7 (± 0.6)	12
Fendorf *et al.* (1997)	4.0 – 8.0	3.8 (± 0.8)	20
Current work (Calculated)	-	**5.0**	-

Table 8.3.2. Comparison of As(V) complex co-ordination when adsorbed onto goethite and analysed using EXAFS.

In general, the results from the calculations (Table 8.3.1) show that the complexation of the arsenate molecule onto the goethite surfaces is a highly favourable exothermic reaction, and the (011) and (111) surfaces readily accommodate this surface adsorption mechanism. The complexation energies are unusually high and examples of different complexation reactions involving CO adsorption onto zeolites and gold have negative energies in the range of –0.10 to –1.46 eV (Broqvist *et al.*, 2004, Kim *et al.*, 2001 and Jungsuttiwong *et al.*, 2001). The calculated complexation energies may be high and negative as a result of vacuum conditions imposed on the simulations. In reality the As molecule may lose the O^{2-} ion or some of the OH^- groups as it interacts with the goethite surface. Also, arsenic within a solution would require the dispersion of water molecules surrounding the goethite surfaces before complexation. Therefore the absolute values for the complexation energies may not be directly analogous to complexation in 'real' conditions. However, observations of the general energy trends and the formation of complexes for different

goethite surfaces are relevant as they allow for a first indication of the adsorption mechanisms.

The table also shows a weak relationship between the more favourable surfaces for complexation and the smaller site densities. There is no quantifiable relationship between the adsorption site density and the complexation type favourable to that surface. The most stable complex was formed on the (011) surface with Monodentate–Mononuclear (MM) formation (Figure 8.3.1).

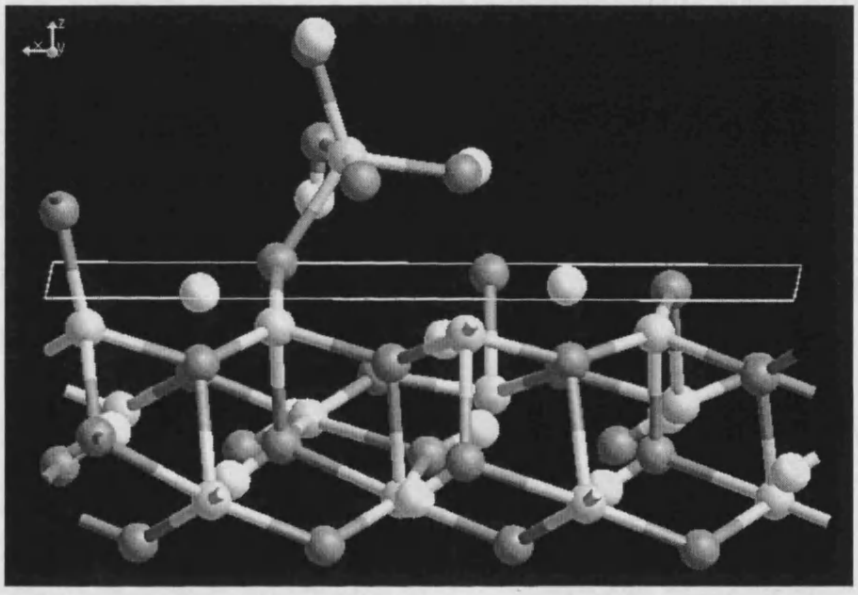

Figure 8.3.1. Simulated adsorption of arsenate molecule onto (011) surface. Lowest energy configuration (MM).

The (012) surface does not form any monodentate or mononuclear complexes but does show preferred trinuclear bonding. Unlike most of the other surfaces the As(V) on the (012) surface complexes is bonded to six other ions (Figure 8.3.2).

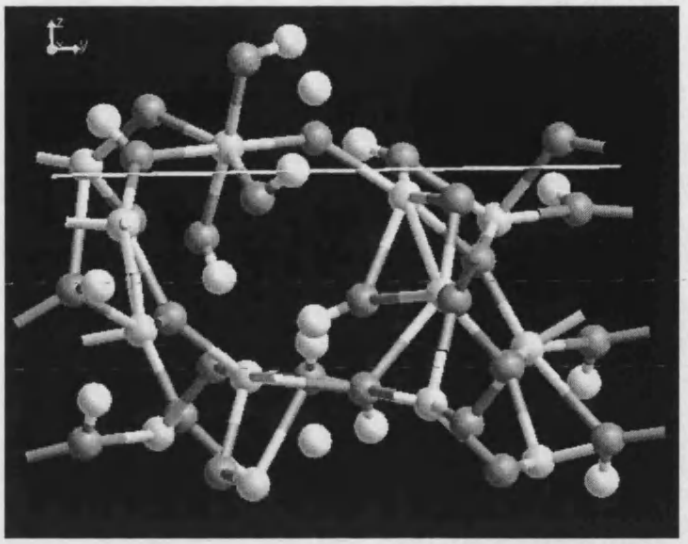

Figure 8.3.2. Simulated adsorption of arsenate molecule onto (012) surface. TT complexation and As in 6 co-ordination.

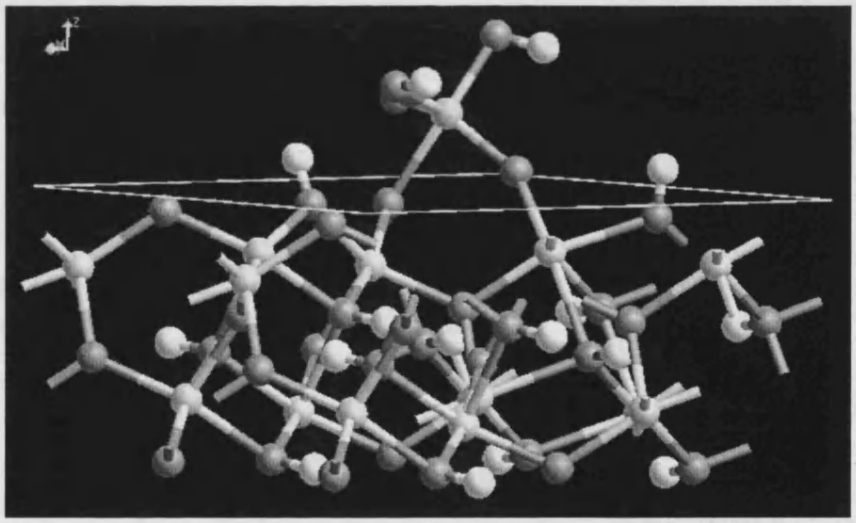

Figure 8.3.3. Simulated adsorption of arsenate molecule onto (210) surface. Lowest energy configuration (BB).

The least favourable for complexation were the (101) and (210) surfaces and the calculations show that the arsenate molecule interactions with these goethite surfaces involve bidentate (BB) bonding (Figure 8.3.3). Tridentate complexes are highly favourable on the (010) and (012) surfaces (Figure 8.3.2). Binuclear complexes were the most common throughout all of the studied

surfaces and mononuclear and trinuclear complexes were formed in relatively minor proportions. The energetics of these are summarised in Table 8.3.1, which shows that all reactions were exothermic.

The As(V) in the (010), (012) and (110) surface complexes formed was bonded to six other ions. This less common co-ordination of the arsenate results from the increased number of Fe(III) ions bonded by the complex. Although the simulated results were not conclusive there is a suggestion that as the co-ordination of As increases the number of bonded surface Fe(III) ions also increases. It is unlikely that the arsenic ion co-ordination and the number of bonded Fe(III) will increase further as the distribution of surface Fe will inhibit this.

If the complexation energies only are considered, then it is clear that some surfaces form lower energy complexes than others. The energy of complexation with respect to the different surfaces is ordered from lowest to highest as follows:

$$(011) < (111) < (120) < (010) < (012) < (110) < (100) < (210) < (101)$$

The surfaces that demonstrate the lowest complexation energies include the (011) and (111) with MM and BB complexes. As the formation energy increases, the complexes formed change to BB and TT. This trend suggests that the initial structures forming between arsenate and goethite are mononuclear and as these sites are filled the more energetically expensive bi- or tri-nuclear structures will form.

8.3.3. Adsorption Sites

From the structures of the surfaces that have been successfully optimised for adsorption there is a definite trend regarding the initial and final position of the arsenate molecule. Appendix 8A presents the results of the adsorption models and this is summarised for the lowest energy complex in Table 8.3.3. The previous section also provided some examples of the optimised surface complexes and their final adsorption sites.

SURFACE	LOWEST COMPLEXATION ENERGY – INITIAL ADSORPTION SITE	LOWEST COMPLEXATION ENERGY – OPTIMISED ADSORPTION SITE
(011)	Between 3 x Fe3	Above & between 3 x Fe3
(111)	Above Fe3	Above O2 & between 2 x Fe3
(120)	Between 2 x Fe3	Gap between 2 x Fe3
(010)	Gap between Fe3 & 2 x O2	Gap between 4 x Fe3
(012)	Above & between 3 x Fe3	Gap between 3 x Fe3
(110)	Gap between 2 x Fe3	Gap between 2 x Fe3
(100)	Above Fe3	Above & between 2 x Fe3
(210)	Above Fe3	Above & between 2 x Fe3
(101)	Above OH	Gap between 2 x Fe

Table 8.3.3. Summary of the most stable adsorption site configurations on each surface before and after optimisation. Fe3 denotes surface Fe(III) ions, O2 the oxygen anion and OH the hydroxyl group.

The table demonstrates that for the majority of surfaces the most stable complexes formed were initially docked on sites above a goethite surface Fe ion and on optimisation the adsorbed complex shifts into structural gaps in the surface structure. The (011) surface shows preferential MM complex bonding, and although the molecule was initially placed between three surface Fe ions, it attached to the closest ion after optimisation. The (120) and (110) stable surface complexes were initially docked between two Fe ions and as a result the optimised complexes were BB (See Table 8.3.1). The most favourable site

for complexation on the (010) and (012) surfaces was initially between three surface ions and the optimised structures involve TT binding. Therefore as a general rule, if the arsenate molecule can be initially docked between more than one surface Fe then BB or TT optimised complexes are formed between structural gaps with the arsenate bonding to the nearest Fe ions.

Therefore, the es maps previously described (Section 8.3.2) do provide an indication of areas where es forces surrounding under co-ordinated Fe ions would attract the arsenate molecule. Docking sites that were chosen above or between surface oxygen ions were not energetically favourable.

Another important observation from the simulations is that the final structure depends on the initial docking orientation of the arsenate molecule. Half of the models involved docking the molecule in two orientations:

(1) The upright position with the double bonded oxygen anion pointing away from the surface.

(2) For the other half the molecule was docked in its 180 position:

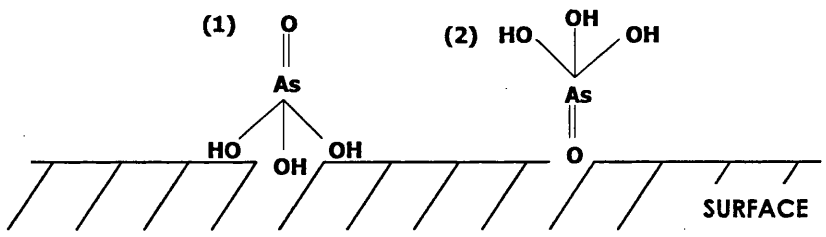

Almost all of the simulations for all surfaces show a preference for docking the molecule in its 180 position (2). Only the less energetically favourable complexes formed with the molecule docked in its upright position. This is probably due to greater electrostatic interaction between the O^{2-} ion in the As molecule and the Fe^{3+} in the goethite surface. The current simulations have concentrated on these two extreme molecular orientations. From the simulations, and starting with one of the two initial molecule orientations, the optimised complexes demonstrate slight changes of the orientation to a more favourable position. By choosing slightly different initial molecule positions at different angles between 0 and 180 , the outcome may result in the same optimised results. However, this can only be verified by further modelling.

8.3.4. Complexation As(V)-Fe(III) Distances

The average distances between the As(V) ion and surface Fe(III) is also specific to the type of complex formed, and can be compared with those distances previously measured using spectroscopic techniques.

Table 8.3.4 summarises the average As(V)-Fe(III) distances for the different complexes formed on each of the simulated surfaces. The different surfaces show contrasting ordering in the As-Fe distances for the various adsorption complexes, although the average distances for all surfaces indicates the overall preferences. The average distances demonstrate that the mononuclear complexes (MM and BM) form the shortest and strongest linkages (As(V)–Fe(III) are 3.40 Å and 3.19 Å respectively). Binuclear complexes (BB) form intermediate As(V)–Fe(III) distances (3.43 Å) and trinuclear complexes have the largest (3.44 Å). The mononuclear complex As-Fe distances also show the least variation throughout the modelled surfaces whereas the binuclear demonstrate the greatest differences.

SURFACE	MM As(V)-Fe(III) DISTANCE (Å)	BM As(V)-Fe(III) DISTANCE (Å)	BB As(V)-Fe(III) DISTANCE (Å)	TRINUCLEAR As(V)-Fe(III) DISTANCE (Å)
(110)	3.47	3.34	3.43	-
(101)	3.39	3.24	3.43	3.23
(111)	3.50	3.00	3.47	3.42
(120)	3.41	-	3.59	3.88
(011)	3.33	-	3.47	3.39
(010)	-	-	3.41	3.44
(012)	-	-	3.35	3.29
(100)	3.32	-	3.38	-
(210)	-	-	3.37	-
AVERAGE DISTANCES	**3.40**	**3.19**	**3.43**	**3.44**

Table 8.3.4. Summary of particular complex As-Fe distances for simulated arsenate molecule formation onto various goethite surfaces.

To compare the simulated complex results with those of previous spectroscopic studies the (110) surface must be considered as it is the surface most commonly cited in published work and one of the most important surfaces observed in

natural goethite morphology. From the calculations, the average As(V)-Fe(III) distances for BM formation is the smallest of those highlighted in Table 8.3.4, hence this complex is more tightly held and less likely to break than the others as a result of disturbing forces. The BM As(V)-Fe(III) distance on the (110) surface is 3.34 Å, which gets larger with the formation of BB complexes (3.43 Å), and is greatest in the MM formations (3.47 Å). Fendorf *et al.* (1997) have also observed this order of As-Fe distance during an EXAFS study of the As(V) mechanisms of adsorption onto the (110) goethite surface. Their results are given, with other publications in Table 8.3.5. The trinuclear formations, which are rarely commented upon in other literature reviews of arsenate complexation on iron-oxide and aluminium-oxide surfaces, were energetically less favourable than the other simulated complexes. This may explain why these complexes are not readily observed using experimental adsorption techniques and subsequent spectroscopic analysis.

Table 8.3.5 highlights the As(V)-Fe(III) distances derived from other studies in comparison with those established from the current atomistic simulations. The differences may be a result of the difficulty in reproducing experimentally derived spectra and also an over-estimation of repulsive forces, or under-estimation of attractive forces acting between ions involved in complexation. However, the simulated distances are overall within 12 % of the spectroscopic results derived by Fendorf *et al.* (1997) and show better agreement than those simulated by Ladiera *et al.* (2001) when compared to spectroscopic analyses for arsenate complexes on gibbsite ($Al_2O_3.3H_2O$) (Table 8.3.6). Therefore in general, the relative distances for the different complexes are correctly modelled.

REFERENCE	MM As(V)-Fe(III) DISTANCES (Å)	BM As(V)-Fe(III) DISTANCES (Å)	BB As(V)-Fe(III) DISTANCES (Å)
Current Atomistic Simulations	3.40 (within 6 %)	3.19 (within 12 %)	3.43 (within 6 %)
PUBLISHED SPECTROSCOPIC STUDIES			
Fendorf *et al.*, 1997	3.52 (± 0.02)	2.85 (± 0.02)	3.24 (± 0.02)
Waychunas *et al.*, 1993	-	-	3.29 (± 0.04)
Farquhar *et al.*, 2002	-	-	3.31 (± 0.02)
Manning *et al.*, 1998	3.57	-	3.38
Sherman & Randall, 2003	-	-	3.30 (± 0.05)
O'Reilly *et al.*, 2001	-	-	3.30 (± 0.01)

Table 8.3.5. Comparison of current simulated As(V)-Fe(III) distances with those derived from spectroscopic studies, for various complexes adsorbed onto goethite as a whole. The percentages in brackets for the current study are compared with the spectroscopic results of Fendorf *et al.*

Similar disparity is also observed for the As(V)-Al(III) distances from two studies of the adsorption of arsenate onto aluminium-oxide surfaces (Table 8.3.6). Arai *et al.* (2001) used x-ray techniques to measure As(V)-Al distances for As complexes on aluminium-oxide and their results also show the increasing As(V)-Fe(III) distance trend for different arsenate complexes on goethite. The distances observed from the Arai *et al.* (2001) study are similar to those found by Fendorf *et al.* (1997) for goethite but contrast with those derived by Ladiera *et al.* (2001) using DFT (Density Functional Theory) methods to model As(V)-Al(III) distances of arsenate adsorbed onto gibbsite surfaces.

	REFERENCE	MM As(V)-Al DISTANCES (Å)	BM As(V)-Al DISTANCES (Å)	BB As(V)-Al DISTANCES (Å)
SPECTROSCOPIC	Arai *et al.*, 2001[a]	3.54 – 3.66	2.07 – 2.64	3.03 – 3.41
DFT SIMULATIONS	Ladiera *et al.*, 2001[b]	3.02 (within 14 %)	3.18 (within 35 %)	3.09 (within 16 %)

Table 8.3.6. Summary of the different complex As(V)-Al distances obtained by [a]EXAFS and [b]DFT simulations. The percentages in brackets relate to the greatest difference of the modelled distances to those derived spectroscopically.

The shorter As(V)-Fe(III) distances would suggest that stronger bonds exist between the arsenate molecule and the goethite surfaces. Therefore the BM and MM complexes should be more strongly held than the BB and trinuclear formations. The latter may be the first to desorb under a change in the chemical and physical environment.

Previous research [Waychunas *et al.* (1993), Manning *et al.* (1998), Farquhar *et al.* (2002), Sherman & Randall (2003), and Sun & Doner (1996)] into arsenate adsorption onto goethite, demonstrates the abundance of binuclear (bidentate) complexes formed on the goethite surface. In most of these studies only the dominant (110) only were considered, and spectroscopic methods were the main method of analysis.

Analysis of the main mechanisms of adsorption onto the equivalent (110) surface simulated by the current study also confirms that bidentate-binuclear complexation is the most favourable.

8.4. ARSENIC SUBSTITUTIONS

If, during adsorption, the arsenic is strongly bonded to the surface, then ion-exchange may occur between As and Fe(III) on the goethite surface, with the possibility of further migration into the bulk structure. Therefore, substitution simulations were performed to investigate the energetics of bulk structure migration. Substitution simulations for As(III) and As(V), respectively, involve:

(1) replacing a Fe(III) surface cation with an As(III) cation; or
(2) the replacement of a surface Fe(III) ion with As(V) whilst simultaneously removing another Fe(III) and substituting an oxygen anion with a hydroxyl group to maintain charge neutrality within the crystal.

The Kröger-Vink notation is used to describe defects and their reactions, where the defect species is given in terms of a position (subscript) and an effective charge (superscript). The charge may be positive ($^{\bullet}$), negative ($^{\prime}$) or neutral (^{x}). Therefore, the charge neutral substitutions for As(III) and As(V), respectively, are as follows:

$$\textbf{(1)} \qquad As_{Fe}^{x}$$

$$\textbf{(2)} \qquad As_{Fe}^{\bullet\bullet} + V_{Fe}^{III} + (OH)_{O}^{\bullet}$$

The interatomic potentials used for the As(V) substitution are those previously used for the simulation of the arsenate molecule. However, in this case the As(III) potentials have been fitted to an arsenolite structure (As_2O_3), as no further modelling was undertaken on other arsenite molecules, the details of which can be found in the Appendix 7B.

The simulated substitution results are summarised in Table 8.4.1 for both the As(III) and As(V) substitutions with Fe. The substitution energy represents the energy for the substitution of As only, and the defect energy is that for As with the corresponding charge compensating defect. Those surfaces chosen for the adsorption simulations in the preceding sections were used.

SURFACE	As(V) SUBSTITUTION ENERGY (eV)	As(V) DEFECT REACTION ENERGY (eV)	As(III) SUBSTITUTION ENERGY (eV)	As(III) DEFECT REACTION ENERGY (eV)
(210)	-37.27	-16.39	5.28	-10.03
(111)	-31.85	-10.97	5.04	-10.51
(101)	-30.16	-9.28	5.83	-8.93
(100)	-29.84	-8.96	6.39	-7.81
(012)	-21.10	-0.22	4.39	-11.81
(110)	-13.24	+7.64	4.23	-12.13
(010)	-12.30	+8.58	5.13	-10.33

Table 8.4.1. Substitution and defect energies for As(V) and As(III) and goethite.

Model limitations inhibit the comparison between As(III) and As(V) substitutions because of neutrality constraints. Although As(III) substitution is straightforward the substitution for As(V) requires the removal of other ions as a 'unit' to maintain charge neutrality. Therefore the substitution energy defined for As(V) cannot be compared directly with the energetics of the As(III) substitutions. However, individual comparisons across the different surfaces for As(III) and As(V) provide useful information.

The preferred surface for As(III) substitution is the (110), while for As(V) substitutions it is the (210) surfaces. There is no obvious trend between the favoured substitution surfaces and those favoured for arsenic complexation or between the favourable substitution sites for As(V) and As(III) substitution.

To compare the As(V) and As(III) substitutions more comprehensively a set of defect reactions are considered:

(1) For As(III):

$$As_2O_3 + 2Fe_{Fe} \Rightarrow 2As_{Fe} + Fe_2O_3$$

Energy of reaction (E):

$$E = 2E_{(AsFe)} + E(Fe_2O_3) - E(As_2O_3)$$

Where: $E(Fe_2O_3) = -150.37$ eV per unit formula (Jones *et al.*, 2000)
$E(As_2O_3) = -129.78$ eV per unit formula
$E_{(AsFe)}$ = Substitution energy derived.

(2) For As(V):

$$AsO(OH)_3 + 2Fe^{x}_{Fe} + OH_{OH} \Rightarrow As^{\bullet\bullet}_{Fe} + V^{III}_{Fe} + V^{\bullet}_{OH} + 2FeOOH + H_2O$$

Energy of reaction (E):

$$E = E_{(AsFe)} + E_{(VFe)} + E_{(VOH)} + 2E(FeOOH) + E(H_2O) - E(AsO(OH)_3)$$

Where:

$E(FeOOH)$	= -85.44 eV per unit formula
$E(H_2O)$	= -9.0994 eV for water molecule (de Leeuw and Parker (1997)
$E(AsO(OH)_3)$	= -200.86 eV
$E_{(AsFe)} + E_{(VFe)} + E_{(VOH)}$	= substitution energy derived.

The results of the defect calculations are given in Table 8.4.1. They reveal that the As(V) defects are still generally more energetically favourable than the As(III), but that some surfaces show a greater preference towards the As(III) than As(V). The As(V) defect calculations for the (010) and (110) surfaces suggest that this type of incorporation will not occur on these surfaces. The most important surface in the calculated crystal morphology (Chapter 7.3) was the (100) and on this surface the energy for complexation of the arsenate molecule is more favourable than that for the substitution or defect calculations. On the less important morphological surfaces the incorporation of As defects would arise as these are shown to be more energetically favourable.

In conclusion, while the substitution and defect energies can be used as an indication of surface mechanisms, their theoretical values may not correspond to those under 'real' conditions. Similar to the complexation simulations it is possibly due to the vacuum conditions of the models.

8.5. ADSORPTION MECHANISMS: Experimental Vs Modelling

The adsorption simulations have highlighted the dominance of particular complexes on different surfaces, and show that the most recurrent formation throughout is BB. This formation was found to be the most stable (energetically) on many of the surfaces. Another observation from these simulations is the variation in As(V)-Fe(III) distance with different complexes (BM < MM < BB < Trinuclear). This may suggest that those formations with greater distances are less strongly held and more susceptible to desorption. If this is indeed observed in natural samples, then it is reasonable to assume that the majority of complexes observed under natural groundwater conditions would be either BM or MM.

Although the simulated formations provide some knowledge of the adsorption mechanisms expected for each surface, they do not account for the amount of arsenic present. This was best demonstrated by the experimental work of the current research as it considered the effect of different arsenic solution concentrations upon adsorption. Fendorf *et al.* (1997) observed three different complexes formed between As(v) and the (110) surface of goethite, depending on the amount of surface coverage. Figure 8.5.1 illustrates the change from monodentate to BM and finally BB complexes with increasing surface coverage. This enhances the findings of the adsorption simulations, as both show that the lowest energy configuration was MM, with BB formations generally created with larger complexation energies. This suggests that as the As concentration increases the process commences with the lowest energy configurations (MM) occurring first, and once those complexation sites are filled the higher BB and TT energy sites begin to fill.

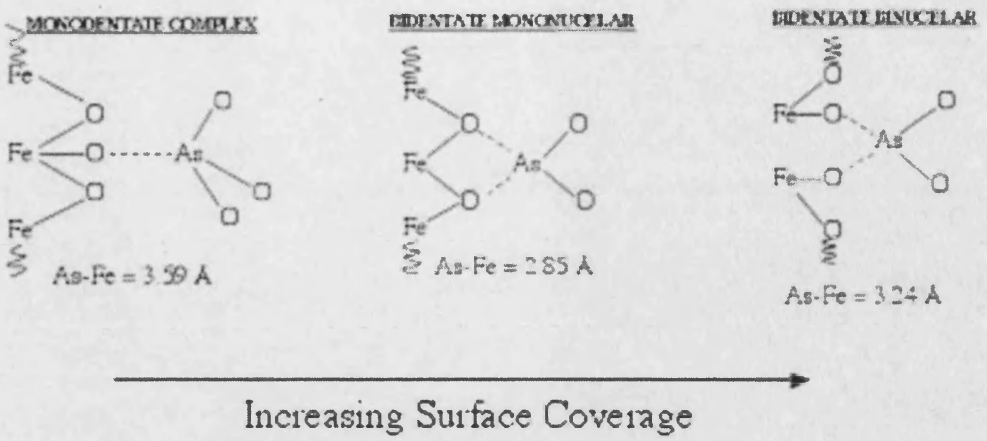

Figure 8.5.1. Schematic illustration of the change to adsorbed complex with increasing surface coverage (reproduced from Fendorf *et al.*, 1997)

Waychunas *et al.* (1993) also observed a decrease in the formation of monodentate As(v)-goethite complexes with increasing As/Fe ratio, while bidentate complexes remained in constant proportions as the ratio increased. The bidentate configurations are thought to be both thermodynamically and kinetically favourable. A suggestion as to why the monodentate complexes appear to decrease with increasing coverage is that they may become obscured by the increasing bidentate formation, or that initial monodentate complexes alter to bidentate (Waychunas *et al.*, 1993). Another possible reason for this change is that smaller units, which have geometrically restricted surface area, attract the monodentate complexes, whilst bidentate complexes form on larger units. The apparent decrease in monodentate formations would then be a result of the relative area distributions of the surfaces (Waychunas *et al.*, 1993). As a collective, the calculations from the current study show a general trend from more stable MM or BB complexes to higher energy BB or TT formations.

By using the simulated crystal morphology as an indication of dominant surfaces it is the (101), (100), (011), (210) and (111) faces, in that order, that show dominance. These same surfaces show progression from BB or MB complexes on the surfaces, with a smaller contribution from MM complexes and negligible or no TT formation. The (011) and (111) surfaces show

significantly lower complexation energies than the other surfaces. All the other named surfaces may therefore contribute only a small affinity for adsorption as the energy for complexation is significantly larger. Of the (011) and (111) surfaces the (011) surface has the higher potential for adsorption, forming lower energy MM complexes. This surface contributes more towards the crystal morphology (Figure 7.3.3, Chapter 7.3) compared with that of the (111) surface. By simplifying the process to the two surfaces the observation suggests that adsorption may follow a non-linear adsorption process. Starting with the low energy, more abundant MM sites filling unhindered first, the process corresponds to the near-linear section of the isotherm. Then the less favourable and scarcer BB sites begin to fill, relating to proportionally reduced adsorption and the lower gradient section of non-linear isotherms. This observation is also satisfied by the non-linear isotherm descriptions for the current batch experiments.

If this collective trend is assumed, then the experimental adsorption partitioning may be explained. In the early stages where the complexation energy for MM sites is most favourable, the rate of change of sorption to concentration, $\Delta S/\Delta C$ is greatest corresponding to the high gradient on the adsorption isotherm. As the site fill density increases, only then do the less favourable binuclear and trinuclear sites start to fill and may be hindered by an energy barrier preventing further complexation. This is characterised by a reduced $\Delta S/\Delta C$. This lowering in gradient implies non-linear functionality in the isotherm. The physical proportion of binuclear and trinuclear sites available on any surface is also likely to be smaller than MM and BB, as more surface iron atoms are required for such attractions.

The effect of pH upon the mechanism of adsorption of As(v) and As(III) onto goethite (110) surface has been studied previously by Manning *et al.* (1998), who found that at low pH hydrogen bonding arose, with the formation of As(V)-Fe BB complexes. However, at intermediate and high pH, the mechanism of bonding changed towards As(V)-Fe MM adsorbed formations (Figure 8.5.2). With respect to the As(III)-Fe MM surface complexes, there was no change to the surface complex with increasing pH. The current calculations were done at

circum-neutral pH and may relate to a predominance of MM complexes, but also the presence of BB complexes.

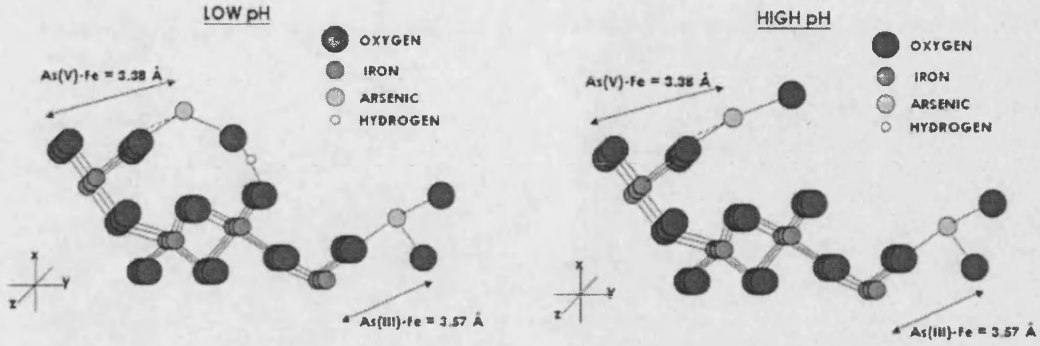

Figure 8.5.2. Change in the As complexation mechanisms onto the goethite (110) surface, with increasing pH (reproduced from Manning *et al.*, 1998).

Sun and Doner (1996) have also identified different inner-sphere complexes formed between arsenate (As(V)) and arsenite (As(III)) onto the (110) goethite surface. Using T-FTIR spectroscopy techniques, their results confirm those of Manning *et al.* (1998); with As(V) forming BB complexes and As(III) forming MM configurations.

9. CONCLUSIONS AND FURTHER WORK

9.1. CONCLUSIONS

The research study has provided an insight to many of the processes that contribute to arsenic sorption in groundwater systems. The results of batch and column experiments and the insights from computer simulations provided details and descriptive parameters for these processes. A contribution to adsorption under dynamic flow interactions and introduction of a different redox environment was achieved. Adsorption for the different groundwater conditions were quantified in terms of partition coefficients and compared with each other and with those currently used to model the transport of arsenic in gourndwater. In general the experiments show the importance in considering dynamic adsorption under flow conditions and the redox environment when defining partition coefficients as both conditions provide for significantly less adsorption than under equilibrium, aerobic environments. The effects of this motion are quantified and together with the redox work, open the door to further studies and a more complete understanding of generalised arsenic adsorption.

9.1.1. Batch Experiments

This research study has investigated arsenate adsorption onto goethite, in particular to understand adsorption under natural groundwater conditions. Previous studies were interested principally in the effects of solution pH and ionic concentration upon the adsorption, and the spectroscopic analysis of the adsorption complexes formed upon the surfaces of metal oxides and oxyhydroxides. The BGS – Mott MacDonald study into arsenic transport within the groundwater of Bangladesh (BGS and MML, 1999) uses partition coefficients derived from simulated equilibrium adsorption isotherms of arsenic (As(V) and

As(III)) onto iron-oxides. Their approach does not represent sufficiently the actual adsorption of the arsenic transportation in groundwater as a function of redox, pH and the flow parameters of groundwater.

By building upon previous studies, adsorption isotherms and corresponding partition coefficients have been derived for the series of batch experiments presented herein. These investigated As(V) adsorption onto goethite. The results agree well with published results by illustrating the decrease in arsenate adsorption with increasing solution pH. From the batch experiments adsorption isotherms were derived and quantified in terms of the mass of arsenic adsorbed per mass goethite used against the equilibrium arsenic concentration in solution. The isotherms are non–linear and agree with the Freundlich and the Langmuir isotherms. These isotherms are well established in the description of arsenic adsorption and have been used in a number of previous studies (Bowell, 1994, Pierce & Moore, 1982 and Smedley & Kinniburgh, 2002).

Isotherm coefficients were quantified by curve fitting and coefficient estimation techniques and these produced consistent values. The linear partition coefficients (K_d) determined from the batch experiments range from 1000 to 19000 l/kg, whereas the Freundlich K_f coefficient ranged between 8000 and 19000 l/kg with the exponent 'n' between 0.46 and 0.86. The Langmuir adsorption model Q_0 values are between 15000 and 28000 l/kg and K_l between 0.5 and 2.9. The ranges of the derived partition coefficients and the Freundlich 'n' value enclose those previously published, lending support to the values determined herein. For As(V)–goethite adsorption partition coefficient published values range from 192 to 1800 lkg^{-1} by Bowell (1994) and Hingston *et al.* (1972) respectively and the Freundlich 'n' exponent range includes the value of 0.66 found by Thirunavukkarasu *et al.* (2003).

Both the Linear K_d and Freundlich K_f coefficients show an inverse linear relationship with solution pH. The Langmuir K_l and Q_o parameters also show this relationship with pH, but it is not as well defined. No obvious relationship was identified between the Freundlich exponent 'n' and solution pH. The inverse relationships with pH are due to the surface charge of goethite and the Point of Zero Charge, PZC. Below the PZC, which for goethite is at pH 7.3, the surface

has a positive charge and attracts the negative arsenic ion complex, but at more alkaline conditions the goethite surface has negative charge and repels anions. Similar trends are widely cited by other published work (e.g., Pierce & Moore, 1982; Bowell, 1994; Manning and Goldberg, 1997).

With all controllable variables held constant, the K_d, K_f and Q_o parameters decrease with an inverse power function as the goethite mass increases. This occurs by definition of the adsorption isotherm and is consistent with proportionally greater adsorption with more available goethite mass.

Attributing the best-fit isotherm for batch adsorption is marginal between the Freundlich and Langmuir, as both seem to fit the experimental data equally well. This may be because adsorption has not attained saturation of available adsorption sites, as required by the Langmuir isotherm limit. The graphical interpretation of the Freundlich isotherm is, however, slightly better and so is the definition with respect to the solution pH and the goethite mass.

9.1.2. Column Experiments

The column experiments introduced pseudo–real simulation conditions to provide an insight of the kinetic effects on adsorption of arsenate onto goethite under dynamic conditions. Their value is that they are more likely to mimic flow conditions in natural groundwater. The objectives were to study the difference between batch equilibrium adsorption coefficients, and dynamic column coefficients.

The derived Linear K_d coefficients ranged between 45 and 1300 l/kg. These values are collectively up to two orders of magnitude lower than those derived from the equilibrium experiments with batch K_d of 1000 – 19000 l/kg. The Freundlich K_f coefficient values lie between 600 and 19600 l/kg and the majority are also less than the equilibrium experimental values of 8000 – 19000 l/kg. The 'n' exponent of the Freundlich isotherm was taken as a constant for all arsenic

BTC simulations, and only the K_f value was modified. The value for 'n' was chosen from the batch results, for solution pH 6, identical to the column effluent pH. Perhaps by not allowing some freedom to 'n', the K_f value is not directly representative of the column adsorption. However, the general trends observed compare well with those observed for the linear column K_d. The derived column partition coefficients are generally within the same order of magnitude as published values.

The linear K_d and Freundlich K_f values obtained for the column experiments show a decrease with increased goethite mass within the columns. This relationship is also identified with the batch K_d and K_f and is described in terms of a power function (with exponent between –0.8 and –1.3). The batch Q_o values also demonstrate this relationship.

A comparison between the influent arsenic concentration and partition coefficients shows a poorly defined trend, with a slight decrease in K_d with increasing As, and an initial increase in K_f with increasing As, until 600 $\mu g l^{-1}$, followed by a decrease thereafter. The partition coefficients should remain the same with respect to the solute concentration, by definition. However, factors such as chemical disequilibrium, may be contributing to this dual gradient phenomenon.

The column experiments also suggest the presence of kinetic effects as demonstrated by a relationship between the linear flow velocity and the partition coefficients. Using the collective results plotted for the individual columns there is a distinct decrease in the K_d and K_f values as the flow velocity increases which is more pronounced in those columns with greater goethite mass. The effective porosity does not change markedly over the range of flow velocities and does not affect the variation of adsorption nor the partition coefficient.

More specific results indicate that the partition coefficients, K_d and especially K_f decrease with increasing velocity, and also that K_f increases with respect to influent arsenic concentration, which is not a trend that is found strongly with the linear K_d.

Therefore, in general the Linear K_d values determined from the column experiments are less than those determined through the equilibrium batch experiments. This is probably a result of chemical disequilibrium because not all of the goethite mass within the column is in contact with the solute, with various flow paths bypassing some goethite grains. The kinetic effect causing chemical disequilibrium manifests itself by insufficient contact time between the arsenic in solution and the goethite surface. The result is reduced arsenic adsorption compared with equilibrium sorption. This is particularly important as it highlights the possible errors that could ensue and the corrections to consider if transport models are used in the prediction of arsenic, or any other contaminant transport, using equilibrium partition coefficients. Without making provisions for this an over-estimation of the adsorption of arsenic would result.

The subsequent 'desorption' of arsenic from the column experiments has also highlighted the degree of sorption irreversibility. The observed mass balance between the adsorption and desorption phases demonstrate that on average 12 % of the arsenic remains sorbed or trapped within stagnant porewaters. There have been a number of previous studies that observed this hysteresis (Fuller *et al.*, 1993, Puls & Powell, 1992 and Darland & Inskeep, 1997), attributable to the strong binding that occurs between arsenic and the goethite surfaces upon adsorption. The rate of desorption in batch experiments can take over 96 hours to complete, mainly the result of diffusion of arsenic from pores (Fuller *et al.*, 1993).

The redox column experiment demonstrated the effect of introducing the reductant catechol into a column containing pre-sorbed As(V) on goethite surfaces. A pseudo-partition coefficient (K_{red}) of 500 l/kg describes the As partitioning during the reducing phase. The anaerobic K_{red} is up to a quarter of the aerobic (K_{ox}) column partition coefficients derived for the same column. Analysis of the column effluent and the solid phase indicate that arsenic was released by both arsenic reduction and reductive dissolution of iron (goethite). This illustrates the importance of determining partitioning under various redox conditions. Using aerobic coefficients to describe transport in reduced groundwater would lead to an under-estimate of the amount of arsenic movement.

With the continued release of arsenic and iron during the reducing phase, the relative proportions of arsenic in porewater, compared with the amount of arsenic adsorbed, will define different values for partitioning. Hence the change in concentration gradients could drive re-sorption, and complicate the description of arsenic adsorption.

9.1.3. Atomistic Modelling

From the simulation of the bulk goethite structure, a number of important surfaces have been created, modelled, and atomically 'relaxed' to their lowest energy, most stable configurations. The energetics of the relaxed surfaces give an indication of the most stable surfaces, and hence those most likely to occur in natural goethite crystals. The most stable surfaces identified were the (100) and (101), with (111) as one of the least stable. The simulation of the goethite morphology using the BFDH (Bravais-Friedel-Donnay-Harker) method illustrates that the set of faces observed on the crystal surface structure equate to those identified experimentally (Cornell and Schwertmann (1996), Barrón *et al.* (1997), Rakovan *et al.* (1999) and Manceau *et al.* (2000)). The important simulated morphological surfaces are the (100), (101), (210), (011) and (111) surfaces. Although small discrepancies were found regarding the order of surface stability of the simulations herein compared with those of Steele *et al.* (2002) they may be due to the model purity and the initial potential set derivation. Discrepancies with natural goethites include the simulated particle size and growth kinetics as well as the lack of surface solvation. All natural goethite will show a degree of hydration whereas the simulated goethite assumes 'dry' surfaces in this new modelling work. Although hydration has not been incorporated in the atomic modelling, the results of the adsorption simulations give some indication of adsorption sites, and the importance of the way in which the arsenic is attached to the surface. A number of energetically favourable surfaces were studied by the adsorption simulations, including dominant morphological surfaces and known natural cleavage planes.

The substitution of an As(V) and As(III) atom into the goethite surface structure illustrates the possible effect of cation exchange, when arsenic is strongly adsorbed on the surface. The results demonstrate that the substitution of As(V) is highly favourable, particularly on the (210) goethite surface. Defect energy calculations indicate that As(V) incorporation is generally more energetically favourable than As(III) on most surfaces.

A new model for a viable neutrally charged arsenate molecule ($AsO(OH)_3$) was made and used in the adsorption simulations onto the neutrally charged goethite surfaces. This molecule is known to exist in natural groundwater, although the anionic species is more common. Simulations with this molecule reveal the more energetically favourable adsorption complexes formed, and the most favourable sites, on the modelled surfaces were monodentate-mononuclear.

The majority of the surfaces studied show that the arsenate molecule has a particular affinity towards surface Fe(III). The optimised adsorption structures mostly form in positions above surface Fe(III) ions, and the adsorption structures with the lowest energy are those where the arsenate molecule is initially positioned above surface Fe(III) ions. By contrast, the adsorption sites on the (010) and (101) surfaces occur above either surface oxygen anions or hydroxyl oxygen and the arsenate molecule moves towards gaps between surface iron ions on relaxation. After optimisation most simulations show favourable adsorption between structural gaps. In almost all of the optimised adsorption structures the most favourable position for the arsenate molecule is where the oxygen anion is perpendicular to the surface and the three hydroxyl groups point into the goethite surface structure, initially shielding the As(V) atom. There is no obvious correlation between the initial site of adsorption and the final optimised complexes formed between the arsenate molecule and the goethite surface.

The collective results demonstrate that the lowest energy formation is generally monodentate–mononuclear, with bidentate–binuclear the least energetically favourable complex. In almost all of the optimised adsorption models, the arsenate within the molecule is bonded to five other ions including surface

oxygen anions or hydroxyl oxygen. The energetics involved in complexation with respect to the different surfaces show that the (011) and (111) surfaces have the lowest 'complexation' energies, while the (101) surface has the highest formation energy. Hence, the adsorption of the arsenate molecule would tend towards those surfaces where it can bind with the least energy.

The As(V)-Fe(III) atomic distances vary depending on the type of complex formed on the surface. The shortest distance (3.19 Å) is observed in the binuclear–monodentate (BM) complexes. The distance increases for monodentate–mononuclear (MM) (3.40 Å), to bidentate–binuclear (BB) (3.43 Å) and then to trinuclear complexes (3.44 Å). This order of increasing As(V)-Fe(III) atomic distance has also been observed by Fendorf *et al.* (1997), although the distances that they observed using spectroscopic analyses are generally smaller. The difference in As-Fe distances also suggests that those complexes most likely to desorb are the trinuclear, with the longest distances and the weakest bonds, whereas the bidentate–mononuclear (BM) complexes have shorter and stronger links to the surface and will be harder to break if desorption occurs.

Fendorf *et al.* (1997) also identified a change in complexation with increasing surface coverage of arsenate onto the (110) goethite surface, from MM to BM and then to BB, respectively. The current results on the same surface compare well with Fendorf *et al.* (1997), illustrating that: (a) the MM complexes formed with low surface coverage are the more energetically favourable and so would be the first to become filled, and (b) with increasing coverage, the energetically more costly structures (BB) will form.

The equilibrium batch results in this study are defined by non-linear adsorption corresponding to either the Freundlich or Langmuir isotherms. In the simulated goethite morphology, only the (011) and (111) surfaces may contribute significantly to adsorption of arsenic because of considerably smaller complexation energies for these surfaces. The (011) surface constitutes a relatively large proportion of the crystal morphology and also forms the most energetically favourable MM complex. The process forming these MM complexes on the (011) surface corresponds to the linear section of the

adsorption isotherm. By contrast, the (111) surface has a smaller contribution towards the morphology and the formation of BB complexes is less energetically favourable. Adsorption onto the (111) surface is characterised by the lower gradient sections of the isotherm and demonstrate the existence of a non-linear adsorption mechanism.

Although the effect of changing the solution pH was not modelled in this study, an EXAFS study by Manning *et al.* (1998) on arsenic retention on the (110) goethite surface revealed that the complexation mechanism for As(V) changes from BB to MM with increasing pH, whilst the As(III) complex remains MM throughout. This highlights the importance and need for further atomic simulations regarding arsenic – goethite surface interactions to explain the experimental adsorption isotherms. Sun and Doner (1996) also observed a difference between As(V) and As(III) adsorption formations, with As(V) forming BB and As(III) forming MM complexes.

9.2. FURTHER WORK

This study has successfully used experimental and modelled simulations for arsenate interactions with goethite in groundwater. The experiments have demonstrated that partition coefficients derived for dynamic conditions are less than those for equilibrium adsorption. If the macroscopic transport of arsenic is to be simulated and predicted more accurately, reliable partition coefficients defining adsorption and desorption of arsenic in dynamic groundwater conditions must be established.

The pH effect upon equilibrium adsorption has been widely studied, but not the effect under dynamic conditions. The chemical kinetics that influence the goethite PZC (point of zero charge) may contribute towards improved partition coefficients. As the arsenate adsorption complexes formed on goethite are known to change with pH (Manning *et al.*, 1998), it follows that the rate at which those complexes form could be affected by imposed dynamic conditions. In order to identify the effect of kinetics for different types of surface reactions or complexes formed, a set of batch experiments would be required. The batches would be sampled at intervals and the solid-phase material analysed using spectroscopic techniques such as EXAFS and T-FTIR, to derive the adsorption complexes formed. The results of these experiments may also tie-in with changes to the adsorption structures resulting from variations in surface coverage. It follows that for a relatively short period of observation, surface coverage would be constrained by the kinetics of adsorption, compared with coverage at equilibrium. If batch adsorption experiments were allowed to continue beyond the equilibration time, which is typically 24 hours, other arsenic – goethite interactions may be observed. For example, surface cation exchange may occur between arsenic and surface iron. If contact is prolonged the migration of arsenic into the bulk structure may occur. Although the effect of surface cation exchange was simulated within this study, it could be taken further by including arsenic migration into the bulk structure, employing various impurity defect analogies within the models.

With reference to the adsorption of arsenic under various redox conditions, the current study has brought to attention the validity of such research. The results show that the pseudo-partition coefficient describing the release of arsenic under reducing conditions is less than that for the oxic equivalent. Although some solid-phase analysis has been done using analytical and high resolution SEM, further investigation would prove invaluable. The use of EXAFS would help to identify the arsenic structures formed on the goethite as reduction evolves. This progressive solid-phase analysis would be better explored using batch methods and sequentially extracting solid material for analysis at consecutive time intervals. Similarly, the comparison between equilibrium and dynamic adsorption and desorption in various redox environments would also help to distinguish between those partition coefficients that are more specific to individual environmental conditions. In order to eliminate possible interference caused by the incursion of oxygen, all redox experiments should be carried out in an oxygen-free environment, unlike those in this study.

It has not been possible to measure the arsenic species concentration in the redox column effluent, although an indication of the division between As(V) and As(III) would help to explain the desorption processes in reducing conditions. In an investigation of arsenic desorption from goethite under reducing conditions, Haury (2001) identified initial arsenic release caused by the reduction of As(V) to As(III). The arsenic reduction induces re-oxidation at the goethite surface, with subsequent arsenic adsorption. The reducing agent used, Catechol, simultaneously reduces the goethite and this adds to the complexity surrounding the surface interactions. It may be possible to assess the mineral – solute interactions at particular stages of reduction, by enforcing redox potentials. In which case it would be possible to quantify adsorption at various redox conditions with partition coefficients that are more relevant to groundwater environments where arsenic requires surveillance. Similar redox experiments using microbial reduction could also be carried out to simulate reduction in areas where microbial reduction occurs.

Aside from the experimental work, the atomic models may be employed to describe surface interactions under reducing conditions. An initial improvement to the atomistic simulations would require the addition of a

hydroxylated goethite surface. The 'dry' surfaces currently simulated have not been able to reproduce those energetically favourable surfaces simulated by other studies, or some of those that commonly dominate natural goethite crystals. This has been attributed to the lack of hydroxyls on the surface. Using quantum mechanical models rather than classical mechanic models could be employed to model charged arsenic ions to give a more accurate description of adsorption and complexation (Sherman and Randall, 2003).

Regarding the interactions of arsenic with goethite under various redox conditions, an initial step would involve similar adsorption simulations to those in this study, but instead using an arsenite molecule. Not only would this help to explain the adsorption mechanisms involved for the arsenite species, but the difference between As(V) and As(III) adsorption mechanisms could help to describe the desorption processes occurring in a reducing environment. In parallel with As(III) adsorption modelling, the subsequent reduction of the goethite surface could also be simulated with the reduction of Fe(III) to Fe(II) and the breakdown of the oxidised structure.

REFERENCES

Accelrys (2004). http://www.accelrys.com

Akber-Knutson S. & Bukowinski M.S.T. (2004). The Energetics of Aluminium Solubility into $MgSiO_3$ Perovskite at Lower Mantle Conditions. *Earth and Planetary Science Letters, 220(3-4), pp. 317-330.* http://www.seismo.berkley.edu/~manga?eps260/buko.pdf

Anderson M.A., Ferguson J.F. & Gavis J. (1976). Arsenate Adsorption on Amorphous Aluminium Hydroxide. *Journal of Colloid and Interface Science, 54(3), pp. 391-400.*

Appelo C.A.J. & Postma D. (1994). Geochemistry, Groundwater and Pollution. *A.A. Balkema Publishers, Rotterdam, Netherlands.*

Appelo C.A.J. & Postma D. (1999). A Consistent Model for Surface Complexation on Birnessite (-MnO_2) and its Application to a Column Experiment. *Geochimica et Cosmochimica Acta, 63 (19/20), pp. 3039-3048.*

Aragon A. & Thomson B. (2002). Rapid Small-Scale Column Testing for Arsenic Adsorption Media. *http://ipec.utulsa.edu/Ipec/Conf2002/Aragon_Thomson_Chwlika_50.pdf*

Arai Y., Elzinga E.J. & Sparks D.L. (2001). X-Ray Absorption Spectroscopic Investigation of Arsenite and Arsenate Adsorption at the Aluminium Oxide-Water Interface. *Journal of Colloid and Interface Science, 235, pp. 80-88.*

Armienta M.A., Vielasenor G., Rodriguiz R., Ongley L.K. & Mango M. (2001). The Role of Arsenic-Bearing Rocks in Groundwater Pollution at Zimapan Valley, Mexico. *Environmental Geology, 40(4-5), pp. 571-581.*

Atkins P.W., Clugston M.J., Frazer M.J. & Jones R.A.Y. (1988). Chemistry: Principles and Applications. *First Edition, Longman Group Ltd, Essex, UK.*

Baes C.F. & Sharp R.D. (1983). A Proposal for Estimation of Soil Leaching and Leaching Constants for Use in Assessment Models. *Journal of Environmental Quality, 12, pp. 17-28.*

Baram P.S. & Parker S.C. (1996). Atomistic Simulation of Hydroxide Ions in Inorganic Solids. *Special Issue on Interatomic Potentials, Phil. Mag. B., 73(1), pp.49-58.*

Bargar J.R., Persson P. & Brown Jr. G.E. (1999). Outer-Sphere Adsorption of Pb(II) EDTA on Goethite. *Geochimica et Cosmochimica Acta, 63(19/20), pp. 2957-2969.*

Barnett M.O., Jardine P.M., Brooks S.C. & Selim H.M. (2000). Adsorption and Transport of Uranium (VI) in Subsurface Media. *Soil Science Society of America Journal, 64, pp. 908-917.*

Barrón V., Gálvez N., Hochella Jr. M.F. & Torrent J. (1997). Epitaxial Overgrowth of Goethite on Hematite Synthesised in Phosphate Media: A Scanning Force and Transmission Electron Microscopy Study. *American Mineralogist, 82, pp. 1091-1100.*

Berg M., Tran H.C., Nguyen T.C., Pham H.V., Schertenleib R. & Geiger W. (2000). Arsenic Contamination of Groundwater and Drinking Water in Vietnam: A Human Health Threat. *Environmental Science and Technology, 35(13), pp. 2621 – 2626.*

Bhumbla D.K. & Keefer R.F. (1994). Arsenic Mobilisation and Bioavailability in Soils. *In: Arsenic in the Environment, Part I: Cycling and Characterisation (Ed. Nriagu J.O.), pp. 51-82.*

Born M. & Huang K. (1954). Dynamical Theory of Crystal Lattices. *Oxford University Press, Clarendon, UK.*

Bostock L. & Chandler S. (1993). Core Maths for A-Level. *Stanley Thornes (Publishers) Ltd, Cheltenham, UK.*

Bowell R.J. (1994). Sorption of Arsenic by Iron Oxides and Oxyhydroxides in Soils. *Applied Geochemistry, 9, pp. 279-286.*

British Geological Survey & Mott MacDonald Ltd [BGS & MML] (1999). Phase 1: Rapid Investigation Phase, Main Report. *Groundwater Studies for Arsenic Contamination in Bangladesh. Department of Public Health Engineering (DPHE).*

Carrillo A. & Drever J.I. (1998). Adsorption of Arsenic by Natural Aquifer Material in the San Antonio-El Triunfo Mining Area, Baja California, Mexico. *Environmental Geology, 35(4), pp. 251-257.*

Carrillo-Chavez A., Drever J.I. & Martinez M. (2000). Cases and Solutions: Arsenic Content and Groundwater Geochemistry of the San-Antonio-El Triunfo, Carrizal and Los Planes Aquifers in Southernmost Baja California. *Environmental Geology, 39(11), pp. 1295-1303.*

Catlow C.R.A. (1977). Point Defect and Electronic Properties of Uranium Dioxide. *Proceedings of the Royal Society of London, A, 353, pp. 533-561.*

Catlow C.R.A. (2003). Computer Modelling of Materials: An Introduction. *In: Computational Materials Science, NATO Science Series III: Computer and Systems Sciences – Vol. 187 (Ed. Catlow R. & Kotomin E.), pp. 1-29.*

Chakraborti D., Biswas B.K., Chowdury T.R., Basu G.K., Mandal B.K., Chowdury U.K., Mikherjee S.C., Gupta J.P., Chowdury S.R. & Rathone K.C. (1999). Arsenic Groundwater Contamination and Sufferings of People in Rajnardgaon District, Madhya Pradesh, India. *Current Science India, 77(4), pp. 502-504.*

Chakravarty S., Dureja V., Bhattacharyya G., Maity S., Bhattacharjee S. (2002). Removal of Arsenic From Groundwater Using Low Cost Ferruginous Manganese Ore. *Water Research, 36(3), pp. 625-632.*

Chemviz (2003). http://chemviz.ncsa.uiuc.edu

Collins D.R. & Catlow C.R.A. (1992). Computer Simulation of Structures and Cohesive Properties of Micas. *American Mineralogist, 77, pp. 1172-1181.*

Collins C.R., Sherman D.M. & Vala Ragnarsdottir K. (1999). Surface Complexation of Hg^{2+} on Goethite: Mechanism from EXAFS Spectroscopy and Density Functional Calculations. *Journal of Colloid and Interface Science, 219, pp. 345-350.*

Cormack A.N. (1999). Classical Computer Simulations. *In: Microscopic Properties & Processes in Minerals (Ed. Wright K. & Catlow C.R.A.), NATO ASI Series C, 543, pp. 337-350.*

Cornell R.M. & Schwertmann U. (1996). The Iron Oxides: Structure, Properties, Reactions, Occurrence and Uses. *VCH Weiheim, Federal Republic of Germany.*

Cox M.C. (1994). A-Level and AS-Level Chemistry Reference Guide. *Longman Group Ltd, Essex, UK.*

Cummings D.E, Caccavo F. Jr., Fendorf S. & Rosenzweig R.F. (1999). Arsenic Mobilization by The Dissimilatory Fe(III)-Reducing Bacterium Shewanella alga BrY. *Environmental Science and Technology, 33, pp. 723-729.*

Cuthbert M. (1999). Modelling the Transport of Arsenic to Hand Pumped Tube-Wells in the Holocene Alluvial Aquifer of Bangladesh. *Unpublished MSc. Thesis, Department of Geological Sciences, UCL, UK.*

Cygan R.T. (2001). Molecular Modelling in Mineralogy and Geochemistry. *Reviews in Mineralogy and Geochemistry (Ed. Cygan R.T. & Kubicki J.D.), pp. 1-35.*

Darland J.E. & Inskeep W.P. (1997). Effects of Pore Water Velocity on The Transport of Arsenate. *Environmental Science & Technology, 31(3), pp. 704-709.*

De Brouwere K., Smolders E. & Merckx R. (2004). Soil Properties Affecting Solid-Liquid Distribution of As(V) in Soils. *European Journal of Soil Science, 55(1), pp. 165-173.*

De Leeuw N.H. & Parker S.C. (1997). Atomistic Simulation of the Effect of Molecular Adsorption on the Surface Structure and Energetics of Calcite. *J. Chem. Soc. Faraday Transactions, 94, pp. 467-475.*

De Leeuw N.H., Cooper T.G., Nelson C.J., Mkhonto D. & Ngoepe P.E. (2003). Computer Simulation of Surfaces of Metals and Metal-Oxide Materials. *Computer Materials Science (Ed. Catlow C.R.A. & Kotomin E.A.), NATO Science Series III: Computer & Systems Sciences, 187, pp. 218-244.*

Del Razo L.M., Arellano M.A. & Cebrián M.E. (1990). The Oxidation States of Arsenic in Well Water from a Chronic Arsenicism Area of Northern Mexico. *Environmental Pollution, 64, pp. 143-153.*

Dick B.G. & Overhauser A.W. (1958). Theory of the Dielectric Constant of Alkali Halide Crystals. *Phys. Rev., 112, pp. 90-103.*

Domenico P.A. & Schwartz F.W. (1998). Physical and Chemical Hydrogeology. *Second Edition, John Wiley & Sons, New York.*

Driehaus W., Seith R. & Jekel M. (1995). Oxidation of Arsenic (III) With Manganese Oxides in Water Treatment. *Water Research, 29, pp. 297-305.*

Duda R. & Rejl L. (1990). Minerals of The World. *Arch Cape Press, New York.*

Dzombak D.A. & Morel F.M.M. (1990). Surface Complexation Modelling – Hydrous Ferric Oxide. *Wiley Publishers.*

Ewald P.P. (1921). The Calculation of Optical and Electrostatic Lattice Potential. *Ann. Phys. (Leipzip), 64, pp. 253-287.*

Farquhar M.L., Charnock J.M., Livens F.R. & Vaughan D.J. (2002). Mechanisms of Arsenic Uptake from Aqueous Solution by Interaction with Goethite, Lepidicrocite, Mackinawite and Pyrite: An X-Ray Absorption Spectroscopy Study. *Environmental Science and Technology, 36(8), pp. 1757-1762.*

Fendorf S., Eick M.J., Grossl P. & Sparks D.L. (1997). Arsenate and Chromate Retention Mechanisms on Goethite. 1. Surface Structure. *Environmental Science and Technology, 31(2), pp. 315-320.*

Ferguson J.F. & Gavis J. (1972). A Review of the Arsenic Cycle in Natural Waters. *Water Res., 6, pp. 1259-1274.*

Fetter C.W. (1994). Applied Hydrogeology. *Third Edition, Prentice-Hall Inc., New Jersey.*

Fetter C.W. (1998). Contaminant Hydrogeology. *Second Edition, Prentice-Hall Inc., New Jersey.*

Fisher L. (1999). Investigations of The Ad-/Desorption and Diffusion Processes of Heavy Metals and Aluminium With Goethites of Different Crystallinity – Experimental Results and Process Modelling. *Unpublished Thesis, Landw. Fak. Diss., Bonn.*

Fitts J.P., Foster A.L., Savage K.S., Trainor T.P., Parks G.A., Basler J., Madix R.J. & Brown G.E. Jr. (1997). Environmental Geochemistry of Chromium, Selenium and Arsenic at Mineral – Water Interfaces: Field and Laboratory Studies. *Experimental Progress Report, Stanford Synchrotron Radiation Laboratory, pp. 7-186.*

Fuller C.C., Davis J.A. & Waychunas G.A. (1993). Surface Chemistry of Ferrihydrite: 2. Kinetics of Arsenate Adsorption and Coprecipitation. *Geochimica et Cosmochimica Acta, 57, pp/ 2271-2282.*

Fullick A. & Fullick P. (1994). Chemistry. *First Edition, Heinemann Advanced Science, Heinemann Educational Publishers, Oxford, UK.*

Gaboriaud F. & Ehrhardt J-J. (2003). Effects of Different Crystal Faces on the Surface Charge of Colloidal Goethite (α-FeOOH) Particles: An Experimental and Modelling Study. *Geochimica et Cosmochimica Acta, 67(5), pp. 967-983.*

Gadewar S.B., Hofmann H.M. & Doherty M.F. (2004). Evolution of Crystal Shape. *Crystal Growth and Design, 4(1), pp. 109-112.*

Gale J.D. (1997). GULP: A Computer Program for the Symmetry Adapted Simulation of Solids. *J. Chem. Soc. Faraday Trans., 93, pp. 629-637.*

Gale J.D. (2001). Simulating the Crystal Structures and Properties of Ionic Materials from Interatomic Potentials. *Reviews in Mineralogy & Geochemistry (Ed. Cygan R.T. & Kubicki J.D.), pp. 37-62.*

Gale J.D. (2003). Personal Communication.

Gale J.D. & Rohl A.L. (2003). The General Utility Lattice Program (GULP). *Molecular Simulations, 29(5), pp. 291-341.*

Gay D.H. & Rohl A.L. (1994). MARVIN: A New Computer Code for Studying Surfaces and Interfaces and its Application to Calculating the Crystal Morphologies of Corundum and Zircon. *J. Chem. Soc. Faraday Trans., 91, pp. 1-12.*

GDIS (2003). http://gdis.seul.org

Goldberg S. & Glaubig R.A. (1988). Boron and Silicon Adsorption on an Aluminium Oxide. *Soil Science Society of America Journal., 52, pp/ 87-91.*

Goldberg S. & Johnston C.T. (2001). Mechanisms of Arsenic Adsorption on Amorphous Oxides Evaluated Using Macroscopic Measurements, Vibrational Spectroscopy, and Surface Complexation Modelling. *Journal of Colloid and Interface Science, 234, pp. 204-216.*

Goldberg S. (2002). Competitive Adsorption of Arsenate and Arsenite on Oxides and Clay Minerals. *Soil Science Society of America Journal, 66, pp. 413-421.*

Gorby M.S. (1994). Arsenic in Human Medicine. *In: Arsenic in the Environment: Part II – Human Health and Ecosystem Effects (Ed. Nriagu J.O.), p. 1-16.*

Gualtieri A.F. & Venturelli P. (1999). In Situ Study of the Goethite – Hematite Phase Transformation by Real Time Synchrotron Powder Diffraction. *American Mineralogist, 84, pp. 895-904.*

Halter W.E. & Pfeifer H-R. (2001). Arsenic (V) Adsorption onto α-Al_2O_3 Between 25 C and 70 C. *Applied Geochemistry, 16, pp. 793-802.*

Haron M.J., Wan Yunus W.M.Z., Yong N.L. & Tokunaga S. (1999). Sorption of Arsenate and Arsenite Anion by Fe(III)-Poly(hydroxamic Acid) Complex. *Chemosphere, 39(14), pp. 2459-2466.*

Harrington J.M., Fendorf S.E. & Rosenzweig R.F. (1998). Biotic Generation of Arsenic (III) in Metal(loid) – Contaminated Fresh-Water Lake Sediments. *Environmental Science & Technology, 32, pp. 2425-2430.*

Haury V. (2001). Redox-Induziete Speziesvertelung Von Arsen im Eisenreduktion-Smilieu Hervorgerufen Durch Catechol. *Unpublished PhD Thesis, University of Heidelberg.* (http://www.ub.uni-heidelberg.de/archiv/1772).

Hingston F.J., Posner A.M., Quirk J.P. (1972). Anion Adsorption by Goethite and Gibbsite. I: The Role of Proton in Determining Adsorption Envelopes. *Journal of Soil Science, 23, pp. 177-192.*

Hofmann A., Pelletier M., Michot L., Stradner A., Schurtenberger P. & Kretzschmar R. (2004). Characterisation of The Pores in Hydrous Ferric Oxide Aggregates Formed By Freezing and Thawing. *Journal of Colloid and Interface Science, 271, pp. 163-173.*

Islam F.S., Gault A.G., Boothman C., Polya D.A., Charnock J.M., Chatterjee D. & Lloyd J.R. (2004). Role of Metal – Reducing Bacteria in Arsenic Release From Bengal Delta Sediments. *Nature, 430, pp. 68-71.*

Jackson B.P. & Miller W.P. (2000). Effectiveness of Phosphate and Hydroxide for Desorption of Arsenic and Selenium Species from Iron Oxides. *Soil Science Society of America Journal, 64, pp. 1616-1622.*

Jones C.A., Langner H.W., Anderson K., McDermott T.R. & Inskeep W.P. (2000). Rates of Micorbially Mediated Arsenate Reduction and Solubilization. *Soil Science Society of America Journal, 64, pp. 600-608.*

Jones F., Rohl A.L., Farow J.B. & Van Bronswijk W. (2000). Molecular Modelling of Water Adsorption on Hematite. *Phys. Chem. Chem. Phys., 2, pp. 3209-3216.*

Kent D.B., Davis J.A. & Anderson L.C.D. (1995). Transport of Chromium and Selenium in a Pristine Sand and Gravel Aquifer: Role of Adsorption Processes. *Water Resources Research, 31, pp. 1041-1050.*

Khaodhiar S., Azizian M.F., Osathaphan K. & Nelson P.O. (2000). Copper, Chromium, and Arsenic Adsorption and Equilibrium Modelling in an Iron-Oxide-Coated Sand, Background Electrolyte System. *Water, Air, and Soil Pollution, 119, pp. 105-120.*

Klein C. & Hurlbut C.S.Jr. (1993). Manual of Mineralogy. *Twenty First Edition (After Dana J.), John Wiley & Sons, New York.*

Krauskopf K.B. & Bird D.K. (1997). Introduction to Geochemistry. *Third Edition, McGraw-Hill Inc., New York.*

Kuhlmeier P.D. (1997). Partitioning of Arsenic Species in Fine-Grained Soils. *Journal of Air and Waste Management Association, 47, pp. 481-490.*

Ladiera A.C.Q., Ciminelli V.S.T., Duarte H.A., Alves M.C.M. & Ramos A.Y. (2001). Mechanism of Anion Retention from EXAFS and Density Functional Calculations: Arsenic (V) Adsorbed on Gibbsite. *Geochimica et Cosmochimica Acta, 65(8), pp. 1211-1217.*

Leach A.R. (2001). Molecular Modelling: Principles and Applications. *Second Edition, Pearson Education EMA.*

Levinson R. (2004). http://www.rsc.org/pdf/LearnNet/rsc/AA-txt.pdf

Lewis G.V. & Catlow C.R.A. (1985). Potential Models for Ionic Oxides. *J. Phys. (C): Solid State Physics, 18, pp. 1149-1161.*

Lima-de-Faria J. (1963). Dehydration of Goethite and Diaspore. *Zeitschrift für Kristallographie, 119, pp. 176-203.*

Lin T-F. & Wu J-K. (2001). Adsorption of Arsenite and Arsenate Within Activated Alumina Grains: Equilibrium and Kinetics. *Water Res., 35(8), pp. 2049-2057.*

Loeppert R.H., Jain A., Raven K. & Wang J. (1997). Arsenate and Arsenite Retention and Release in Oxide and Sulphide Dominated Systems. *Technical Report No. 176, Texas Water Resources Institute, Texas A & M University.*

Lu J.J. & Ulrich J. (2003). An Improved Prediction Model of Morphological Modifications of Organic Crystals Induced by Additives. *Cryst. Res. Technol., 38(1), pp. 63-73.*

Lumsdon D.G., Meeussen J.C.L., Paterson E., Garden L.M. & Anderson P. (2001). Use of Solid Phase Characterisation and Chemical Modelling for Assessing the Behaviour of Arsenic in Contaminated Soils. *Applied Geochemistry, 16(6), pp. 571-581.*

Madhavan N. & Subramanian V. (2000). Sulphide Mining As a Source of Arsenic in the Environment. *Current Science, 78(6), pp. 702-708.*

Manceau A., Nagy K.L., Spadini L. & Vala Ragnarsdottir K. (2000). Influence of Anionic Layer Structure of Fe-Oxyhydroxides on the Structure of Cd Surface Complexes. *Journal of Colloid and Interface Science, 228, pp. 305-316.*

Manning B.A. & Goldberg S. (1997). Arsenite and Arsenate Adsorption on Californian Soils. *Soil Science, 162(12), pp. 886-895.*

Manning B.A., Fendorf S.E. & Goldberg S. (1998). Surface Structures and Stability of Arsenite on Goethite: Spectroscopic Evidence for Inner-Sphere Complexes. *Environmental Science and Technology, 32(16), pp. 2383-2388.*

Matis K.A., Zouboulis A.I., Zamboulis D & Valtadorou A.V. (1999). Sorption of As(V) by Goethite Particles and Study of Their Flocculation. *Water, Air and Soil Pollution, 111, pp. 297-316.*

McArthur J.M., Ravenscroft P., Safiullah S. & Thirwall M.F. (2001). Arsenic in Groundwater: testing pollution mechanisms for sedimentary aquifers in Bangladesh. *Water Res. Research, 37, 109-117.*

McArthur J.M., Banerjee D.M., Hudson-Edwards K.A., Mishra R., Purohit R., Ravenscroft P., Cronin A., Howarth R.J., Chatterjee A., Talukder T., Lowry D., Houghton S. & Chada D.K. (2004). Natural Organic Matter in Sedimentary Basins and its Relation to Arsenic in Anoxic Ground Water: The Example of West Bengal and its Worldwide Implications. *Applied Geochemistry, 19(8), pp. 1255-1293.*

Miller G.P. (2004). Arsenic Partitioning: Making Predictions Using PHREEQC. http://wwwbm.cr.usgs.gov/Arsenic/FinalAbsPDF/miller.pdf

Nagai T., Kagi H. & Yamanaka T. (2003). Variation of Hydrogen Bonded O – O Distances in Goethite at High Pressure. *American Mineralogist, 88. pp. 1423-1427.*

Naqvi S.M., Vaishnavi C. & Singh H. (1994). Toxicity and Metabolism of Arsenic in Vertebrates. *In: Arsenic in The Environment, Part II: Human Health and Ecosystem Effects (Ed. Nriagu J.O.), pp. 55-92.*

Nickolaidis N.P. & Lackovic J. (2001). Arsenic Remediation Technology – AsRT. *Environmental Research Institute, United Technologies Research Centre.* http://clu-in.org/contaminantfocus/default.focus/sec/arsenic/cat/

Nickson R.T., McArthur J.M., Ravenscroft P., Burgess W.G. & Ahmed K.M. (2000). Mechanism of Arsenic Release to Groundwater in Bangladesh and West Bengal. *Applied Geochemistry, 15, pp. 403-413.*

Nimick D.A. (1998). Arsenic Hydrogeochemistry in an Irrigated River Valley – A Re-evaluation. *Ground Water, 36(5), pp. 743-753.*

Nordstrom D.K. & Wilde F.D. (1998). 6.5. Reduction – Oxidation Potential (Electrode Method). *USGS TWRI Book 9.*

Norman N.C. (1998). Chemistry of Arsenic, Antimony and Bismuth. *Blackie Academic & Professional, London & New York.*

O'Reilly S.E., Strawn D.G. & Sparks D.L. (2001). Residence Time Effects on Arsenate Adsorption/Desorption Mechanisms on Goethite, *Soil Society of America Journal, 65, 67-77.*

Ostergren J.D., Trainor T.P., Bargar J.R., Brown Jr. G.E. & Parks G.A. (2000[I]). Inorganic Ligand Effects on Pb(II) Sorption to Goethite (α-FeOOH) – I. Carbonate. *Journal of Colloid and Interface Science, 225, pp. 466-482.*

Ostergren J.D., Brown Jr. G.E., Parks G.A. & Persson P. (2000[II]). Inorganic Ligand Effects on Pb(II) Sorption to Goethite (α-FeOOH) – II. Sulphate. *Journal of Colloid and Interface Science, 225, pp. 483-493.*

Pang L., Close M., Schneider D. & Stanton G. (2002). Effect of Pore-Water Velocity on Chemical Non-equilibrium Transport of Cd, Zn, and Pb in Alluvial Gravel Columns. *Journal of Contaminant Hydrology, 57, pp. 241-258.*

Parker S.C. & Price G.D. (1985). A Study of the Structures and Energetics of Magnesium Silicates. *Physica 131B, pp. 290-299.*

Parkhurst D.L. (1995). Users Guide to PHREEQC – A Computer Program For Speciation, Reaction-Path, Advective Transport, and Inverse Geochemical Calculations. *US Geological Survey Water Resources Inv. Rep., 95-4227, pp. 143.*

Pertlik F. (1978). Structure Refinement of Cubic As_2O_3 (Arsenolite) With Single-Crystal Data. *Czech. J. Phy., B28, pp. 170-176.*

Pierce M.L. & Moore C.B. (1982). Adsorption of Arsenite and Arsenate on Amorphous Iron Oxyhydroxide. *Water Res., 16, pp. 1247-1253.*

Pivovarov S. (2002). Structure of the Oxide-Solution Interface. *Encyclopaedia of Surfaces and Colloid Science, pp. 1-9.*

Polya D.A., Rowland H.A.L., Gault A.G., Diebe N.H., Jones J.C. & Cooke D.A. (2004). Geochemistry of Arsenic – Rich Shallow Groundwaters in Cambodia. *Goldschmidt 2004, Copenhagen 8th – 13th June, A291,* www.goldschmidt2004.dk.

Pracht J., Bowenigk J., Isenbeck-Schröter M., Keppler F. & Schöler H.F. (2001). Abiotic Fe(III) Induced Mineralisation of Phenolic Substances. *Chemsosphere, 44, pp. 613-319.*

Puls R.W. & Powell R.M. (1992). Acquisition of Representative Ground Water Quality Samples for Metals. *Ground Water Monitoring Review, 12(3), pp. 167-176.*

Purton J. & Catlow C.R.A. (1990). Computer Simulation of Feldspar Structures. *American Mineralogist, 75, pp. 1268-1273.*

Raab A. & Feldmann J. (2003). Microbial Transformation of Metals and Metalloids. *Science Progress, 86(3), pp. 179-202.*

Rakovan J., Becker U. & Hochella Jr. M.F. (1999). Aspects of Goethite Microtopography, Structure, Chemistry, and Reactivity. *American Mineralogist, 84, pp. 884-894.*

Randall S.R., Sherman D.M., Vala Ragnarsdottir K. & Collins C.R. (1999). The Mechanism of Cadmium Surface Complexation on Iron Oxyhydroxide Minerals. *Geochimica et Cosmochimica Acta, 63 (19/20), pp. 2971-2987.*

Ravenscroft P., McArthur J.M. & Hoque B.A. (2001). Geochemical and Palaeohydrological Controls on Pollution of Groundwater by Arsenic. *In: Arsenic Exposure and Health Effects IV (Eds. Chappell W.R., Abernathy C.O. and Calderon R., pp. 53-78. Elsevier Science Ltd, Oxford.*

Rochette E.A., Li G.C., Bostick B.C. & Fendorf S. (2000). Kinetics of Arsenate Reduction by Dissolved Sulphide. *Environmental Science & Technology, 34, pp. 4714-4720.*

Sanders M.J., Leslie M. & Catlow C.R.A. (1984). Interatomic Potentials for SiO_2. *J. Chem. Soc.: Chem. Comm. pp. 1271-1273.*

Scheidegger A.M. & Sparks D.L. (1996). Critical Assessment of Sorption/Desorption Phenomena on Natural Materials. *Soil Science, 161(12), pp. 813-831.*

Schroder K.P., Sauer J., Leslie M., Catlow C.R.A. & Thomas J.M. (1992). Bridging Hydroxyl-Groups in Zeolitic Catalysts – A Computer Simulation of Their Structure, Vibrational Properties and Acidity in Protonated Faujasites. *Chem. Lett., 188, pp. 320-325.*

Schwartz R., Juo A., Mcinnes K. & Cervantes C. (1998). Anion Transport in Fine-Textured Ultisol in Costa Rica. *Proceedings of The 16th World Congress of Soil Science, Montpellier, France. International Society of Soil Science.* Http://www.cprl.ars.usda.gov/wmru/rschwartz/isss.pdf

Schwertmann U. & Cornell R.M. (2000). Iron Oxides in the Laboratory: Preparation and Characterisation. *Second Edition.*

Sherman D.M. (2002). Environmental Geochemistry. http://mineral.gly.bris.ac.uk/envgeochem.

Sherman D.M. & Randall S.R. (2003). Surface Complexation of Arsenic (V) to Iron (III) (hydr)oxides: Structural Mechanism From *ab initio* Molecular Geometries and EXAFS Spectroscopy. *Geochimica et Cosmochimica Acta, 67(22), 4223-4230.*

Sing K.S.W. (1997). Analysis of Physisorption Isotherms. Determination of Surface Area and Porosity. *Physical Adsorption: Experiment, Theory and Applications (Ed. Fraissard J.), NATO ASI Series; C: Mathematical and Physical Sciences, 491, pp. 9-16.*

Smedley P.L., Nicolli H.B., Macdonald D.M.J., Barros A.J. and Tullio J.O. (2002). Hydrogeochemistry of Arsenic and Other Inorganic Constituents in Groundwaters From La Pampa, Argentina. *Applied Geochemistry, 17, pp. 259-284.*

Smedley P.L. & Kinniburgh D.G. (2002). A review of the Source, Behaviour and Distribution of Arsenic in Natural Waters. *Applied Geochemistry, 17(5), pp. 517-568.*

Smith E., Naidu R. & Alston A.M. (2002). Chemistry of Inorganic Arsenic in Soils: II. Effect of Phophorus, Sodium and Calcium on Arsenic Sorption. *Journal of Environmental Quality, 31, pp. 557-563.*

Srinivasan P. & Mercer J.M. (1987). BIO1D: One-Dimensional Model for Comparison of Biodegradation and Adsorption Processes in Contaminant Transport. *GeoTrans Inc., Washington DC.*

Steele H.M., Wright K., Nygren M.A. & Hillier I.H. (2000). Interactions of the (001) Surface of Muscovite with Cu(II), Zn(II), and Cd(II): A Computer Simulation Study. *Geochimica et Cosmochimica Acta, 64(2), pp. 257-262.*

Steele H.M., Wright K. & Hillier I.H. (2002). Modelling the Adsorption of Uranyl on the Surface of Goethite. *Geochimica et Cosmochimica Acta, 66(8), pp. 1305-1310.*

Stollenwerk K.G. (2003). Geochemical Processes Controlling Transport of Arsenic in Groundwater: A Review of Adsorption. *Arsenic in Groundwater (Ed. Welch A.H. & Stollenwerk K.G.), Chapter 3, pp. 67-100.*

Su C. & Suarez D.L. (2000). Selenate and Selenite Sorption on Iron Oxides: An Infrared and Electrophoretic Study. *Soil Science Society of America Journal, 64, pp. 101-111., Division S-2 – Soil Chemistry.*

Sun X. & Doner H.E. (1996). An Investigation of Arsenate and Arsenite Bonding Structures on Goethite by FTIR. *Soil Science, 161(2), pp. 865-872.*

Suzuki S., Suzuki T., Kimura M., Takagi Y., Shinoda K., Tohji K. & Waseda Y. (2001). EXAFS Characterisation of Ferric Oxyhydroxides. *Applied Surface Science, 169-170, pp. 109-112.*

Szytula A., Burewicz A., Dimitrijevic Z., Krasnioki S., Rzany H., Todorovic J., Wanic A. and Wolski W. (1968). Neutron Diffraction Studies of α-FeOOH. *Phys. Stat. Sol., 26, pp. 429-434.*

Tasker P.W. (1979). The Stability of Ionic Crystals. *Journal of Physics, C: Solid State Physics, 12, pp. 4977-4984.*

Thirunavukkaiasu O.S., Viraraghavan T. & Subramanian K.S. (2003). Arsenic Removal From Drinking Water Using Granular Ferric Hydroxide. *Water, South Africa, 29, pp. 161-170.*

Tossel J.A. (1997). Theoretical Studies on Arsenic Oxide and Hydroxide Species In Minerals and Aqueous Solution. *Geochimica et Cosmochimica Acta, 61(8), pp. 1613-1623.*

USGS (1999). http://www.brr.cr.usgs.gov/Arsenic/
& http://webserver.cr.usgs.gov/trace/arsenic.

Vaishya R.C. & Gupta S.K. (2002). Modelling Arsenic(III) Adsorption from Water by Sulphate-Modified Iron-Oxide Coated Sand (SMIOCS). *Journal of Chemical Technology and Biotechnology, 78, pp. 73-80.*

Van Westrenen W., Allan N.L., Blundy J.D., Lavrentiev M. Yu., Lucas B.R. & Purton J.A. (2003). Trace Element Incorporation into Pyrope – Grossular Solid Solutions: An Atomistic Simulation Study. *Phy. Chem. Minerals, 30, pp. 217-229.*

Verma S., Singh M.K., Wadhawan V.K. & Suresh C.H. (2000). Growth Morphology of Zinc Tris(thiaurea) Sulphate Crystals. *Pramana – Journal of Physics, 54(6), pp. 879-888.*

Voth-Beach L.M. & Shrader D.E. (1985). Reduction of Interference in the Determination of Arsenic and Selenium by Hydride Generation. *Spectroscopy 1, pp. 60-65.*

Waychunas G.A., Rea B.A., Fuller C.C. & Davis J.A. (1993). Surface Chemistry of Ferrihydrite: Part 1. EXAFS Studies of The Geometry of Co-precipitated and Adsorbed Arsenate. *Geochimica et Cosmochimica Acta, 57, pp. 2251-2269.*

Weckler B. & Lutz H.D. (1998). Lattice Vibration Spectra. Part XCV. Infrared Spectroscopic Studies on the Iron Oxide Hydroxides Goethite (α), Akaganeite (β), Lepidocrocite (χ), and Feroxyhite (δ). *Eur. J. Solid State Inorg. Chem., 35, pp. 531-544.*

Welch A.H., Lico M.S. & Hughes J.L. (1988). Arsenic in Groundwater of the Western United States. *Ground Water, 26, 333-347.*

Welch A.H. & Lico M.S. (1998). Factors Controlling As and U in Shallow Groundwater, South Carson Desert, Nevada. *Applied Geochemistry, 13(4), pp. 521-539.*

Wimmer E. (1996). Computational Materials Design and Processing: Perspectives for Atomistic Approaches. *Material Science and Engineering, B37,pp. 72-82.*

Wright K., Watson G.W., Parker S.C. & Vaughan D.J. (1998). Simulation of the Structure and Stability of Sphalerite (ZnS) Surfaces. *American Mineralogist, 83, pp. 141-146.*

Wright K., Cygan R.T. & Slater B. (2002). Impurities and Nonstoichiometry in the Bulk and on the (10_4) Surface of Dolomite. *Geochimica et Cosmochimica Acta, 66(14), pp. 2541-2546.*

Yokoyama T., Takahashi Y. & Tarutani T. (1993). Simultaneous Determination of Arsenic and Arsenious Acids in Geothermal Water. *Chem. Geol., 103, pp. 103-111.*

Yoshida T. & Nakashima S. (2000). Dissolution of Goethite by Catechol: Adsorption and Surface Complexes. *Journal of Conference Abstracts, 5(2), pp. 116., Goldschmidt Conference 2000.*

ACKNOWLEDGEMENTS

I would like to thank all those who assisted with the analytical work presented within this thesis, and particularly Vic Din and Gary Jones from the Natural History Museum Mineralogy Laboratories, and Tony Osborn from the University College London Wolfson Laboratory for Environmental Geochemistry. I would also like to thank Dr. Julian Gale for his assistance with some of the atomic simulations, and the School of Physical and Mineral Sciences at the University of the North In the North (UNIN), South Africa for allowing me to spend an enjoyable two months within their department diversifying my knowledge of computer modelling techniques.

Finally I would like to thank my friends and family who have given support and encouragement.